Materials and Methods for Microfluidic Fuel Cells

by

Ben Nearingburg

A thesis submitted in partial fulfillment of the requirements for the degree of

Doctor of Philosophy

In

Materials Engineering

Department of Chemical and Materials Engineering
University of Alberta

Abstract

Microfluidic fuel cell (MFC) devices are a promising route towards on-chip power generation for microfluidic and lab-on-a-chip systems. Current MFCs leverage fabrication techniques and materials that have been inherited from micromachining technology and macro-scale fuel cell devices. Both, these methods and materials can be costly and difficult to integrate into larger microfluidic networks or lab-on-a-chip devices. In order to fully explore the utility of MFCs, device should be composed of common microfluidic materials (*i.e.* formed from the same materials as the rest of the device) and amendable to fabrication alongside other components of microfluidic devices (*i.e.* not require specialized equipment/techniques for patterning). This thesis set out to improve the applicability of MFC devices by enhancing fabrication methods and describing new functional materials to better align MFCs with microfluidic device architectures. To achieve this goal, I focused my efforts on improving individual sub-components of the MFC device architecture to yield more effective devices. Throughout this thesis, emphasis was placed upon leveraging techniques amenable to low-cost bench-top processing (*i.e.* those that do not require expensive capital equipment) to broaden the applicability of MFC devices. My work was applied to three components of planar MFC devices (where a device consists of a single sided microchannel and a flat capping layer). First, proton exchange membranes capable of *in situ* patterning were developed and characterized. Second, oxygen transport through air breathing polymer layers was assessed through finite element modelling to better understand factors governing air breathing MFC devices. Finally, a new technique, multi-layer *in situ* laminar flow lithography, was introduced and characterized. This technique was shown to allow for patterning of multi-layer metal films to yield independent catalytic electrodes. Functional alkaline direct methanol fuel cell devices were then fabricated and characterized using the technique. The utility and applicability of each of these techniques to both MFCs and the wider field of microfluidics was assessed and possible applications discussed.

Preface

This thesis contains work which has been previously published in literature. Chapter 3 uses content published in “Photopolymerizable sulfonated poly(ethylene glycol) proton exchange memrbanes for microfluidic and fuel cell applications” Nearingburg B, Elias A L *Journal of Membrane Science* 389 (2012) 148-154. Copyright © 2011 Elsevier B .V. I performed all experimental results and data processing. In Chapter 4, Section 4.2 and Section 4.3 use content published in “Finite element analysis of oxygen transport in microfluidic cell culture devices with varying channel architectures, perfusion rates, and materials” Zahorodny-Burke M, Nearingburg B, Elias A L *Chemical Engineering Science* 66 (2011) 6244-6253. Copyright © 2011 Elsevier. In this publication, M. Zahorodny-Burke derived an initial finite element modelling simulation for microfluidic cell culture devices which I later generalized for a variety of fluid flow profiles and adapted to model microfluidic fuel cell devices. Chapter 5, uses content from “Patterning multilayer microfluidic electrochemical devices by maskless laminar flow lithography” Nearingburg B, Elias A L *RSC Advances* Accepted for publication June 19, 2014. In this work, I performed all fabrication, experimentation, and data processing. Through all of my published work Dr. Anastasia Elias has contributed as a supervisory author and has assisted with manuscript preparation, editing, and general advice.

```
for α={family, friends, colleagues}
    for β ={support, understanding, and patience}
    To my α for your β
    end
end
```

Acknowledgements

While the title page of this thesis implies myself as its sole author, preparation of this manuscript (and the work contained within) has been a collaborative effort with family, friends, and colleagues. First I would like to thank two people in particular. First I would like to thank my Mom for all her steady support during the course of my degree. I would also like to thank Dr. Anastasia Elias. Her guidance, input, and has been essential to all aspects of my work and has been greatly appreciated.

Over the course of my work many people have helped out in various ways. I would like to thank all of the other members, past and present, of The Elias Group for their comments (and criticism) over the years. Help, advice, and the occasional belay from Dr. Ken Harris is greatly acknowledged. Many thanks also go out to Dr. Chris Holt for his assistance in procuring characterization equipment for some of the early experiments in my work.

I would not have been able to achieve any of this work without the steady support of my friends. Avery, Anthony, Brian, Dan (Ft. Mack), Dan (Seattle), Eric, James, Jen, Jeremy, Pat, Paul, Rone, Steven, Vern, and Wyatt all of you guys are awesome and have kept me happy and healthy over the long journey that is a PhD.

Lastly, I would also like to acknowledge the financial assistance of Alberta Innovates Technology Futures during the course of my degree.

Table of Contents

Abstract

Preface

Dedication

Acknowledgements

Table of Contents

List of Tables

List of Figures

List of Symbols and Abbreviations

Chapter 1 General Introduction 1
- 1.1 Motivation 1
- 1.2 Purposed Approach 2
- 1.3 Organization of Thesis 3
- 1.4 References 4

Chapter 2 Literature Review 6
- 2.1 Microfluidics 6
  - 2.1.1 The Microfluidic Environment 6
- 2.2 Microfluidic Fuel Cells 12
  - 2.2.1 Principles, History, Motivation 12
  - 2.2.2 Miniaturized Fuel Cell Devices 20
  - 2.2.3 Development of MFC Devices 21
  - 2.2.4 Microfluidic Fuel Cell Devices 23
- 2.3 Materials and Fabrication Methods for MFCs 34
  - 2.3.1 MFC Base Materials 34
  - 2.3.2 Ion Exchange Membranes 40
  - 2.3.3 Electrode Materials 43
- 2.4 Modelling in Microfluidic Devices 46
- 2.5 Conclusions 49
- 2.6 References 49

Chapter 3 Materials in Microfluidic Fuel Cells: Proton Exchange Membranes 62
- 3.1 Overview and Motivations 63
- 3.2 Nucleophilic Substitution Reactions 65
- 3.3 Free Radical Photopolymerization 67

3.4 Characterization Methods 69
3.5 Results and Discussion 74
3.6 Future Work 87
3.7 Conclusions 89
3.8 References 90

Chapter 4 Materials in Microfluidic Fuel Cells: Oxygen Transport in Microfluidic Devices 93
4.1 Overview and Motivations 94
4.2 Oxygen Diffusion in Microfluidic Devices 96
4.3 Oxygen Utilization in Cell Culture Devices 100
4.4 Oxygen Utilization in Microfluidic Fuel Cells 109
4.5 Future Work 119
4.6 Conclusions 121
4.7 References 122

Chapter 5 Microfluidic Fuel Cells Fabricated and Operated via Laminar Flow 125
5.1 Overview and Motivation 125
5.2 Previous Usage of Laminar Flow Lithography 126
5.3 Finite Element Modelling of Multi-Layer Laminar Flow Lithography 127
5.4 Experimental Applications of Laminar Flow Lithography 146
5.5 Ag-Ni MFCs Fabricated by Laminar Flow Lithography 155
5.6 Future Work 165
5.7 Conclusions 166
5.8 References 167

Chapter 6 Conclusion 171
6.1 Contributions to Knowledge and Summary of Work 171
6.2 Proposed Research Directions 177
6.3 References 179
6.4 Grand Unified Bibliography 180

List of Tables

Table 2.1 Design and current/voltage parameters for flow-over electrode devices.

Table 2.2 Design and current/voltage parameters for flow-through electrode devices.

Table 2.3 Design and current/voltage parameters for air-breathing MFC devices.

Table 2.4 Properties of common microfluidic materials. Data obtained from Nunes *et al.* 2010, Niles *et al.* 2008, Du *et al.* 2010, Nielsen *et al.* 2004.

Table 2.5 Modern ion exchange membrane materials. Data obtained from Smitha *et al.* 2005.

Table 3.1 Ion exchange capacity and contact angle measurements for sulfonated and unsulfonated membrane samples.

Table 4.1 Values used to construct the cell culturing device FEM simulation.

Table 4.2 Values used to construct the ABMFC FEM simulation.

Table 5.1 Summary of experimental material, etchant, flow, and etch width parameters used to calibrate the FEM model for quantitative predictions of LFL etch processes.

List of Figures

Figure 2.1 Schematic diagram of flow streamlines for turbulent and laminar flow regimes. In turbulent flow, fluids can exhibit chaotic swirling and mixing leading to a complicated flow profile. In laminar flow, fluids flow in parallel linear layers leading to a more stable flow profile, with the highest velocities seen at the center of the channel, and the lowest velocities along the walls. The arrows depict the parabolic flow profile that is experimentally observed and theoretically predicted (Equation 2.5) for pressure driven flow in microfluidic channels. The transition between turbulent and laminar flow occurs for Reynolds numbers of approximately between 2000 and 4000.

Figure 2.2 Schematic diagram of a basic fuel cell. In this device, there are two chambers (the anode and cathode half cells) which are separated by an electrolyte. In each chamber, a chemical reaction occurs which consumes a reactant product to produce and consume protons and electrons at the anode and cathode surfaces, respectively. Electrons are passed from the anode to the cathode through an external circuit (shown here with resistance *R*) to do work. The electrolyte is a layer (typically a membrane) which chemically and electrically separates the anode and cathode half cells while allowing for diffusion of protons.

Figure 2.3 (a) Schematic diagram of a conventional macroscale PEM fuel cell stack. Each cell consists of serpentine anode and cathode electrodes coupled by a membrane electrode assembly. Figure from Mehta *et al.* (2003). Copyright © 2003, reprinted with permission from Elsevier. (b) An optical image of a commercial scale H_2/O_2 fuel cell stack. Image from Proton Motor Fuel Cell Systems (Germany), used with permission.

Figure 2.4 Schematic current/voltage profile for a typical fuel cell across its operational range. The diagram illustrates the dominate loss mechanisms associated with each area.

Figure 2.5 Schematic diagram of the first reported membraneless MFC device produced by Ferrigno *et al.* Their device used a PDMS microchannel which had been bonded to a class slide combined with carbon on Au electrodes. Anolyte and catholyte streams flowed streams of reduced and oxidized aqueous vanadium ions, respectively. Reprinted with permission from Ferrigno et al. *J. Am. Chem. Soc.* 124 (2002) 12930-12931. Copyright © 2002, American Chemical Society.

Figure 2. 6 Examples of micromachined mini-FCs (a) an optical image of a micropatterned Si substrate formed using reactive ion etching for use in a miniaturized reformed methanol fuel cell, from Morse *et al.* 2007, used with permission. Copyright © 2007, Elsevier. (b) Schematic diagram of a micropatterned Si miniaturized DMFC device using Si microchannels for anolyte and catholyte, from Motokawa *et al.* 2004. Figure Copyright © 2004, Elsevier, used with permission. (c) Schematic diagram of a miniaturized direct methanol fuel cell sandwiched between two patterned Si wafers, from Yen *et al.* 2003. Figure Copyright © 2003, Elsevier, used with permission.

Figure 2. 7 Graphs displaying the number of publications published per year as indexed by Web of Science (Thompson Reuters). Applied search parameters were "microfluidic+fuel+cell", with results obtained on March 13 2014.

Figure 2.8 Schematic diagram showing the relationship between the functional components of a MMFC device and how they relate to overall device performance. This figure serves as a roadmap for implementation of a MMFC device implementation. Image adapted from Shaegh *et al.* 2011. Figure Copyright © 2011 Hydrogen Energy Publications, used with permission.

Figure 2. 9 Schematic diagram of the two main types of MFC devices (a) stacked and (b) planar. In stacked devices, both the upper and lower surfaces are patterned with microfluidic channels and are either used in membraneless implementations or separated by a solid electrolyte membrane. In planar devices, fuel and oxidant solutions are flowed side-by-side and laminar flow is used to create an 'effective membrane' separating the half cells.

Figure 2.10 Flow-over electrode device configurations with a (a) Y shaped device architecture with various electrode orientations. (b-f) Cross sectional schematics of (b) top/bottom, (c) side-wall, (d) channel base electrodes (e) channel base in a groove microchannel and (f) a "three-dimensional" electrode geometry featuring cylindrical electrodes placed parallel to the microchannel and running throughout its length. All schematics are shown as cross sections looking at a slice along the length of the microchannels. Figure from Shaegh *et al.* 2011. Copyright © Hydrogen Energy Publications 2011, used with permission.

Figure 2.11 Schematic diagrams of flow-through MFC implementations. In all schematics, electrodes are formed of porous carbon which allows for anolyte and catholyte solutions to pass through the electrodes. (a) Flow through radial porous electrodes. Figure from Salloum *et al.* 2008. Copyright © 2008 Elsevier, used with permission. (b) and (c) Two different orientations of flow through planar electrodes in a vanadium based MFC device. Reprinted with permission from Kjeang *et al. J. Am. Chem. Soc.* 130 (2008) 4000-4006. Copyright © 2008 American Chemical Society.

Figure 2.12 Schematic diagrams of air breathing MFC devices. (a) A flow through stacked MFC device using a porous carbon gas diffusion electrode and formic acid anolyte. Reprinted with permission from Jayashree *et al. J. Am. Chem. Soc.* 127 (2005) 16758-16759 [107]. Copyright © 2005, American Chemical Society. (b) A stacked MFC device using a flow through anode and gas diffusion cathode. Figure from Shaegh *et al.* 2012. Copyright © 2011, Hydrogen Energy Publications, used with permission.

Figure 2.13 Schematic diagram of an elastomer micromoulding process. (a) First a bare silicon wafer is obtained which is then (b) coated with photoresist (a material that selectively becomes more/less soluble upon exposure to specific wavelengths of light). (c) The photoresist coated wafer is exposed with a desired structure through a selective masking layer (in this example to pattern an array of circles). (d) The wafer is then etched and after removing the photoresist layer an array of raised Si structures remains. (e) Liquid elastomer (in this case PDMS) is poured onto the patterned Si surface and cured into a solid structure. (f) Finally, the solid PDMS surface is peeled off from the wafer yielding a micropatterned polymer film. Reprinted by permission from Macmilan Publishers Ltd: *Nature* Weibel et al. 2007, Copyright 2007.

Figure 2.14 (a) Schematic diagram showing a PDMS based microfluidic microbial fuel cell. A micropatterned PDMS layer is combined with a micropatterned layer of SU-8 (photoresist) deposited on a Si wafer to create a sealed stacked device architecture. Reproduced from Qian *et al.* 2009 with permission of The Royal Society of Chemistry. (b and c) Schematic diagram and optical image of a PDMS based hydrogen-oxygen fuel cell using arrays of microchannels patterned into a PDMS surface. Reprinted with permission from Mitrovski *et al. Langmuir* 20 (2004) 6974-6976. Copyright © American Chemical Society.

Figure 2.15 Schematic and optical image of a MFC devices patterned using a thin layer of COP. Reproduced from Tominaka *et al.* 2009 with permission of The Royal Society of Chemistry.

Figure 2.16 (a) Schematic diagram of proton conducting channels within a Nafion membrane. Sulfonic acid (SO_3) groups separate from the hydrophobic polymer bulk and arrange into clusters forming hydrophilic water channels. Figure from Smitha *et al.* 2005. Copyright © 2005, Elsevier, used with permission. (b) Chemical formula and (c) structural diagram of a typical Nafion polymer chain. Figure from Chen *et al.* 2009. Copyright © 2009, Elsevier B. V, used with permission.

Figure 2.17 (a) Schematic diagrams and optical images of the first reported usage of laminar flow based patterning techniques by Kenis *et al*. Figure reproduced from Kenis *et al. Science* 285 (1999) 83-85. Reprinted with permission from AAAS. (b) Schematic diagrams of the differences between conventional wet etching processes and laminar flow based etching processed. Reproduced from Mu *et al.* 2009 with permission of The Royal Society of Chemistry.

Figure 2.18 Schematic diagram of the stages of solving a fluid flow problem using FEM. (a) A solution geometry is shown with input and output velocity boundary conditions. (b) The domain is broken down into smaller elements with more regular dimensions. (c) Each individual element is simultaneously solved with simplified boundary conditions.

Figure 2.19 (a) Schematic diagrams showing three successive stages of mesh refinement. In each stage, as the mesh is refined the solution (shown as a colored velocity field representative of a fluid simulation solved via FEM) becomes more precise. (b) Schematic diagram showing how interpolation function refinement can yield better approximations of a complex analytical solution.

Figure 3.1 Schematic diagrams showing the two polymers used in the blend to form the PEM material. Active sites are indicated with arrows showing the groups involved in chemical crosslinking and sulfonation. For both polymers, repeat units are shown in brackets.

Figure 3.2 Schematic diagram showing formation of a PEGDA-sPEGPEA PEM within a microchannel. Processing starts with (a) a patterned empty microchannel which is (b) filled with liquid PEGDA-sPEGPEA monomer. (c) The microchannel is then selectively exposed to UV light through a photomask to photopolymerize a membrane in the middle of the microchannel. (d) After photopolymerization excess liquid monomer is removed from the microchannel leaving a solid PEGDA-sPEGPEA membrane. In all schematics, the top surface of the microchannel has been omitted for clarity.

Figure 3.3 (a) Schematic diagram of the nucleophilic substitution reaction used to transfer a sulfonic acid group onto PEGPEA through reaction with sulfuric acid. The reaction was undertaken under constant reflux for two hours at 70 °C. (b) Optical image of PEGDA-sPEGPEA polymer blends of different weight percentages in liquid form.

Figure 3.4 (a) FTIR spectra for non-crosslinked sPEGPEA (top) and PEGPEA (bottom), spectra have been offset by a constant for clarity. (b) XPS data showing the atomic percent of sulfur measured on the surface of a PEGDA-sPEGPEA membrane as a function of sPEGPEA weight fraction directly after crosslinking (‘as processed’) and a membrane that had been equilibrated in water (‘water equilibrated’) for 24 hours to remove any residual sulfuric acid. A Nafion reference is also shown for comparison. Copyright © 2011 Elsevier B.V. Used with permission.

Figure 3.5 Water absorption of sulfonated and unsulfonated polymer membranes as a function of PEGDA volume concentration. There is no data for sulfonated neat PEGDA as the sulfonation reaction was only carried out on the PEGPEA phase. Copyright © 2011 Elsevier B.V. Used with permission.

Figure 3.6 Cryo SEM images showing (a) 1000x and (b) 11300x magnification of a water swollen 25:75 weight percent PEGDA:sPEGPEA membrane sample. Images show thin scaffolds of polymer surrounded by large amounts of ice. In (b) some of the upper ice surface has been removed through use of a focused ion beam. Images used with permission of Martin Kupsta, NRC NINT.

Figure 3.7 Proton conductivity for sulfonated PEGDA-sPEGPEA membranes in their acid and water equilibrated states. Copyright © 2011 Elsevier B.V. Used with permission.

Figure 3.8 Elastic modulus of a) sulfonated and b) unsulfonated membranes as measured by DMA relative to a Nafion reference sample in each figure. Each sample was measured in both dry and wet states. Copyright © 2011 Elsevier B.V. Used with permission.

Figure 3.9 Optical images of PEGDA-sPEGPEA membranes of (a) 200 µm and (b) 50 µm width photopolymerized within PDMS microchannels as well as (c) a large array of 5 µm wide PEGDA-sPEGPEA lines photopolymerized on a cleaned glass slide. Copyright © 2011 Elsevier B.V. Used with permission.

Figure 3.10 Schematic diagram of DPPA a higher order acrylate polymer. Each of the five terminal acrylate groups capable of participating in crosslinking reactions are shown with arrows.

Figure 4.1 a) Schematic diagram of a cross section of the simulated microchannel structure used in the FEM model. Relevant boundary conditions are included in italics as well as equations for both diffusion and convection of oxygen within the microchannel and oxygen permeable capping layer. The parabolic velocity profile applied in model is schematically shown in grey. In both cell culture bioreactor and ABMFC simulations the lower (channel/substrate) interface was taken as a uniform infinitely thin oxygen consuming layer (depicted as cells). Copyright © 2011 Elsevier. Used with permission. b) Curve showing the oxygen concentration at the base of the microchannel as a function of position for varying built in mesh sizes. Figure is based on a FEM simulated geometry consisting of a 100 µm tall microchannel with a 1900 µm thick PDMS capping layer flowing 10^{-4} m/s of fluid.

Figure 4.2 Dimensionless oxygen availability along the bottom of the microchannel at (a) $u_{av}=10^{-2}$ m/s (b) 10^{-4} m/s and (c) 10^{-6} m/s. The y-axis shows oxygen concentration normalized to the saturation value of oxygen in the media. The x-axis shows length along the microchannel normalized to microchannel length. For each u_{av} several solutions were evaluated: an analytical solution, a numerical solution based on uniform flow velocity, and a numerical solution with a parabolic flow velocity profile. For both numerical solutions thin (25 µm) and thick (1.9 mm) oxygen permeable layers are shown. Figure Copyright © 2011 Elsevier. Used with permission.

Figure 4.3 Oxygen concentration within a PDMS capping layer for a FEM simulation with low 10^{-6} m/s flow. Two different PDMS capping layer thicknesses are shown a) 1.9 mm and b) 25 µm. Copyright © 2011 Elsevier. Used with permission.

Figure 4.4 Effect of PDMS capping layer thickness on steady state oxygen concentration at the bottom of the microchannel (in the plane of the cells), for media flowing at 10^{-6}m/s. Copyright © 2011 Elsevier. Used with permission.

Figure 4.5 Effect of microchannel height (*H*) on steady state oxygen concentration at the bottom of the microchannel (in the plane of the cells). The microchannel was simulated with a 1.9 mm PDMS capping layer with media flowing at 10^{-6}m/s. Copyright © 2011 Elsevier. Used with permission.

Figure 4.6 Simulated oxygen concentration at the bottom of the microchannel for COC and PMMA capping layers of 1.9 mm thickness at flow rates of 10^{-2}, 10^{-4}, and 10^{-6} m/s. Both polymers have virtually identical concentration profiles at each corresponding flow rate. Copyright © 2011 Elsevier. Used with permission.

Figure 4.7 Schematic diagram of the planar ABMFC model geometry with characteristic oxygen concentration

profiles at the cathode surface across the length of the microchannel superimposed. In the optimal oxygen concentration state, there is a non-zero concentration of oxygen available at each point across the microchannel. For the insufficient oxygen state only a fraction of the microchannel (x=0 to x=L_1) is able to sustain current producing electrochemical reactions. Channel geometry has been exaggerated for clarity.

Figure 4.8 Oxygen concentration profiles inside microchannels for four different current densities. For 10^1 mA/cm^2 and 10^0 mA/cm^{2,} oxygen concentration was predicted to reach zero before the end of the microchannel length. This indicates that the max density that can be achieved is 10^{-1} mA/cm^2. All simulations were carried out with a 100 µm thick PDMS capping layer and flowing 8x10^{-4} m/s of aqueous catholyte solution saturated with oxygen.

Figure 4.9 Simulated oxygen concentration at the bottom of microchannels for (a) 100 µm and (b) 1900 µm thick COC, PMMA, and PDMS capping layers. Microchannels were 100 µm deep and flowing 8x10^{-4} m/s of catholyte solution saturated with oxygen. A cathodic current of 0.1 mA/cm^2 was assumed for both simulations. The simulated microchannel was 15 mm in length.

Figure 4.10 Simulated oxygen concentration at the cathode surface across the length of the microchannel for four different applied current densities. Simulations flowed (a) 8x10^{-4} (b) 8x10^{-5} and (c) 8x10^{-6} m/s of catholyte solution through the 100 µm deep microchannel with a 100 µm thick PDMS capping layer.

Figure 4.11 Maximum simulated output cathodic current density values predicted by FEM modelling varying (a) PDMS capping layer thickness (at 8x10^{-4} m/s catholyte flow rate) and (b) catholyte flow rate (at 100 µm PDMS capping layer thickness). For both simulations, a 100 µm deep microchannel was assumed.

Figure 5.1 Schematic diagrams illustrating the inlets of the simulated channel geometry as well as the input parameters used in the FEM simulation process for (a) two stream and (b) three stream (bottom) processes. Geometric properties of the channel, including inlet angle Θ_{inlet} and middle inlet width W_{mid}, are shown in (a). Water and etchant flow rates are given as U_w and U_E, respectively. Etchant is supplied at a concentration of C_E while water is set to zero etchant concentration. (c) An image showing a characteristic mesh geometry in a 1 mm by 1 mm region in the middle of a simulated mirochannel. (d) Optical micrograph (left) and simulated concentration profiles (right) showing the relationship in shape of a three stream ferric chloride LFL process and a simulation of steady state etchant concentration at the end of the microchannel x = 20 mm. In the simulated profile, concentrated etchant is shown as red while pure water is shown as blue. Copyright © Royal Society of Chemistry 2014. Used with permission.

Figure 5.2 (a) A lithographically patterned silicon wafer bound to an aluminium mount for hot embossing. (b) A wafer of embossed COC devices after sputter coating. Metal deposition has been restricted from the inlet and outlet of each microchannel by applying a thin PDMS shadow mask. (c) A single COC device prior to bonding to the

PDMS capping layer with a reversible silicone adhesive. (d) A bound COC device ready for two stream LFL processing with access ports highlighted.

Figure 5.3 (a) Simulated concentration profiles for three stream LFL processes with varying inlet angle configurations. Concentrated etchant is shown as red, while pure water is shown as blue. (b) Simulated concentration profiles for three stream LFL processes at the microchannel inlet for differing sizes of middle inlet and flow rates. For the middle (50 µm) wide inlet, optical images show similarly shaped LFL etch profiles at the same flow rate ratio as the corresponding simulations. All processes were simulated flowing 100 µL/min ($4.5x10^{-2}$ m/s) from each of the outer water inlets. Copyright © Royal Society of Chemistry 2014. Used with permission.

Figure. 5.4 (a) An optical image showing the physical etch pattern from a two stream process is compared to a simulated concentration profile with the same input parameters (a 500 s etch with nitric acid flowed at $4.5\ x10^{-2}$ m/s (100 µL/min) and deionized water flowed at $8.9\ x10^{-2}$ m/s (200 µL/min)). The physical etch width is related to simulated concentration at the location of the Ag/Au interface, shown as $y=y_E$ (measured from the edge of the channel). (b) Comparison of measured and simulated etch widths achieved for nitric acid, ferric chloride, and potassium iodide/iodine etchants over a range of etchant to water flow rate ratios. Data points used to calibrate the simulation are highlighted with circles. Both nitric acid and potassium iodide/iodine were calibrated using two stream LFL processes, while ferric chloride was calibrated using three stream LFL using diffusivity and concentration values described in Section 5.2. Copyright © Royal Society of Chemistry 2014. Used with permission.

Figure. 5.5 Simulations exploring etch uniformity as a function of flow rate for two and 3 stream processes. The fraction of the channel etched at x=5 mm from the channel inlet for (a) two and (b) three stream LFL processes for both varying flow rates and etchant:water flow rate ratios. The fraction of the channel etched corresponds to etch width. The fraction of the channel etched as a function of channel length is also shown for (c) two and (d) three stream devices at various flow rates, and shows that the width of the etched region can broaden significantly along the length of the channel, particularly at low flow rates. In the three stream etch process, the etchant at the two lowest flow rates ($4.5x10^{-4}$ and $9.0x10^{-4}$ m/s) expanded to fill the entire channel before reaching the outlet. Copyright © Royal Society of Chemistry 2014. Used with permission.

Figure 5.6 (a) Simulated concentration profiles for asymmetric three stream LFL processes with varying water flow rates. Vw_1 and Vw_2 describe the water flow rates of the top and bottom inlets, respectively. All simulations used a constant etchant inflow of $2.2x10^{-1}$ m/s (50 µL/min). (b) Location of etchant maximum at x=2 mm from the channel inlet for varying flow rate ratios. Simulated and experimentally measured maxima locations (as determined by the center of the etched region) are shown each performed with the same etchant and water flow rates. Copyright © Royal Society of Chemistry 2014. Used with permission.

Figure 5.7 LFL process flow to pattern electrodes in bi-metallic Ag-Ni devices. (a) – (d) Schematic diagrams of (a) an Ag-Ni bilayer film deposited in a COC microchannel, (b) two stream LFL removing a portion of the upper Ag film, (c) three stream LFL patterning an electrically isolating gap and (d) the resultant Ag-Ni device structure. Schematic diagrams are shown in cross section looking down the microchannel with etchant flowing into the page. Channel dimensions have been exaggerated for clarity. (e) – (g) Optical images of the microchannel (e) the top Ag surface before LFL patterning, (f) exposed Ag and Ni regions after two stream LFL, and (g) electrically isolated Ag and Ni regions after three stream LFL. Copyright © Royal Society of Chemistry 2014. Used with permission.

Figure. 5.8 LFL process flow to pattern electrodes in tri-metallic Ag-Ni-Au devices. (a) – (f) Schematic diagrams of (a) an Ag-Au-Ni tri-layer film deposited in a COC microchannel, (b) two stream LFL removing a portion of the upper Ag film, (c) three stream LFL patterning removing a band of Au in the middle of the microchannel, (d) three stream asymmetric LFL isolating the Ag-Ni interface, (e) three stream asymmetric LFL isolating the Au-Ni interface, and (f) the resultant Ag-Ni-Au device structure. The Ag-Ni interface was intentionally under-etched to lessen the effect of undercutting on subsequent asymmetric patterning. Schematic diagrams are shown in cross section looking down the microchannel with etchant flowing into the page. Channel dimensions have been exaggerated for clarity. (g) – (i) Optical images of the microchannel (g) exposed Ag and Au regions after two stream LFL processing, (h) exposed Ag, Au, and Ni regions after three stream LFL, and (i) electrically isolated Ag, Au, and Ni regions after two stages of asymmetric three stream LFL.

Figure. 5.9 Images showing the pitch of LFL in our devices. Experiments flowed 5 µL/min of ferric chloride between two streams of deionized water at 500 µL/min. Etching was carried out for 120 s. Images were taken at x = 10 mm from the microchannel inlet.

Figure. 5.10 (a) A two channel Ag-Ni device after sputtering (before LFL processing), and FEM simulations of (b) two stream and (c) three stream parallelized LFL patterning. Simulations were carried out using the same method as Section 5.2 with applied flow rates as indicated. In three stream LFL, 80 µL/min of etchant was applied to the middle inlet of each microchannel independently.

Figure 5.11 (a) Schematic diagram of the thin film stacks used for LFL characterization experiments and Ag-Ni MFC devices and (b) optical image of an Ag-Ni MMFC device after LFL processing before electrochemical processing. The inset image in (b) shows a magnified view of the middle of the main microchannel (with an Ag region on the top and a Ni region on the bottom separated by bare, transparent, COC).

Figure 5.12 Current/voltage profiles for (a) electrochemical removal of electrically connected Ag from the anode half-cell and (b) electrochemical conversion of Ni into catalytic Ni$(OH)_2$/NiOOH. (c) Optical image of a Ni film that had been partially immersed in KOH solution during electrochemical processing resulting in distinct Ni and Ni$(OH)_2$/NiOOH regions.

Figure. 5.13 MFC Characteristics. Representative current-voltage relationships for 1.2 M methanol and 145 mM hydrogen peroxide reactant solutions are shown in (a); power-voltage relationships for the same systems are shown in (b). (c) Output power characteristics as a function of reactant flow rate and hydrogen peroxide concentration (measurements were repeated 3 times on the same device with averages and standard deviation shown). (d) Optical image of a LFL patterned MMFC. Copyright © Royal Society of Chemistry 2014. Used with permission.

List of Abbreviations

ABMFC	Air-breathing MFC
AEM	Anion exchange membrane
ATR-FTIR	Attenuated total reflection FTIR
COC	Cyclic-olefin-copolymer
COP	Cyclic-olefin-polymer
CV	Cyclic voltammetry
DMA	Dynamic mechanical analysis
DMFC	Direct methanol fuel cell
DPPA	Dipentaerythritol pentaacrylate
FEM	Finite element modelling
FRPP	Free radical photo-polymerization
FTIR	Fourier transform infrared spectroscopy
IEM	Ion exchange membrane
LFL	Laminar flow lithography
MEA	Membrane electrode assembly
MFC	Microfluidic fuel cell
Mini-FC	Miniaturized fuel cell
MMFC	Membraneless MFC
PDMS	Poly(dimethylsiloxane)
PEG	Poly(ethylene-glycol)
PEGA	Poly(ethylene-glycol acrylate)
PEGDA	Poly(ethylene-glycol diacrylate)
PEGPEA	Poly(ethylene-glycol phenyl-ether-acrylate)

PEM	Proton exchange membrane
PMMA	Poly(methyl methacrylate)
SEM	Scanning electron microscopy
sPEGPEA	Sulfonated PEGPEA
XPS	X-ray photoelectron spectroscopy

Chapter 1

Introduction

“An expert is a person who has made all the mistakes that can be made in a very narrow field.”

Niels Bohr

1.1 Motivation

Fuel cells have long been described as an effective means of power generation for a wide range of applications from motor vehicles, to portable electronics [1]. Since the early 2000’s efforts have been undertaken to implement fuel cells on a micro-scale for the purposes of providing onboard power generation for microfluidic and lab-on-a-chip devices [2]. Creating functional microfluidic fuel cells (MFCs) has proven to be a difficult challenge due to the incompatibilities between conventional macro-scale fuel cell technologies and the micro-scaled environment. Extensive research in literature has been carried out over the past decade to optimize the MFC device platform with focus placed on improving the materials and device geometry [3,4,5].

An ideal fuel cell is a device capable of transducing the chemical potential energy of anolyte and catholyte solutions into electrical potential energy without losses [6]. As was also said in a seminal 2004 review by Stone *et al*. an ideal microfluidic device is cheap and “capable of simple analytical tasks” [7]. MFCs aim to satisfy both of these goals and produce effective power generation in a scalable (and easily fabricated) device architecture which could be integrated and fabricated with the rest of a microfluidic or lab-on-a-chip device. To achieve this, an MFC device design should satisfy three parameters, devices should be: fabricated using techniques compatible with conventional microfluidic processing techniques, operated at normal microfluidic environmental conditions (*i.e.* temperature, pressure, etc.), and composed of inexpensive materials. Current MFC devices differ from this ideal in several ways. Firstly, MFCs are often produced in *stacked* architectures with many layers (requiring complicated alignment procedures which can increase the cost of device fabrication) [8]. Secondly, many modern MFC devices inherit both materials and fabrication techniques from macroscale fuel cell devices. Such devices require integration of commercial preformed proton exchange membranes and specially crafted gas diffusion electrodes [9]. Lastly, MFC devices are usually reliant on materials such as precious metal catalysts to achieve favourable outputs which substantially increase cost per device [10]. Materials and methods to align the MFC architecture with the benefits of microfluidic devices are intently sought and are the subject of this thesis.

1.2 Purposed Approach

This thesis aims to improve the applicability of MFC devices by designing materials and methods to better align the MFC device architecture with the benefits of a microfluidic architecture. This is achieved in several ways. Focus is placed on developing techniques capable of producing *planar* MFC devices. In a planar architecture, all of the patterned components of an MFC are restricted to a single sided microchannel and bonded to a flat capping layer. This structure is analogous to conventional microfluidic devices and allows for an MFC to be easily integrated into a larger device. Achieving effective planar devices requires addressing several design and fabrication challenges. As both anode and cathode half cells occupy the same channel, electrodes (composed of different materials) must be deposited and subsequently patterned independently. A planar approach can also lead to substantial crossover between anolyte and catholyte solutions, causing less favourable electrical output characteristics and poor fuel utilization [11]. This thesis describes the development of materials and *in situ* fabrication methods to address these concerns which can lessen the reliance upon complicated (and costly) conventional processing techniques.

1.3 Organization of Thesis

Chapter 2 gives a detailed review of the required background for design and improvement of MFC devices. The chapter starts with a review of the microfluidic environment (in terms of both characteristic behavior, and the history of its development) and then describes fuel cells (on both a macro and micro-scale). Specific focus is placed on reviewing the evolution of both completed MFC devices as well as their functional components (micropatterned polymers, polymer electrolyte membranes, and electrode materials). Methods to simulate the behavior of MFC devices through finite element modelling (FEM) are also reviewed.

In Chapter 3, a sulfonated aromatic hydrocarbon polymer is developed and characterized as an *in situ* photopolymerizable proton exchange membrane. Two phase polymer blends based on inexpensive functionalized poly(ethylene-glycol) derivatives are formed and methods to adapt the material into microfluidic devices are presented. The advantages of an *in situ* fabrication method and their applicability to planar MFC devices are discussed.

Chapter 4 describes FEM simulations undertaken to model oxygen transport in planar microfluidic devices. Two analogous microfluidic systems are discussed: air breathing microfluidic fuel cell devices and microfluidic cell culturing bioreactors. The effect of device geometry, applied flow rates, and device materials on oxygen transport behavior are assessed. Results are used to provide guidance on appropriate design and operation parameters for implementation of effective air breathing microfluidic devices.

Chapter 5 describes the development of a fabrication technique, multi-layer laminar flow lithography which is used to pattern multi-layer film stacks deposited into polymer microchannels *in situ* to yield electrodes. Relationships governing patterning processes are evaluated by both FEM simulations and experiments which efforts focused on yielding independent electrodes of multiple materials. Both tri-metallic Ag-Ni-Au, and bi-metallic Ag-Ni devices are fabricated. Ag-Ni devices are then operated and characterized as membraneless alkaline direct methanol fuel cells.

Chapter 6 presents summaries of each chapter highlighting the importance of the obtained results to MFCs and the broader field of microfluidics. Also presented is a description of the overall conclusions gained from this work and directions for future improvements to the MFC device architecture.

1.4 References

---

[1] "Fuel cells: History and updating. A walk along two centuries" Andujar J M, Segura F *Renewable and Sustainable Energy Reviews* 13 (2009) 2309-2322.

[2] "Microfluidic fuel cells: a review" Kjeang E, Djilali N, Sinton D *Journal of Power Sources* 186 (2009) 353-369.

[3] "A review on membraneless laminar flow-based fuel cells" Shaegh S A M, Nguyen N, Chan S H *International Journal of Hydrogen Energy* 36 (2011) 5675-5694.

[4] "Microfluidic fuel cells: a review" Kjeang E, Djilali N, Sinton D *Journal of Power Sources* 186 (2009) 353-369.

[5] "Mass transfer and performance of membrane-less micro fuel cell: A review" Nasharudin M N, Kamarudin S K, Hasran U A, Masdar M S *International Journal of Hydrogen Energy* 39 (2014) 1039-1055.

[6] "A review on fuel cell technology and power electronic interface" Kirubakaran A, Jain S, Nema R K *Renewable and Sustainable Energy Reviews* 13 (2009) 2430-2440.

[7] "Engineering Flows In Small Devices: Microfluidics Toward a Lab-on-a-Chip" Stone H A, Stroock A D, Ajdari A *Annu. Reviews of Fluid Mechanics* 36 (2004) 381-411.

[8] "Micromachined polymer electrolyte membrane and direct methanol fuel cells – a review"

Nguyen N T, Chan S H *J. Micromechanics and Microengineering* 16 (2006) R1-R12.

[9] "Microfabricated fuel cells" Wainright J S, Savinell R F, Liu C C, Litt M *Electrochemica Acta* 48 (2003) 2869-2877.

[10] "Overview on the challenges and developments of micro-direct methanol fuel cells (DMFC)" Kamarudin S K, Daud W R W, Ho S L, Hasran U A *Journal of Power Sources* 163 743-754.

[11] "Improved fuel utilization in microfluidic fuel cells: A computational study" Bazylak A, Sinton D, Djilali N *Journal of Power Sources* 143 (2005) 57-66.

Chapter 2

Literature Review

"I was born not knowing and have had only a little time to change that here and there"

Richard Feynman

2.1 Microfluidics

2.1.1 The Microfluidic Environment

Microfluidics is a term given to a class of devices which involve the transport, manipulation, or integration of fluid flow in an environment where one of the critical dimensions (be it length, width, or height) is on the order of 1- 1000 µm [1,2]. As fluids are restricted to smaller and smaller size scales, their characteristic behavior changes. When reduced to a microfluidic scale, many every-day assumptions regarding turbulent mixing and surface tension found on the macroscale are no longer valid. Through proper engineering, as discussed below, microscale effects can be harnessed for many useful applications.

The roots of microfluidics as a scientific field sprouted as an offshoot from the integrated computer circuits industry where, since the 1970s, a strong emphasis has been placed on miniaturization of processes and devices as a means to increase processing power and data density [3]. Microcircuitry was able to revolutionize the modern world by allowing for ever increasingly complex numerical calculations. Microfluidics allows for miniaturization and optimization of chemical reactions (be they for organic synthesis, sensing or other applications [4,5,6]) and biological processes (such as characterization of microbes, drug discovery, and lab-on-a-chip diagnostic systems [7,8]). Possible applications for microfluidics are as widespread as for microcircuits and have to potential to lead to a similar impact [9].

It is difficult to cite one specific publication or individual that defined the start of the microfluidic era but progress towards modern microfluidic devices owes a great deal to early work done in the mid twentieth century. In the 1950s efforts were taken to develop ink-jet printer technology which led to precise control and characterization of nanolitre scale fluids [10,11]. Later researchers in the 1990s such as Manz *et al.* (1990) and Mathies *et al.* (1995) are credited with the first implementations of microscaled total analysis systems (µTAS) and microscaled capillary electrophoresis systems respectively [12,13]. These systems leveraged exceedingly small volumes of fluids to perform characterization and sensing applications. Their devices closely resembled modern microfluidic systems in both structure and intent. After having demonstrated the utility of µTAS systems to improve upon contemporary macro-scale electrophoretic characterization, other groups began to implement more microscaled components. Such efforts gradually led to increasingly complex devices and the development of an extensive microscaled toolkit featuring components such as valves, pumps, mixers. These developments expanded the applicability of microfluidics beyond electrophoretic systems to more diverse microfluidic implementations such as chemical factories and integrated sensors [14,15,16,17,18,19]. Throughout the development of microfluidics, great emphasis has been placed upon understanding theoretical aspects of device operation on a micro-scale. Researchers have investigated the physical properties of small volumes of fluid through both first-principles calculations and computer simulations. Both methods have given clues of how to better exploit the microfluidic environment for future devices [20,21,22].

Microfluidic devices derive their functional properties from the interplay of geometric, mechanical, and materials properties that are found in a microscaled architecture [23]. The most effective way to gain an appreciation for the utility of miocrofluidics is to illustrate the differences between normal every-day (macroscale) fluid flow and microscaled fluid flow. Specifically, differences in fluid characteristics are highlighted by comparing the values of three ratios: the surface area to volume ratio, the Reynolds number, and the Peclet number [24].

Conventional macroscale fluid properties (*i.e.* those found in fluid systems like gas pumps or draught lines), and microscale fluid properties (*i.e.* flow within a microfluidic channel or capillary tube), are here compared with two characteristic test cases. The first test case describes a macroscopic pipe of

0.1 m diameter flowing 10 µL/min of water and is analogous to a garden hose, while the second is a 1000 µm diameter cylindrical microchannel flowing 10 µL/min of water. The surface area to volume ratio is a metric which gauges the relative importance of boundary effects (*i.e.* properties determined by interfaces between a fluid and its container) versus bulk effects (*i.e.* properties caused by the fluid itself) [25]. For the aforementioned test cases, surface area to volume ratios scale on the order of 40 and 4000, respectively. The relative magnitude of these values shows that for microfluidic devices boundary effects are of significant importance *as boundary effects will become more dominant as the relative amount of surface area increases*. The Reynolds number is the ratio of the inertial forces and the viscous forces seen by a fluid and give a sense of the type of mixing expected in a given fluid system. Specifically, the Reynolds number is defined as $Re=QD_h/vA$, where Q is the volumetric flow rate, D_h is the hydraulic diameter, v is the kinematic viscosity of the fluid, and A is the cross-sectional area of the channel. As the Reynold's number increases, flow is more likely to be dominated by turbulent mixing [22]. Reynold's numbers for the microfluidic and macrofluidic devices are 12.7 and 127000 respectively, indicating that viscous processes (*i.e.* forces due to internal friction of the fluid) dominate microfluidic flow. A general rule of thumb is that Reynold's numbers below ~2000 correspond to laminar flow while those higher correspond to turbulent flow; most microfluidic devices exist well below this threshold value [26]. Fluids flowing in microfluidic channels typically flow in well-defined laminar layers.

The final ratio, the Peclet number, gives an indication of the relative importance of diffusion and convection as transport mechanisms within a flowing fluid. The Peclet number is defined as $P=UH/D$, where U is a characteristic flow velocity, H is a characteristic length of the microchannel, and D is the diffusion coefficient of the particle of interest [27]. The microfluidic test device has a Peclet number $1\text{x}10^8$ times larger than the macroscale test device. On the microscale, transport across the width of a channel is largely due to diffusion, whereas in the macroscale convection is more important. Summarizing the results of these ratios gives a description of a 'normal' microfluidic architecture as being an environment that allows for fluid flow to be dominated by interfaces rather than bulk fluid properties, in which flow is laminar (without turbulence), and dissolved materials are transported across the channel width through diffusion rather than convection. This suite of properties describes what is typically thought of as a microfluidic system [28]. It is important to note that through proper tuning of device geometry, applied flow rates, or chosen fluids these properties can be altered independently. Of the aforementioned characteristics of microscaled fluid flow, perhaps the most well-known (and useful) property is laminar flow.

As described above, laminar flow is a term given to describe the movement of fluids dominated by viscous rather than inertial processes. Illustrations depicting both types of fluid flow are given in Figure 2.1. Laminar flow in microfluidic channels can be derived by solving the three dimensional Navier-Stokes equation (Equation 2.1).

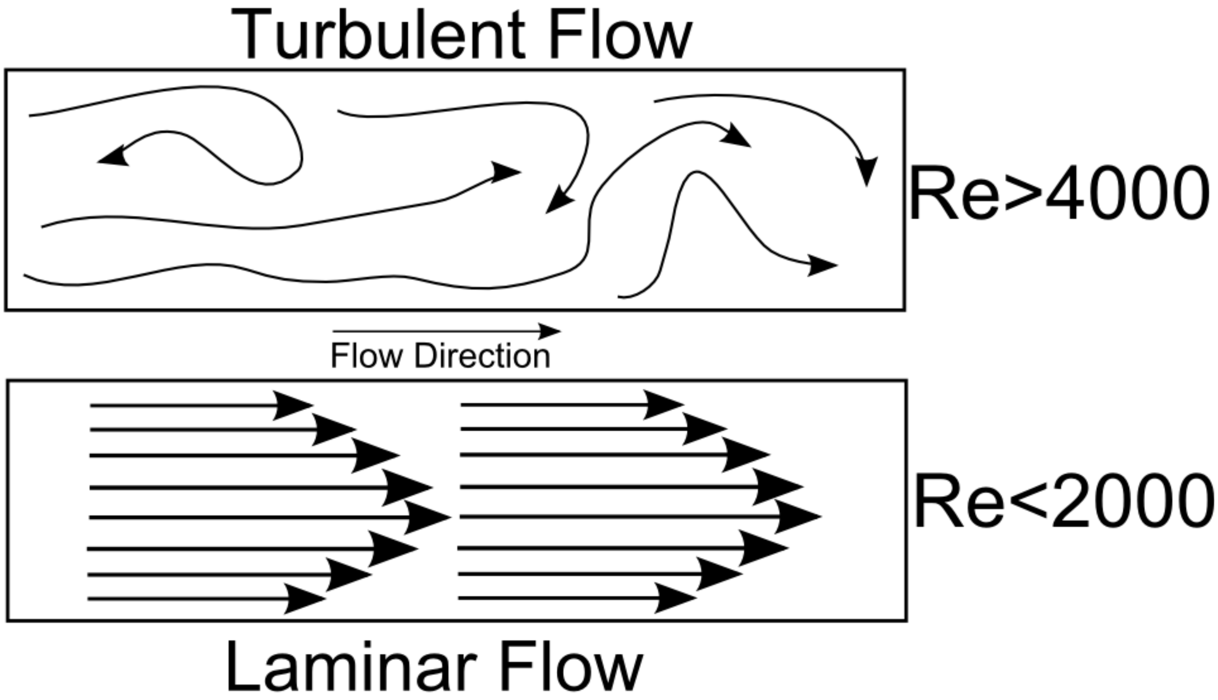

Figure 2.1 Schematic diagram of flow streamlines for turbulent and laminar flow regimes. In turbulent flow, fluids can exhibit chaotic swirling and mixing leading to a complicated flow profile. In laminar flow, fluids flow in parallel linear layers leading to a more stable flow profile, with the highest velocities seen at the center of the channel, and the lowest velocities along the walls. The arrows depict the parabolic flow profile that is experimentally observed and theoretically predicted (Equation 2.5) for pressure driven flow in microfluidic channels. The transition between turbulent and laminar flow occurs for Reynolds numbers of approximately between 2000 and 4000.

$$\rho\left(\frac{\partial\bar{u}}{\partial t}+\bar{u}\cdot\nabla\bar{u}\right)=-\nabla p+\mu\nabla^2\bar{u}+\bar{f} \tag{2.1}$$

where u is the velocity at any given point in the microchanel, p is applied pressure used to drive the fluid, μ is the kinematic viscosity of the fluid, ρ is the fluid density, and f represents any body forces acting on the fluid. A microfluidic channel geometry leads to low Reynolds numbers, fluid flow is laminar, and the non-linear convective term is small and can be neglected. This yields a simplified relationship termed Stokes Flow (Equation 2.2)

$$\rho\frac{\partial\bar{u}}{\partial t}=-\nabla p+\mu\nabla^2\bar{u}+\bar{f} \tag{2.2}$$

This relationship can be solved by combining with the mass continuity equation (Equation 2.3).

$$\frac{\partial\rho}{\partial t}+\nabla\cdot(\rho\bar{u})=0 \tag{2.3}$$

The solution this system of equations describes the flow velocity at any given point in the microchannel. Solving the equations specifically for a rectangular microchannel (as shown in Bruus 2011 [[29]]) yields a linear relationship between applied pressure and fluid velocity in the middle of the microchannel given in Equation 2.4:

$$\nabla p=\frac{32\mu LU}{D_h^2} \tag{2.4}$$

where L is the length of the microchannel, U is the applied flow rate, and D_h is the hydraulic diameter of the microchannel. A microfluidic environment creates well defined velocity profiles which can be calculated using simple equations (unlike in macroscopic systems where turbulence leads to ill-defined flow profiles). This is a meaningful result as the simple relationship between applied pressure and flow rate can be used to determine appropriate flow conditions either analytically or through numerical simulation methods.

Within microfluidic channels, a no-slip boundary condition exists at fluid/channel interfaces. This forces zero flow velocity at channel walls, leading to maximal flow velocity in the middle of the microchannel. Velocity decays at a known rate from the center of the channel, as shown in Equation 2.5 for flow in rectangular microchannels, where u is the average velocity in the middle of the microchannel, H is half of the channel width and y is the position along the width of the microchannel ranging from 0 to *H* [30]. As a result of this flow regime, fluids pumped through microchannels tend to exhibit stable, controllable parabolic velocity profiles (also termed Poiseuille flow) [31]. Such profiles, as described in Equation 2.5, are symmetric about a plane in the middle of the microchannel width at (*y*=0) and for flow in a straight, well defined microchannel invariant across channel length (*x*).

$$u(x) = 6\overline{u}\,\frac{y}{H}\left(1 - \frac{y}{H}\right) \tag{2.5}$$

While less visually interesting than the swirling eddies of turbulent flow, steady laminar flow profiles are of great utility and can be exploited to passively replace complex mixing and regulatory systems found in macroscale devices. Much of the functionality of microfluidic devices comes flowing parallel streams of fluid within a microchannel with limited mixing.

Some of the earliest examples of devices engineered to harness the microfluidic environment functioned by using laminar flow to create precise micromixers. Kamholz *et al.* in 1999 showed that by using a simple T shaped rectangular microchannel and two fluids of differing diffusivity, the precise concentrations of both solutions could be well predicted at any point in the microchannel and used to monitor a chemical reaction [32]. Other work showed how the stable diffusive interface offered by laminar flow can be used as an 'effective membrane', mimicking physical membranes found in electrochemical cells (such as the fuel cells later presented in this thesis) leading to simplified device architecture and fabrication [33]. After demonstrating the benefits of laminar flow to create simple diffusive micromixers, researchers turned their attention to more ambitious problems. Efforts were then taken to create complex integrated devices coupling laminar flow in microchannels to functionalized materials, chemical sensors, and electrical circuits [34,35,36]. The early 2000s saw an explosion of interest in integrated microfluidic systems, and numerous devices were developed using electrodes within planar microchannels to create analysis systems and electrochemical microreactors [37,38]. Throughout the development of microfluidics, the scope and quality of devices has been enhanced through the translation of macroscaled processes to microscaled architectures extending the possible applications of microfluidic systems and spurring on further growth. One goal for further development in microfluidics is to implement microfluidic devices which are self-contained (*i.e.* not reliant upon external macroscale devices) for all aspects of their operation (including factors such as power generation or fluid pumping) [39,40].

While laminar flow is often thought of as the most well-known property of the microfluidic environment for microfluidic electrochemical devices, much of the utility of a microscaled architecture comes from high surface area to volume ratios. As discussed above, a microfluidic architecture offers extremely large amounts of surface area in a small device volume. This results in a considerably greater fraction of a fluid in contact with the walls of a microchannel than a macrochannel. The high surface area to volume ratio of microchannels has been leveraged to great benefit for development of small scale heterogenous catalysis reactors, chemical sensors, and microfluidic electrochemical cells [38,41,42]. As an example, in 2001, Jensen *et al.* demonstrated two orders of magnitude increase in mass transfer coefficients in a micropatterned packed-bed reactor compared to an equivalent macroscaled system [43,44]. Sensing devices have leveraged additional surface area to improve detection resolution and improve the functionality of optical and electrical sensing mechanisms [45,46]. Electrochemical cells have also benefitted from microscaled implementations as mass transport, reaction temperature, and electrical potentials can all be carefully tuned by controlling the surface properties in microfluidic reactors [47,48]. Microfluidics has come a long way from the initial electrophoretic devices of the early 1990s and has slowly expanded in scope to encompass a wide variety of diverse device implementations.

2.2 Microfluidic Fuel Cells

2.2.1 Principles, History, and Motivation

Microfluidic fuel cells (MFCs) are an emerging class of microfluidic devices which show promise for small scale, on-board power generation in microscaled devices [49]. Like sensors and electrochemical factories, MFCs can benefit from high surface area to volume ratios to boost reaction kinetics and theoretically improve power generation characteristics. A fuel cell is a type of electrochemical device where chemical potential energy, the energy stored within chemical compounds, is continuously converted to electrical energy during an ongoing electrochemical reaction from externally supplied reactants [50]. At its most basic, a fuel cell consists of three components: an anode half cell (where a chemical reaction causes electrons to be liberated from a reactant at an electrode), a cathode half cell (where electrons are accepted at an electrode during a reaction), and a means to link the two half cells both chemically (such that charge balance is maintained) and electrically (through an external circuit, so useful work can be done) [51]. Chemical coupling is primarily achieved through use of an electrolyte solution and selectively permeable membrane [52]. A schematic diagram of a simple fuel cell is shown in Figure 2.2. Many different classes of fuel cells exist and are made distinct due to differences in the type of electrode, electrolyte, and reactants used.

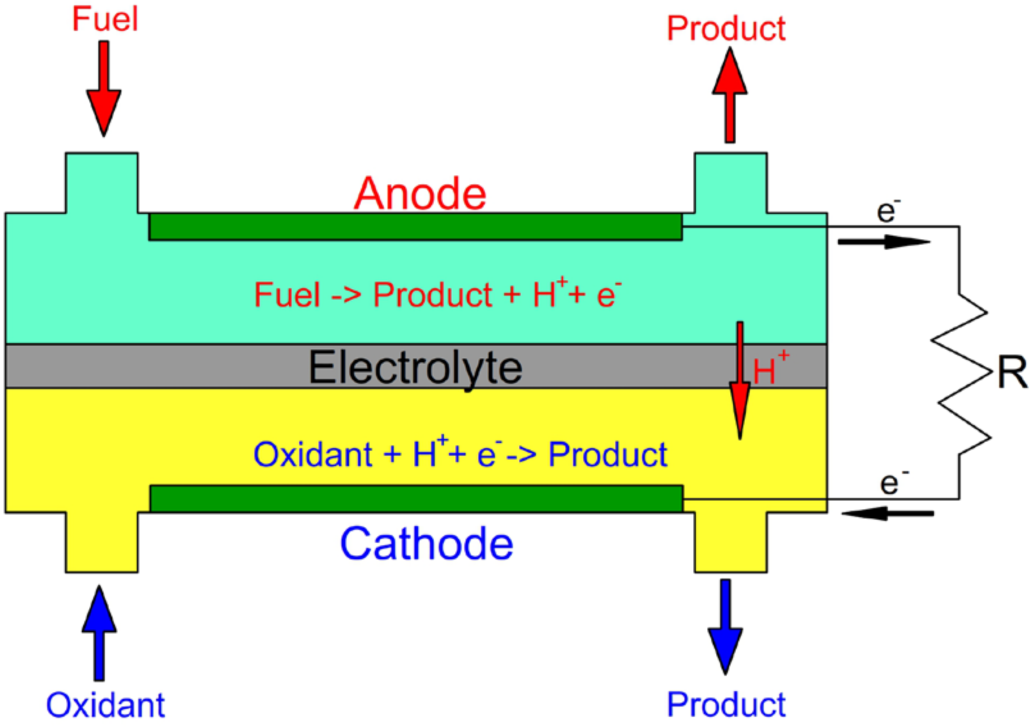

Figure 2.2 Schematic diagram of a basic fuel cell. In this device there are two chambers (the anode and cathode half cells) which are separated by an electrolyte. In each chamber, a chemical reaction occurs which consumes a reactant product to produce and consume protons and electrons at the anode and cathode surfaces, respectively. Electrons are passed from the anode to the cathode through an external circuit (shown here with resistance *R*) to do work. The electrolyte is a layer (typically a membrane) which chemically and electrically separates the anode and cathode half cells while allowing for diffusion of protons.

The most common fuel cell implementation explored to date (and that most widely known) is the proton exchange membrane (PEM) fuel cell. In this type of device, two half-cells are separated by a solid electrolyte membrane which allows for transport of protons while restricting flow of other ions and electrons [53]. In this way, PEMs allow for isolation of fuel and oxidant while preserving electrical and ionic conductivity. PEM fuel cell systems have been the subject of countless research projects since their inception in the 1960s with considerable focus placed on large scale H_2/O_2 based devices.

Commercial and research efforts have yielded functional macroscale devices for use in systems such as automobiles [54]. Examples of large scale fuel cell devices are shown in Figure 2.3. In such large scale systems, H_2/O_2 fuel cells use gaseous reactants and typically operate at temperatures around 50-100 °C and working pressures near 50 atm. These operating conditions lead to challenges with both fuel integration (*i.e.* storage of compressed hydrogen) as well as the mechanical and chemical stability of reaction chambers [55]. These problems are even more apparent when H_2/O_2 PEM devices are implemented on the microscale, where the addition of bulky high pressure fuel inlets complicates device design and operation. As such, H_2/O_2 based PEM fuel cells have seen limited development for usage in small scale self-contained device structures such as in lab-on-a-chip systems [56,57].

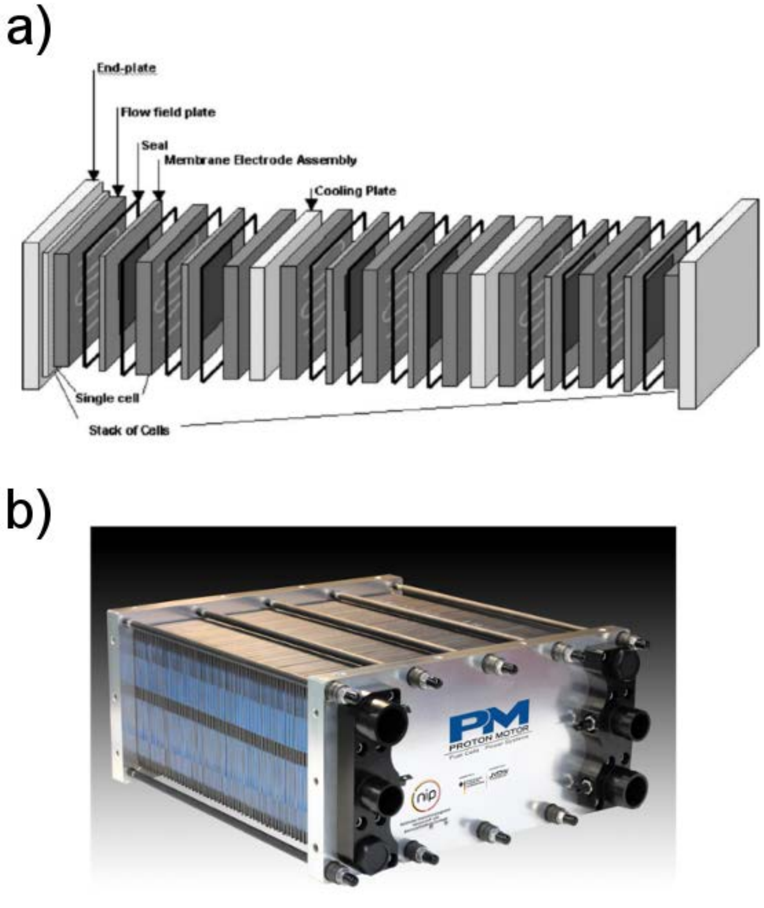

Figure 2.3 (a) Schematic diagram of a conventional macroscale PEM fuel cell stack. Each cell consists of serpentine anode and cathode electrodes coupled by a membrane electrode assembly. Figure from Mehta *et al.* (2003). Copyright © 2003, reprinted with permission from Elsevier [58]. (b) An optical image of a commercial scale H_2/O_2 fuel cell stack. Image from Proton Motor Fuel Cell Systems (Germany), used with permission [59].

For microfluidic implementations, a more useful device architecture uses liquid fuel solutions rather than gaseous hydrogen. To date, methanol is among the most widely documented liquid fuel compounds [60,61]. A fuel cell based on the oxidation of methanol yielding carbon dioxide is termed a direct methanol fuel cell (DMFC). In terms of output cell potential, both H_2/O_2 fuel cells and DMFC have similar theoretical potentials of 1.23 and 1.18 V, respectively (based on the difference in the chemical potential between the reactants in each half cell, as describe below in Equation 2.6). However, compared to H_2, methanol offers several key theoretical and practical benefits. First, the energy density of a typical gas stream of hydrogen used in macroscale fuel cells (at 5000 Psi) is on the order of 500-1000 Wh/kg [57]. Liquid methanol has a considerably higher energy density of 5500 Wh/kg [57]. For small scaled devices, where space is at a premium, methanol offers a larger theoretical amount of power output for a given volume of fuel. The main motivation for using a liquid such as methanol as a fuel source for MFCs is derived from required operating conditions. DMFC devices can be operated under ambient pressure flowing liquid solutions. Ambient operation conditions allow for a considerably wider range of compatible materials and lessen the mechanical and chemical stability required for device operation [62].

There are however several challenges that limit the effectiveness of DMFC based devices on both a macro and micro scale. These limitations can be seen schematically on a current/voltage profile for a typical fuel cell as is shown in Figure 2.4. Firstly, reaction kinetics of methanol oxidation are less favourable than for hydrogen oxidation. This leads to inefficiencies termed kinetic losses (also called anode overpotentials or activation losses) where energy is expected to convert the fuel compound to a more reactive state where the oxidation reaction can take place. Activation losses are most apparent at low current output levels, as shown in Figure 2.4 and lead to lower output voltages and less effective power generation [63]. Secondly, conventional solid electrolyte membrane materials such as Nafion (a commercial sulfonic acid fluoro-polymer) have high methanol permeability at operational conditions. This results in a significant amount of fuel passing from the anode to cathode chamber. Mixing between the anode and cathode chambers lowers fuel utilization and can create parasitic current (*i.e.* fuel from the anode reacting on the cathode to produce a mixed potential which lowers the cathode cell voltage) [64].

The maximum theoretical potential possible for a given fuel cell can be calculated by solving the Nernst Equation (Equation 2.6) for each half cell reaction and then adding the oxidation (anode) and reduction (cathode) potentials.

$$E = E^0 - \frac{RT}{nF} \ln \frac{\coprod_{\text{products},i} a_i^{\upsilon_i}}{\coprod_{\text{reactants},j} a_j^{\upsilon_j}} = E^0 - \frac{RT}{4F} \ln \frac{1}{a_{O_2}(a_{H+})^4} \tag{2.6}$$

For a typical DMFC, the anode half-cell reaction is the catalytic oxidation of methanol on Pt given in Equation 2.7.

$$CH_3OH + H_2O \text{ -> } CO_2 + 6H^+ + 6e^- \tag{2.7}$$

The cathode half-cell reaction is the catalytic reduction of oxygen on Pt as shown in Equation 2.8.

$$3/2O_2 + 6H^+ + 6e^- \text{ -> } 3\ H_2O \tag{2.8}$$

The overall cell reaction is then given by Equation 2.9 with a standard cell potential of 1.18 V.

$$3/2O_2 + CH_3OH \text{ -> } CO_2 + 2H_2O \tag{2.9}$$

As a result of the cell potentials (at 25 °C and 1 atm and concentrated reagents) the maximum achievable output potential possible from a DMFC device is 1.18V. However, the output voltage of an actual fuel cell device will always be less than the maximum potential due to physical limitations that decrease the efficiency of energy production which are shown schematically in Figure 2.4.

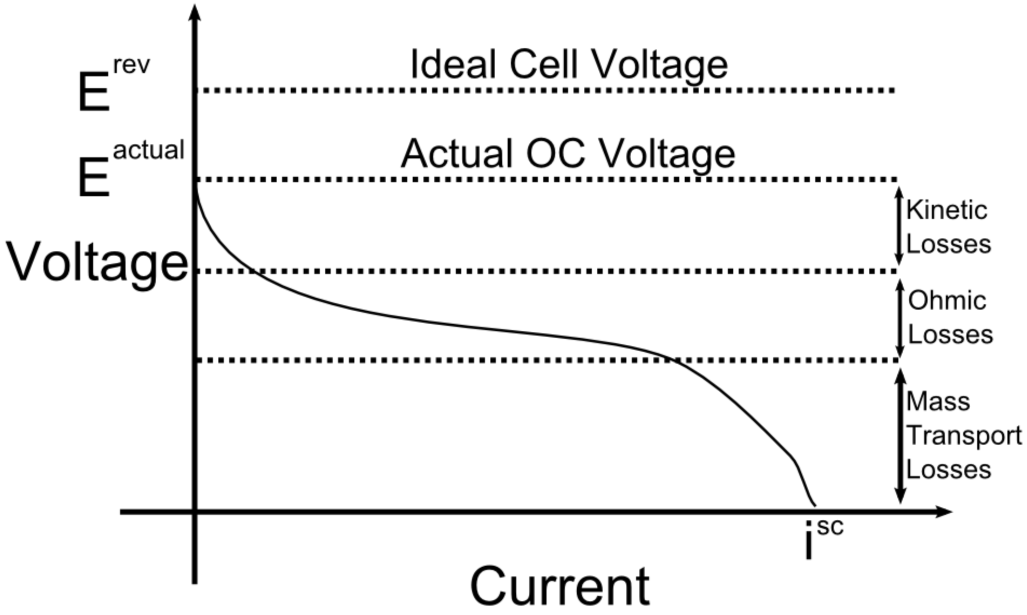

Figure 2.4 Schematic current/voltage profile for a typical fuel cell across its operational range. The diagram illustrates the dominate loss mechanisms associated with each area.

Inefficiencies can be broadly classified into three groups. Firstly, devices can be limited due to reaction kinetics (also termed concentration polarization). These losses occur as energy is required to convert a fuel molecule into an activated form where it can oxidize yielding electrons and ions. Secondly, electrical losses (also described as ohmic losses) lessen efficiency due to resistivity in electrodes, electrolyte solutions, and external wires. Finally, at high current output levels there limited supply of reactants (termed mass transport losses) which lead to a device being unable sustain current generation due to a lack of fuel or oxidant molecules at the electrode surface [[58]]. A proper fuel cell architecture, be it macroscale or microscale, seeks to use engineered materials and methods to lessen these limitations.

The small volume and high surface area to volume ratio offered by a microfluidic channel is doubly beneficial to fuel cell functionality. Decreasing device volume necessitates smaller anode and cathode chambers which are spaced more closely together (reducing the distance needed for ions to diffuse between half cells and thereby decreasing ohmic resistance). Simultaneously, as device size is scaled down the surface area to volume ratio increases. A high surface area to volume ratio means that there is also more available area for electrode deposition which intern allows for more catalytic reactions sites. Increasing the reaction rate leads to increased current output and higher fuel utilization [65]. A microfluidic size scale also can aid in reducing mass transport losses as the low Reynolds number in micro-scaled geometries leads to laminar flow, which can be effectively modeled allowing for numerical processes (such as finite element modelling or computational fluid dynamics) to effectively optimize fuel supply and utilization.

Given the possible benefits of scaling down fuel cell devices, there were multiple efforts to create miniaturized fuel cell devices throughout the early 2000s which leveraged standard micromachining processes which produced devices of smaller and smaller size scale [56,66]. These fuel cell implementations were often composed of micropatterned Si wafers and operated with gaseous hydrogen fuel, analogous to macroscale fuel cells. Micromachined devices were typically fabricated using clean-room processing technologies inherited from microelectronic fabrication including photolithography, and reactive ion etching. Utilization of microelectronic fabrication techniques involved high capital costs (the processing equipment as well as maintaining a clean-room environment) and complicated fabrication methods. Furthermore, devices required solid electrolyte membranes, such as Nafion, further increasing device cost.

Perhaps the most important development in the history of MFC devices was demonstration of the first membraneless MFC (MMFC) device in 2002 reported by Ferrigno *et al.* working in George Whiteside's group at Harvard, shown schematically in Figure 2.5 [67]. Rather than creating a small size adaptation of a conventional fuel cell architecture, their device leveraged the innate properties of the microfluidic domain, namely laminar flow, to yield a simplified and cost effective device architecture. This lead to their device being the first 'true' microfluidic fuel cell. In their device, a Y shaped rectangular microchannel was fabricated in a polymer surface (poly(dimethylsiloxane), PDMS) using soft-lithography. Streams of vanadium (V) and vanadium (II) were passed the inlets of the device and merged into two stable fluid streams in the main microchannel. Due to the low Reynold's number of the microchannel, the two fluids interacted by only diffusive mixing leading to a small region of mixed fluids between two stable V (V) and V (II) streams. Near each sidewall, the bottom of the microchannel had been patterned with carbon on Au electrodes which served as anode and cathode electrodes. In this way, Ferrigno *et al.* were able to emulate the behavior of a conventional fuel cell with a simplified device architecture.

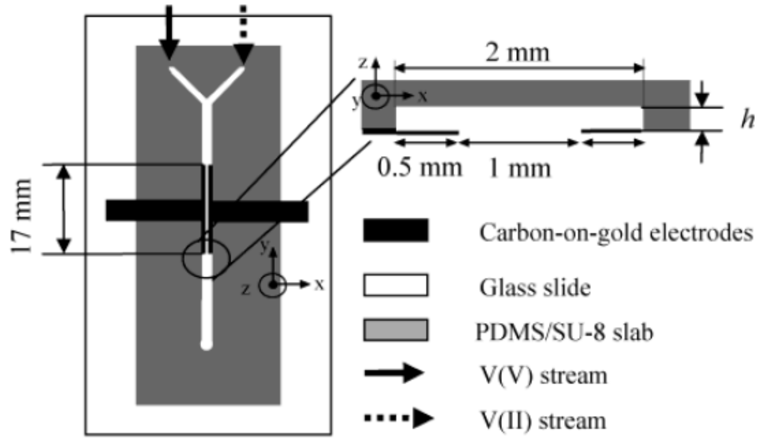

Figure 2.5 Schematic diagram of the first reported membraneless MFC device produced by Ferrigno *et al.* Their device used a PDMS microchannel which had been bonded to a class slide combined with carbon on Au electrodes. Anolyte and catholyte streams flowed streams of reduced and oxidized aqueous vanadium ions, respectively. Reprinted with permission from Ferrigno et al. *J. Am. Chem. Soc.* 124 (2002) 12930-12931. Copyright © 2002, American Chemical Society [67].

Ferrigno *et al.*'s device demonstrated that specifically engineering a device to leverage the properties of the microfluidic environment can yield favourable results. Specifically, their device showed that laminar flow based diffusive gradients (as described previously for applications such as passive micromixers) could take a more active role and function as 'effective membranes' removing the need for a physical isolation of the anode and cathode half cells. Molecules would be selectively separated through their relative diffusivities rather than permeability through a physical membrane [24]. An 'effective membrane' allowed for MFC devices to be constructed in a planar environment, where patterning is restricted to only one side of a device. Using polymer soft-lithography, these planar fuel cells could be produced quickly, cheaply, and effectively without the complicated and costly tools found in Si processing. Demonstrating that laminar flow isolation can be used to produce functional fuel cells spurred significant development by other research groups and lead to the larger field of microfluidic fuel cells that is found today. Further development of MFC technology has sought to improve the utility of devices through new device architectures and methods as is discussed below [68].

2.2.2. Miniaturized Fuel Cell Devices

While membraneless MFC technology evolved during the 2000s, parallel efforts were made to continue development of scaled-down conventional fuel cell devices (here termed miniaturized fuel cells, mini-FCs). These devices followed a design principle that is directly evolved from macroscaled systems and were fabricated by independently microfabricating anode and cathode half cells which are then mechanically bound together in close proximity [69]. Most often, devices are divided by a polymer electrolyte membrane which can also be directly integrated into the electrode surface in a single hybrid structure termed a membrane-electrode-assembly or MEA [70]. Mini-FCs have been developed using both gaseous and liquid fuel streams and also include combined reformed liquid devices where a fuel (methanol) is converted to H_2 and then used as a H_2/O_2 fuel cell [57,71]. There are several motivations for choosing a mini-FC architecture. Firstly, as shown in Figure 2.6, these types of devices can achieve exceedingly small (often on the order of 10s-100s of microns) spacing between anode and cathode half cells by use of a thin membrane layer. Decreasing the distance between the anode and cathode decreases ohmic resistance, boosting device efficiency as the diffusion length between the electrodes is smaller. Secondly, by integrating highly-selective membrane materials inherited from macroscale devices, fuel utilization is improved as anolyte and catholyte solutions are strongly isolated. Finally, a mini-FC architecture is amendable to using micropatterned Si substrates. Si based devices are able to operate at higher temperatures and pressures than polymer membraneless devices which can lead to more favourable reaction kinetics and higher power output [57]. Despite these benefits, usage of mini-FCs as integrated components in microfluidic systems has been limited due to complicated and costly fabrication. Mini-FCs require patterning processes including clean-room photolithography and micromachining. There are also challenges with integrating miniaturized fuel cells into a self-contained microfluidic chips due to integrated regulatory systems to control gas flow, and concentration which necessitate bulky interfaces with the external environment [72]. Finally, mini-FCs rely upon materials used in conventional macroscale fuel cell devices such as commercial PEMs (*i.e.* Nafion) and GDEs which add considerable material cost. Electrodes also typically rely upon precious metal Pt/Pd catalysts.

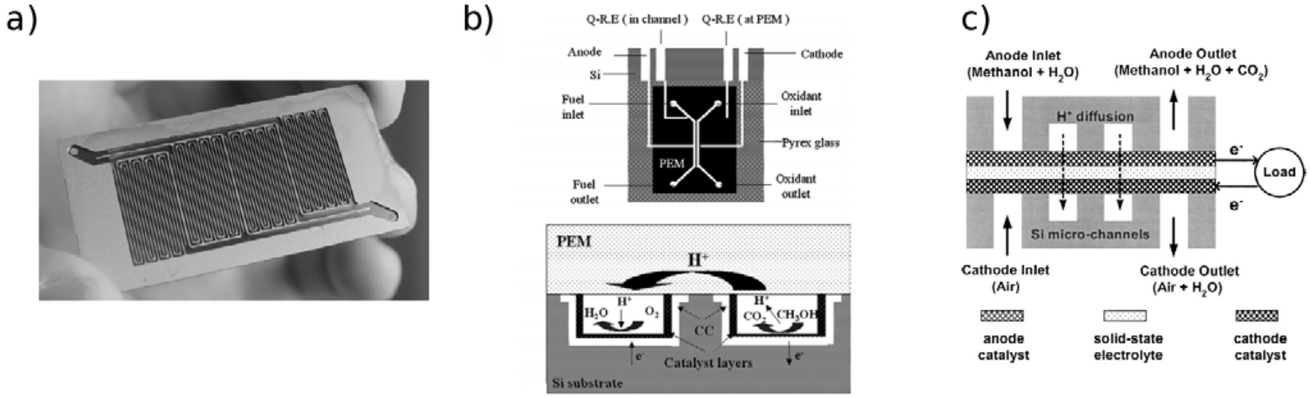

Figure 2. 6 Examples of micromachined mini-FCs (a) an optical image of a micropatterned Si substrate formed using reactive ion etching for use in a miniaturized reformed methanol fuel cell, from Morse *et al.* 2007, used with permission. Copyright © 2007, Elsevier. [73] (b) Schematic diagram of a micropatterned Si miniaturized DMFC device using Si microchannels for anolyte and catholyte, from Motokawa *et al.* 2004. Figure Copyright © 2004, Elsevier, used with permission. [74] (c) Schematic diagram of a miniaturized direct methanol fuel cell sandwiched between two patterned Si wafers, from Yen *et al.* 2003. Figure Copyright © 2003, Elsevier, used with permission. [75].

2.2.3. Development of MFC Devices

Since their inception in 2002, MFC have been established as distinct subclass of microfluidic devices and substantial progress has been made towards creating highly functional devices. As of the end of 2013, 280 papers related to microfluidic fuel cells have been published with increasing participation as shown in Figure 2.8. Research has been focused on many different aspects of the MFC architecture including selection of reagents (combinations of fuel and oxidant for anolyte and catholytes), variations in device geometries (to improve fuel utilization and device efficiency), as well as fabrication technologies (creating MFCs more cheaply).

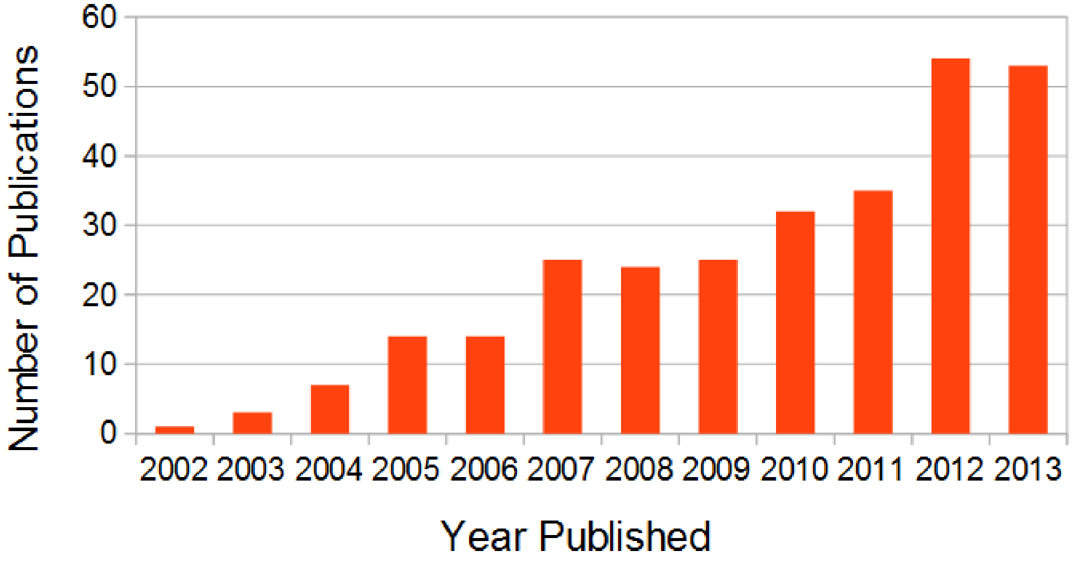

Figure 2. 7 Graphs displaying the number of publications published per year as indexed by Web of Science (Thompson Reuters). Applied search parameters were “microfluidic+fuel+cell”, with results obtained on March 13 2014.

In a 2011 review, Shaegh *et al.* consolidated the specific challenges facing optimization of membraneless MFC device implementations into an elegant flow chart shown in Figure 2.8. They described the output performance of MFC devices as being due to the combination of theoretical open-circuit potential, minus the trio of aforementioned inefficiencies: activation losses, mass-transport losses, and ohmic losses. Shaegh *et al.* graphically illustrated how the components of an MFC device interrelate to yield the overall device performance. Throughout the development of MFC technology, research has been undertaken to create new architectures and materials to minimize the effects of these losses.

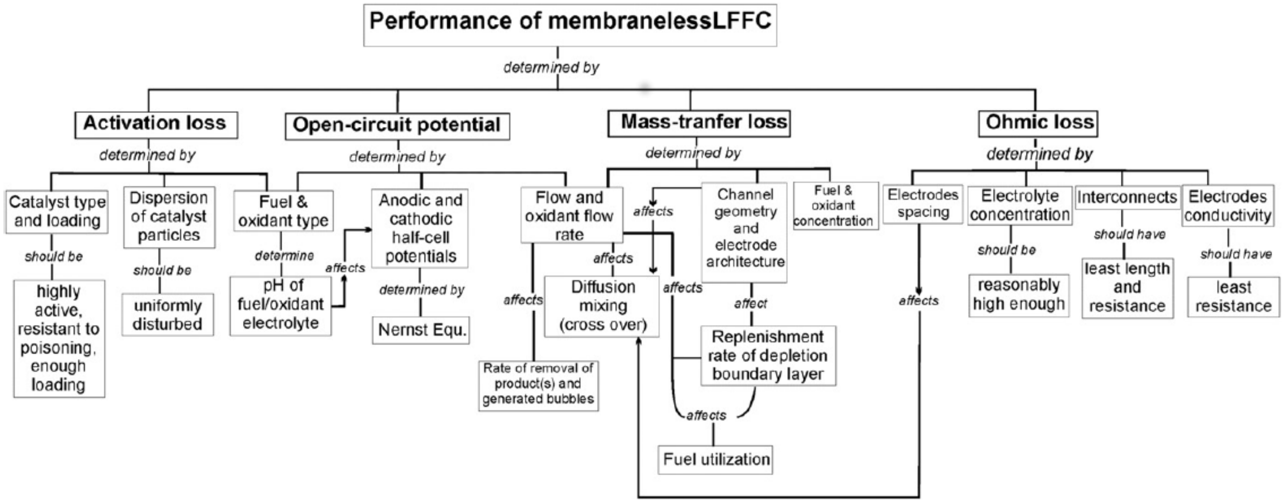

Figure 2.8 Schematic diagram showing the relationship between the functional components of a MMFC device and how they relate to overall device performance. This figure serves as a roadmap for implementation of a MMFC device implementation. Image adapted from Shaegh *et al.* 2011. Figure Copyright © 2011 Hydrogen Energy Publications, used with permission [76].

2.2.4 Microfluidic Fuel Cell Devices

After the first MFC device was developed by Ferrigno *et al.*, further research investigated the utility of a wide range of novel membraneless device architectures. MFC devices can be broadly classified into two groups those fabricated planar or sandwiched architectures, as shown schematically in Figure 2.9.

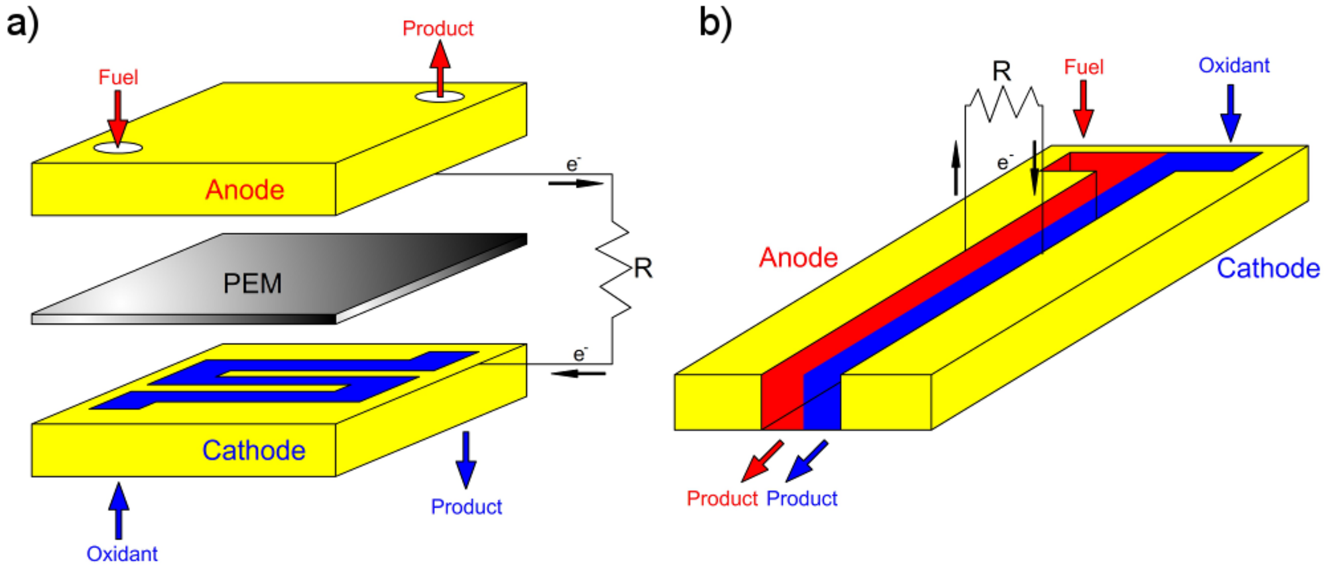

Figure 2. 9 Schematic diagram of the two main types of MFC devices (a) stacked and (b) planar. In stacked devices, both the upper and lower surfaces are patterned with microfluidic channels and are either used in membraneless implementations or separated by a solid electrolyte membrane. In planar devices, fuel and oxidant solutions are flowed side-by-side and laminar flow is used to create an 'effective membrane' separating the half cells.

Stacked devices more closely resemble mini-MFCs where anode and cathode half cells are independently fabricated and subsequently bonded. Compared to planar devices, a sandwiched architecture allows for simplified fabrication of electrodes. Each electrode can be deposited using conventional techniques (on flat surfaces) and subsequently bound together. However this type of device does require patterning of both top and bottom surfaces of the device and fine alignment between the top and bottom layers. If required, a stacked, membraneless MFC device can be converted into a membrane containing architecture in a straightforward manner (adding a membrane between the patterned anode and cathode surfaces).

The main benefit of a planar architecture is decreased fabrication complexity. As all of the fluid elements of the device are contained within a single surface, only single sided microchannel patterning is required to create a device. Additionally, sealed devices can be formed by bonding to a featureless capping layer which does not require microscale alignment. Simplified fabrication means that a planar MFC device can be fabricated in a conventional laboratory bench-top environment, rather than a clean-room facility (as is required for micromachined fuel cells).

Planar or 'side-by-side' MFCs are built with an architecture where the entire fuel cell device is contained within a single-sided microchannel which is later sealed at the top. Electrodes are located on the channel walls (either sidewalls or channel bottom, or combinations thereof) and electrically isolated through selective deposition/patterning techniques [77,78,79,80]. To date, integration of conventional proton exchange membranes into planar devices has been limited to two reports, both of which required complex multi-stage patterning to achieve [81,82]. In both methods, Nafion was first patterned onto the surface of a flat substrate and then precisely aligned below a patterned microchannel prior to bonding. Alternatively, membraneless-operation may be implemented as in the work of Ferringo *et al.* described above.

Early efforts to improve MFC implementations directly expanded on the work of Ferrigno *et al.* and involved similar devices with Y or T shaped microchannels using two parallel fluid streams using more conventional fuels and oxidants than vanadium redox couples. Noteworthy publications in 2004 and 2005 by Choban *et al.* demonstrated two different MFC systems using formic acid and methanol as fuel compounds. In their work they examined fuels using dissolved oxygen and potassium permanganate oxidants [33,83]. These devices, using two stream co-laminar flow in Y shaped microchannels, achieved maximum output voltage and power densities of 1.1V/1.4V and 2.4 mW/cm^2 / 12 mW/cm^2, for formic acid and methanol respectively. By using fuel compounds that were applicable to conventional larger scale liquid fuel cell devices, comparisons in device efficiency and applicability could now be made. MFC devices were found to be less efficient at power generation than their micromachined counterparts based upon conventional fuel cell technologies but were both considerably less expensive and easier to fabricate. By the mid-2000s researchers had begun to identify areas of concern in MFC technology and seek out methods and materials to mitigate them. The focal points for further development of MFC devices were addressing limited mass transport to electrode surfaces and poor fuel utilization.

The stable fluid flow properties offered by laminar flow were revealed to be a double edged sword. While allowing for isolation of anode and cathode half cells, laminar parabolic fluid flow (coupled with a no-slip boundary condition) leads to low mass flow rates directly above the channel interfaces (*i.e.* the walls of the microchannel) *where the catalytic electrodes are located*. As such, the supply of reagents and removal of products from electrode surfaces places limits on sustainable current production. Beyond mass transport limitations, flow over MFC devices have also been found to lead to low levels of fuel utilization. Mass transport losses also decrease the fuel utilization of flow over systems, described by Kjeang *et al.* in a 2009 review as the largest source of losses hindering MFC performance [49]. It has also been shown that in some devices, fuel utilization rates as low as 10% were achieved (due to the fact that not all of the reactants were able to react at electrodes while passing through the device). In a macroscopic device, this issue would be addressed by recirculating the reactants through the device. However, even in a low Reynolds number microchannel there is a small, but non-zero, amount of diffusive mixing between anolyte and catholyte solutions. Most MFC devices use precious metal (Pt or Pd) catalysts which, while highly efficient, catalyse both anode and cathode reactions non-selectively. Consequently, recirculation is normally not feasible as catalysts, on each electrode, will react with both anolyte and catholyte solutions and result in mixed potentials (*i.e.* current consuming reactions on the anode and current producing reactions on the cathode), decreasing the output of the half-cell [49].

Seeking to address mass transport losses and fuel utilization limitations, researchers started exploring novel methods to improve performance by moving away from the architecture used by Ferrigno *et al.* By 2006, a host of new MFC devices had been presented which can be classified into three sub-groups devices with (1) flow-over electrodes, (2) flow-through electrodes, and (3) air breathing cathodes.

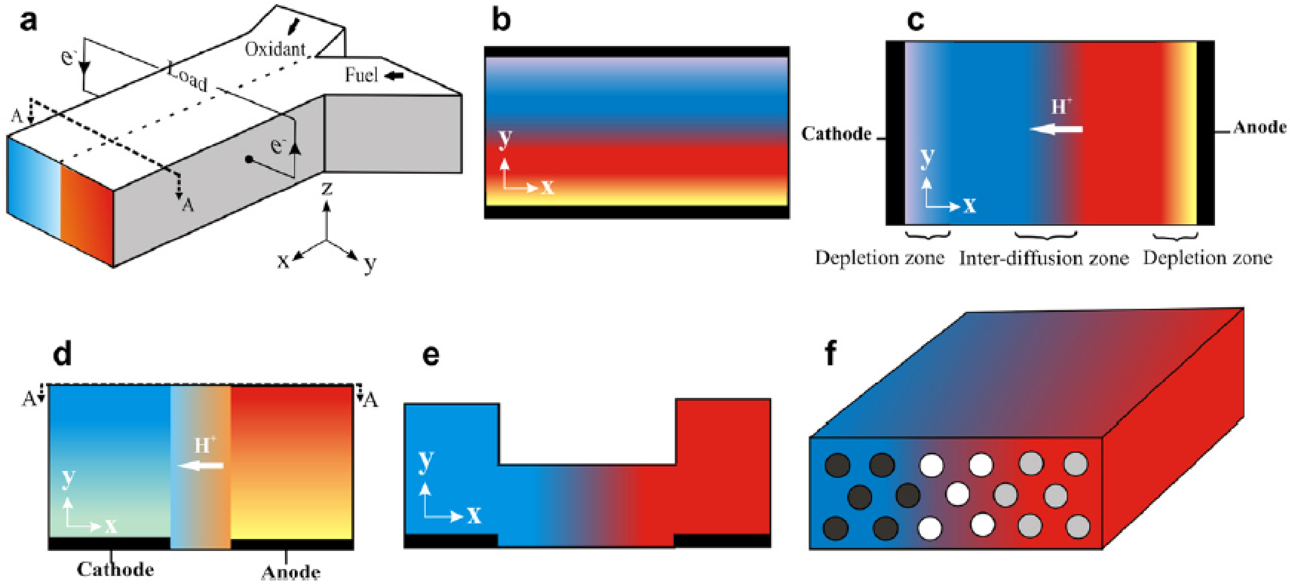

Figure 2.10 Flow-over electrode device configurations with a (a) Y shaped device architecture with various electrode orientations. (b-f) Cross sectional schematics of (b) top/bottom, (c) side-wall, (d) channel base electrodes (e) channel base in a groove microchannel and (f) a "three-dimensional" electrode geometry featuring cylindrical electrodes placed parallel to the microchannel and running throughout its length. All schematics are shown as cross sections looking at a slice along the length of the microchannels. Figure from Shaegh *et al.* 2011. Copyright © Hydrogen Energy Publications 2011, used with permission [76].

Flow-over Systems

In flow-over systems, anolyte and catholyte fluid streams passed over catalytic electrodes deposited on either the channel side-walls or bottom, as shown schematically in Figure 2.10. Devices of this structure are straightforward to fabricate by either simply placing metallic slabs/wires under a sealed microchannel, or using more expensive conventional lithographic techniques. Flow-over device are however are most susceptible to mass transport losses and are difficult to maintain high levels of current output [76,84,85]. Improvements to flow over MFCs sought to improve device functionality through modifications to geometry as well as fuel/oxidant selection. Advances to flow-over MFCs were demonstrated by Yoon *et al.* in 2006 with integration of additional inlets to a conventional Y channel design to destabilize the fluid near the electrode, improve mass transport, and Bazylak *et al.* who described a tapered electrode geometry decreasing parasitic current generation by matching electrode geometry to diffusive broadening [86,87]. Kjeang *et al.* described a different route to improving mass flow, by inserting three dimensional graphite rod electrodes into the bulk of the microchannel [88]. These improvements to flow-over MFCs involved modifying the device geometry to improve performance.

Other groups have tried to improve flow-over device functionality through modification of fuel/oxidant solutions, as well as tailoring catalytic elements of electrode surfaces. In 2005, Choban *et al.* reported a Y shaped device which used the isolation granted by laminar flow to allow for independent selection of pH by flowing different reactants carried in different electrolytes in the anode and cathode half cells [83]. This simple modification allows for independent optimization of the reaction conditions in each half cell, allowing for more effective devices. Also in 2005, Hasegawa *et al.* demonstrated a MFC based on hydrogen peroxide based anolyte and catholyte solutions using a similar method with sodium hydroxide and sulfuric acid electrolytes [89]. There is significant room for future utilization of these methods to allow for more effective optimization anode and cathode half-cell reactions beyond variable pH but also temperature, concentrations of dissolved gases. The design parameters (including anode/cathode half -cell materials and electrolyte) as well as reported electrical characteristics are given in Table 2.1. The majority of flow-over devices reported to date have used precious metal (Pt/Pd) catalysts in sulfuric acid electrolyte solutions, and have differentiated themselves by the location (side-walls, bottom surface, top surface, or combinations thereof) and structure of electrodes within the microchannel. Maximum output power densities have varied considerably from 5 µW/cm^2 to 38 mW/cm^2.

Table 2.1 Design and current/voltage parameters for flow-over electrode devices.

Author	**Fuel [Anode] / Oxidant [Cathode]**	**Electrolyte**	**Maximum Power Density [mW/cm^2]**	**Maximum Current Density [mA/cm^2]**	**Novel Design Features**
Choban *et al*. [83]	Methanol [Pt/Ru nanoparticles]/Dissolved O_2 [Pt black nanoparticles]	Sulfuric acid or potassium hydroxide	12	40	Mixed media operation
Choban *et al.* [33]	Methanol [Pt black]/Dissolved O_2 [Pt black]	Sulfuric acid	2.8	8	-
Cohen *et al.* [90]	Formic Acid [Pt]/Dissolved O_2 [Pt]	Sulfuric acid	0.18	1.5	Stackable microchannels
Cohen *et al.* [91]	Hydrogen [Pt] / oxygen [Pt]	Potassium hydroxide or sulfuric acid	0.75	0.85	Aqueous hydrogen and oxygen inflow streams
Dector *et al.* [92]	Formic acid [Pd] / O_2/air/hydrogen peroxide [Pt]	Sulfuric acid	6.7	30.4	Multiple catholyte solutions
Ferrigno *et al*. [67]	V (II) [C]/ V (V) [C]	Sulfuric acid	38	80	-
Hasegawa *et al.* [89]	Hydrogen peroxide [Pt]/ hydrogen peroxide [Pt]	Sodium hydroxide or sulfuric acid	23	76	-
Huo *et al.* [93]	Methanol [Pt/Ru]/ hydrogen peroxide [Pt/C]	Sulfuric acid	12.24	~45	Ladder shaped microchannel
Kjeang *et al.* [94]	Formic acid [Pd] / hydrogen peroxide [Pt or Pd]	Phosphate buffer	30	150	Groove shaped microchannel
Li *et al.* [95]	Formic Acid [Pt/Ru black]/ Dissolved O_2 [Pt]	Sulfuric acid	0.58	1.5	Laser-machined
Mitrovski and Nuzzo [78]	Hydrogen [Pt/Pd] / air [Pt]	Sulfuric acid or sodium hydroxide	0.7	1.2	-
Mitrovski *et al.* [85]	Hydrogen [Pt] / oxygen [Pt]	Sulfuric acid or sodium hydroxide	0.7	1.6	-
Moore *et al.* [96]	Ethanol and NAD+ [Alcohol dehydrogenase] / Oxygen [Pt]	Phosphate	0.005	0.05	Bioanode
Morales-Acosta *et al.* [97]	Formic Acid [Pd/MWCNT]/Dissolved O_2 [Pd/MWCNT]	Sulfuric acid	3.3	11.5	Pd/multi-wall-carbon-nanotubes Catalysts
Moreno-Zuria *et al.* [98]	Formic acid [Pd] / dissolved O_2 [Pd]	Sulfuric acid	8.3	~20	Pd nanocube catalysts
Sun *et al.* [99]	Formic acid [Pt] / potassium permanganate [Pt]	Sulfuric acid	0.7	2.6	Three co-laminar streams
Sung and Choi [100]	Methanol [NiOOH/Ni(OH)$_2$] / hydrogen peroxide [Ag$_2$O]	Potassium hydroxide	0.03	1.1	Interdigitated mixed anolyte/catholyte

Flow-through systems

The second type of planar membraneless MFC devices utilize flow-through electrodes, as shown in Figure 2.11, and were introduced in 2008 by Kjeang *et al.* [101]. In their device architecture, vanadium (II) anolyte and vanadium (V) catholyte solutions passed through porous carbon paper electrodes (hence the ‘flow-through’ name), ensuring high levels of mass transfer to both electrodes. Kjeang *et al.* demonstrated a flow-through architecture that yielded considerably improved performance compared to a conventional flow-over devices, and had fuel utilizations of up to 94%. Also in 2008, a flow-through architecture was shown by Salloum *et al.* They used more conventional fuel/oxidants of formic and potassium permanganate, respectively. While less effective than the non-catalytic vanadium device by Kjeang *et al.*, Salloum *et al.*’s device was found to improve fuel utilization up to 58% while flowing 100 µL/min of reactants [102]. As found in these studies, flow-through devices create more favourable fuel utilization through increased surface area but complicate device fabrication, techniques to create high surface area electrodes *in situ* are highly desirable. Further studies applied flow through electrodes to other fuel/oxidant combinations as well as parallelized device structures [103,104]. A flow-through device architecture offers considerable benefits to MFC device functionality. By flowing anolyte and catholyte through porous electrodes, the high surface area to volume ratio associated with microfluidic channels is compounded with the high surface area of porous structures to yield electrodes with exceptionally high electro-active areas. Relevant output parameters for flow through devices are given in Table 1.2. To date, development of flow-through MFC devices has been centered on two fuel compounds, vanadium redox couples and formic acid. A wide variety of device geometries with different flow profiles have been examined including circular radial flow microchannels and rectangular microchannels with parallelized arrays of porous electrodes. Flow through MFC implementations have demonstrated considerably higher power output densities than flow-over devices (to date ranging from 0.4 to ~1200 mW/cm^2)

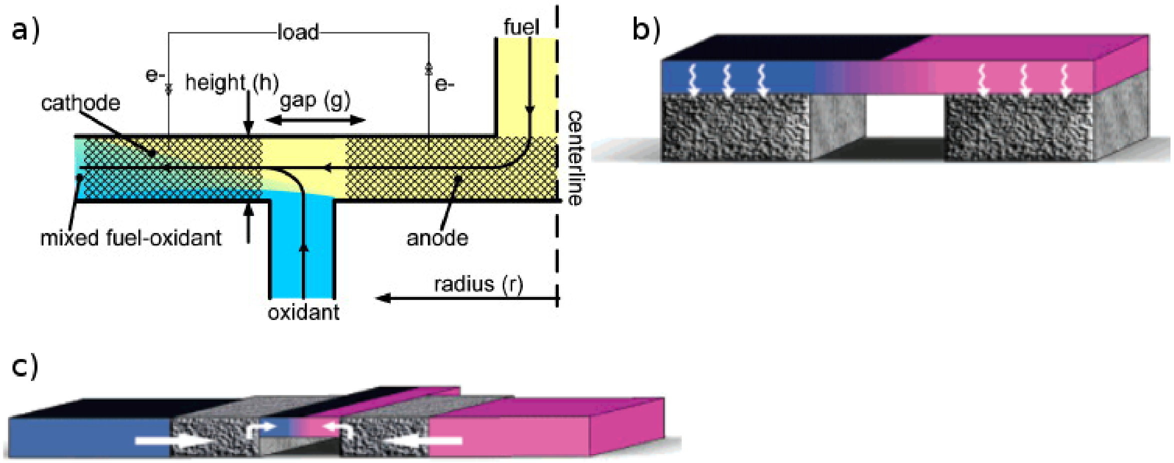

Figure 2.11 Schematic diagrams of flow-through MFC implementations. In all schematics, electrodes are formed of porous carbon which allows for anolyte and catholyte solutions to pass through the electrodes. (a) Flow through radial porous electrodes. Figure from Salloum *et al.* 2008 [102]. Copyright © 2008 Elsevier, used with permission. (b) and (c) Two different orientations of flow through planar electrodes in a vanadium based MFC device. Reprinted with permission from Kjeang *et al. J. Am. Chem. Soc.* 130 (2008) 4000-4006 [101]. Copyright © 2008 American Chemical Society.

Table 2.2 Design and current/voltage parameters for flow-through electrode devices.

Author	**Fuel [Anode] / Oxidant [Cathode]**	**Electrolyte**	**Maximum Power Density [mW/cm^2]**	**Maximum Current Density [mA/cm^2]**	**Design Features**
Fuerth *et al.* [103]	Formic acid [Pt] / Potassium permanganate [Pt]	Sulfuric acid	0.4016	0.8032	Up-scaled design
Ho *et al.* [104]	V (II) [C] / V (V) [C]	Sulfuric acid	1200 [two coupled devices]	~1800 [two coupled devices]	Planar design for parallelized operation
Kjeang *et al.* [105]	Formic acid [Pt] / sodium hypochlorite [Pt or Pd]	Sodium hydroxide	52	230	3D structured electrodes
Kjeang *et al.* [88]	V (II) [C] / V (V) [C]	Sulfuric acid	35	92	Graphite porous electrodes
Kjeang *et al.* [106]	V (II) [C] / V (V) [C]	Sulfuric acid	70	243	Porous electrodes
Kjeang *et al.* [101]	V (II) [C] / V (V) [C]	Sulfuric acid	131	326	Porous flow through electrodes
Salloum *et al.* [102]	Formic acid [Pt] / potassium permanganate [Pt]	Sulfuric acid	2.8	5	Sequential radial flux

Air-breathing cathodes

A final type of membraneless MFC geometry, shown schematically in Figure 2.12, was introduced in 2005 and utilizes air-breathing cathodes. In these type of devices – as shown by Jayashree *et al.* – a porous gas diffusion electrode (as often found in macroscopic systems) is used as a cathode in a sandwiched configuration with laminar flow isolation used to isolate it from a flow-over type anode [107]. Air-breathing systems allow for access to an abundance of oxygen (far greater amounts than can be provided by dissolved oxygen in aqueous solutions) supplied from gas diffusion electrode devices. Consequently, current and power output characteristic of air breathing devices are usually limited by the amount of electrons supplied by the anode half-cell, and often have enhanced output compared to other MFCs [108]. Like flow-through MFCs, air-breathing systems do require integration with non-conventional microfluidic materials (precious metal containing gas diffusion electrodes), which can lead to fabrication challenges and increased device cost. To date, air-breathing device architectures are most amendable to a sandwiched device configuration. Air-breathing MFC devices have been shown to produce devices capable of long-term operation with favourable electrical outputs given in Table 2.3. To date, air breathing devices have employed a variety of channel geometries and used methods from flow-through devices to further enhance anodic current generation. While maximum output power densities, ranging from 4 – 70 mW/cm^2, are not as high as for flow-through devices, air breathing systems use more conventional fuel compounds (formic acid and methanol as opposed to vanadium redox couples). Further work is needed to determine the most effective materials (and methods) to supply oxygen into the MFC device.

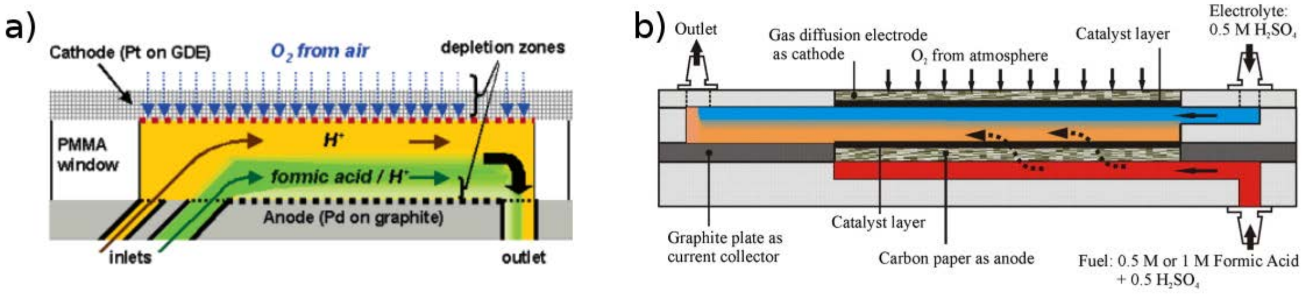

Figure 2.12 Schematic diagrams of air breathing MFC devices. (a) A flow through stacked MFC device using a porous carbon gas diffusion electrode and formic acid anolyte. Reprinted with permission from Jayashree *et al. J. Am. Chem. Soc.* 127 (2005) 16758-16759 [107]. Copyright © 2005, American Chemical Society. (b) A stacked MFC device using a flow through anode and gas diffusion cathode. Figure from Shaegh *et al.* 2012 [109]. Copyright © 2011, Hydrogen Energy Publications, used with permission.

Table 2.3 Design and current/voltage parameters for air-breathing MFC devices.

Author	**Fuel [Anode] / Oxidant [Cathode]**	**Electrolyte**	**Maximum Power Density [mW/cm^2]**	**Maximum Current Density [mA/cm^2]**	**Design Features**
Brushette *et al.* [110]	Formic acid [Pd black], methanol [Pt/Ru black], ethanol [Pt/Ru black], sodium borohydrate [Pt black], or hydrazine [Pt black] / air [Pt black]	Sulfuric acid or potassium hydroxide	26	130	
Hollinger *et al.* [111]	Methanol [Pt/Ru] / O_2 gas [Pt]	Sulfuric acid	70	655	Methanol at high temperature and pure O_2 gas feed
Jarashree *et al.* [108]	Methanol and potassium hydroxide [Pt/Ru] / air [Pt]	Sulfuric acid	17	120	
Jayashree *et al.* [107]	Formic acid [Pd black nanoparticles] / Air [Pt black nanoparticles]	Sulfuric acid	26	130	
Shaegh *et al.* [112]	Formic acid [Pd black] / air [GDE]	Sulfuric acid	7.9		PMMA device, extensive modeling
Shaegh *et al.* [109]	Formic acid [Pd black] / air [GDE]	Sulfuric acid	29	86	Fuel reservoir
Whipple *et al.* [113]	Methanol [Pt/Ru] / air [Pt or Ru_xSe_y]	Sulfuric acid	4	62	Ru_xSe_y cathode catalyst
Zhu *et al.* [114]	Formic acid [Pd/Nafion] / air [GDE]	Sulfuric acid	21.5 [/cm^3]	118.3 [/cm^3]	Cylindrical electrodes

As will be presented later in this thesis, methods to unify the beneficial properties of all three membraneless device architectures are highly desirable. Flow-over devices can be easily produced with rapid prototyping techniques. Porous electrode devices are able to ensure high fuel utilization by forcing anolyte and catholyte to pass through the electrode. Air breathing devices allow for usage of oxygen from the external environment to reduce cathode half-cell limitations. Achieving optimal devices requires development of new methods and materials.

2.3 Materials and Fabrication Methods for MFCs

In the previous section, the development of MFC devices was reviewed. Improvements to the MFC device architecture have been achieved by adapting materials and geometries to yield more favourable reaction conditions. One of the most beneficial aspects of MFCs is their compatibility with rapid prototyping techniques, whereby devices can be produced cheaply and quickly [115]. As such, traditional materials that function effectively in mini-FCs such as silicon, glass, or ceramics are often unfavourable in microscaled implementations. This section will review current materials used in macroscale as well as microscale fuel cell devices, and describe areas where new novel materials are required to advance the functionality of MFCs. Both materials and required fabrication techniques are described with specific focus is placed on materials used in planar MFC implementations. Three key materials are reviewed: the base materials that compose the devices, ion exchange membranes used to divide the half-cells, and catalytic electrodes used to produce current.

2.3.1 MFC Base Materials

During design of a microfluidic fuel cell device, great emphasis is placed on the components which can most directly improve device performance, electrode and electrolyte membrane materials. The device base material (that which composes the bulk of the device and into which a microchannel is patterned) can also play a significant role in device fabrication and operation. As described in Section 2.2.2, mini-MFC devices are often fabricated using traditional microelectronic materials (*i.e.* silicon and glass). Microelectronic materials are well suited to precise high value applications, such as integrated circuits, but are expensive and require more costly fabrication techniques than membraneless MFC devices produced through rapid prototyping [116]. As with other microfluidic devices, modern MFCs are usually composed of polymers: repeat unit chemical structures which have been integrated into all aspects of the modern world [117]. Polymers are an ideal class of materials for MFC device fabrication given their widely varying (and tailorable) properties. Characteristics such as elastic modulus, optical absorbance, chemical resistance, and thermal stability can all be controlled through usage of different chemistries or blends of polymer compounds [118]. MFC devices can be formed using both thermoset materials such as poly(dimethyl-siloxane) and thermoplastic materials such as poly(methyl-methacrylate) [118]. Thermosets are polymers which are formed from monomers (often liquids or malleable solids) that undergo irreversible covalent crosslinking reaction when exposed to a specific trigger (usually heat but also some forms of high energy irradiation) cannot be melted after polymerization [119]. Thermoplastics are polymers which can be melted and reformed upon heating; these materials can therefore be shaped (with microscale precision) using techniques such as hot-embossing. Elastomers are a special class of thermosets, which are defined as highly deformable low elastic modulus polymers. Elastomeric materials have come to dominate microfluidic device designs due to their ease of fabrication and low cost [120].

Like most microfluidic systems, polymer MFC devices stand in the shadow of a particular polymer, PDMS, a transparent elastomer which is likely the most widely utilized, reported, and characterized material in all of microfluidics [121,122]. Some of the first MFC devices produced, by Ferrigno *et al.* and Mitrovski *et al.*, were formed out of PDMS microchannels, and it has remained a staple of MFC development to the present day [67,85]. The main benefit of PDMS as a microfluidic material is its ability to easily produce inexpensive microfluidic devices through elastomer micromolding. Elastomer micromoulding is a process where a liquid elastomer is poured on top of a pre-patterned master, usually a micropatterned Si wafer produced through conventional photolithographic techniques, patterned with a negative relief of the desired microchannel [123,124]. Upon heating, the elastomer cures into a solid crosslinked polymer structure in the desired shape and can be removed from the master. As the structure of the master is unchanged by this process, many copies of the elastomer can be formed without repeating the microscaled patterning processes needed to form the master. This process is shown schematically in Figure 2.13. PDMS surfaces can also be either reversibly or irreversibly bound together. A reversible bond can be formed by mechanically pressing two PDMS films together. A strong irreversible bond between PDMS surface can be achieved by activating the surfaces (often either with exposure to a UV/ozone system or an oxygen plasma) prior to merging the surfaces.

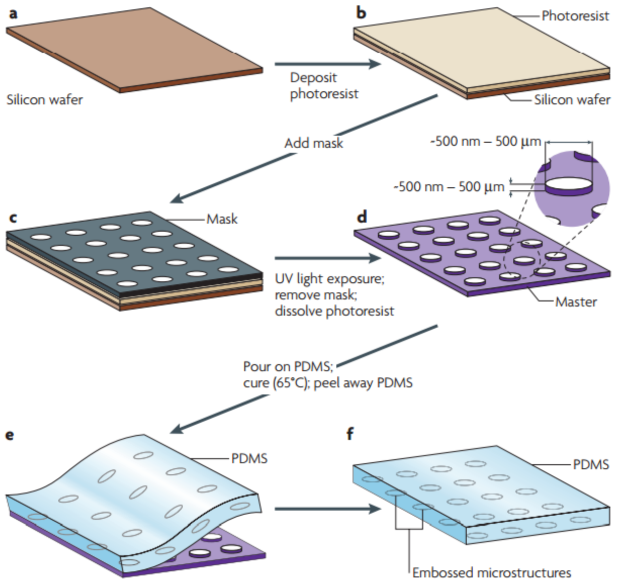

Figure 2.13 Schematic diagram of an elastomer micromoulding process. (a) First a bare silicon wafer is obtained which is then (b) coated with photoresist (a material that selectively becomes more/less soluble upon exposure to specific wavelengths of light). (c) The photoresist coated wafer is exposed with a desired structure through a selective masking layer (in this example to pattern an array of circles). (d) The wafer is then etched and after removing the photoresist layer an array of raised Si structures remains. (e) Liquid elastomer (in this case PDMS) is poured onto the patterned Si surface and cured into a solid structure. (f) Finally, the solid PDMS surface is peeled off from the wafer yielding a micropatterned polymer film. Reprinted by permission from Macmilan Publishers Ltd: *Nature* Weibel et al. 2007, Copyright 2007 [125].

Despite the processessability of PDMS, it does possess some qualities that may be unfavourable for usage in planar MFCs. Firstly, PDMS demonstrates relatively poor adhesion to metals. This is a concern when depositing electrodes on sidewalls or the bottom of microchannels as electrodes can deform with applied thermal/mechanical strain [126]. Secondly, PDMS is exceedingly porous to gases such as oxygen, and water vapour [127]. High porosity can be beneficial or detrimental to device operations, as it can allow for oxygen permeable cathodes (aiding output current density), but also lead to catalyst poisoning (if gases such as carbon monoxide or sulfur are introduced from the external environment), or mixed potentials (if oxygen permeates the anode half-cell and reacts at the catalytic electrode surface) [128]. Non-specific diffusion of gases is especially relevant for emerging applications such as microfluidic microbial fuel cells, where one of the half cells requires anaerobic conditions to facilitate microbial metabolism [129,130]. Thirdly, while being hydrophobic with a water contact angle of usually between 90-120^{o}, PDMS is permeable to liquids such as methanol as well as many other organics. Due to this property, PDMS films swell appreciably if in prolonged exposure to such compounds and may transport small amounts of organics through their bulk into other regions of the device (especially ill-suited if designing an MFC as an on-board power source for a lab-on-a-chip device where sample isolation is essential) [116,131]. Lastly, being an elastomer, PDMS has an elastic modulus in the MPa range, meaning that it is exceptionally deformable [132]. For MFC applications, where brittle deposited electrodes and integrated circuit elements are combined within a microchannel, devices completely formed of PDMS can easily buckle electrical connections leading to failure of devices. Additionally, at high flow rates fluid pressure can lead to channel deformation resulting in unstable fluid flow [133,134]. Despite these limitations, PDMS remains common in MFC devices. PDMS MFCs can either be formed entirely of PDMS channels or use a combination of a soft micropatterned PDMS surface (containing microfluidic channels) combined with a hard flat base material (typically glass or silicon) as is shown in Figure 2.14.

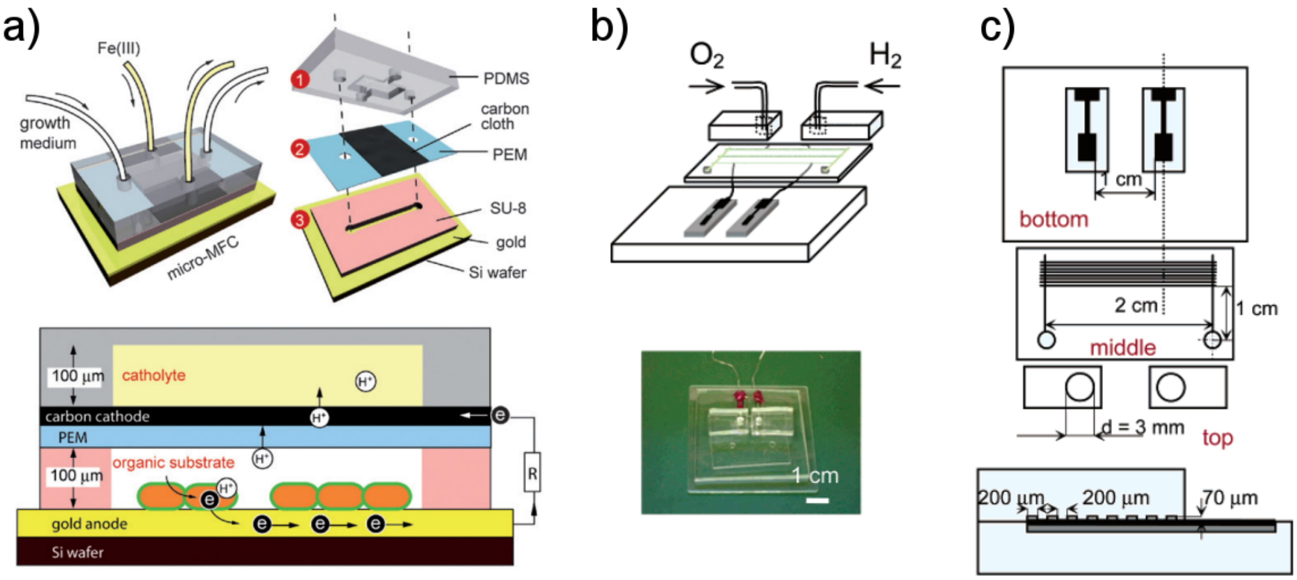

Figure 2.14 (a) Schematic diagram showing a PDMS based microfluidic microbial fuel cell. A micropatterned PDMS layer is combined with a micropatterned layer of SU-8 (photoresist) deposited on a Si wafer to create a sealed stacked device architecture. Reproduced from Qian *et al.* 2009 with permission of The Royal Society of Chemistry [135]. (b and c) Schematic diagram and optical image of a PDMS based hydrogen-oxygen fuel cell using arrays of microchannels patterned into a PDMS surface. Reprinted with permission from Mitrovski *et al.* *Langmuir* 20 (2004) 6974-6976. Copyright © American Chemical Society [85].

Significant efforts to address some of the limitations caused by PDMS based devices have also been taken to adapt thermoset materials such as thermoplastic materials such as poly(methylmethacrylate) (PMMA), and cyclic-olefin-polymers/co-polymers (COP/COC). Comparisons in material properties between PDMS, PMMA, and COC are given in Table 2.4 [118,136].

Table 2.4 Properties of common microfluidic materials. Data obtained from [136,137,138,139]

	Polydimethylsiloxane (PDMS)	**Cyclic Olefin Copolymer (COC)**	**Polymethyl methacrylate (PMMA)**
Polymer Type	Elastomer	Thermoplastic	Thermoplastic
Typical Material Properties			
Density [10^3kg/m3]	1.2	1.02	1.16
Glass Transition Temperature [°C]	-120	70-136	~105
Operational Temperature Range [°C]	-40 – 150	-73 – 80	-70 – 100
Elastic Modulus [MPa]	~0.7	~2600	~3000
Gas Permeability	High	Low	Low
Typical Optical Properties			
Transmission of visible light	High	High	High
UV Resistance	Good	Good	Good
Typical Chemical Resistance			
Acids	Fair	Good	Good
Alkalis	Poor	Good	Excellent
Organic Solvents	Poor	Fair	Poor

For MFCs, thermoplastic materials such as PMMA and COC offer significant benefits in terms of chemical compatibility, metal adhesion, and gas permeability [140]. Typically both materials are supplied in the form of thin sheets which can be effectively patterned with microchannels by means of hot embossing, a technique where a film of polymer is pressed with a patterned Si wafer with high pressure above its glass transition temperature, where the films are soft and can be shaped [141]. After embossing, films are cooled below their glass transition temperature, becoming mechanically rigid, and retain the structure of the master. Like elastomer micromoulding, this process requires a single pre-formed master which can be used to produce many devices. Several groups including

Brushett et al. 2009 have used PMMA to form MFC devices [110]. Tominaka *et al.* 2009 showed that using COP as a base material, MFC devices could be produced with output characteristics identical to those produced on micropatterned Si substrates as shown in Figure 2.15 [142].

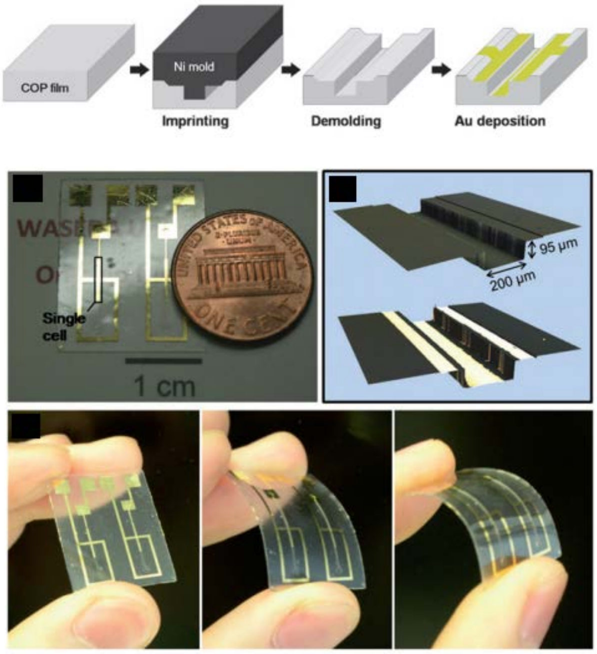

Figure 2.15 Schematic and optical image of a MFC devices patterned using a thin layer of COP. Reproduced from Tominaka *et al.* 2009 with permission of The Royal Society of Chemistry [142].

Polymeric material offer many benefits compared to traditional microelectronic materials. It is likely that future MFC devices will rely upon polymers (and combinations of polymers) to leverage the benefits this highly variable class of materials. The base material for a MFC device should be chosen understanding the beneficial and detrimental qualities associated with each material, and their effect of device operation.

2.3.2 Ion Exchange Membranes

While significant effort in miniaturized fuel cell device design has been focused upon membraneless systems (utilizing the laminar flow-based diffusive gradient to isolate the half cells), membrane containing devices continue to be developed and often yield higher output power and current profiles (and better fuel utilization) than comparable membraneless systems [49]. Membrane containing devices allow for more favourable output parameters due to less fuel crossover (due to the presence of a selective barrier) and less ohmic resistance (due to shorter diffusion lengths as the anode and cathode can be moved closer together without bulk mixing) [73]. As was described in Section 2.2.3, membrane containing devices are usually implemented in a sandwich architecture, analogous to macroscale MEA based fuel cells, which complicates their integrated into lab-on-a-chip type devices. Combining the high surface area and low production costs achievable in planar MFC devices with the improved output characteristics when using an ion exchange membrane is highly desirable.

An ideal IEM membrane consists of three functional properties: infinite conductivity of charge carriers (protons or hydroxide ions depending on PEM or AEM systems), zero electronic conductivity (forcing all electrical current through the external circuit), and stability during device operation (in terms of the membrane's chemical, mechanical, and electrochemical properties) [53]. Pursuit of IEM materials which satisfy these requirements has led to a diverse field replete with many innovative methods and materials. Development of IEM materials (specifically, PEMs) have their beginnings in early space exploration in the 1960s as an alternative power supply to bulky batteries [65]. These early materials were based on sulfonated polystyrene functionalized with sulfonic acid but were limited by low mechanical strength and short operating lifetimes [143]. The most important development in the history of IEM research was the development of Nafion (by DuPont), a perfluorosulfonic acid containing polymer which was able to increase fuel cell power output by two orders of magnitude and remain functional for long times scales [143]. Nafion (and related polymers) are still to this day considered the most effective PEM material due to the unique microstructure shown in Figure 2.16 [144].

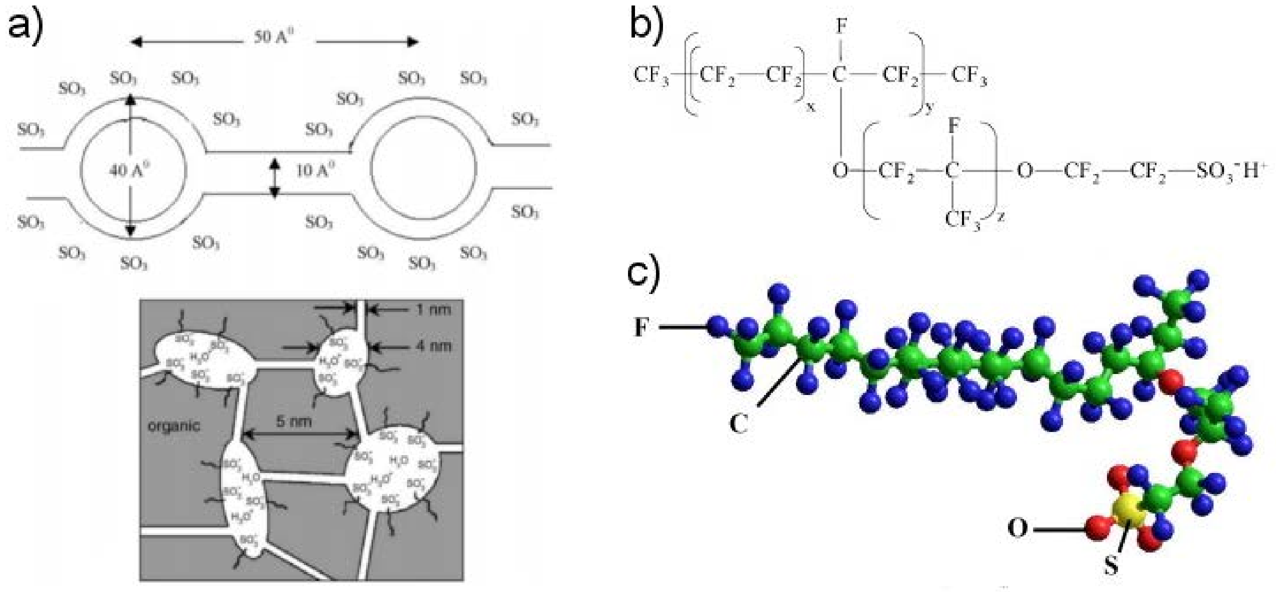

Figure 2.16 (a) Schematic diagram of proton conducting channels within a Nafion membrane. Sulfonic acid (SO_3) groups separate from the hydrophobic polymer bulk and arrange into clusters forming hydrophilic water channels. Figure from Smitha *et al.* 2005 [143]. Copyright © 2005, Elsevier, used with permission. (b) Chemical formula and (c) structural diagram of a typical Nafion polymer chain. Figure from Chen *et al.* 2009 [145]. Copyright © 2009, Elsevier B. V, used with permission.

The high proton conductivity in Nafion films has been explained as being caused by nanoscaled pores, consisting of clusters of sulfonic acid functional groups, which permeate the structure and are linked by water channels. These channels serve as highly conductive conduits that allow for protons to travel through the membrane by 'hopping' between sulfonic acid sites (in a method termed the Grothus mechanism) [146]. Pores are small enough that movement of other ions and compounds through the water channels is restricted.

Nafion is however limited by several materials properties: firstly it is costly, it also is of limited utility at higher temperatures (due to membrane dehydration and softening of the polymer backbone structure). Finally, Nafion exhibits high permeability to methanol making it ill-suited to DMFC based devices [143,147]. Given these limitations, significant efforts have been undertaken to find other materials suitable to replace Nafion. Notable results can be divided by the type of polymer used with the advantages and disadvantages of four groups of promising replacement materials (perflouroniated compounds, partially fluorinated compounds, non-fluorinated hydrocarbons, and non-fluorinated aromatic hydrocarbons) given in Table 2.5.

Table 2.5 Modern ion exchange membrane materials. Data obtained from Smitha *et al.* 2005 [143].

	Perfluorinated Compounds	**Partially Fluorinated Compounds**	**Non-fluorinated hydrocarbons**	**Non-fluorinated aromatic hydrocarbons**
Polymer Structure	-Fluorocarbon backbone like Nafion -Fluorocarbon side-chains -Clustered structure consisting of closed channels of sulfonic acid groups	-Fluorocarbon backbone -Hydrocarbon or aromatic chain grafted onto backbone	-Hydrocarbon base typically modified with polar functional groups	-Aromatic base typically modified with polar functional groups and/or sulfonic acid
Typical Physical Properties	-Mechanically strong and chemically stable in oxidative and reductive conditions -Good thermal stability	-Mechanically strong but degrade quickly in harsh conditions	-Good mechanical strength -Poor chemical and thermal stability	-Good mechanical strength -Good chemical and thermal stability
Performance In PEM MFCs	-Long operational lifetimes -High proton conductivity and excellent cell resistance	-Moderate proton conductivity -Short operational lifetimes -Moderate cell resistance	-Poor proton conductivity -Low durability -Excessive swelling in aqueous environments	-Moderate proton conductivity (retains moderate conductivity at elevated temperatures) -Good water absorption in MEAs

Of the different types of materials designed to replace Nafion, the most relevant to later discussion in this thesis are modified non-fluorinated aromatic polymers. Rather than using a fluoropolymer backbone like Nafion (which requires costly and environmentally hazardous chemistry to achieve), aromatic polymers use a standard hydrocarbon backbone allowing for reduced production cost. Aromatic hydrocarbon polymers can also integrate selective proton conductivity through chemical addition of sulfonic acid functional groups [148]. A multitude of aromatic polymers including polystyrene, polysulfone, and polyetheretherketone (as well as their associated derivatives) have been examined for their utility as IEM materials each demonstrating favourable specific properties but none to date being overall more effective than Nafion [149,150,151]. Research is ongoing to evaluate more complex combinations of functional groups and polymer backbones to increase the effectiveness all types of polymer IEMs [152].

When applied to a microfluidic scale device, membranes have been integrated by either using pre-formed materials mechanically pressed between two surfaces, or *in situ* patterning [79, 81, 82,153,154,155]. The first method, allows for direct usage of commercial IEMs (usually Nafion) by simply squishing a membrane between two layers of polymer. Other groups have used selectively deposited preformed membranes by patterning a line of Nafion and using a mask aligner to finely position the film within a microchannel [69,81]. Bonding pre-formed commercial membrane materials either limits MFC device geometry to sandwich style stacked geometries or required complicated processing. The second type of membrane integration process involves *in situ* techniques. *In situ* processes are beneficial in that they allow for the rest of device fabrication to proceed by whatever method is optimal but offer significant challenges to create well sealed, mechanically stable structures. *In situ* fabricated membranes have been used in other types of microfluidic devices to form surfaces such as chitosan membranes and selectively permeable hydrogels but, to date, their usage in planar MFC devices has remained unexplored [156,157].

2.3.3 Electrode Materials

Electrode materials are of significant importance for proper fuel cell operation. In an MFC device an ideal electrode surface would carry out the desired half-cell reaction at 100% efficiency (*i.e.* consuming all of the supplied reactants) and at the theoretically maximum voltage rate (*i.e.* the voltage determined from the Equation 2.6 for given reaction conditions). The most effective way to achieve high reaction rates and voltage generation is through use of precious metal catalysts [158]. Through their combination of chemical inertness and extremely fast reaction kinetics, precious metals are able to effectively catalyze the reactions of common microfluidic fuels such as hydrogen, methanol, and formic acid as well as oxidants such as dissolved oxygen, and potassium permanganate [159]. To date, MFC devices have almost exclusively relied upon electrodes composed of platinum and palladium as was shown in Tables 2.1, 2.2, and 2.3. Methods to lead towards higher power and current densities have gone about two routes: increasing the accessible surface area, of improving catalyst performance. To increase surface area, precious metal electrodes are either directly deposited as roughened metallic films or embedded in a support material with higher surface area (such as porous carbon). As was described in Section 2.2.4, modified electrode geometries such as flow-through porous electrodes can greatly increase the accessible electrode surface area and have been found to lead to extensive improvements in both fuel utilization and output characteristics [104]. Other methods to increase surface area have included usage of nanostructured materials such as in Moreno-Zorea *et al.*, where Pt nanocubes were used to increase the apparent surface area of anodes from 0.09 cm^2 (for a flat electrode) to 10.6 cm^2 [98]. The second method to improve electrode performance has been to modify the chemical structure of catalyst surfaces. Metals such as Ru have been integrated into catalysts to improve reaction kinetics, or tailor a catalyst for a specific reaction [160].

While precious metal catalysts offer excellent catalytic properties they do suffer from several limitations. Firstly, (and most importantly to MFC device operation) they are non-selective [128]. In most MFC implementations, Pt/Pd electrodes will catalyze both anode and cathode half-cell reactions. Consequently, if there is mixing of anolyte and catholyte solutions (as was found to occur in membraneless device implementations), reactions can occur in the opposite half-cell leading to the generation of mixed potentials lowering output voltages and power output [161]. Secondly, precious metal catalysts are expensive. When aimed towards powering devices such as single use (*i.e.* mass produced) lab-on-a-chip diagnostic systems, precious metal electrodes can be prohibitively expensive and mitigate the low cost benefits of rapid-prototyping techniques. Given these concerns, research has been taken to explore other electrode materials which can be tailored selectively catalyze a specific anode or cathode half-cell reaction composed of lower cost materials. Less expensive transition metals such as Co, Fe, Ni, and Mn have been shown to catalyze the oxidation of methanol as well as ternary compounds such as Mo-Ru-Se [128,162,163,]. One specific example of a non-precious metal MFC device was shown in 2007 by Sung *et al.* who used pre-mixed anolyte and catholyte solutions with Ni and Ag based electrodes. Their device demonstrated that through proper selection of electrode materials MFC devices could also function without relying on laminar flow isolation. Their work did however show the concern with non-precious metal catalysts, as voltage and power generation efficiencies were considerably compromised compared to their precious metal counterparts. Work is on-going to develop more effective electrode materials for MFC devices. Development of selective low cost-catalysts is a key area of focus for both micro and marcoscale fuel cell devices.

Even when an effective catalytic electrode material is well known, some of the most challenging aspects of MFC fabrication are found integrating electrodes into a microfluidic architecture. Electrodes in planar devices are typically deposited through one of three methods, vapour deposition, electrodeposition, and 'macro-scale positioning'. Vapour deposition is a term to describe thermal processes such as sputtering or evaporation where a sample of a material is heated (through exposure to a plasma, heat source, or electron beam) causing emission of a plume of atoms which deposit on a substrate [164]. Electrodeposition is a process where an electrode is formed on top of a conductive surface through an electrochemical reaction from solution. Electrodeposition is able to create thin electrodes of many different materials but does require a conductive 'seed layer' onto which the electrodes will form. To achieve small scale (10s of 100s of microns) size scales for electrodes both vapour deposition and electrodeposition techniques rely upon photolithographic processing. As was described in Section 2.2, this leads to increases in fabrication complexity, and cost and is desirable to be avoided.

Another method to pattern electrodes without lithography was introduced in the late 1990s work by Kenis *et al.* They described etching processes using laminar flow as a means to isolate an active fluid stream (*i.e.* an etchant) from a passive fluid stream (*i.e.* an inert fluid such as water) to perform simple lithographic patterning within a sealed microchannel as is shown in Figure 2.17a. These techniques have been adapted by other authors for purposes such as patterning high aspect ratio microchannels as shown in Figure 2.17b. To date, laminar flow patterning processes have not been applied to MFCs.

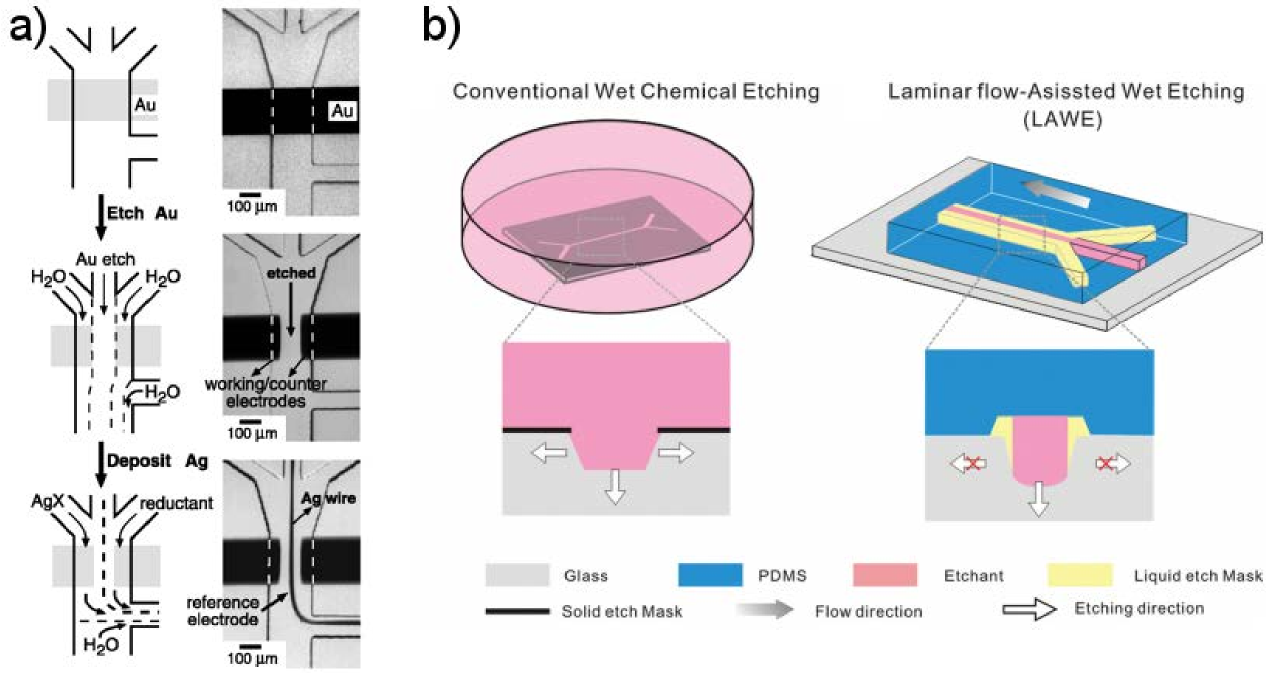

Figure 2.17 (a) Schematic diagrams and optical images of the first reported usage of laminar flow based patterning techniques by Kenis *et al.* [165]. Figure reproduced from Kenis *et al. Science* 285 (1999) 83-85. Reprinted with permission from AAAS. (b) Schematic diagrams of the differences between conventional wet etching processes and laminar flow based etching processed. Reproduced from Mu *et al.* 2009 with permission of The Royal Society of Chemistry [166].

2.4 Modelling in Microfluidic Devices

One of the most effective methods to understand aspects of microfluidic devices is through modelling and computer simulations. While significant work has been placed on developing MFC devices, efforts have also been taken to better understand individual aspects of microfluidic device operation including evolution of flow profiles, mass transport of dissolved compounds, and mixing of distinct phases [167,168,169]. Simulations involve many specific types of modelling (computational fluid dynamics, lattice-Boltzmann methods, and finite element modelling), which are differentiated by the means by which they solve the analytical equations governing processes within microfluidic devices. One of the most effective methods to simulate behavior in microfluidic devices, and that used later in this thesis, is using finite element modelling (FEM).

Finite element modelling (FEM) is numerical method which is able to solve complex mathematical systems through successively evaluated calculations. As FEM is leveraged heavily in later chapters of this thesis, a brief description of the core principles governing the method are presented here. In FEM analysis, approximate solutions to complex mathematical systems (often partial differential equations such as the Navier-Stokes equation) are obtained by breaking down a solution space (*i.e.* the area where the problem is being solved, such as a microfluidic channel geometry) into smaller regions with simple boundary conditions which can be solved with simple, well-behaved, test solutions (also termed interpolation functions). Through careful selection of test solutions, individual elements can be solved with simple boundary conditions. By dividing the solution space and coupling boundary conditions between adjacent regions (termed ‘elements’, hence the name FEM) solutions to computational difficult problems can be obtained for arbitrary geometries as shown schematically in Figure 2.18. In each element the ‘true’ (*i.e.* analytical) solution is approximated by an interpolation function which differs from the analytical solution by a factor termed the residual.

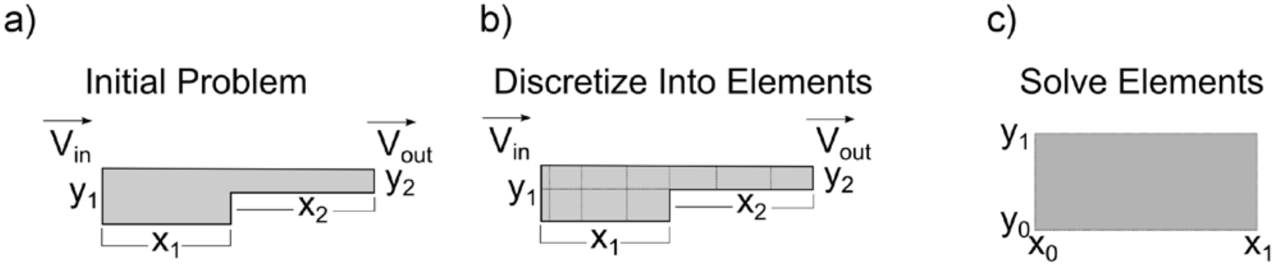

Figure 2.18 Schematic diagram of the stages of solving a fluid flow problem using FEM. (a) A solution geometry is shown with input and output velocity boundary conditions. (b) The domain is broken down into smaller elements with more regular dimensions. (c) Each individual element is simultaneously solved with simplified boundary conditions.

The elegance of the FEM method however is derived from the ability to converge towards the ‘true’ solution by successively reducing the residual of a problem through two routes: mesh refinement or interpolation function refinement, shown schematically in Figure 2.19. In mesh refinement, the discretized elements which composed the solution space are made smaller. In this way, the test solutions are able to better approximate the behavior in each element (in the same way that if a circle approximated with linear segments will converge to the true shape as segment length decreases). As a mesh is further refined, the FEM method ensures that successive solutions converge towards the analytical solution. In test-solution refinement, better approximations of the analytical solution are obtained by adding additional terms to each test solution (in the same way that a 1D sawtooth waveform can be better represented by a cubic function than a square function in Figure 2.19).

Though combination of both of these refinement methods, physically accurate solutions to complex microfluidic behavior can be obtained.

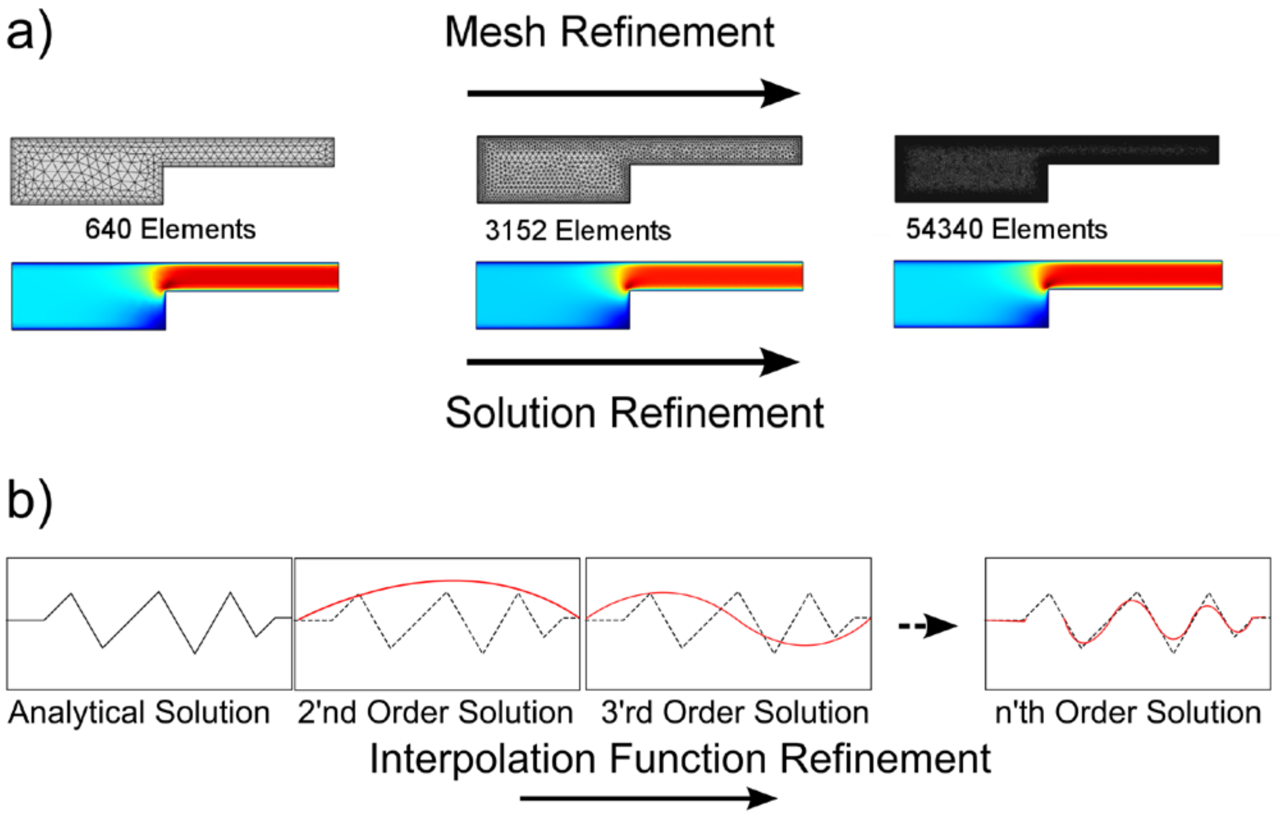

Figure 2.19 (a) Schematic diagrams showing three successive stages of mesh refinement. In each stage, as the mesh is refined the solution (shown as a colored velocity field representative of a fluid simulation solved via FEM) becomes more precise. (b) Schematic diagram showing how interpolation function refinement can yield better approximations of a complex analytical solution.

FEM can be used both as a predictive tool (to determine how to design an MFC device), or as an after the fact justification to rationalize device behavior. Simulations have become an essential part of MFC design and will guide future optimization, both in this thesis and in the field as a whole.

2.5 Conclusion

This section has described the origin and development of microfluidic fuel cell devices. Emphasis was placed upon identifying areas of concern where new materials and fabrication techniques are needed to spur on further innovation. This primer gives appropriate background and motivation for the work I have performed in this thesis which is described in the following three chapters. The next chapter describes my efforts to develop a new sulfonated aromatic PEM material (comparable to Nafion as described above) that is also compatible with *in situ* integration into planar MFC devices.

2.6 References

---

[1] "The origins and the future of microfluidics" Whitesides G M *Nature* 442 368-373. (2006)

[2] "A personal stroll through the historical development of Canadian microfludics" Harrison J, *Lab on A Chip* 13 2013 2500-2503.

[3] "Chemical modification of polymeric microchip devices" Muck A, Svatos A *Talanta* 74 (2007) 333-341.

[4] "Multiphase microfluidics: from flow characteristics to chemical and material synthesis" Gunther A, Jensen K F *Lab on A Chip* 6 (2006) 1487-1503.

[5] "Reactions in droplets in microfluidic channels" Song H, Chen D L, Ismagilov R F *Angewandte Chemie-International Edition* 45 (2006) 7336-7356.

[6] "Control and detection of chemical reactions in microfluidic systems" deMello A J *Nature* 442 (2006) 394-402.

[7] "Microfluidic diagnostic technologies for global public health" Yager P, Edwards T, Fu E, Hellen K, Nelson K, Tam M R, Weigl B H *Nature* (2006) 412-418.

[8] "Microscale technologies for tissue engineering and biology" Khademhosseini A, Langer R, Borenstein J, Vacanti J P *Proceedings of the National Academy of Sciences of the United States of America* 103 (2006) 2480-2487.

[9] "The burgeoning power of the shrinking laboratory" Ramsey J M *Nature Biotechnology* 17, 1061 - 1062 (1999)

[10] "Progress and trends in ink-jet printing technology" Le H P *Journal of Imaging Science and Technology* 1 (1998) 49-62.

---

[11] "Microfluidic platforms for lab-on-a-chip applications" Haeberle S, Zengerle R *Lab on A Chip* 7 (2007) 1094-1110.

[12] "Miniaturized Total Chemical Analysis Systems: a Novel Concept In Chemical Sensing" Manz A, *Sensors and Actuators B* (1990) 244-248.

[13] "Ultra-High Speed DNA Sequencing Using Capillary Electrophoresis Chips" Woolley A T, Mathies R A *Analytical Chemistry* 67 (1995) 3676-3680.

[14] "Technology and Applications Of Microengineered Reactors" Gavriilidis A, Angeli P, Cao E, Yeong K K, Wan Y S S *Chemical Engineering Research and Design* 80 (2002) 3-30.

[15] "A piezoelectric micropump based on micromachining of silicon" Van Lintel H T G *Sensors and Actuators* 15 (1988) 153-167.

[16] "Prototype miniature blood gas analyzer fabricated on a silicon wafer" Shoji S, Esashi M, Matsuo T *Sensors and Actuators* 14 (1988) 101-107.

[17] "Engineering Flows In Small Devices: Microfluidics Towards a Lab-On-a-Chip", Stone H A, Stroock A D, Ajdari A *Annu. Reviews Fluid Mechanics* 2004 36: 381-411.

[18] "Continuous Microfluidic Reactors For Polymer Particles" Seo M, Nie Z, Xu S, Mok M, Lewis P C, Graham R, Kumacheva E *Langmuir* 21 (2005) 11614-11622.

[19] "Integrated Microfluidic Devices" Erickson D, Li D *Analytica Chimica Acta* 507 (2004) 11-26.

[20] "Liquid Flow in microchannels: experimental observation and computational analyses of microfluidic effects" Koo J, Kleinstreuer C *Micromechanics and Microengineering* 13 (2003) 568-579.

[21] "Diffusion and Flow Development In Co-Flowing Microchannel Streams" Oak J, Pence D V, Liburdy J A *Microscale Thermophysical Engineering* 5:3 (2001) 233-246.

[22] "Microfluidics - a review" Gravesen P., Branebjerg, J., Jensen O. S. J. *Micromech. Microeng.* 3 (1993) 168-182.

[23] "Materials For Microfluidic Chip Fabrication" Ren K, Zhou J, Wu H *Accounts Of Chemical Research* 46 (2013) 2396-2406.

[24] "Controlled Microfluidic Interfaces" Atencia J, BeebeD J *Nature* 437 (2005) 648-655.

[25] "Microfluidics: Fluid Physics at the nanoliter scale" Squires T M, Quake S R *Reviews of Modern Physics* 77 (2005) 977-1026.

[26] "Transition From Laminar To Turbulent Flow In Liquid Filled Microtubes" Sharp K V, Adrian R J *Experiments In Fluids* 36 (2004) 741-747.

---

[27]"Micromixers—a review" Nguyen N T and Wu Z J. *Micromech. Microeng.* 15 (2005) R1–R16.

[28] "Microfluidic Sub-millisecond Mixers for the study of chemical reaction kinetics" Desai A, Bokenkamp D, Yang X, Tai Y C *Transducers '97* (1997) 167-170.

[29] "Acoustofluidics 1: Governing equations in microfluidics" Bruus H *Lab on A Chip* 11 (2011) 3742-3751.

[30]"Microfluidic Cell Culture Devices" Elias A. L., Nearingburg B, Zahorodny-Burke M in *Microfluidics and Nanofluidics Handbook.* CRC Press Editors: Mitra S K, Chakraborty S, 2011.

[31]"Microfabricated Devices For Fluid Mixing and Their Applications for Chemical Sensing" Kakuta M, Bessoth F G, Manz A *The Chemical Record* 1 (2001) 395-405.

[32] "Quantitative Analysis Of Molecular Interaction in a Microfluidic Channel: The T-Sensor" Kamholz A E, Weigl B H, Finlayson B A, Yager P *Analyical Chemistry* (1999) 71, 5340-5347.

[33] "Microfluidic Fuel Cell Based On Laminar Flow" Choban E R, Markoski L J, Wieckowski A, Kenis P J A *Journal Of Power Sources* 128 (2004) 54-60.

[34] "Microfluidic Sensing: state of the art fabrication and detection techniques" Wu J, Gu M *Journal of Biomedical Optics* 16 (2011) 080901.

[35] "Microfluidic large-scale integration" Thorsen T, Makerkl S J, Quake S R *Science* 298 (2002) 580--584.

[36]"Microfluidics: Applications for analytical purposes in chemistry and biochemistry" Ohno K, Tachikawa K, Manz A *Electrophoresis* 29 (2008) 4443-4453.

[37] "Micro-structured analytical instrumentation for the analysis of liquids" Grab B, Weber G, Neyer A, Schilling M, Hergenroder R, *Spectrochimica Acta Part B: Atomic Spectroscopy* 57 (2002) 1575-1583.

[38]"Micro reactors: principles and applications in organic synthesis" Fletcher P D I, Haswell S J, Pombo-Villar E, Warrington B H, Watts P, Wong S Y F, Zhang X, *Tetrahedron* 58 (2002) 4735-4757.

[39]"Microfluidic lab-on-a-chip platforms: requirements , characteristics, and applications" Mark D, Haeberle S, Roth G, von Stetten F, Zengerle R *Chemical Society Reviews* 39 (2010) 1153-1182.

[40] "Lab-On-A-Chip: A Component View" Lim Y C, Kouzani A Z, Duan W *Microsystem Technologies* 16 (2010) 1995-2015.

[41] "Microreactors as tools for synthetic chemists – The chemists' round-bottomed flask of the 21st century?" Geyer K, Codee J D C, Seeberger P H *Chemistry – A European Journal* 12 (2006) 8434-8442.

[42] "Microflow electroorganic synthesis without supporting electrolyte" Horcajada R, Okajima M, Suga

---

S, Yoshida J *Chemical Communications* 10 (2005) 1303-1305.

[43] "Microreactor Engineering - is small better?" Jensen K F *Chemical Engineering Science* 56 (2001) 293-303.

[44] "Microfabricated Multiphase Packed-Bed Reactors: Characterization of Mass Transfer and Reactions" Losey M W, Schmidt M A, Jensen K F (2001) *Industrial and Engineering Chemistry Research* 40 (2001) 2555-2562.

[45] "Fabrication of Multilayer Systems Combining Microfluidic and Microoptical Elements for Fluorescence Detection" Roulet J C, Vokel R, Herzig H P, Verpoorte E, de Rooij N F, Dandliker R, *Journal of Microelectromechanical Systems* 10 (2001) 482-491.

[46] "Electrochemical Detection in Polymer Microchannels" Rossier J S, Roberts M A, Ferrigno R, Girault H H *Analytical Chemistry* 71 (1999) 4294-4299.

[47] "The application of micro reactors for organic synthesis" Watts P, Haswell S J *Chemical Society Reviews* 34 (2005) 235-246.

[48] "Electrochemical Microfluidics" Zimmerman W B *Chemical Engineering Science* 66 (2011) 1412-1425.

[49] "Microfluidic Fuel Cells: A Review" Kjeang E, Djihali N, Sinton D *Journal Of Power Sources* 186 (2009) 353-369.

[50] "Fuel Cells: Reaching the Era of Clean and Efficient Power Generation in the Twenty-First Century" Srinivasan S, Mosdale R, Stevens P, Yang C *Annual Reviews Energy Environmental* 24 (1999) 281-328.

[51] "Review of proton exchange membrane fuel cell models" Bıyıkoglu A *International Journal of Hydrogen Energy* 30 (2005) 1181-1212.

[52] "Proton exchange membrane fuel cell from low temperature to high temperature: Material challenges" Shao Y, Yin G, Wang Z, Gao Y *Journal of Power Sources* 167 (2007) 235-242.

[53] "Proton exchange membrane fuel cells" Vishnyakov V M *Vacuum* 80 (2006) 1053-1065.

[54] "Onboard Fuel Conversion For Hydrogen-Fuel-Cell-Driven Vehicles" Trimm D L, Onsan Z H *Catalysis Reviews* 43 (2001) 31-84.

[55] "The current status of fuel cell technology for mobile and stationary applications" de Bruijn F *Green Chemistry* 7 (2005) 132-150.

[56] "Miniature fuel cells for portable power: Design considerations and challenges" Maynard H L, Meyers J P *Journal of Vacuum Science and Technology B* 20 (2002) 1287-1297.

---

[57] “Micro-fuel-cells- Current development and applications” Kundu A, Jang J H, Jung C R, Lee H R, Kim S H, Ku B, Oh Y S *Journal of Power Sources* 170 (2007) 67-78.

[58] “Review and Analysis of PEM Fuel Cell design and manufacturing” Mehta V, Cooper J S *Journal Of Power Sources* 114 (2003) 32-53.

[59] “PM 400 Fuel Cell Stack” Image obtained from A. Schoentag (Proton Motor Systems) Image Copyright © Proton Motor Fuel Cell GmbH, Benzstr. 7, D-82178 Pucheim, Germany, used with permission.

[60] “Architecture for portable direct liquid fuel cells” Qian W, Wilkinson D P, Shen J, Wang H, Zhang J *Journal of Power Sources* 154 (2006) 202-213.

[61] “Direct Methanol Fuel Cells” McGrath *Journal of Industrial Engineering Chemistry* 10 (2004) 1063-1080.

[62] “Small direct methanol fuel cells with passive supply of reactants” Zhao T S, Chen R, Yang W W, Xu C *Journal of Power Sources* 191 (2009) 185-202.

[63] “A review on fuel cell technologies and power electronic interface” Kirubakaran A, Jain S, Nema R K *Renewable and Sustainable Energy Reviews* 13 (2009) 2430-2440.

[64] “Mass transport phenomena in direct methanol fuel cells” Zhao T S, Xu C, Chen R, Yang W W *Progress in Energy and Combustion Science* 35 (2009) 275-292.

[65] “PEM Fuel Cell Electrodes” Litster S, McLean G *Journal of Power Sources* 130 (2004) 61-76.

[66] “MEMS-based power generation techniques for implanting biosensing applications” Lueke J, Moussa W A *Sensors* 11 (2011) 1433-1460.

[67] “Membraneless Vanadium Redox Fuel Cell Using Laminar Flow” Ferrigno S, Stroock A D, Clark T D, Mayer M, Whitesides G M *Journal of the American Chemical Society* 124 (2002) 12930-12931.

[68] “Overview on the challenges and developments of micro-direct methanol fuel cells (DMFC)” Kamarudin S K, Daud W R W, Ho S L, Hasran U A *Journal Of Power Sources* 163 (2007) 743-754.

[69] “Microfabricated microfluidic fuel cells” Kamitani A, Morishita S, Kotaki H, Arscott S *Sensors and Actuators B: Chemical* 154 (2011) 174-180.

[70] “Polymer Electrolyte Membranes for Fuel Cells” Lee J S, Quan N D, Hwang J M, Lee S D, Kim H, Lee H, Kim H S *Journal of Industrial Engineering Chemistry* 12 (2006) 175-183.

[71] “A MEMS-based reformed methanol fuel cell for portable power” Morse J D, Graff R T, Spadaccini C, Park H G,Hart E K *Journal Micromechanics and Microengineering* 17 (2007) S237-S242.

---

[72] “Micro-electro-mechanical systems (MEMS)-based micro-scale direct methanol fuel cell development” Yao S, Tang X, Hsieh C, Alyousef Y, Vladimer M, Fedder G K, Amon C H *Energy* 31 (2006) 636-649.

[73] “Micro-fuel cell power sources” Morse J D *International Journal of Energy Research* 31 (2007) 576-602.

[74] “MEMS-based design and fabrication of a new concept micro direct methanol fuel cell (u-DMFC)” Motokawa S, Mohamedi M, Momma T, Shoji S, Osaka T *Electrochemistry Communications* 6 (2004) 562-565.

[75] “A micro methanol fuel cell operating at near room temperature” Yen T J, Fang N, Zhang X, Lu G Q, Wang C Y *Applied Physics Letters* 83 (2003) 4056-4058.

[76] “A review on membraneless laminar flow-based fuel cells” Shaegh S A M, Nguyen N, Chan S H *International Journal of Hydrogen Energy* 36 (2011) 5675-5694.

[77] “Characterization of a membraneless direct-methanol fuel cell” Sprague I B, Dutta P, Ha S *Proceedings of the Institution of Mechanical Engineers, Part A: Journal Of Power and Energy* 233 (2009) 799-808.

[78] “A passive microfluidic hydrogen-air fuel cell with exceptional stability and high performance” Mitrovski S M, Nuzzo R G *Lab on A Chip* 6 (2006) 353-361.

[79] “A hybrid sequential deposition fabrication technique for micro fuel cells” Stanley K G, Czyzewska E K, Vanderhook T P K, Fan L L Y, Abel K A, Wu Q J M, Parameswaran M *Journal of Micromechanics and Microengineering* 15 (2005) 1979-1987.

[80] “Design, fabrication, and characterization of a planar silicon-based, monolithically integrated micro laminar flow fuel cell with a bridge shaped microchannel cross-section” Lopez-Montesinos P O, Yossakda N, Brushet F R, Pelton W E, Kenis P J A *Journal of Power Sources* 196 (2011) 4638-4645.

[81] “Rapid fabrication of microfluidic polymer electrolyte membrane fuel cell in PDMS by surface patterning of perflourinated ion-exchange resin” Song Y A, Batista C, Sarpeshkar R, Han J *Journal of Power Sources* 183 (2008) 647-677.

[82] “Monolithic micro-direct methanol fuel cell in polydimethylsiloxane with microfluidic channel-integrated Nafion strip” Shen M, Walter S, Gijs M A M *Journal of Power Sources* 193 (2009) 761-765.

[83] “Membraneless laminar flow-based micro fuel cells operating in alkaline, acidic, and acidic/alkaline media” Choban E R, Spendelow J S, Gancs L, Wieckowski A, Kenis P J A *Electrochimica Acta* 50 (2005)

5390-5398.

[84] "Characterization of Limiting Factors In Laminar Flow-Based Membraneless Microfuel Cells" Choban E R, Waszczuk P, Kenis P J A *Electrochemical and Solid State Letters* 8 (2005) A348-A352.

[85] "Microfluidic devices for energy conversion: planar integration and performance of a passive, fully immersed H2O2 fuel cell" Mitrovski S M, Elliott L C C, Nuzzo R G *Langmuir* 20 (2004) 6974-6976.

[86] "Active control of the depletion boundary layers in microfluidic electrochemical reactors" Yoon S K, Fichtl G W, Kenis P J A *Lab On A Chip* 6 (2006) 1516-1524.

[87] "Improved fuel utilization in microfluidic fuel cells: A computational study" Bazylak A, Sinton D, Djilali N *Journal of Power Sources* 143 (2005) 57-66.

[88] "Planar and three-dimensional microfluidic fuel cell architectures based on graphite rod electrodes" Kjeang E, McKechnie J, Sinton D, Djihali N *Journal Of Power Sources* 168 (2007) 379-390.

[89] "Electricity Generation From Decomposition of Hydrogen Peroxide" Hasegawa S, Shimotani K, Kishi K, Watanabe H *Electrochemical and Solid State Letters* 8 (2005) A119-A121.

[90] "Fabrication and preliminary testing of a planar membraneless microchannel fuel cell" Cohen J L, Westly D A, Pechenik A, Abruna H D *Journal of Power Sources* 139 (2005) 96-105.

[91] "A dual electrolyte H2/O2 planar membraneless microchannel fuel cell system with open circuit potentials in excess of 1.4V" Cohen J L, Volpe D J, Westly D A, Pechenik A, Abruna H D *Langmuir* 12 (2005) 3544-3550.

[92] "Formic acid microfluidic fuel cell evaluation in different oxidant conditions" Dector A, Esquivel J P, Gonzalez M J, Guerra-Balacazar M, Ledesma-Garcia J, Sabate N, Arriga L G *Electrochimica Acta* 92 (2013) 31-35.

[93] "Microfluidic Direct Methanol Fuel Cell with Ladder-Shaped Microchannel for Decreased Methanol Crossover" Huo W, Zhou Y, Zhang H, Zou Z, Yang H *International Journal of Electrochemical Science* 8 (2013) 4827-4838.

[94] "Hydrogen peroxide as an oxidant for microfluidic fuel cells" Kjeang E, Brolo A G, Harrington D A, Djilali N, Sinton D *Journal of The Electrochemical Society* 154 (2007) B1220-B1226.

[95] "A laser micromachined polymeric membraneless fuel cell" Li A, Chan S H, Nguyen N T *Journal of Micromechanics and Microengineering* 17 (2007) 1107.

[96] "Microchip-based ethanol/oxygen biofuel cell" Moore C M, Minteer S D, Martin R S *Lab on A Chip* 5 (2005) 218-225.

---

[97] “Performance increase of microfluidic formic acid fuel cell using Pd/MWCTs as catalyst” Morales-Acosta D, Rodriguez H, Godinez L A, Arriga L G *Journal of Power Sources* 195 (2010) 1862-1865.

[98] “Formic acid microfluidic fuel cell based on well-defined Pd nanocubes” Moreno-Zuria A, Dector A, Esquivel J P, Gonzalez M J, Guerra-Balacazar M, Ledesma-Garcia J, Sabate N, Arriga L G, Chavez-Ramirez A U *Journal of Physics: Conference Series* 476 (2013) 012033.

[99] “Characterization of microfluidic fuel cell based on multiple laminar flow” Sun M H, Casquillas G V, Guo S S, Shi J, Ji H, Ouyang Q, Chen Y *Microelectronic Engineering* 84 (2007) 1182-1885.

[100] “A membraneless microscale fuel cell using non-noble catalysts in alkaline solution” Sung W, Choi J W *Journal of Power Sources* 172 (2007) 198-208.

[101] “A microfluidic fuel cell with flow-through porous electrodes” Kjeang E, Michel R, Harrington D A, Djilali N, Sinton D *Journal of the American Chemical Society* 130 (2008) 4000-4006.

[102] “Sequential flow membraneless microfluidic fuel cell with porous electrodes” Salloum K S, Hayes J R, Frissen C A, Posner J D *Journal of Power Sources* 180 (2008) 243-252.

[103] “Up-scaled microfluidic fuel cells with porous flow-through electrodes” Fuerth D, Bazylak A *Journal of Fluids Engineering* 135 (2013) 021102.

[104] “Planar multiplexing of microfluidic fuel cells” Ho B, Kjeang E *Journal of Fluids Engineering* 135 (2013) 021304.

[105] “An alkaline microfluidic fuel cell based on formate and hypochlorite bleach” Kjeang E, Michel R, Harrington D A, Sinton D, Djilali N *Electrochemica Acta* 54 (2008) 698-705.

[106] “High-performance microfluidic vanadium redox fuel cell” Kjeang E, Proctor B T, Brolo A G, Harrington D A, Djilali N, Sinton D *Electrochimica Acta* 52 (2007) 4942-4946.

[107] “Air Breathing laminar flow-based microfluidic fuel cell” Jayashree R S, Gancs L, Choban E R, Primak A, Natarajan D, Markoski L J, Kenis P J *Journal of The American Chemical Society* 127 (2005) 16758-16759.

[108] “Air-Breathing Laminar Flow-Based Direct Methanol Fuel Cell with Alkaline Electrolyte” Jayashree R S, Egas D, Spendelow J S, Natarajan D, Markoski L J, Kenis P J A *Electrochemical and Solid State Letters* 9 (2006) A252-A256.

[109] c

[110] “Investigation of fuel and media flexible laminar flow-based fuel cells” Brushette F R, Jayashree R S, Zhou W P, Kenis P J A *Electrochimica Acta* 54 (2009) 7099-7105.

---

[111] "Nanoporous separator and low fuel concentration to minimize crossover in direct methanol laminar flow fuel cells" Hollinger A S, Maloney R J, Jayashree R S, Natarajan D, Markoski L J, Kenis P J A *Journal of Power Sources* 195 (2010) 3523-3528.

[112] "An air-breathing microfluidic formic acid fuel cell with a porous planar anode: experimental and numerical investigations" Shaegh S A M, Nguyen N T, Chan S W *Journal of Micromechanics and Microengineering* 20 (2010) 105008.

[113] "Ruthenium cluster-like chalcogenide as a methanol tolerant cathode catalyst in air-breathing laminar flow fuel cells" Whipple D T, Jayashree R S, Egas D, Alonso-Vante N, Kenis P J A *Electrochimica Acta* 54 (2009) 4384-4388.

[114] "Air-breathing direct formic acid microfluidic fuel cell with an array of cylinder anodes" Zhu X, Zhang B, Ye D D, Li J, Liao Q *Journal of Power Sources* 247 (2014) 346-353.

[115] "Rapid Prototyping of Micro-Direct-Methanol Fuel Cell in PDMS With Microchannel Integrated Nafion Strip" Shen M, Walter S, Gijs M A M *Solid-State Sensors, Actuators, and Microsystems Conference 2009* (2009) 533-536.

[116] "Polymeric microfluidic system for DNA analysis" Sun Y, Kwok Y C *Analytica Chimica Acta* 556 (2006) 80-96.

[117] "Recent Developments In Polymer MEMS" Liu C, *Advanced Materials* 19 (2007) 3783-3790.

[118] "Polymer microfluidic devices" Becker H, Locascio L E *Talanta* 56 (2002) 267-287.

[119] "Fabrication of thermoset polyester microfluidic devices and embossing masters using rapid prototyped polydimethylsiloxane molds" Fiorini G S, Jeffries G D M, Lim D S W, Kuyper C L, Chiu D T *Lab on a Chip* 3 (2003) 158-163.

[120] "Polymer microfabrication technologies for microfluidic systems" Becker H, Gartner C *Anal Bioanal Chem* 390 (2008) 89-111.

[121] "Soft Lithography for Microfluidics: a Review" Kim P, Kwon K W, Park M C, Lee S H, Kim S M, Suh K Y *Biochip Journal* 2 (2008) 1-11.

[122] "Fabrication of microfluidic systems in poly(dimethylsiloxane)" McDonald J C, Duffy D C, Anderson J R, Chiu D T, Wu H, Schueller O J, Whitesides G M *Electrophoresis* 1 (2000) 27-40.

[123] "Soft Lithography" Xia Y, Whitesides G M *Annual Reviews Material Science* 28 (1998) 153-184.

[124] "Rapid, cost-efficient fabrication of microfluidic reactors in thermoplastic polymers by combining photolithography and hot embossing" Greener J, Li W, Ren J, Voicu D, Pakharenko V, Tang T,

---

Kumacheva E *Lab On A Chip* 10 (2010) 522-524.

[125] "Microfabrication meets microbiology" Weibel D B, DiLuzio W R, Whitesides G M *Nature Reviews Microbiology* 5 (2007) 209-218.

[126] "Recent developments in PDMS surface modification for microfluidic devices" Zhou J, Ellis A V, Volecker N H *Electrophoresis* 31 (2010) 2-16.

[127] "Engineers are from PDMS-land, Biologists are from Polystyrenia" Berthier E, Young E W, Beebe D *Lab on a Chip* 12 (2012) 1224-1237.

[128] "Progress in preparation of non-noble electrocatalysts for PEM fuel cell reactions" Zhang L, Zhang J, Wilkinson D P, Wang H *Journal of Power Sources* 156 (2006) 171-182.

[129] "A uL-scale micromachined microbial fuel cell having high power density" Choi S C, Lee H, Yang Y, Parameswaran P, Torres C I, Rittmann B E, Chae J *Lab On A Chip* 11 (2011) 1110-1117.

[130] "Continuous flow membrane-less air cathode microbial fuel cell with spunbound olefin diffusion layer" Tugtas A E, Cavdar P, Calli B *Bioresource Technology* 102 (2011) 10425-10430.

[131] "PDMS absorption of small molecules and consequences in microfluidic applications" Toepke M W, Beebe D J *Lab on a Chip* 6 (2006) 1484-1486.

[132] "Poly(dimethylsiloxane) as a material for fabricating microfluidic devices" McDonald J C, Whitesides G M *Accounts of Chemical Research* 35 (2002) 491-499.

[133] "Microfluidic Electronics" Cheng S, Wu Z *Lab on A Chip* 12 (2012) 2782-2791.

[134] "Stretchable gold conductors on elastomeric substrates" Lacour S P, Wagner S, Huang Z, Suo Z *Applied Physics Letters* 82 (2003) 2404-2406.

[135] "A 1.5 uL microbial fuel cell for on-chip bioelectricity generation" Qian F, Baum M, Gu Q, Morse D E *Lab on a Chip* 9 (2009) 3076-3081.

[136] "Cyclic Olefin Polymers: emerging materials for lab-on-a-chip applications" Nunes P S, Ohlsson P D, Ordeig O, Kutter J P *Microfluid Nanofluid* 9 (2010) 145-161.

[137] "Cyclic olefin polymers: innovative materials for high-density multiwall plates" Niles W D, Coassin P J *ASSAY and Drug Development Technologies* 6 (2008) 577-590.

[138] "Measuring the Young's Relaxation Modulus of PDMS using stress relaxation nanointendation" Du P, Lu H, Zhang X *Mater. Res. Soc. Symp. Proc.* 1222 (2010) 1222-DD02-03.

[139] "Nanoimprint lithography in the cyclic olefin copolymer, Topas, a highly ultraviolet-transparent and chemically resistance thermoplast" Nielsen T, Nilsson D, Bundgaard F, Shi P, Szabo P, Geschke O,

---

Kristensen A *Journal of Vacuum Science and Technology B* 22 (2004) 1770-1775.

[140] "Bonding Of Thermoplastic Polymer Microfluidics" Tsao C, DeVoe D L *Microfluidics and Nanofluidics* 6 (2009) 1-16.

[141] "Review on micro moulding of thermoplastic polymers" Heckele M, Schomburg W K *Journal of Micromechanics and Microchaning* 14 (2004) R1-R14.

[142] "Bendable fuel cells: on-chip fuel cell on a flexible polymer substrate" Tominaka S, Nishizeko H, Mizuno J, Osaka T *Energy and Environmental Science* 2 (2009) 1074-1077.

[143] "Solid polymer electrolyte membranes for fuel cell applications - a review" Smitha B, Sridhar S, Kahn A A *Journal of Membrane Science* 259 (2005) 10-26.

[144] "A review of polymer electrolyte membrane fuel cells: Technology, applications, and needs on fundamental research" Wang Y, Chen K S, Mishler J, Cho S C, Adroher X C *Applied Energy* 88 (2011) 981-1007.

[145] "Molecular structure and transport dynamics in Nafion and sulfonated poly(ether ether ketone ketone) membranes" Chen P Y, Chiu C P, Hong C W *Journal of Power Sources* 194 (2009) 746-752.

[146] "Thermodynamics and Proton Transport in Nafion II: Proton Diffusion Mechanisms and Conductivity" Choi P, Jalani N H, Datta R *Journal of The Electrochemical Society* 152 (2005) E123-E130.

[147] "Gas permeation properties of SPE membranes" Sakari T, Takenaka H, Wakabayashi N, Kawami K, Tori K *Journal of. The Electrochemical Society* 132 (1985) 1328.

[148] Sulfonated aromatic hydrocarbon polymers as proton exchange membranes for fuel cells" Higashihara T, Matsumoto K, Ueda M *Polymer* 50 (2009) 5341-5357.

[149] "Proton conductivities and methanol permeabilities of membranes made from partially sulfonated polystyrene-block-poly(ethyelene-ran-butylene)-block-polystyrene copolyers" Kim J, Kim B, Jung B *Journal of Membrane Science* 207 (2002) 129-137.

[150] "Ionomeric membranes for proton exchange membrane fuel cell (PEMFC): sulfonated polysulfone associated with phosphatoantimonic acid" Genova-Dimitrova P, Baradie B, Foscallo D, Poinsignon C, Sanchez J Y *Journal of Membrane Science* 185 (2001) 59-71.

[151] "Synthesis and characterization of sulfonated poly(ether ether ketone) for proton exchange membranes" Xing P, Robertson G P, Guiver M D, Mikhailenko S D, Wang K, Kaliaguine S *Journal of Membrane Science* 229 (2004) 95-106.

[152] "Polymer membranes for high temperature proton exchange membrane fuel cell: Recent advances

---

and challenges" Bose S, Kuila T, Nguyen T X H, Kim N H, Lau K, Lee J H *Progress In Polymer Science* 36 (2011) 813-843.

[153] "Membranes and microfluidics: a review" deJong J, Lammertink R G H, Wessling M *Lab on A Chip* 6 (2006) 1125-1139.

[154] "Chemicofunctional Membrane for Integrated Chemical Processes on a Microchip" Hisamoto H, Shimuzu Y, Uchiyama K, Tokeshi M, Kikutani Y, Hibara A, Kitamori T *Analytical Chemistry* 75 (2003) 350-354.

[155] "*In Situ* fabricated porous filters for microsystems" Moorthy J, Beebe D J *Lab on A Chip* 3 (2003) 62-66.

[156] "In situ generation of pH gradients in microfluidic devices for biofabrication of freestanding, semi-permeable chitosan membranes" Luo X, Berlin D L, Betz J, Payne G F, Bentley W E, Rubloff G W *Lab on A Chip* 10 (2010) 59-65.

[157] "Quantitatively controlled in situ formation of hydrogel membranes in microchannels for generation of stable chemical gradients" Choi E, Jun I, Chang H, Park K M, Shin H, Park K D, Park J *Lab on a Chip* (2012) 302-308.

[158] "Platinum monolayer fuel cell electrocatalysts" Adzic R R, Zhang J, Sasaki K, Vukmirovic M B, Shao M, Wang J X, Nilekar A U, Mavrikakis M, Valerio J A, Uribe F *Topics In Catalysis* 46 (2007) 249-262.

[159] "Palladium in fuel cell catalysts" Anatoli E *Energy and Environmental Science* 2 (2009) 915-931.

[160] "Pt submonolayers on Ru nanoparticles, A novel low Pt loading, high CO tolerance fuel cell electrocatalyst" Brankovic S R, Wang J X, Adzic R R *Electrochemical and Solid-State Letters* 4 (2001) A217-A220.

[161] "Methanol-tolerant electrocatalysts for oxygen reduction in a polymer electrolyte membrane fuel cell" Gupta S, Tryk D, Zecevic S K, Aldred W, Guo D, Savinell R F *Journal of Applied Electrochemistry* 28 (1998) 673-682.

[162] "A review on non-precious metal electrocatalysts for PEM fuel cells" Chen Z, Higgins D, Yu A, Zhang L, Zhang J *Energy and Environmental Science* 4 (2011) 3167-3192.

[163] "A class of non-precious metal composite catalysts for fuel cells" Bashyam R, Zelenay P *Nature* 443 (2006) 63-66.

[164] "Ionized physical vapour deposition (IPVD): A review of technology and applications" Helmersson U, Lattermann M, Bohlmark J, Ehiasarian A P, Gudmundsson J T *Thin Solid Films* 513 (1-24).

---

[165] “Microfabrication inside capillaries using multiphase laminar flow patterning” Kenis P J, Ismagilov R F, Whitesides G M *Science* 285 (1999) 83-85.

[166] “Laminar flow used as “liquid etch mask” in wet chemical etching to generate glass microstructures with an improved aspect ratio” Mu X, Liang Q, Hu P, Ren K, Wang Y, Luo G *Lab On A Chip* 9 (2009) 1994-1996.

[167] “A unified scaling model for flow through a lattice of microfabricated posts” Srivastava N, Din C, Judson A, MacDonald N C, Meinhart C D *Lab on a Chip* 10 (2010) 1148-1152.

[168] “Mixing processes in a zigzag microchannel: finite element simulations and optical study” Mengeaud V, Josserand J, Girault H H *Anal. Chem.* 74 (2002) 4279-4286.

[169] “Topology optimization of microfluidic mixers” Andreasen C S, Gersborg A R, Sigmund O *International Journal For Numerical Methods in Fluids* 61 (2009) 498-513.

Chapter 3[*]

Materials in Microfluidic Fuel Cells: Proton Exchange Membranes

> "Chemistry lab-work was my first challenge, I still carry the scars of my first discovery, that test tubes are fragile"
>
> ***Edward Teller***

3.0 Introduction

Chapter 2 gave an introduction to the realm of microfluidic fuel cells. It described the microfluidic environment as well as both the materials and methods used in micro-scale fuel cells implementations. It was shown that throughout the development of modern microfluidic fuel cell devices there has been a tradeoff between high efficiency (in terms of fuel utilization and electrical output characteristics) and fabrication challenges (in terms of both cost and complexity). In the literature, planar membraneless microfluidic fuel cell devices have been implemented using inexpensive rapid prototyping fabrication techniques such as elastomer micro-molding. However, membraneless devices have suffered from less favourable output characteristics when compared to stacked membrane-containing devices. Fabrication of membrane containing devices has been shown to involve many stages of complicated (and costly) multi-layer clean-room processing. Methods to combine the benefits of both membrane containing and membraneless device architectures are highly desirable, and are the subject of this chapter. Here, a process is described which allowed for *in situ* patterning of a low cost poly-ethylene-glycol derivative polymer proton exchange membrane into a planar membraneless fuel cell architecture. After determining an appropriate synthesis procedure, the developed membrane materials were characterized for relevant chemical and mechanical properties including chemical structure, water contact angle, ion exchange capacity, proton conductivity, and elastic modulus. Membrane integration methods and future directions for enhancement of our membrane material are also discussed.

---

[*] Chapter 3 was reproduced in part from "Photopolymerizable sulfonated poly(ethylene glycol) proton exchange membranes for microfluidic and fuel cell applications" Nearingburg B, Elias A L *Journal of Membrane Science* 389 (2012) 148-154.

3.1 Overview and Motivations

As was described in Section 2.2, MFC devices can be broken down into membraneless (*i.e.* those utilizing a laminar flow gradient to separate anode and cathode half cells) and membrane containing implementations. Membraneless devices involve simplified fabrication and can be easily adapted into a planar architecture. Membrane-containing devices are typically composed of stacks of micropatterned channels as well as integrated gas diffusion and proton exchange layers. A method to combine the ease of fabrication of membraneless planar devices, while retaining the segregation offered by membrane containing devices is highly desirable. Photopolymerization offers a route to achieve such an implementation and is the subject of this chapter. This work aimed to improve the utility of planar MFC devices through development of a material which can both function as a proton exchange membrane and also be easily inserted into a planar architecture. Typically, integration of proton exchange membranes (or more generally ion exchange membranes including materials that are selective to anions) in microfluidic devices has accomplished by using preformed solid polymer membranes (often perfluorinated compounds such as Nafion) which are mechanically bound between two planar half-cell layers in what is termed a 'sandwich architecture' (see Figure 2.9) [1]. Commercial perfluorinated membranes such as Nafion have been shown to be costly and difficult to integrate into planar architectures without complicated patterning and alignment techniques [2]. Previous work in literature has investigated hydrocarbon based PEM materials in macro-scale fuel cells [3,4,5]. The applicability and utility of hydrocarbon based membranes for *in situ* patterning in microfluidic devices has not been explored [6]. This chapter, describes a method which developed a chemically functionalized hydrocarbon polymer blend which was combined with *in situ* free radical photopolymerization to achieve patterning of proton exchange membrane materials within sealed microchannels.

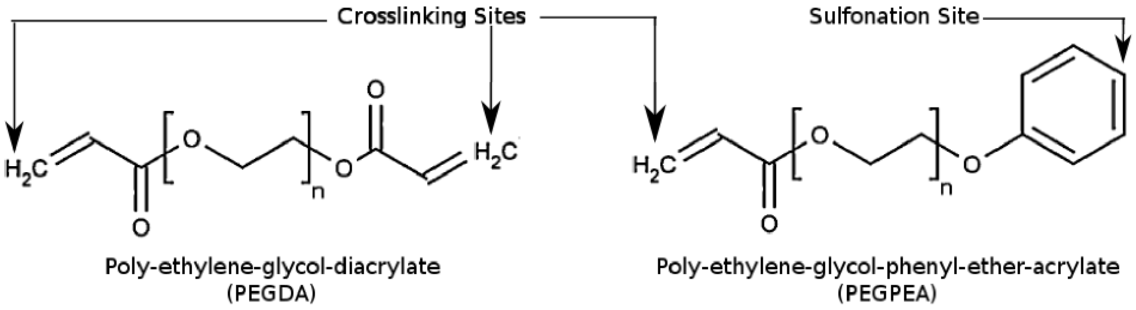

Figure 3.1 Schematic diagrams showing the two polymers used in the blend to form the PEM material. Active sites are indicated with arrows showing the groups involved in chemical crosslinking and sulfonation. For both polymers, repeat units are shown in brackets.

The PEM material in this investigation was based on widely available poly-ethylene-glycol (PEG) derivatives, specifically, derivatives of poly-ethylene-glycol-acrylates (PEGA) and diacrylates (PEGDA). PEGA and PEGDA compounds are organic polymers which possess reactive terminal functional groups. In this investigation, these functional groups allow for chemical linkages (*i.e.* crosslinking forming solid polymer networks) as well as selective chemical reactivity (*i.e.* improve proton conductivity) [7]. The thermal and mechanical properties of both PEGA and PEGDA derivatives can also be tailored based on adjusting the number of repeat units in the polymer chains (shown as n in Figure 3.1) [7]. Two PEG compounds were chosen, PEG-diacrylate (PEGDA-700 Sigma Aldrich #455008) and PEG-phenyl-ether-acrylate (PEGPEA-236 Sigma Aldrich #407321). With two terminal acrylate groups per polymer chain, PEGDA is used as a crosslinking agent. Higher levels of crosslinking (*i.e.* more chemical bonds between polymer chains) increase the mechanical stability of the polymer structure and can resist swelling when placed in aqueous environments. Through a sulfonation reaction (described below), the aromatic group in PEGPEA is used to increase proton conductance. The chemical structure of both compounds, along with their reactive terminal groups are shown in Figure 3.1. Both compounds were mutually soluble liquid monomers at room temperature conditions. Liquid monomers allowed for our *in situ* fabrication technique as they could be flowed into sealed microchannels and then reacted to form solid membranes. This process is shown schematically in Figure 3.2. However, before a functional PEM could be formed from a PEGDA-

PEGPEA polymer blend proton conductivity had to be enhanced as is described in the next section.

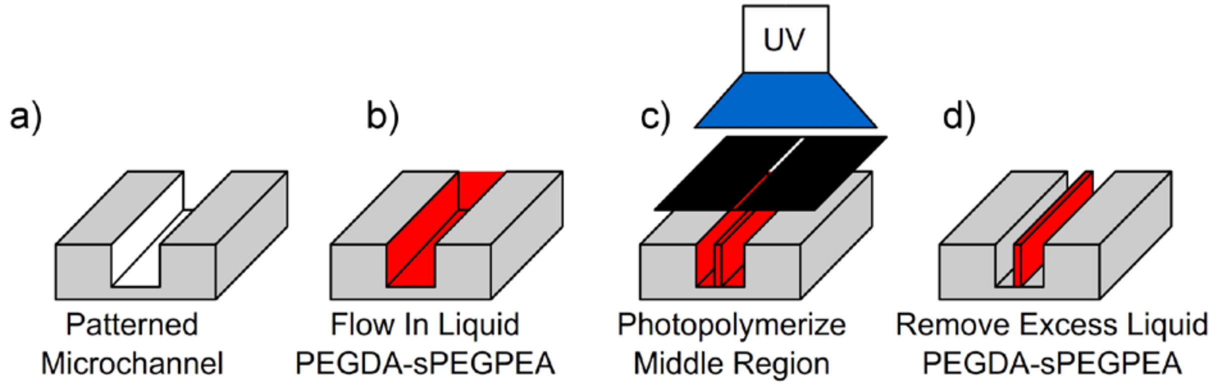

Figure 3.2 Schematic diagram showing formation of a PEGDA-sPEGPEA PEM within a microchannel. Processing starts with (a) a patterned empty microchannel which is (b) filled with liquid PEGDA-sPEGPEA monomer. (c) The microchannel is then selectively exposed to UV light through a photomask to photopolymerize a membrane in the middle of the microchannel. (d) After photopolymerization excess liquid monomer is removed from the microchannel leaving a solid PEGDA-sPEGPEA membrane. In all schematics, the top surface of the microchannel has been omitted for clarity.

3.2 Nucleophilic Substitution Reactions

In order to be of utility as PEM membranes, the PEGDA-PEGPEA polymer blend network must possess a chemical structure that is favourable to the transport of protons. In commercial materials such as Nafion (as well as other functionalized polymers described in literature in Section 2.3.2), proton conductivity is achieved by the addition of sulfonic acid (SO_3^-) functional groups. Sulfonic acid groups are chemical structures that can cycle between two states, SO_3^- and hydrogenated form SO_3H. In an aqueous environment, protons can be effectively transported by hopping from one SO_3^- site to an adjacent SO_3^- site. In this way, protons generated in the anode half cells can eventually pass through the bulk of the membrane into the cathode half-cell [8]. Further details on this process, termed the Grothus mechanism, can be found in Section 2.3.2. Sulfonated polymers are currently the most effective means documented for selectively transferring protons in aqueous fuel cell devices [9]. Previous work in literature has involved formation of PEM materials for macroscale fuel cells using sulfonated polymers such as polystyrene, polysulfone, and poly(ether-ether)-ketone to great success [3,5,10]. These materials offer favourable chemical and mechanical properties but are difficult to pattern *in situ* by photolithographic techniques.

In this work, sulfonic acid groups were added to PEGPEA through a nucleophilic substitution reaction. This reaction involved a nucleophile (part of an external compound) which reacted with the partial charge on a leaving group (part of a larger compound which is replaced by the nucleophile) and displaced the leaving group forming a substituted compound as well as a byproduct [11]. In these experiments, SO_3^- from sulfuric acid was used to replace a partially charged hydrogen atom on the terminal phenyl ring of PEGPEA. This reaction yielded sulfonated PEGPEA (sPEGPEA) and water as a by-product. The reaction is shown schematically in Figure 3.3a. Specifically, PEGPEA was sulfonated by reacting with 95-98% sulfuric acid (Sigma Aldrich #258105) which had been combined with water and neat PEGPEA as 2mL:2mL:8mL, respectively. The reaction was carried out in a sealed glass vessel and left under reflux at 70 °C for two hours. After the reaction was completed, samples were thoroughly washed with deionized water to remove excess sulfuric acid from the sPEGPEA phase. Samples were then vacuum dried for 24 hours, which removed excess water. Verifying the effectiveness and extent of the sulfonation reaction was critical to material processing and was measured by two techniques, Fourier transform infrared spectroscopy (FTIR) and x-ray photoelectron spectroscopy (XPS). Both techniques are described below in Section 3.4. After having successfully transferred sulfonic acid groups to the PEGPEA polymer phase, liquid PEGDA-sPEGPEA polymer blends were formed through vortex mixing. Specific mass fractions of the liquid phase of each polymer were combined in 5 mL glass vials followed by two minutes of high speed vortex mixing. Representative liquid polymer blends are shown in Figure 3.3b. Polymer blends were used for preparation of multiple samples and were stable over several months (stored in the dark at room temperature).

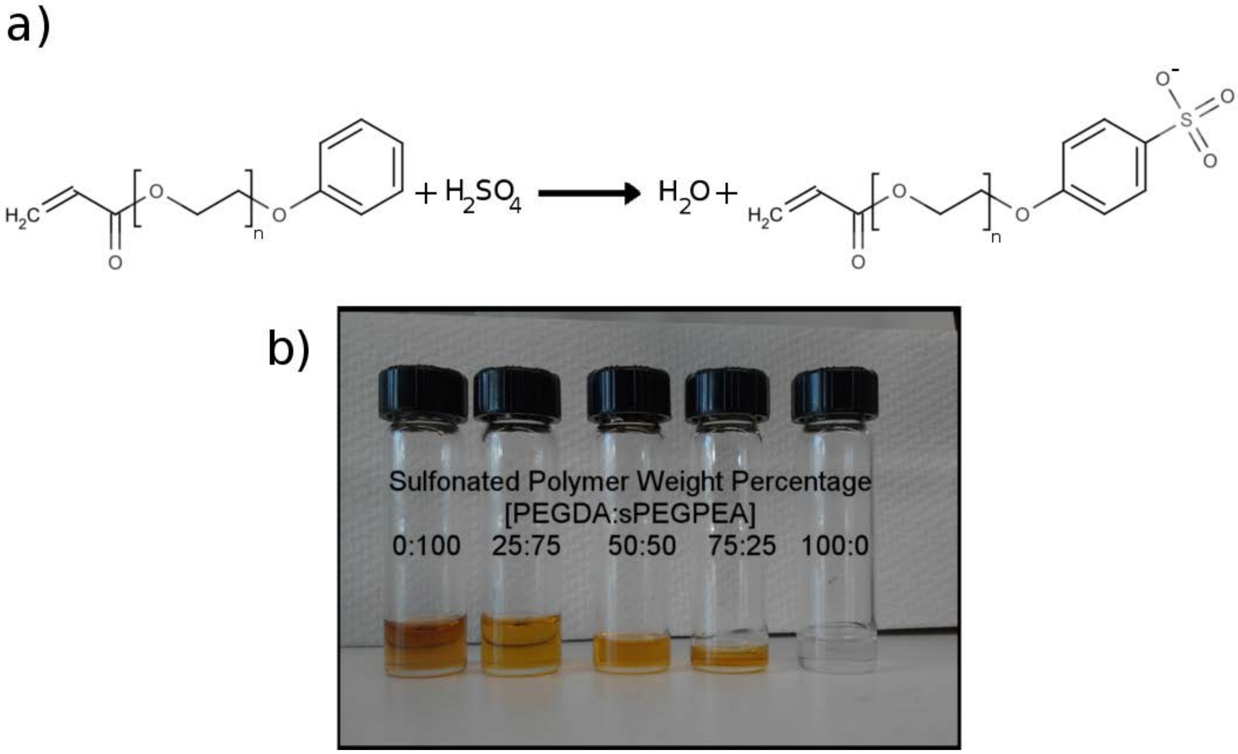

Figure 3.3 (a) Schematic diagram of the nucleophilic substitution reaction used to transfer a sulfonic acid group onto PEGPEA through reaction with sulfuric acid. The reaction was undertaken under constant reflux for two hours at 70 °C. (b) Optical image of PEGDA-sPEGPEA polymer blends of different weight percentages in liquid form.

3.3 Free Radical Photopolymerization

Here, PEGDA-sPEGPEA blends are photopolymerized into solid PEMs through *in situ* free radical photopolymerization (IS-FRPP). IS-FRPP is a variant of radical polymerization wherein highly energetic free radical compounds allow for the lengthening of polymer chains through successive addition of monomer units [12]. Free radicals attach to the terminal groups of polymer chains and provide additional reactivity sufficient to allow for further bonding. In FRPP generation of free radical compounds is accomplished through addition of a photosensitive compound. When exposed to specific wavelengths of light, the compound (termed a photo-initiator) will decompose yielding radicals which will start the polymerization process [13]. When used with acrylate and diacrylate compounds, FRPP allows for rapid formation of chemical crosslinks between polymer chains reacting liquid polymer solutions into a mechanically stable solid membranes. A significant benefit of FRPP, when applied to microscaled devices, is the ability to initiate polymerization without direct contact to the substrate (*i.e.* by shining a light through an optically transparent surface). Optical methods allow for *in situ* processing methods where a solid polymer structure can be formed within a sealed microfluidic device [14]. A further benefit of FRPP is derived from the selectivity of the crosslinking process. As only regions exposed to a sufficiently high intensity of light will undergo crosslinking a partially transparent photomask (the same as found for conventional photolithographic techniques) can allow for patterning of micron scale features.

In this investigation, small quantities of 2,2-dimethoxy-2-phenylacetophenone (Sigma Aldrich #196118) photoinitiator were used to generate free radicals sufficient to crosslink the PEGDA-sPEGPEA polymer blend. After forming PEGDA-sPEGPEA polymer blends 0.01 wt%, photoinitiator was added to the mixture which was then subjected to 2 minutes of further vortex mixing. The blended PEGDA-sPEGPEA-photoinitiator mixture was cured into solid structures using two methods. Samples for usage in material characterization experiments were photopolymerized on a benchtop by exposing to 365 nm UV radiation from a 8W lamp for 15 minutes. Samples used for *in situ* membrane polymerization were formed using an ABM Mask Aligner with (65 mW/cm^2 intensity at 400 nm for 40 s) exposing micron scale patterns through a quartz photomask illuminating liquid PEGDA-sPEGPEA-photoinitiator within the microchannel. This process was shown schematically in Figure 3.2. After photocrosslinking, membranes were vacuum dried for one hour at room temperature to remove excess water. Samples intended for material characterization were cut into required shape/orientation after vacuum drying depending on intended application. Nafion reference samples were prepared from a liquid resin (Sigma Aldrich #527084) and were processed by drop casting resin into a polystyrene mold and heating at 70 °C for three hours to remove excess solvent. After solvent was removed, solid Nafion membranes were cut to specific shapes as required.

3.4 Characterization Methods

Once membranes of chemically functionalized PEGDA-sPEGPEA polymer blends had been formed, extensive characterization experiments were undertaken. Membranes were characterized using a number of techniques to determine the chemical, electrochemical, and physical properties of the materials. A brief outline of the characterization techniques used is described below with results and discussion presented in Section 3.5.

3.4.1 Fourier Transform Infrared Spectroscopy

The first method used to characterize the membrane materials was Fourier transform infrared spectroscopy (FTIR). FTIR is an optical technique where light passes through a material and wavelength dependent transmittance values are gathered. Analysis of transmittance curves yielded information about the chemical structure of the membrane materials [15]. In this investigation, a modified version of FTIR, attenuated total reflection FTIR (ATR-FTIR), was used. In ATR-FTIR evanescent waves reflect off the surface of a sample rather than passing through its bulk (as for conventional FTIR) removing the need for pre-processing of samples prior to measurement.

ATR-FTIR was used as one means to verify the effect of the nucleophilic substitution reaction to form sPEGPEA. By taking ATR-FTIR spectra of samples before and after the reaction, comparisons between the absorption spectra could be made and changes in chemical structure were deduced. Specifically, the addition of a sulfonic acid group onto the terminal phenyl ring of PEGPEA will cause additional absorbance peaks to form at wavenumbers specified in the literature [3,16,17].

FTIR experiments were carried out on a Nicolet Nexus 670 FTIR using a Harrick grazing ATR sample mount. Samples were collected over a range of 650-4000 cm^{-1} with a wavenumber resolution of 1 cm^{-1}. Each sample consisted of 128 scans, the results of which were averaged to create the presented spectra.

3.4.2 X-ray Photoelectron Spectroscopy

Another technique used to analyze the chemical structure of the crosslinked membrane materials was x-ray photoelectron spectroscopy (XPS). XPS is a surface analysis technique where high energy x-rays are fired at a sample causing emission of photoelectrons from atoms within the top 1-10 nm of a sample. The wavelength of emitted electrons is dependent upon both the elemental nature and specific bonding of atoms on the sample surface and can provide direct confirmation of the chemical structure of a sample [18]. In this investigation, XPS was used as a second check to verify the extent of reaction of the nucleophilic substitution reaction.

XPS spectra were obtained using a Kratos Analytical AXIS Ultra XPS system at the University of Alberta ACSES characterization facility. Photocrosslinked solid membrane samples were measured after vacuum drying. Each sample was measured in 3 locations with average results and deviations presented.

3.4.3 Contact Angle Measurement

As discussed in Section 2.3.2, when used in aqueous environments, PEMs must possess sufficiently hydrophilicity to allow for favourable transport of protons but not overly hydrophilic to allow for bulk transport of water [19]. In this investigation, the hydrophilicity of PEGDA-sPEGPEA membranes was directly evaluated by measuring the water contact angle (the shape of a droplet of water on the surface of the membrane). Based upon surface charging effects, a water droplet of a given size will assume different shapes depending upon the hydrophilicity of the material. Strongly hydrophilic surfaces will ‘wet’ completely and broaden the water droplet (or if samples are exceedingly hydrophilic be absorbed into the surface of the material). Hydrophobic surfaces will cause the droplet to minimize its exposed surface area and assume a more spherical shape [20]. The contact angle is then defined as the angle between the surface and the droplet. Contact angle measurements were undertaken using a First Ten Angstroms FTA 100 apparatus consisting of a balance table, a calibrated micropipet, and a camera at the University of Alberta nanoFab facility. Measurements were performed by placing 0.5 µL droplets of deionized water on an optically flat membrane surface (which was prepared by photopolymerizing the membrane samples between two glass slides). Each sample was measured 3 times with averages and standard deviations presented.

3.4.4 Water Absorbance and Ion Exchange Capacity

Contact angle measurements determine surface hydrophilicity of materials when exposed to small amount of water. For PEMs to be used in aqueous environments it is also important to evaluate the bulk interaction of membrane materials when they are fully immersed in water. Bulk properties of the membrane materials were evaluated through two studies: water absorbance and ion exchange capacity. Water absorbance involved placing a sample of the membrane material of known mass in a large container of water and measuring the change in mass after a specified time interval. By comparing the saturated wet mass to the dry mass the amount of water uptake into the bulk of the membrane could be measured.

Specifically, water absorption values were calculated using $\%_{Uptake}=((m_{wet}-m_{dry})/m_{dry})*100$. Samples were soaked in water for 24 hours prior to measuring the wet state. Wet masses were obtained after lightly drying the surface with a lab wipe to remove excess water clinging to the outer membrane surface. Dry masses were measured after the wet masses were obtained after vacuum drying the wet samples for 24 hours at room temperature. Water absorption characterization was repeated four times per sample composition with results averaged and standard deviations presented.

Ion exchange capacity was measured using an acid/base titration method. Membrane samples of equal mass (40 mg) were prepared and first equilibrated in 1M hydrochloric acid for 24 hours to fully protonate all containing sulfonic acid groups. Acidified membranes were then removed from the acidic solution (briefly dried to remove acid on the surface of the samples,) and then placed in 1.14 M sodium chloride (EMD-Millipore #SX0420-1) for twenty four hours to release stored hydrogen ions. After which, membranes were removed from the salt solution. The acidified salt solution was titrated against 0.05 M NaOH while monitoring the solution pH with an Orion 5 Star pH meter. Ion exchange capacity was then defined through measuring the amount of NaOH (JT Baker #3140) required to return the NaCl solution to its initial pH through $IEC=(V_{KOH}*C_{KOH})/m_{dry}$.

A final means of water absorbance characterization applied was cryogenic scanning electron microscopy (cryo-SEM). In this technique, a sample was first immersed in water and soaked for several days to ensure maximum water uptake. The sample was then quickly placed in liquid nitrogen, flash-freezing absorbed water. Flash-freezing preserved the microstructure associated with the swollen water state. After freezing, the sample was imaged in a SEM to allow direct visualization of the porous microstructure. For these experiments, a Leica EM VCT100 was used to prepare a 25:75 PEGDA-sPEGPEA membrane. The frozen membrane was then coated with a 5 nm thick Pt film using an EM SCD500. Samples were imaged in a Zeiss NVision 40 FIB/SEM with applied voltages of 2 – 5 kV. Experiments were conducted at the NRC, National Institute for Nanotechnology. Due to limited access to instrumentation, only 25:75 PEGDA:PEGPEA samples were imaged.

3.4.5 Proton Conductivity

Perhaps the most important property to measure for any candidate PEM material, is the proton conductivity. This is the electrical conductivity of the membrane using protons as charge carriers (contrary to the conventional electrical conductivity which uses electrons as charge carriers). To be an effective candidate PEM material, membranes must have low electrical conductivity (*i.e.* not allow for the flow of electrons between half cells) while maintaining high proton conductivity. This combination of anisotropic positive and negative charge transport forces current through an external circuit while maintaining internal charge balance within the fuel cell.

In this investigation, proton conductivity was evaluated using a Lucaslabs 302 Four Point Probe apparatus combined with a Princeton Applied Research Versastat 3 electro-impedance spectrometer. In order to assess the frequency dependent impedance behavior of the membranes, samples were evaluated at applied frequencies varying from 1 Hz to 1 MHz with proton conductivity defined as the value of the real component of the impedance at the frequency when the impedance is purely resistive (*i.e.* $Z=R+jX$ when $X=0$) as $\sigma=1/\rho=(1/R)*C*t$ where R is the resistance in Ohms, t is the sample thickness, and C is a geometric constant. PEGDA-sPEGPEA and Nafion samples were cut into flat squares of 20 mm by 20 mm length and width and 1 mm in thickness. Four point probe contacts were placed in the middle of the samples and pressed until firmly contacting the sample surface. All samples were prepared by immersing in 1 M H_2SO_4 for 24 hours to fully protenate the membranes. Some samples (termed 'water soaked) were then subsequently immersed in an excess of deionized water for 24 hours to remove any bulk absorbed acid.

3.4.6 Dynamic Mechanical Analysis

Mechanical stability is an important property for macroscale and microscale PEM materials. Membranes must be sufficiently rigid to resist deformation when exposed to high flow rates to avoid tearing or allowing leakage between half cells [21]. For these experiments, the mechanical properties of the membrane materials were measured through dynamic mechanical analysis (DMA). DMA is a technique which uses cyclic loading/unloading of a sample by applying a known force to determine mechanical properties. Specifically, our work measured the elastic modulus, a property that is representative of the nature of a material to deform via plastic or elastic processes [22]. Mechanical characterization of the membranes consisted two different methods of measuring elastic modulus, both using a Perkin-Elmer DMA 8000. An immersion bath accessory was used to obtain wet measurements. Samples were evaluated in either tension or compression modes with tension (the more accurate measurement method, though with a higher minimum modulus requirement) used for samples unless otherwise mentioned. Tensions measurements used rectangular films that had been subjected to a pre-loading force of 1 N (thus placing the sample under tension) and then cyclically applying a displacement of 0.01 mm along the pre-loaded force direction at a rate of 1 Hz. Compression measurements were taken by filling a cylindrical sample in a metallic cup and cyclically applying a downwards compressive displacement of 0.01 mm at 1 Hz.

3.5 Results and Discussion

3.5.1 Membrane Formation and Chemical Structure Characterization

Before any practical characterization of the membrane materials could be made, an effective method for producing photopolymerizable PEM materials had to be established. As described above in Section 3.1, PEGDA and PEGPEA were used as base materials for the blended polymer network. PEGDA was used as a crosslinking agent (turning the liquid polymer into a solid membrane upon exposure to light), PEGPEA was used to integrate proton conducting sulfonic acid groups to achieve favourable proton conductivity. Successfully reacting PEGPEA to sPEGPEA (*i.e.* transferring the sulfonic acid group) was essential for membrane functionality. Given the importance of the sulfonation reaction, samples were extensively characterized through FTIR and XPS to confirm the presence of sulfonic acid groups and gauge their concentration.

FTIR spectra were obtained before and after the sulfonation reaction (for PEGPEA and sPEGPEA, respectively). sPEGPEA samples contained additional absorbance peaks at ~1300 cm^{-1} and ~1000 cm^{-1}. Literature values identify those peaks as being characteristic of asymmetric and symmetric stretches of SO_3 groups, respectively as is shown in Figure 3.4a [23,24]. FTIR measurements were taken after soaking membranes in an excess of deionized water for a minimum of one week and as such it is likely that the observed SO_3^- stretches are due to functional groups within the polymer, rather than acid compounds remaining in the polymer bulk. While the FTIR results do suggest that sulfonic acid was transferred to some of the PEGPEA sites, they did not give an indication of the degree of sulfonation (*i.e*. the amount of sulfur present in the polymer which is related to the fraction of possible PEGPEA sites reacted to form sPEGPEA). Knowledge of the sulfur content is critical for evaluating the utility of PEGDA-sPEGPEA membranes as PEMs. High sulfur content corresponds to a higher degree of sulfonation which will intern allow for higher proton conductivity.

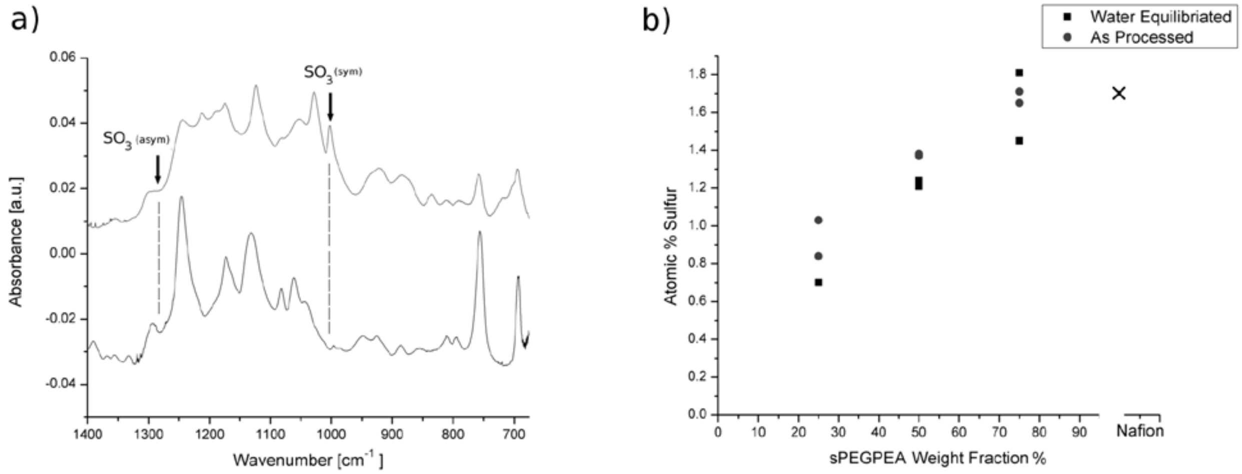

Figure 3.4 (a) FTIR spectra for non-crosslinked sPEGPEA (top) and PEGPEA (bottom), spectra have been offset by a constant for clarity. (b) XPS data showing the atomic percent of sulfur measured on the surface of a PEGDA-sPEGPEA membrane as a function of sPEGPEA weight fraction directly after crosslinking ('as processed') and a membrane that had been equilibrated in water ('water equilibrated') for 24 hours to remove any residual sulfuric acid. A Nafion reference is also shown for comparison. Copyright © 2011 Elsevier B.V. Used with permission.

XPS probed the surface (with ~ 10 nm penetration depth) of the membrane samples to determine their chemical structure. As for FTIR samples, care was taken to remove any bulk acid which may have been absorbed within the polymer bulk. Membranes were prepared for XPS characterization by two methods. The first process probed membranes directly after rinsing their surface. Samples for the second process were subsequently equilibrated in deionized water for 24 hours. To further investigate the degree of sulfonation in composite membranes the weight fraction of sPEGPEA was varied from 25 to 75% with results shown in Figure 3.4b. Pure sPEGPEA (*i.e.* 100% weight fraction) was unable to be characterized via XPS as it was found to be exceedingly hygroscopic. Even after extensive vacuum drying (more than one week), pure sPEGPEA samples lead to prohibitively high levels of outgassing in the vacuum chamber to allow for measurement by XPS. Both sample preparation methods observed significant quantities of sulfur in the surface of the membrane materials. Sulfur concentration was found to vary in a roughly linear manner with the fraction of sPEGPEA utilized. This result was expected as only the sPEGPEA phase was responsible for introduction of sulfur into the membranes. For all three of the examined concentrations, water equilibrated samples displayed 0.2-0.3 less atomic percentage of sulfur than un-equilibrated samples. This suggested that despite thorough rinsing trace sulfuric acid did linger within the bulk of the polymer. Future studies based upon these methods of chemical sulfonation should make certain samples are free of bulk absorbed acids to ensure valid results prior to further characterization.

In addition to PEGDA-sPEGPEA membranes, a Nafion reference sample was also examined by XPS. Nafion was found to yield a similar atomic percentage of sulfur as the 75 weight% sPEGPEA samples. Proton conductivity levels are closely tied to the degree of sulfonation as sulfonic acid sites act to transfer protons. Our XPS results suggested that high concentrations of sPEGPEA have similar sulfur content to Nafion and as such may possess favourable proton conductance. Later characterization evaluated this hypothesis.

FTIR and XPS characterization lead to several important observations. Firstly, measurement results confirmed that PEGPEA molecules were reacted to form sPEGPEA. This showed that our simple single step nucleophilic substitution reflux reaction proceeded as intended. The ability to sulfonate an inexpensive PEG polymer derivative to impart proton conductance by this simple processing method is of great utility when compared to costly (and complicated) fluorine chemistry involved with processing of Nafion and related flouropolymers [[25]]. Secondly, results showed that the degree of sulfonation was linearly related to the mass fraction of sPEGPEA phase. This was a reasonable result and suggested that through changing the relative composition of PEGDA and sPEGPEA proton conductivity can be selectively tuned.

3.5.2 Aqueous Environment Characterization

An effective PEM material requires a moderate level of hydrophilicity. Membrane materials must be sufficiently hydrophilic to allow for the formation of water channels throughout the bulk of the membrane (so that protons are able to travel) but not exceedingly hydrophilic such that the membrane itself is compromised either mechanically (deforming), or chemically (dissolving) when placed in an aqueous environment. Achieving such a balance is a delicate process requiring careful selection of chemical structure. In this work, by varying the relative concentration of (more hydrophobic) PEGDA and (more hydrophilic) sPEGPEA, we intended to create polymer blends with acceptable levels of hydrophillicity.

The hydrophilicity of PEGDA-sPEGPEA membranes in this investigation was evaluated by measuring the contact angle, degree of water absorption, and ion exchange capacity with results presented in Table 3.1 and Figure 3.5.

Table 3.1 Ion exchange capacity and contact angle measurements for sulfonated and unsulfonated membrane samples.

Material	**ICE [mmol/g]**	**Contact Angle [°]**	**ICE [mmol/g]**	**Contact Angle [°]**
[PEGDA:PEGPEA]	Unsulfonated	Unsulfonated	Sulfonated	Sulfonated
[100:0]	1.3 ± 0.1	46 ± 6		
[75:25]	0.80 ± 0.05	54 ± 3	1.2 ± 0.1	22 ± 3
[50:50]	0.35 ± 0.04	59 ± 4	1.9 ± 0.3	~0
[25:75]	0.06 ± 0.03	71 ± 4	3.8 ± 0.6	~0
[0:100]	0.11 ± 0.04	89 ± 5	21.72 ± 1	~0
Nafion			2.6 ± 0.3	62 ± 4

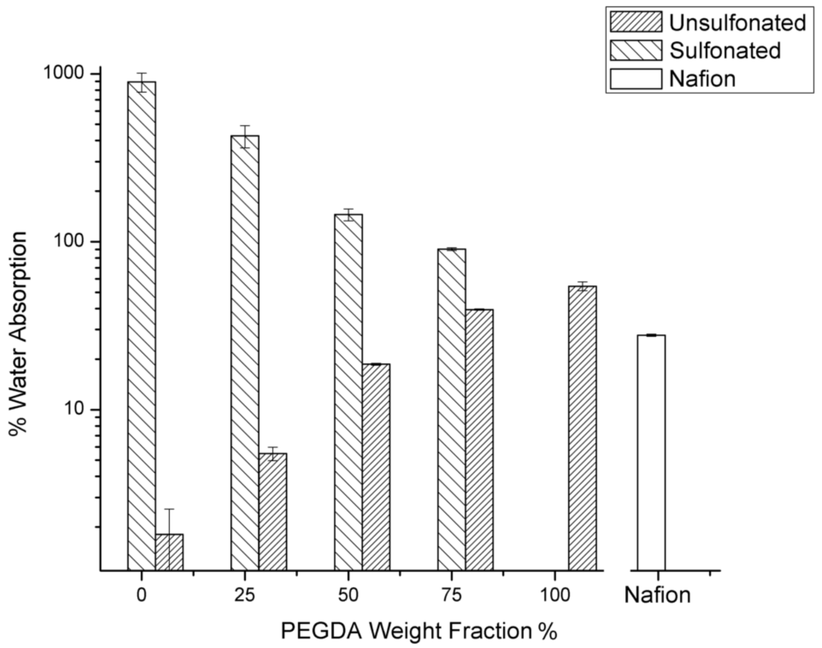

Figure 3.5 Water absorption of sulfonated and unsulfonated polymer membranes as a function of PEGDA volume concentration. There is no data for sulfonated neat PEGDA as the sulfonation reaction was only carried out on the PEGPEA phase. Copyright © 2011 Elsevier B.V. Used with permission.

Contact angle measurements were undertaken for both sulfonated and unsulfonated samples as well as a Nafion reference. For unsulfonated samples, it was found that contact angle increased (*i.e*. water wet the surface less effectively) for increasing PEGPEA content. Contact angle varied from 46±6° for pure PEGDA and 89±5° for pure PEGPEA, respectively. These results suggested that prior to sulfonation, PEGPEA was more hydrophobic than PEGDA and resisted uptake of water into the membrane. Membranes formed with sPEGPEA displayed a profound change in hydrophilicity. Sulfonated membranes were found to possess such exceedingly high hydrophilicity that only 25 wt% sPEGPEA (with a contact angle 22±3°) samples were able to be effectively measured! sPEGPEA concentrations higher than 25 wt% lead to complete wetting of the membrane surface and absorption of water into the polymer bulk. In pure sPEGPEA samples, absorption was accompanied by visible swelling and deformation of the membrane surface. The Nafion reference sample was measured to have a moderate contact angle of 62±4°. The Nafion contact angle value serves as a benchmark for an appropriate level of hydrophilicity. Based upon these results only the 75:25 PEGDA:sPEGPEA sample was found to possess reasonable levels of hydrophilicity.

Contact angle measurement results demonstrated that sPEGPEA, and membranes containing sPEGPEA, have very high affinities towards water. The extent of water absorption was more directly measured by characterizing the bulk water uptake (*i.e.* comparing the mass of membranes before and after equilibrating in an excess of deionized water). This technique allowed for determination of how much water is absorbed into the bulk of the polymer when in an aqueous environment.

The degree of water absorption was measured for the same samples compositions as used in contact angle measurement. Results are shown in Figure 3.5 which are in agreement with contact angle measurements. Unsulfonated membranes possessed relatively low levels of water absorption ranging from 1.8 ± 0.8% to 54 ± 3% decreasing with decreasing amounts of PEGEA. Sulfonated membranes demonstrated significantly increased water absorption with sPEGPEA content. Pure sPEGPEA was measured to absorb 890 ± 110 wt% and was visually observed to undergo significant swelling during water absorption. A Nafion reference was also measured and was found to increase in mass by 27.7 ±0.4 %.

Intimately related to the amount of bulk water absorption is the IEC. IEC was measured for both unsulfonated and sulfonated materials by equilibrating membranes that had been soaked in 1 M HCl in an excess of deionized water and measured the resultant change in pH (indicative of the amount of protons absorbed by the membrane during the acid equilibration process). As for the other aqueous environment characterization techniques, IEC showed opposing trends for unsulfonated and sulfonated samples. Unsulfonated membranes possessed decreasing amounts of IEC with increasing PEGPEA content ranging from 1.3 ± 0.1 mmol/g for pure PEGDA to 0.11 ± 0.04 mmol/g for pure PEGPEA while sulfonated membranes increased from 1.2 ± 0.1 mmol/g 25% sPEGPEA to 21 ± 2 mmol/g for pure sPEGPEA. Such a large disparity in IEC values links directly to the high levels of water absorption measured for sulfonated samples. As the acidified solution is aqueous a large amount of HCl would be absorbed into the bulk of the membrane which was subsequently desorbed when placed in deionized water.

Through all of the measurements of their behavior in aqueous environments PEGDA-sPEGPEA membranes have shown repeatable trends. Sulfonation increased the hydrophilicity of PEGPEA to such a degree that high weight fractions of sPEGPEA resulted in a polymer network which non-specifically stored large amounts of water and acid within its bulk. While these properties could initially be viewed favourably, as they allow for high IEC, high levels of water absorption but must be tempered with the unfavourable properties associated with a highly swollen membrane. Namely, water-swollen membranes allow for non-specific transport of fuel compounds through bulk water channels. Of the membrane compositions measured, only 75:25 PEGDA:sPEGPEA samples displayed acceptable values of water absorption and IEC.

Aqueous environment characterization showed that high weight percent sPEGPEA samples absorbed large amounts of water and acid solution. A likely explanation for their high level of absorption is that the polymer network is exceedingly porous. Porosity was directly measured through cryo-SEM. Cryo-SEM analysis was performed on a 25:75 weight percent PEGDA:sPEGPEA sample which had been equilibrated in water. Representative images of the sample are shown in Figure 3.6. Images revealed the microstructure of the membrane which consisted of a thin scaffold of crosslinked solid polymer surrounded by large amounts of water (in this case ice as the sample was imaged under cryogenic conditions). This analysis confirmed the hypothesis that large amounts of water (and likely acid) were being absorbed within the bulk of the membranes. Due to equipment access limitations only 25:75 weight percent samples were imaged. Future work would evaluate the changing microstructure through cryo-SEM as membrane composition varies and determine the level of interconnectivity of the pores.

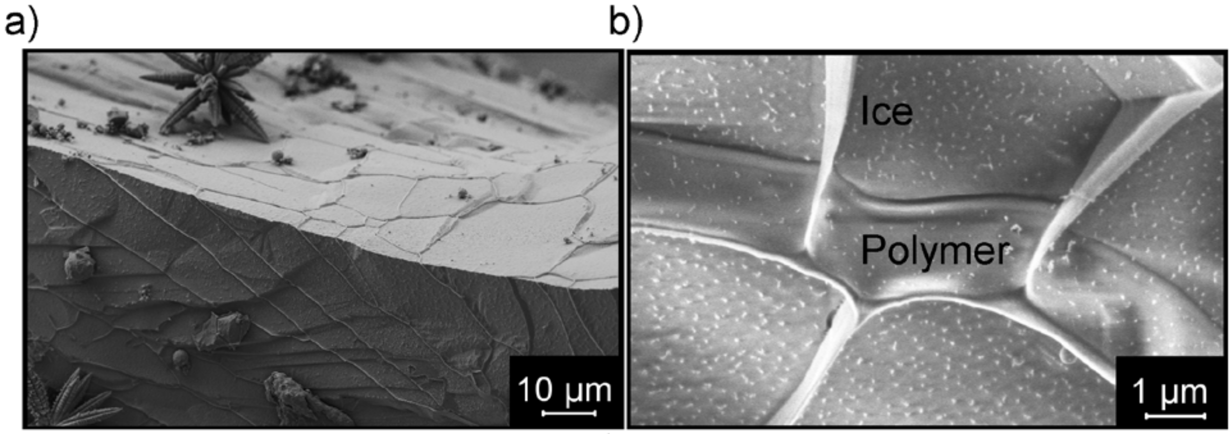

Figure 3.6 Cryo-SEM images showing (a) 1000x and (b) 11300x magnification of a water swollen 25:75 weight percent PEGDA:sPEGPEA membrane sample. Images show thin scaffolds of polymer surrounded by large amounts of ice. In (b) some of the upper ice surface has been removed through use of a focused ion beam. Images used with permission of Martin Kupsta, NRC NINT.

3.5.3 Proton Conductivity Measurements

Proton conductivity is likely the most widely reported metric of the performance of a PEM material. PEGDA-sPEGPEA samples were measured using electrochemical impedance spectroscopy which determined current and voltage profiles as a function of impedance over a range of applied frequencies.

As for other characterization methods, samples were prepared through either equilibration in 1M H_2SO_4 (to protonate the sulfonic acid sites) and directly measuring the proton conductivity, or by acid equilibration followed by equilibrating in an excess of deionized water (to draw out any acid absorbed into the membrane bulk). Proton conductivity values for membrane samples and a Nafion reference are presented in Figure 3.7. Both acid soaked and water soaked samples were found to possess proton conductivity values that varied linearly with %PEGDA weight fraction (*i.e.* as the relative amount of sPEGPEA increased, the proton conductivity increased). Furthermore, the magnitude of the difference in proton conductivity between the acid soaked and water soaked samples became larger with more sPEGPEA present. This reinforced the results of IEC characterization and showed that higher quantities of sPEGPEA lead to more absorption of acid into the polymer bulk.

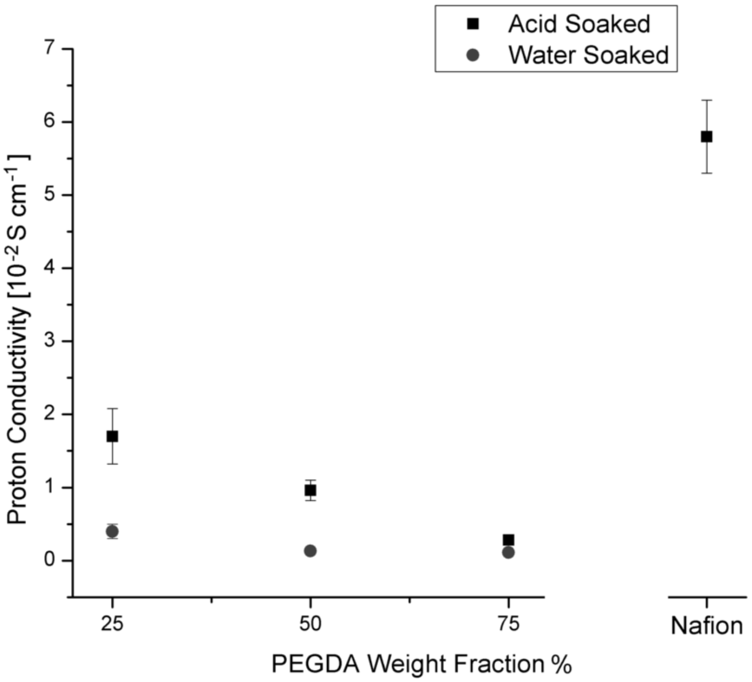

Figure 3.7 Proton conductivity for sulfonated PEGDA-sPEGPEA membranes in their acid and water equilibrated states. Copyright © 2011 Elsevier B.V. Used with permission.

From these results it is clear that while compared to Nafion the produced PEGDA-sPEGPEA membranes possessed increased levels of both water absorption and IEC, their proton conductivities were not similarly enhanced. One likely cause of this disparity is the difference in chemical structure between the produced PEGDA-sPEGPEA membranes and Nafion. In Nafion, a sulfonated fluoropolymer, there is a clear distinction between the hydrophobic and hydrophilic regions of the polymer. Hydrophilic regions self-assemble to form water channels through the polymer. For PEGDA-sPEGPEA membranes, sulfonic acid sites may be less localized spread across the bulk of the polymer. This orientation does not guarantee a flux of protons from one side of the membrane to the other. Additionally, due to the exceedingly high levels of bulk water absorption, protons that enter into the membrane have a significant chance of remaining in the membrane bulk rather than being carried through the material. It should however be directly stated that despite the lower value of proton conductivity PEGDA-sPEGPEA membranes are significantly less expensive than Nafion based implementations and may well suited to microfluidic implementations where low cost is critical if bulk absorption of water can be addressed [26].

3.5.4 Mechanical Characterization

The mechanical properties of polymer blend membranes were characterized with and without sulfonation in both dry and wet states through measurement of elastic modulus. It was expected that the stiffness of the composite membrane materials would vary with the degree of PEGDA content (as PEGDA served as a crosslinking agent, higher concentrations would lead to more crosslinks and a less elastic polymer network). Experimental results agreed with this hypothesis and found significant variations in modulus for both unsulfonated and sulfonated samples with PEGDA content as is shown in Figure 3.8. When immersed in water, unsulfonated samples were found to decrease slightly in measured modulus. Modulus values for sulfonated samples decreased considerably upon immersion and increased deviation in modulus measurement. These results were consistent with the rest of the material characterization experiments. The highly hydrophilic nature of sPEGPEA caused significant absorption of water into the membrane, and formed a less stiff material. The magnitude of modulus reduction was tied to the amount of sPEGPEA in the polymer blend.

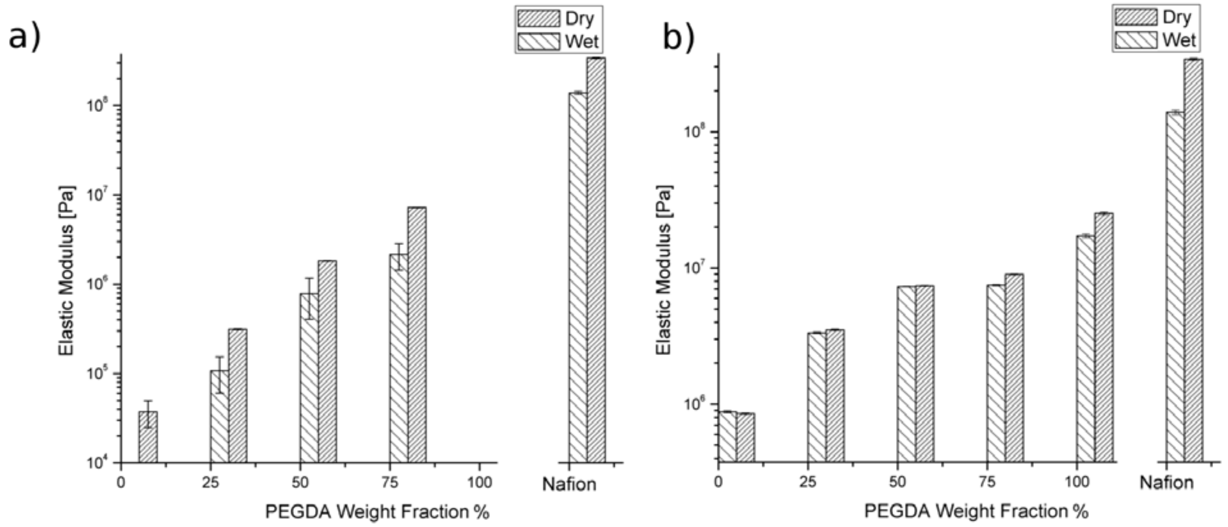

Figure 3.8 Elastic modulus of a) sulfonated and b) unsulfonated membranes as measured by DMA relative to a Nafion reference sample in each figure. Each sample was measured in both dry and wet states. Copyright © 2011 Elsevier B.V. Used with permission.

In microfluidic fuel cell devices operating at high flow rates (on the order to 10s to 100s μL/min), fluid flow in small channels can lead to significant fluid pressure. In these environments, PEGDA-sPEGPEA (especially those with high sPEGPEA content) may be ill-suited for usage as membrane materials due to mechanical deformation. Further experiments focused directly on the mechanical properties of the membrane materials would also investigate the stress-strain properties of PEGDA-sPEGPEA membranes. Such studies could determine how much force/pressure the membranes can sustain before undergoing permanent deformation/breaking and establish an effective flow rate regime for PEGDA-sPEGPEA membranes.

3.5.5 Integration into Microchannels

While characterization of the material properties of the developed PEGDA-sPEGPEA membranes was important to gauge their utility as PEMs, it was only half of the focus of this work. The other aim of the investigation was to evaluate the ability for PEGDA-sPEGPEA membranes to be easily integrated into a microfluidic devices. This was carried out by several methods: in initial trials, samples of PEGDA-sPEGPEA were photopolymerized using a conventional photomask (used for photoresist based optical lithography) where a variety of differently shaped and sized structures PEGDA-sPEGPEA were patterned to determine appropriate patterning parameters (polymer composition, light intensity, exposure time) and their effect of resultant structures. Patterning was evaluated in terms of repeatability, and pitch (*i.e.* the smallest width/resolution of feature possible). Initial patterning experiments were conducted on cleaned glass slides and it was found that repeatable patterning of regular structures down to ~5 µm width was possible using PEGDA-sPEGPEA blends of 75:25 weight percent as is shown in Figure 3.9c. It was found that polymer blends of higher sPEGPEA weight fraction were more difficult to photopolymerize and lead to significantly larger pitch widths. Membranes with high sPEGPEA content were not amendable to micron scale patterning. These results were reasonable as the PEGDA phase is responsible for forming the crosslinked polymer network and less crosslinks will lead to a less localized solid structure. For further trials 75:25 weight percent PEGDA-sPEGPEA samples were used exclusively. These polymer blends were photopolymerized by applying light of 65 mW/cm^2 intensity at 400 nm for 40 s.

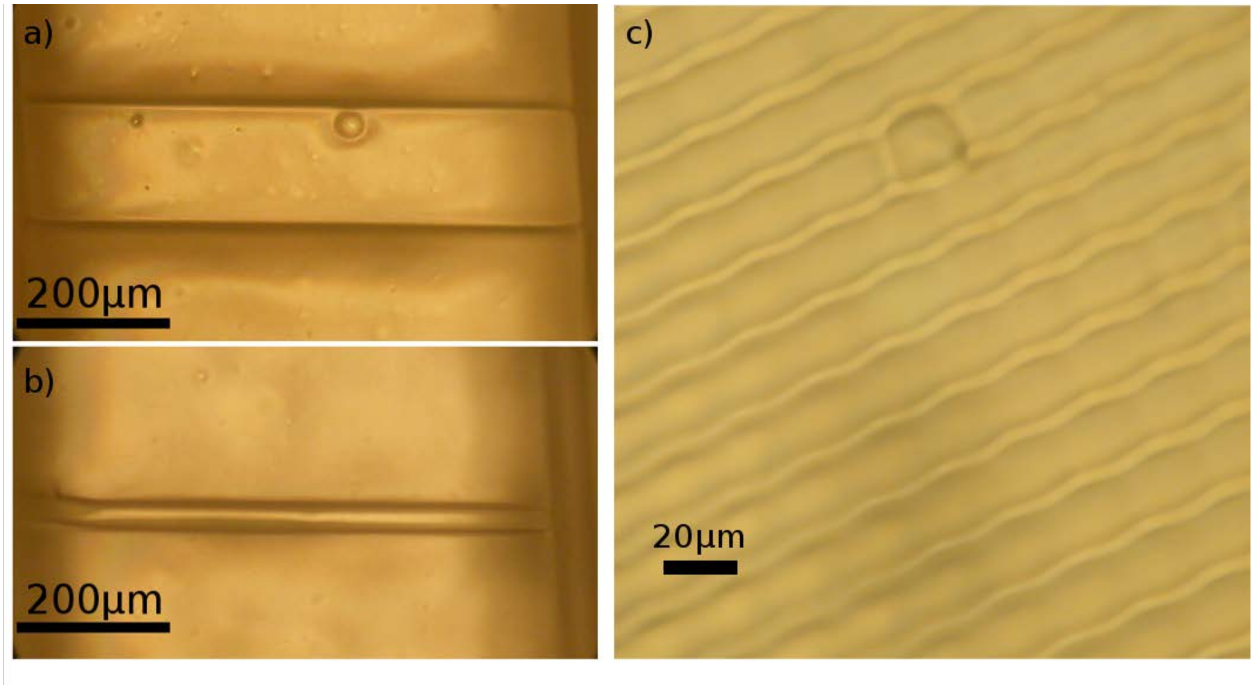

Figure 3.9 Optical images of PEGDA-sPEGPEA membranes of (a) 200 µm and (b) 50 µm width photopolymerized within PDMS microchannels as well as (c) a large array of 5 µm wide PEGDA-sPEGPEA lines photopolymerized on a cleaned glass slide. Copyright © 2011 Elsevier B.V. Used with permission.

After establishing effective processing parameters for 75:25 weight percent PEGDA-sPEGPEA samples, membranes were patterned within PDMS microchannels. To achieve this, 1000 µm wide 50 µm deep PDMS microchannels were produced via standard soft lithography.

For *in situ* patterning, PDMS microchannels were bound to a glass slide by applying 10 minutes of ~36 µW/cm^2 UV-ozone treatment (which also served to increase the wetting of the PEGDA-sPEGPEA phase to the PDMS surface). Directly after bonding, liquid PEDGA-sPEGPEA was flowed through the microchannel until it completely occupied the device. After stopping fluid flow, the PEGDA-sPEGPEA within channel was selectively exposed to UV light using a photomask with 200 and 50 µm wide lines to produce membranes of different size as shown in Figure 3.9a and Figure 3.9b. After photopolymerization, devices were immersed in water to remove unreacted monomer and subsequently imaged. These results demonstrated that *in situ* patterning of PEGDA-sPEGPEA membranes within a microfluidic device is achievable.

3.6 Future Work

Through extensive material characterization of PEGDA-sPEGPEA membranes, two important conclusions were drawn. Firstly, formation of sulfonated proton conducting polymers from PEG derivatives blends was achievable through straightforward bench-top chemistry. Secondly, photolithography was an effective means to attain *in situ* patterning of proton conducting PEGDA-sPEGPEA polymer blends. The material properties of PEGDA-sPEGPEA blends were found to vary with composition and demonstrated that membranes with high sPEGPEA content may be ill-suited to fuel cell applications. Specifically, sPEGPEA was found to exhibit excessively high levels of hydrophilicity which caused exceedingly high bulk water absorption. PEGDA-sPEGPEA membranes containing greater than 25 wt% sPEGPEA absorbed excessive levels of water greatly lessening their effectiveness as PEM materials due to non-specific transfer of ions, lower elastic modulus, and patterning difficulty. 25:75 PEGDA:sPEGPEA samples displayed material characteristics that would render them suitable for usage as PEMs. The demonstrated method of combing photopolymerizable acrylates with proton conducting compounds into polymer blends can be adapted to address the concerns of excess hydrophilicity caused by sPEGPEA by adding another compound to the polymer blend, specifically, a higher order acrylate polymer.

A candidate higher order acrylate is dipentaerythritol pentaacrylate (DPPA) shown schematically in Figure 3.10. DPPA contains five terminal acrylate groups per polymer molecule and as such can serve as a very effective crosslinking agent for both attaching scaffold polymer chains (*i.e.* PEGDA which in this work supported the polymer bulk), but also additional sites for integration of proton conducting sPEGPEA. Increasing the amount of crosslinks would create a more mechanically rigid polymer network which would also resist swelling in aqueous environments (reducing the detrimental effects of non-specific ion transport [27].

Another method to improve the proton conductance of blended acrylate polymers is by emulating the large disparity in hydrophilicity between chemical regions found in Nafion. As previously described in section 2.3.2 Nafion membranes possess a highly hydrophobic bulk permeated with hydrophilic water channels. For future PEG derivative based membranes, this behavior could be emulated by using longer chain length PEGDA molecules. As chain length increases PEGDA molecules become increasingly hydrophobic. Future experiments could tune PEGDA chain length, along with the relative compositions of PEGDA:DPPA:sPEGPEA phases to achieve a phase separated microstructure. In such a microstructure, clusters of sPEGPEA molecules would form connected regions within a well crosslinked scaffold. A polymer blend of DPPA, PEGDA, and sPEGPEA would retain *in situ* photopolymerizability as described in this work.

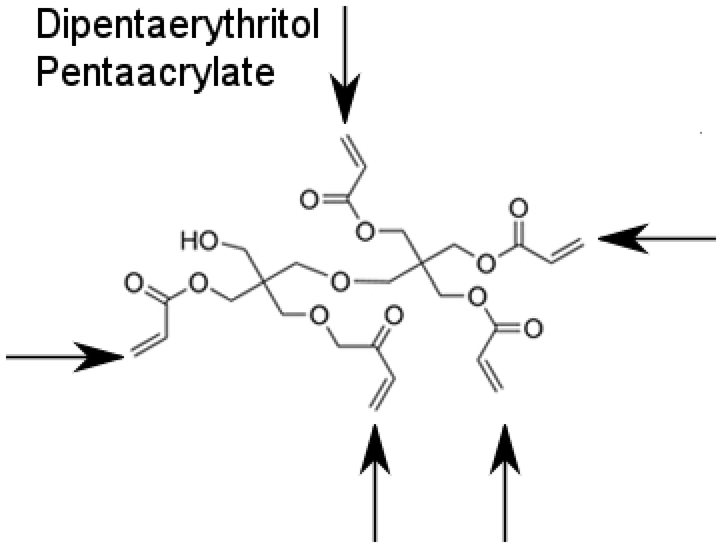

Figure 3.10 Schematic diagram of DPPA a higher order acrylate polymer. Each of the five terminal acrylate groups capable of participating in crosslinking reactions are shown with arrows.

Beyond changes in the chemical structure of the polymer blend, there are also additional characterization techniques which are of utility to evaluate the effectiveness of PEGDA-sPEGPEA membranes within microchannels for other purposes beyond proton conductivity. One of the most useful applications of a porous scaffold polymer would be mechanical sorting of particles or cells within a microchannel. By altering the composition of the polymer blend (changing the porosity of the material and hence the spacing of the scaffold), different sized scaffolds could selectively photopolymerized within a microchannel and restrict the passage of specific particles or cells [28]. Provided a porous barrier to cells would be especially useful for planar microbial MFCs where specific species of microbes must be restricted to the anode or cathode half cells.

3.7 Conclusions

This chapter set out to develop a PEM material that was compatible with *in situ* integration into a microfluidic device. This was achieved by combining PEGDA and functionalized PEGPEA polymers. Extensive characterization has shown that membranes formed from PEGDA-sPEGPEA polymer blends can indeed function as PEMs and through FRP can be formed within microchannels with dimensions scaling down to 5 micron precision. sPEGPEA was shown to be an effective compound for imparting proton conductivity into a hydrocarbon polymer network but possessed unfavourable levels of water absorption. The developed PEGDA-sPEGPEA membranes demonstrated tunable material properties through adjustment of the relative composition of the PEGDA and sPEGPEA phases. Of the compositions evaluated, 75:25 PEGDA:sPEGPEA weight fractions were found to be the most effective membranes in terms of water absorption and mechanical stability. Our method of forming PEG-acrylate/sPEGPEA polymers blends developed in this investigation is applicable to other combinations of polymers and can be used for patterning other functionalized materials within microchannels.

By focusing on a lower cost material and *in situ* processing technique this chapter has shown how the benefits generally associated with ‘sandwiched’ MFC devices (physical isolation of each half-cell using a membrane) can be achieved in a planar architecture. In the next chapter, another component of ‘sandwiched’ devices, gas-diffusing capping layers that can passively supply oxygen to cathode surfaces, are characterized for planar MFCs through finite element modelling.

3.8 References

---

[1] "Polymer Electrolyte Membranes for Fuel Cells" Lee J S, Quan N D, Hwang J M, Lee S D, Kim H, Lee H, Kim H S *Journal of Industrial Engineering Chemistry* 12 (2006) 175-183.

[2] "A review of polymer electrolyte membrane fuel cells: Technology, applications, and needs on fundamental research" Wang Y, Chen K S, Mishler J, Cho S C, Adroher X C *Applied Energy* 88 (2011) 981-1007.

[3] "Proton conductivities and methanol permeabilities of membranes made from partially sulfonated polystyrene-block-poly(ethyelene-ran-butylene)-block-polystyrene copolyers" Kim J, Kim B, Jung B *Journal of Membrane Science* 207 (2002) 129-137.

[4] "Ionomeric membranes for proton exchange membrane fuel cell (PEMFC): sulfonated polysulfone associated with phosphatoantimonic acid" Genova-Dimitrova P, Baradie B, Foscallo D, Poinsignon C, Sanchez J Y *Journal of Membrane Science* 185 (2001) 59-71.

[5] "Synthesis and characterization of sulfonated poly(ether ether ketone) for proton exchange membranes" Xing P, Robertson G P, Guiver M D, Mikhailenko S D, Wang K, Kaliaguine S *Journal of Membrane Science* 229 (2004) 95-106.

[6] "Sulfonated aromatic hydrocarbon polymers as proton exchange membranes for fuel cells" Higashihara T, Matsumoto K, Ueda M *Polymer* 50 (2009) 5341-5357.

[7] "Viscoelastic characterization of UV polymerized poly(ethylene glycol) diacrylate networks with varying extents of crosslinking" Kalakkunnath S, Kalika D S, Lin H, Freeman B D *Journal of Polymer Science B: Polymer Physics* 44 (2006) 2058–2070.

[8] "Thermodynamics and Proton Transport in Nafion II: Proton Diffusion Mechanisms and Conductivity" Choi P, Jalani N H, Datta R *Journal of The Electrochemical Society* 152 (2005) E123-E130.

[9] "Review of the proton exchange membranes for fuel cell applications" Peighambardoust S J, Rowshanzamir S, Amjadi M *International Journal of Hydrogen Energy* 35 (2010) 9349-9384.

[10] "Ionomeric membranes for proton exchange membrane fuel cell (PEMFC): sulfonated polysulfone associated with phosphatoantimonic acid" Genova-Dimitrova P, Baradie B, Foscallo D, Poinsignon C, Sanchez J Y *Journal of Membrane Science* 185 (2001) 59-71.

---

[11] "Aromatic Nucleophilic Substitution Reactions" Burnett J F, Zahler R E *Chemical Reviews* 49 (1951) 273-412.

[12] "Handbook of Radical Polymerization" Matyjaszewski K, Davis T P John Wiley and Sons, 2002.

[13] "Monolithic porous polymer for on-chip solid-phase extraction and preconcentration prepared by photoinitiated in situ polymerization within a microfluidic device" Yu C, Davey M H, Svec F, Frechet J M J *Analytical Chemistry* 73 5088-5096.

[14] "Functional hydrogel structures for autonomous flow control inside microfluidic channels" Beebe D J, Moore J S, Bauer J M, Yu Q, Liu R H, Devadoss C, Jo B H *Nature* 404 (2000) 588-590.

[15] "FTIR Microspectroscopy of Polymeric Systems" Bhargava R, Wang S Q, Koeing J L *Advances in Polymer Science* 163 (2003) 137-191.

[16] "Preparation and properties of PEG hydrogel from PEG macromonomer with sulfonate end groups" Kim J H, Kim J G, Kim D, Kim Y H *Journal Applied Polymer Science* 96 (2005) 56-61.

[17] "Study of EVOH based single ion polymer electrolyte: composition and microstructure effects on the proton conductivity" Zhang Y J, Huang Y D, Wang L *Solid State Ionics* 177 (2006) 65-71.

[18] "The Quantitative analysis of surfaces by XPS: a review" Seah M P *Surface and Interface Analysis* 2 (2004) 222-239.

[19] "PEM Fuel Cell Electrodes" Litster S, McLean G *Journal of Power Sources* 130 (2004) 61-76.

[20] "Contact Angle, Wetting, and Adhesion: a critical review" Good R J *Journal of Adhesion Science and Technology* 6 (1992) 1269-1302.

[21] "Solid polymer electrolyte membranes for fuel cell applications - a review" Smitha B, Sridhar S, Kahn A A *Journal of Membrane Science* 259 (2005) 10-26.

[22] "Dynamic mechanical analyses of polymeric systems of pharmaceutical and biomedical significance" Jones D S *International Journal of Pharmaceutics* 179 (1999) 167-178.

[23] "Preparation and properties of PEG hydrogel from PEG macromonomer with sulfonate end group" Kim J H, Kim J G, Kim D, Kim Y H *Journal of Applied Polymer Science* 96 (2005) 56–61.

[24] "Highly stable proton conducting nanocomposite polymer electrolyte membrane (PEM) prepared by pore modifications: an extremely low methanol permeable PEM" Tripathi B P, Kumar M, Shahi V K *Journal of Membrane Science* 327 (2009) 145–154.

---

[25] “Nafion-based composite polymer electrolyte membranes” Nouel K M, Fedkiw P S *Electrochimica Acta* 43 (1998) 2381-2387.

[26] “Key Requirements of micro fuel cell systems for portable electronics” Chenggang X, Jeanne P , Hallmark J, Bostaph J, Fisher A *Energy Conversion Engineering Conference, 2002* (2004) 603-606.

[27] “Effect of Chemical Structure and Crosslinking Density on the Thermo-mechanical Properties and toughness of meth(actylate) shape memory polymer networks” Safranski D L, Gall K *Polymer* 49 (2008) 4446-4455.

[28] “Microfluidic Device with Integrated Porous Membrane for Cell Sorting and Seperation” Wei H, in “Studying Cell Metabolism and Cell Interactions Using Microfluidic Devices Coupled with Mass Spectrometry” 2013, Springer-Verlag Berlin Heidelberg.

Chapter 4[*]

Materials in Microfluidic Fuel Cells: Oxygen Transport in Microfluidic Devices

> "Oxygen, as you well know, is my hero as well as my foe, and being not only strong but inexhaustible in strategies and full of tricks, I was obliged to call up all my forces to lay hold of him, and make the subtle being my prisoner."
>
> ***Christian Friedrich Schönbein, 1899***

4.0 Introduction

As described in Chapter 2, small size scale grants microfluidic devices many beneficial properties. One of the most underappreciated benefits of a microfluidic architecture is the ability to passively exchange gas through the device with the external environment. Microfluidic devices are able to accomplish this as their geometry is typically both planar and thin. With such an architecture, there is a large surface area for passive gas exchange of compounds both into and out of a device. Through proper engineering, device surfaces composed of polymers can be tailored to achieve specific levels of gas exchange. Passive gas exchange of oxygen has been leveraged previously in the literature for several types of microfluidic devices including microfluidic cell culturing bioreactors (where oxygen is essential for cellular respiration) and microfluidic fuel cells (where oxygen is consumed at air breathing cathodes) [1,2,3]. Passive gas flow allows for simplified device design (complicated control mechanisms are not required) and operation (additional interconnects for providing oxygen are not needed). However, there have remained unaddressed questions regarding the relationship between the material properties of polymeric layers and the concentrations of dissolved gases in actively flowing microfluidic devices. In this chapter, finite element modelling (FEM) is used to simulate the effect of varying capping layer composition (*i.e.* the type of polymer) and geometry on the resultant dissolved gas concentration profile in microfluidic devices. Specifically, simulations were applied to two types of microfluidic devices, a microfluidic cell culturing bioreactor and an air breathing microfluidic fuel cell (ABMFC).

---

[*] Sections 4.2 and 4.3 were reproduced in part from previously published material from "Finite element analysis of oxygen transport in microfluidic cell culture devices with varying channel architectures, perfusion rates, and materials" Zahorodny-Burke M, Nearingburg B, Elias A L *Chemical Engineering Science* 66 (2011) 6244-6253.

4.1 Overview and Motivations

Many types of microfluidic devices rely upon the consumption of dissolved gasses. One of the most important gases to device operation, and the subject of these investigations, is oxygen [4,5]. In this chapter, the ability for oxygen to be passively supplied from the external surroundings through a polymer capping layer was modelled for two types of microfluidic devices. In both models, oxygen was supplied through a polymer capping layer at the top of the microchannel. Firstly, a microfluidic cell culturing bioreactor was simulated where oxygen consuming cells were clustered in a uniform layer on the base of a microfluidic channel (as shown in Figure 4.1). Secondly, planar ABMFCs were simulated in an analogous geometry with oxygen-consuming electrodes deposited on the bottom of rectangular microchannels. As described in Section 2.3.1, in ABMFCs oxygen serves as a terminal electron acceptor (reacting with electrons and ions produced by the anode half-cell reaction) to yield a complete electrochemical reaction. Without a sufficiently high concentration of dissolved oxygen, the output of the fuel cell will be limited by cathodic current production. This will occur regardless of the reaction conditions in the anode half-cell. Here simulations were used as a predictive tool and evaluated MFC device operation in terms of maximum steady state sustainable output current. FEM modelling was shown to be an effective tool for predicting the levels of dissolved oxygen permeability in both types of devices.

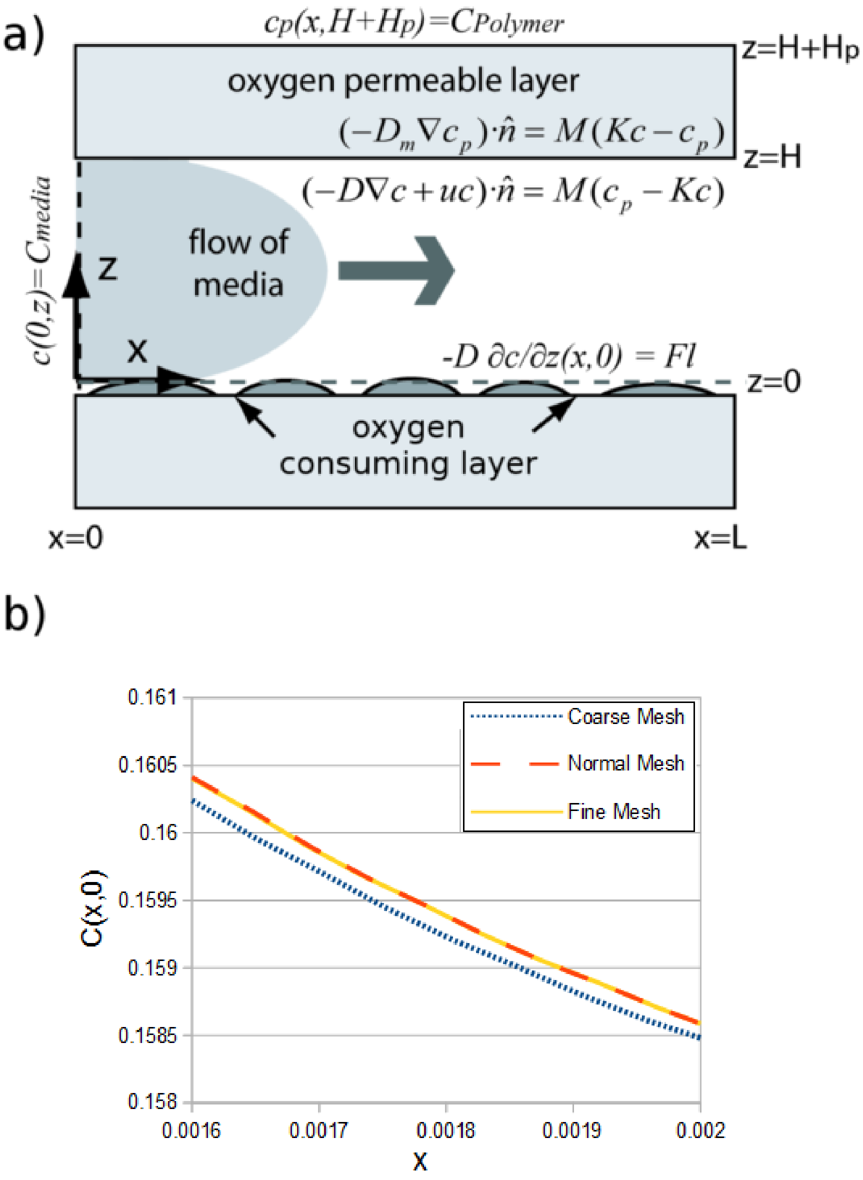

Figure 4.1 a) Schematic diagram of a cross section of the simulated microchannel structure used in the FEM model. Relevant boundary conditions are included in italics as well as equations for both diffusion and convection of oxygen within the microchannel and oxygen permeable capping layer. The parabolic velocity profile applied in model is schematically shown in grey. In both cell culture bioreactor and ABMFC simulations the lower (channel/substrate) interface was taken as a uniform infinitely thin oxygen consuming layer (depicted as cells). Copyright © 2011 Elsevier. Used with permission. b) Curve showing the oxygen concentration at the base of the microchannel as a function of position for varying built in mesh sizes. Figure is based on a FEM simulated geometry consisting of a 100 µm tall microchannel with a 1900 µm thick PDMS capping layer flowing 10^{-4} m/s of fluid.

4.2 Oxygen Diffusion in Microfluidic Devices

Within a microfluidic channel, the availability of oxygen is dependent on many factors including the channel architecture (length, width, and depth), the applied flow rate (how much media is flowed over cells), the material properties of the device (how permeable are the external device surfaces to oxygen), and the rate of consumption of oxygen within the channel (e.g. by cells or by chemical reactions). In the literature, there have been previous numerical studies of oxygen transport in microfluidic cell culture devices [6,7,8,9,10,11]; to my knowledge, no such studies have been undertaken for planar ABMFCs. Previous simulations of oxygen permeability in microfluidic channels have assumed that the upper (permeable) polymer capping layer remained saturated with oxygen at all times (*i.e.* oxygen concentration was set to a fixed value). In this investigation, oxygen concentration was variable throughout the capping layer and microchannel. This model included contributions of oxygen transport from both convection (*i.e.* oxygen supplied from the media flowing through the microchannel) and diffusion (*i.e.* oxygen flowing through the capping layer into the microchannel). Equations were solved via finite element modelling (FEM) in rectangular microchannels. A stiff-spring boundary condition was applied at the polymer capping layer/fluid interface allowing for realistic modelling of oxygen transport through the capping layer.

4.2.1 Finite Element Modelling of Diffusion

As described in Section 2.4, FEM is a numerical technique which allows for solving of complex coupled equations through discretization of a geometry into many smaller regions (also known as elements). Equations are solved within each element and then related to surrounding elements through properly applied boundary conditions. Through iterative calculations, physically accurate solutions can be obtained. This investigation used COMSOL, a commercial FEM software package, to solve for oxygen concentration at points across the microchannel and capping layer. Cell culture bioreactors were modelled using COMSOL 3.5a, while more recent ABMFC simulations were solved using COMSOL 4.2a. All simulations used mass transfer equations from the ‘Chemical and Reaction Engineering Module’ which included contributions from both convection and diffusion. Simulations were solved in two dimensional geometries taken to be in a plane in the middle of the microchannel width. Convection was evaluated by applying a specific flow rate of media with a known initial concentration of oxygen to the inlet of the microchannel. Diffusive contributions were included by solving Fick’s Law, as described below. The polymer capping layer/microchannel interface was modelled using a stiff-spring boundary condition. All simulations were solved for steady state conditions using the UMFPACK equation solver package.

My analysis was conducted using a device geometry which consisted of two rectangular regions, an upper polymeric oxygen permeable capping layer and a lower fluid-filled microchannel. Channel geometries were modelled using triangular elements generated by COMSOL. Bioreactor simulations used a predefined ‘fine’ mesh size while ABMFC simulations involved higher fluid flow and oxygen consumption rates and as such required a more precise predefined ‘extremely fine’ mesh. The number of mesh elements for each model varied with the simulated geometry (*i.e.* dimensions of the microchannel and capping layer regions). Mesh size was chosen such that additional refinement (*i.e.* further subdividing the mesh to yield more elements) did not alter the solution as shown in Figure 4.1b. In all simulations, oxygen concentration was evaluated by solving two mass balance equations:

$$\nabla \cdot (-D_{media} \nabla c + uc) = 0 \tag{4.1}$$

$$\nabla \cdot (-D_{polymer} \nabla c_p) = 0 \tag{4.2}$$

Equations 4.1 and 4.2 describe the concentration of oxygen in the fluid-filled microchannel (c) and polymer capping layer (c_p), respectively. D_{media} and $D_{polymer}$ refer to the diffusivity of oxygen in the fluid and polymer, respectively. u denotes the applied velocity in the microchannel flowing from left to right. Oxygen within the microchannel (Equation 4.1) was transported by both convection and diffusion, while in the capping layer (Equation 4.2) transport was taken to be purely diffusive. In this model, there was a difference in oxygen solubility between the fluid and capping layer which resulted in a non-physical concentration mismatch across the interface. Consequently, a stiff-spring boundary condition was applied to maintain concentration continuity across the interface. Previous work in the literature has applied stiff-spring techniques to model transfer of dissolved compounds across interfaces and has showed that they represent good approximations of physical interfaces [12,13,14]. Specifically, the boundary condition at the interface was given as:

$$(-D\nabla c+uc)\cdot\hat{n}=M(c_p-Kc) \tag{4.3}$$

$$(-D_m\nabla c_p)\cdot\hat{n}=M(Kc-c_p) \tag{4.4}$$

In these equations, *M* was the stiff spring velocity, a term which describes the resistance to transport between microchannel (Equation 4.3) and capping layer (Equation 4.4) regions. K_c was the ratio between the oxygen solubility in the two regions and was defined as $K_c=C_{polymer}/C_{media}$. These equations allowed for realistic coupling between the two regions which are independently evaluated by the model. Additional boundary conditions applied to the model were:

$$c(0,z)=C_{media} \quad (0\le z\le H) \tag{4.5}$$

$$c_p(x,H_p+H)=C_{polymer} \quad (0\le x\le L) \tag{4.6}$$

$$-D\cdot\partial c/dz(x,0)=Fl \quad (0\le x\le L) \tag{4.7}$$

Fluid flowing into the microchannel was taken to be saturated with oxygen. As such, the concentration at the microchannel inlet (*x*=0) was set to the maximum solubility of the fluid (Equation 4.5). The concentration of oxygen at the top of the capping layer (at $H=H_p$, the interface with the external atmosphere) was also assumed to be saturated (Equation 4.6). Oxygen consumption at the base of the microchannel (either due to cellular respiration or cathodic reactions) was described by Equation 4.7 with a uniform downward flux, *Fl*, drawing oxygen out of the microchannel. In cell culture devices, this flux corresponds to the consumption of oxygen by cells, while in ABFMCs the flux corresponds to the consumption of oxygen to generate cathodic current. Two different types of applied velocity profiles across the height of the microchannel were evaluated. The first profile, (Equation 4.8) set a uniform fluid velocity through all points in the microchannel. The second profile, (Equation 4.9) incorporated a parabolic velocity profile. As described in Section 2.1**,** a parabolic velocity profile is a consequence of pressure driven pumping within microfluidic channels. Parabolic flow is a more physically relevant flow profile than uniform flow for pressure driven systems. Differences in predicted oxygen concentrations between both flow profiles were evaluated by the model.

$$u_{(z)}=u_{av}\,,\,u_{(0)}=u_{(H)}=0 \tag{4.8}$$

$$u(z)=6\mathrm{u}_{av}\frac{z}{H}(1-\frac{z}{H}) \tag{4.9}$$

In both equations, u_{av} was the average velocity in the microchannel. Both velocity profiles incorporated no-slip boundary conditions (u=0) at the top and bottom of the microchannel. For ABMFC simulations, only parabolic flow profiles were used.

4.2.2 Analytical Solution of Diffusion

Experimental and theoretical validation is crucial for any modelling process. In this investigation, the numerical FEM model was compared to an analytical solution for oxygen concentration described in literature by Tilles *et al.* (2001) [11]. In their work, Tilles *et al.* solved the steady state dimensionless mass balance equation (Equation 4.10)

$$\frac{\partial C}{\partial x}=\frac{\gamma}{Pe}\frac{\partial C^2}{\partial y^2} \tag{4.10}$$

where *Pe* was the Peclet number (given by *uH/D* defined in Section 2.2), and γ was given by *γ=L/H* (the ratio of the length of the channel over its height).

$$C(x,0)=C_g-Da-\frac{Da}{Sh}+\sum_{n=1}^{\infty}B_n\exp\left[-\frac{\gamma\lambda_n^2x}{Pe}\right] \tag{4.11}$$

Their solution was presented with coefficients B_n specified as:

$$B_n = \frac{4Da(1-\cos(\lambda_n)+4\lambda_n\sin(\lambda_n)(1-C_g+(Da/Sh))}{\lambda_n\sin(2\lambda_n)2\lambda_n^2} \quad (4.12)$$

In Equation 4.11, $C(x,0)$ was defined as the oxygen concentration at position x within the fluid along the top of the microchannel. C_g was defined as the saturation concentration of oxygen in the atmosphere surrounding the device normalized to the inlet concentration in the fluid (i.e. C_{air}/C_{media} with both at saturation). At the inlet of the microchannel, $C(0,0)$, concentration was set to 1. In Equation 4.12, *Da* and *Sh* were the Damkholer and Sherwood numbers, respectively and were defined by two ratios: *Da,* by the ratio of the reaction rate and convective mass transport rate and *Sh*, by the ratio of convective mass transport and diffusive mass transport. λ_n was defined as the n'th roots of the transcendental equation $\tan(\lambda_n)=Sh/\lambda_n$. In this investigation, the mass transfer coefficient was set to σ=1 cm/s based upon the work of Shiku *et al.* (2006) [15]. Solutions to Equations 4.11 and 4.12 were evaluated using Mathematica V.6. The transcendental equation describing λ_n was solved for the first 16 coefficients. Results of the analytical solution were compared to the FEM model in the next section.

4.3 Oxygen Utilization in Cell Culture Devices

In my model, a small thin layer of cells with density α was taken to be uniformly distributed on the surface of a microchannel of length *L* and height *H*. It was assumed that cells consumed oxygen at a constant rate which in this work was represented by a flux through the bottom surface of the microchannel *Fl*. The flux of oxygen leaving the microchannel was based on a zero-order consumption rate assumption used previously in literature [6,11]. The microchannel had a glass substrate (set to be impermeable to oxygen with zero flux to the surroundings) as well as an oxygen permeable capping layer of thickness H_p. The values of all parameters used in the cell culturing device simulations are given in Table 4.1.

Table 4.1 Values used to construct the cell culturing device FEM simulation.

Parameter	Value [Reference]	Description
M	1×10^3 m/s	Stiff Spring Velocity
D_{media}	2.5×10^{-5} cm^2/s [16]	Diffusion Coefficient, Oxygen In Media
D_{PDMS}	3.4×10^{-5} cm^2/s [17]	Diffusion Coefficient, Oxygen In PDMS
D_{COC}	4.6×10^{-8} cm^2/s [7]	Diffusion Coefficient, Oxygen In COC
D_{PMMA}	6.04×10^{-8} cm^2/s [7]	Diffusion Coefficient, Oxygen In PMMA
C_{media}	0.2 mol/m^3 [18]	Saturation Concentration of Oxygen In Media
C_{PDMS}	1.69 mol/m^3 [17]	Saturation Concentration of Oxygen In PDMS
C_{COC}	1.125 mol/m^3 [19]	Saturation Concentration of Oxygen In COC
C_{PMMA}	1.594 mol/m^3 [20]	Saturation Concentration of Oxygen In PMMA
K_{cPDMS}	8.45	Partition Coefficient PDMS/media
K_{cCOC}	5.625	Partition Coefficient COC/media
K_{cPMMA}	7.97	Partition Coefficient PMMA/media
V_{max}	0.38 nmol/s [11]	Maximum Consumption Rate of 10^6 Rat Hepatocyte Cells
α	1.1×10^5 cm^{-2} [11]	Density Of Cells At Bottom of Channel
Fl	4.18×10^{-7} mol/m^2s [11]	Flux At Bottom Of Channel Due To Cell Consumption
L	15 mm	Length Of Channel

The validity of the FEM model was evaluated by comparing the oxygen transport behavior predicted by the model to prior studies in the literature. Specifically, the analytical solution determined by Tilles *et al.* described in Section 4.2.2. Their study used 100 µm deep (H=100 µm) microchannels with 4.125×10^5 rat hepatocytes distributed uniformly on the bottom surface [11]. Figure 4.2 compares the oxygen concentration predicted at the bottom of the microchannel for the analytical solution and this FEM model at three different average fluid velocities (10^{-2}, 10^{-4}, and 10^{-6} m/s) as well as two different PDMS capping layer thicknesses (25 µm and 1.9 mm). Results for both constant and parabolic flow profiles were included.

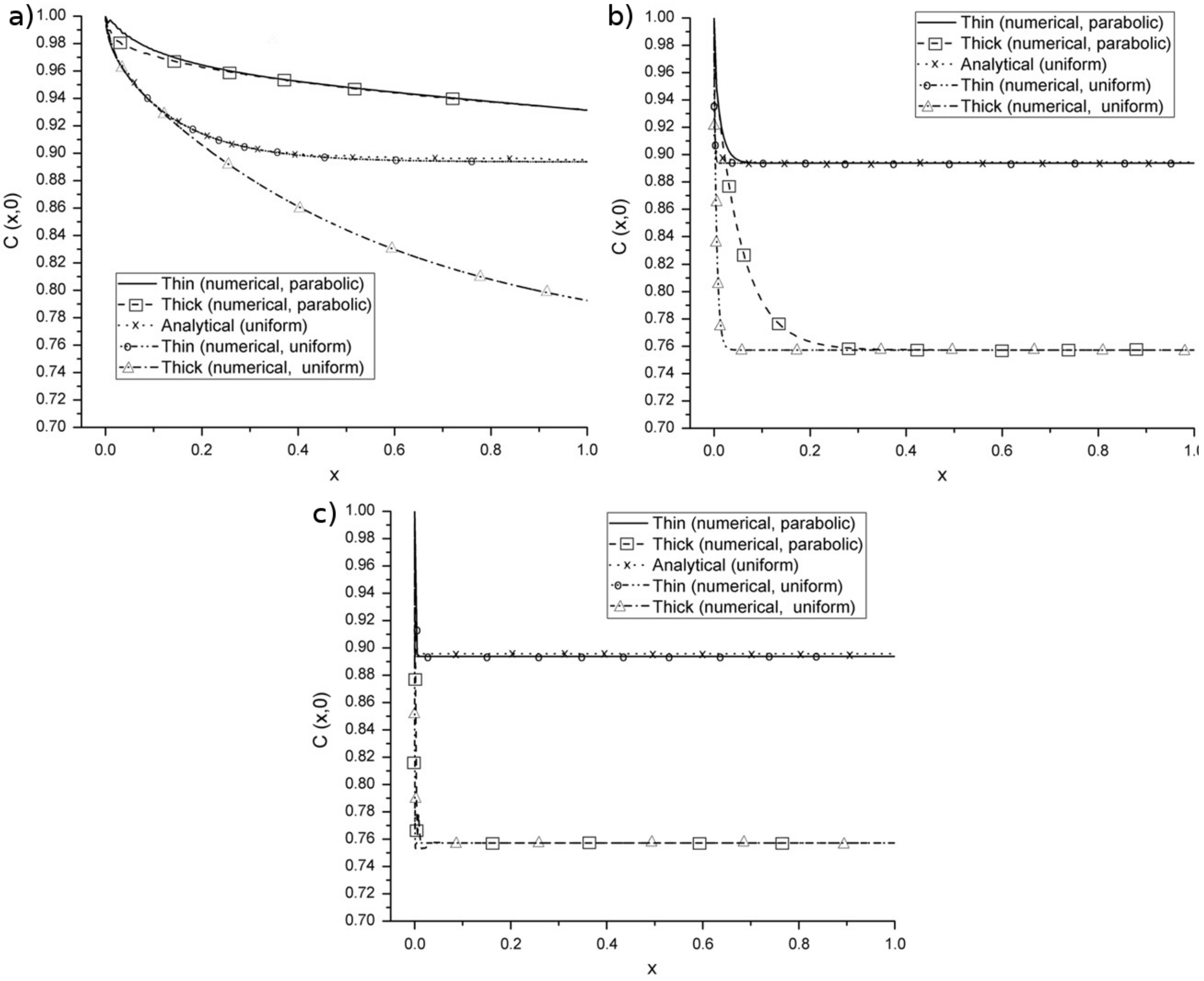

Figure 4.2 Dimensionless oxygen availability along the bottom of the microchannel at (a) $u_{av}=10^{-2}$ m/s (b) 10^{-4} m/s and (c) 10^{-6} m/s. The y-axis shows oxygen concentration normalized to the saturation value of oxygen in the media. The x-axis shows length along the microchannel normalized to microchannel length. For each u_{av} several solutions were evaluated: an analytical solution, a numerical solution based on uniform flow velocity, and a numerical solution with a parabolic flow velocity profile. For both numerical solutions thin (25 µm) and thick (1.9 mm) oxygen permeable layers are shown. Figure Copyright © 2011 Elsevier. Used with permission.

As shown in Figure 4.2, for each combination of flow rate, analytical and FEM simulated oxygen concentration profiles for thin (25 µm) capping layers converged to a constant value. This demonstrated that when the same input parameters are applied the two methods yield similar predictions for oxygen concentrations and showed the validity of the model. For thicker capping layers, the two solutions were found to vary considerably. This discrepancy was justified by considering that the analytical solution assumed a uniformly saturated polymer capping layer. In the FEM model, the oxygen concentration within the capping layer was explicitly calculated and took into account the finite rate of mass transfer possible from the external atmosphere into the device. For thinner capping layers, this effect would be less significant as the capping layer was a less effective barrier between the microchannel and the external environment. The differences between this simulation and the analytical results suggested that oxygen concentration within the capping layer can indeed have a large effect on the resultant concentration within a flowing fluid.

The FEM results shown here demonstrated that at low flow rates (10^{-6} m/s) simulations predicted a gradient in oxygen concentration at the start of the microchannel which eventually converged to a constant value (0.76 and 0.89 for thin and thick capping layers, respectively). The shape of the oxygen concentration profile was explained by considering the relative importance of the main two mechanisms of oxygen transport, diffusion, and convection. Near the inlet of the microchannel, cells were able to consume oxygen primarily from the saturated media. In the middle region of the microchannel, media became oxygen depleted and mass transport from diffusion became significant. By the end of the microchannel, diffusion was the sole means of oxygen mass transport and the concentration converged to a steady value. As flow rate increased, the steady state amount of oxygen supplied by the fluid increased and the effect of diffusion from the capping layer becomes less significant. This effect manifested itself in the changing shape of the oxygen concentration profile across the length of the microchannel. Diffusion dominated transport (as shown in Figure 4.2c) resulted in a flat concentration vs length profile (as both the consumption and supply of oxygen were occurring at steady state from a large reservoir). Convection dominated processes (as shown in Figure 4.2a) relied upon an inflowing flux of oxygen saturated media that became depleted (*i.e*. decreasing in magnitude) along the microchannel length resulting in curved concentration vs length profiles.

These results were in agreement with experimental evidence in literature where oxygen concentration in a microchannel has been measured at varying flow rates [21,22]. For example, in a study by Allen and Bhatia they found that for oxygen transport in a polycarbonate bioreactor, convection and diffusion were the dominant transport mechanisms for high and low flow rates, respectively [6]. For many biological applications, there are benefits to a gradient in oxygen concentration across the length of a device [23,24,25]. For these studies, initial FEM simulations suggested that FEM would be a valuable tool for determining the oxygen concentration gradient and guiding an appropriate choice of flow rates and microchannel architecture.

4.3.1 Oxygen Concentration Gradients within Capping Layers

The most important aspect of my FEM model was the explicit calculation of oxygen concentrations within the polymer capping layer. In the previous section, allowing for variable oxygen concentration within the capping layer displayed a large effect on the resultant oxygen concentration available at the base of the microchannel. In this section, further focus was placed upon the capping layer and evaluated the oxygen concentration in the capping layer at low flow rates (10^{-6} m/s) for thick (1.9 mm) and thin (25 µm) PDMS membranes shown in Figure 4.3.

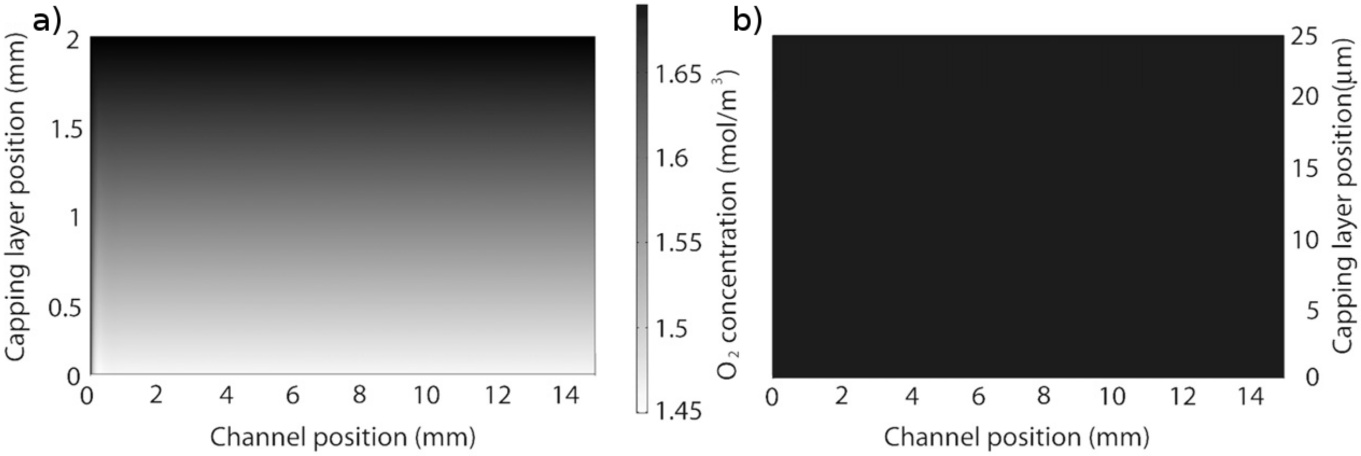

Figure 4.3 Oxygen concentration within a PDMS capping layer for a FEM simulation with low 10^{-6} m/s flow. Two different PDMS capping layer thicknesses are shown a) 1.9 mm and b) 25 µm. Copyright © 2011 Elsevier. Used with permission.

Figure 4.3a shows that for thick membranes simulations predicted a significant change in oxygen concentration from the upper surface, exposed to the external atmosphere, of 1.69 mol/m^3 (the saturation concentration of oxygen in PDMS) and the lower surface, exposed to the microchannel, of 1.45 mol/m^3. Further calculations (not presented) determined at a PDMS capping layer thickness of ~1 cm oxygen concentration was insufficient to allow for cell proliferation (*i.e.* oxygen concentration in the plane of the cells was below sustainable levels). Simulations predicted that thin membranes, as shown in Figure 4.3b, allowed for all points within the membrane to be at saturation. These results were significant as they establish limits for acceptable device geometry in terms of capping layer thickness which must be observed for effective cell growth.

4.3.2 Effect of Device Geometry on Oxygen Concentration

For cell culture bioreactors simulated in this investigation, the key geometric parameters are the capping layer thickness (H_p) and channel depth (H). Figure 4.3 showed that further away from the interface with the external atmosphere oxygen concentration within the capping layer decreases. Consequently, the thickness of the capping layer determines the amount of oxygen available to move into the microchannel through diffusion. The importance of this effect was simulated by modelling PDMS capping layers with thicknesses between 25 µm and 1900 µm. All simulations were evaluated at 10^{-6} m/s inflow rate with steady state oxygen concentration at the bottom of the microchannel shown in Figure 4.4.

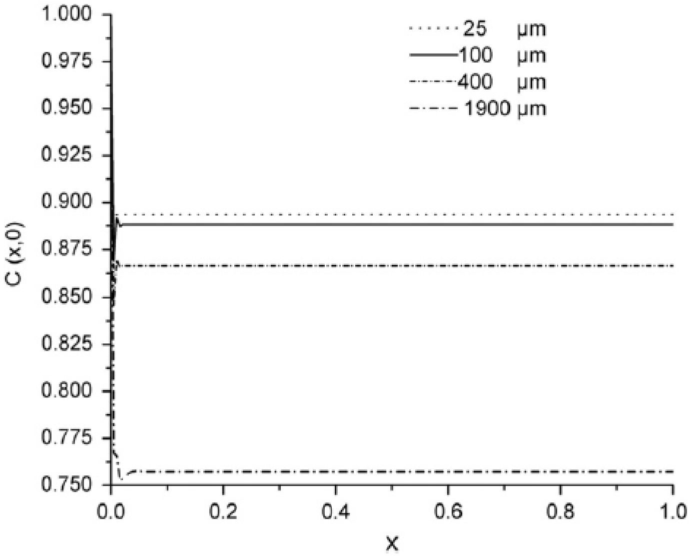

Figure 4.4 Effect of PDMS capping layer thickness on steady state oxygen concentration at the bottom of the microchannel (in the plane of the cells), for media flowing at 10^{-6}m/s. Copyright © 2011 Elsevier. Used with permission.

It was found that for thin PDMS layers (less than 100 µm) there were only small variations in available oxygen. This was a beneficial result as during the course of microfluidic device fabrication small (micron scale) variations in PDMS thickness can be introduced due to improper alignment, or bonding. Simulations predicted that variations on this scale will not lead to large changes in oxygen concentration profiles. For thicker capping layers (400 µm and 1900 µm) simulated oxygen concentrations deviated significantly with increasing thickness. This was another important result as even for a highly permeable material such as PDMS, thick membrane layers can hinder oxygen transport.

Another important parameter of microfluidic device design is channel thickness (described in this model by *H*). Oxygen concentration profiles were simulated for four channel heights (25 µm, 50 µm, 75 µm, and 100 µm) for 1.9 mm thick PDMS capping layers and 10^{-6} m/s inflow rate shown in Figure 4.5.

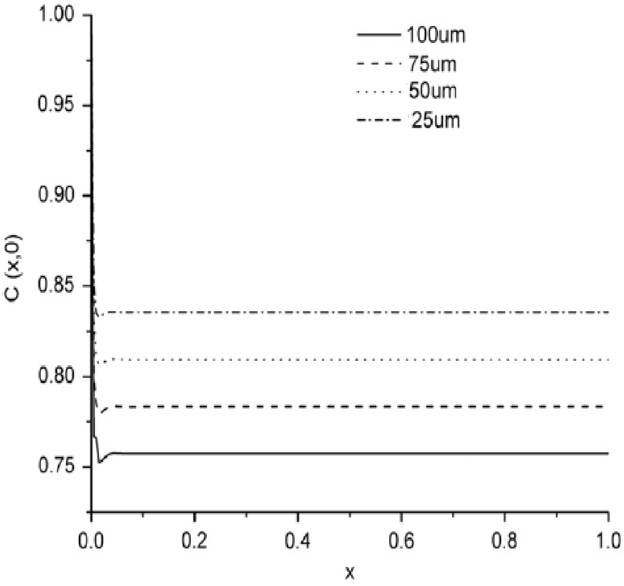

Figure 4.5 Effect of microchannel height (*H*) on steady state oxygen concentration at the bottom of the microchannel (in the plane of the cells). The microchannel was simulated with a 1.9 mm PDMS capping layer with media flowing at 10^{-6}m/s. Copyright © 2011 Elsevier. Used with permission.

Oxygen concentration at the base of the microchannel was found to be more strongly affected by channel thickness than capping layer thickness. When channel thickness was varied from 25 µm to 100 µm oxygen concentration at the microchannel base dropped by near 9%. These results were contrary to my initial expectations which assumed that for larger channels more oxygen would be available through convection from the fluid. At low flow rate (10^{-6} m/s) regimens common to cell culturing devices, simulations demonstrated diffusion through the capping layer as the dominant mass transport mechanism. Simulation results for both capping layer thickness and channel height have highlighted that both parameters are of integral importance in controlling the concentration of oxygen in a microfluidic bioreactor. When designing a microfluidic bioreactor the values of both H and H_p have been shown to be important to yield favourable levels of oxygen transport.

4.3.3 Effect of Varying Capping Layer Composition on Oxygen Concentration

To this point, simulations have used PDMS as a capping layer material. While PDMS is widely used in microfluidic fabrication there are applications which are better suited to other materials. Here we applied my established FEM model to simulate microfluidic devices composed of two other microfluidic capping layer materials PMMA, and COC. PMMA and COC were introduced in Section 2.3, as alternative materials for microfluidic fuel cell device fabrication. Both materials have also have seen usage in microfluidic bioreactors and other types of microfluidic devices [[26,27]]. PMMA and COC are amenable to high-throughput, low cost fabrication by processes such as injection moulding or hot embossing [[28,29]].

Both PMMA and COC possess oxygen solubility values that are similar to PDMS (with specific values given in Table 4.1). However, these materials both have considerably smaller oxygen diffusivities than PDMS (on the order of 1000 times smaller). Smaller diffusivity values mean that it is more difficult for oxygen to travel through PMMA and COC surfaces compared to PDMS. I predicted there would be less oxygen available at the base of PMMA and COC microchannels compared to PDMS. This hypothesis was confirmed by FEM simulations shown in Figure 4.6 where oxygen concentration at the base of the microchannel was plotted for 1.9 mm thick PMMA and COC films at three different flow rate regimes. At each of the measured flow rates, capping layers of PMMA and COC displayed identical oxygen concentration profiles. At high flow rates (10^{-2} m/s) simulations predicted virtually constant oxygen concentration across the length of the microchannel. Medium flow rates (10^{-4} m/s) yielded a linearly decaying oxygen concentration moving down the length of the microchannel with zero concentration reached at x=3. At the lowest flow rate (10^{-6} m/s) oxygen concentration reached zero immediately after the channel inlet. Further simulations (not presented) used the same method and evaluated the effect of thinner PMMA and COC capping layers of 100 µm and 25 µm. Thinner PMMA and COC capping layers displayed identical concentration profiles to those shown in Figure 4.6. These results demonstrated that for low diffusivity materials the oxygen concentration profile was dominated by convective transport from fluid flow. Based upon these results, microfluidic cell culturing devices requiring high concentrations of oxygen composed entirely of low diffusivity materials such as PMMA or COC have additional constraints placed upon their architecture. Device design must account for the importance of convective oxygen mass transport and not rely on oxygen diffusion through the capping layer to maintain a stable cell culture. Mass transport could be increased through several methods including using high flow rates of oxygen saturated fluid, or using small channel dimensions (*i.e.* small enough that non-zero concentrations of oxygen are present throughout the channel length).

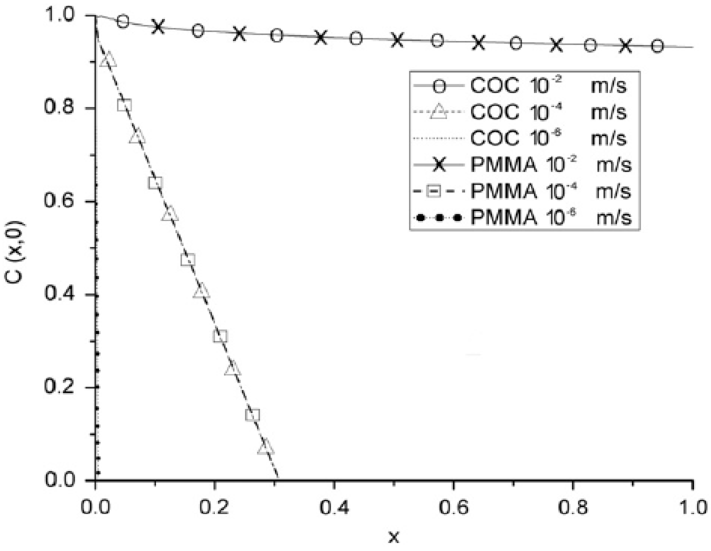

Figure 4.6 Simulated oxygen concentration at the bottom of the microchannel for COC and PMMA capping layers of 1.9 mm thickness at flow rates of 10^{-2}, 10^{-4}, and 10^{-6} m/s. Both polymers have virtually identical concentration profiles at each corresponding flow rate. Copyright © 2011 Elsevier. Used with permission.

4.4 Oxygen Utilization in Microfluidic Fuel Cells

The developed modelling method for oxygen transport within microfluidic bioreactors can be applied to other analogous microfluidic device architectures where oxygen is consumed. In this section, the FEM model was used to simulate oxygen consumption in a planar ABMFC architecture. ABMFCs are fuel cell devices where oxygen is used as a terminal electron acceptor in the cathode half-cell. In order for current to flow from the ABMFC through an external circuit, there must be sufficient oxygen present at the cathode surface to sustain current production. This is true regardless of the reaction conditions in the anode half-cell. Hence, without sufficiently high levels of oxygen at the cathode the fuel cell will be limited terms of output current. In this way, knowledge of the amount of oxygen available at the cathode surface at operating conditions is important to an optimized device design. Typically, microscaled ABMFC devices have been designed in a stacked configuration incorporating a porous cathode gas diffusion electrode (as was described in Section 2.3). Gas diffusion electrodes (often combined with proton exchange membranes as membrane-electrode-assemblies) can be costly and complicated to integrate into microfluidic devices [30]. In this study, the described FEM model was used to simulate oxygen concentration profiles in a planar rectangular microchannel alkaline direct methanol ABMFC device with a bottom electrode and porous upper capping layer. Specifically, the FEM model was used to determine the amount of steady state cathodic current which could be sustained by planar ABMFCs at a variety of operating conditions.

The amount of oxygen consumption in physical ABMFCs can be known precisely by measuring the cathode half-cell potential through cyclic voltammetry and hence determining cathodic current. For alkaline direct methanol fuel cells the cathode half-cell reaction is given by Equation 4.13 where oxygen accepts electrons from the anode half-cell to produce hydroxide ions.

$$\left. 3 \middle/ 2 \right. O_2 + 3\mathrm{H}_2O + 6e^- \rightarrow 6\mathrm{OH}^- \qquad \textbf{(4.13)}$$

As a result of Equation 4.13 for every 6 moles of electrons consumed by the cathode as current, 3/2 moles of O_2 were consumed. Using this relationship combined with Faraday's constant yields Equation 4.14, which relates output current density (*i*) to the rate of oxygen consumption Fl_{O2}.

$$Fl_{O2} = Fl_{e-} \times \left(\frac{3/2}{6}\right) \frac{mol_{O2}}{mol_{e-}} = \frac{i}{4\mathrm{F}} \left[\frac{mol_{e-}}{sm^2}\right] \quad \mathbf{(4.14)}$$

In this simulation, cathode electrodes were deposited on the bottom surface of the two dimensional microchannel and current was assumed to be produced uniformly across the electrode. Simulations considered only the amount of oxygen transported in the cathode half-cell from inflowing catholyte and oxygen diffusing through the top capping layer. ABMFC simulations used the same model as previously described for cell culture devices with modified flow rates, and rates of oxygen consumption. Values used for ABMFC simulations are given below in Table 4.2.

Table 4.2 Values used to construct the ABMFC FEM simulation.

Parameter	Value [Reference]	Description
M	1×10^3 m/s	Stiff Spring Velocity
D_{fluid}	2.5×10^{-5} cm^2/s	Diffusion Coefficient, Oxygen In Catholyte
D_{PDMS}	3.4×10^{-5} cm^2/s [17]	Diffusion Coefficient, Oxygen In PDMS
D_{COC}	4.6×10^{-8} cm^2/s [7]	Diffusion Coefficient, Oxygen In COC
D_{PMMA}	6.04×10^{-8} cm^2/s [7]	Diffusion Coefficient, Oxygen In PMMA
C_{media}	0.2 mol/m^3 [16]	Saturation Concentration of Oxygen In Catholyte
C_{PDMS}	1.69 mol/m^3 [17]	Saturation Concentration of Oxygen In PDMS
C_{COC}	1.125 mol/m^3 [19]	Saturation Concentration of Oxygen In COC
C_{PMMA}	1.594 mol/m^3 [20]	Saturation Concentration of Oxygen In PMMA
K_{cPDMS}	8.45	Partition Coefficient PDMS/Catholyte
K_{cCOC}	5.625	Partition Coefficient COC/Catholyte
K_{cPMMA}	7.97	Partition Coefficient PMMA/Catholyte
i	0.01 – 10 mA/cm^2 [31]	Cathodic Current Density Range
L	15 mm	Length Of Channel

Approximate values for channel thickness, applied flow rates, and output current density were based upon approximate values from literature [32]. ABMFCs and cell culturing bioreactors are analogous systems and the trends presented in Section 4.3 were also relevant to fuel cells. The major difference between ABMFC devices and the bioreactors discussed in the previous section was the magnitude of fluid flow and oxygen consumption. A typical hepatocyte cell culture device will flow between 10^{-5} and 10^{-6} m/s of media over a layer of cells consuming 10^{-7} mol/m^{2}s of oxygen. For MFC devices, output current densities vary on the order of 0.01 - 10 mA/cm^2 which correspond through Equation 4.14 to oxygen utilization rates of 10^{-6} -10^{-4} mol/m^{2}s, orders of magnitude higher than for bioreactors. MFC devices typically flow between 10^{-5} – 10^{-3} m/s of catholyte solution to sustain steady state output. These differences mean that for ABMFCs, high levels of oxygen mass transport are especially critical. Simulations assessed the effect of applied flow rate, capping layer composition, and capping layer thickness on sustainable levels of output cathodic current.

In this study, the FEM model was used to predict steady-state sustainable output cathodic current. This was based upon two assumptions: first, the output of the fuel cell is optimized when the entire cathode surface is producing current (*i.e.* through consumption of oxygen, the cathode surface is generating hydroxide ions which can diffuse to the anode half-cell and participate in anodic current generating reactions). Second, in order to produce steady-state current, each point on the electrode requires a non-zero steady-state concentration of oxygen. Based upon these assumptions sufficient sustainable cathodic output current was defined as a current value for which there is a non-zero concentration of oxygen at the electrode surface. At this state (assuming idealized reaction kinetics) an ABMFC architecture will be operating at peak cathode half-cell efficiency (*i.e.* overall current output from the device is then limited by current derived from fuel consumption at the anode half-cell). The two operational states simulated by the model with, insufficient oxygen concentration, and sufficient oxygen concentration at the cathode surface, are shown schematically in Figure 4.7. Oxygen utilization was simulated using a two dimensional fuel cell architecture with a cathode deposited on the bottom of a 15 mm long rectangular microchannel. Flow rates on the order of $8*10^{-4}$ and

$8*10^{-6}$ (corresponding to 1 -100 µL/min at the evaluated channel geometry) and are simulated for current densities varying from 0.01 - 10 mA/cm^2.

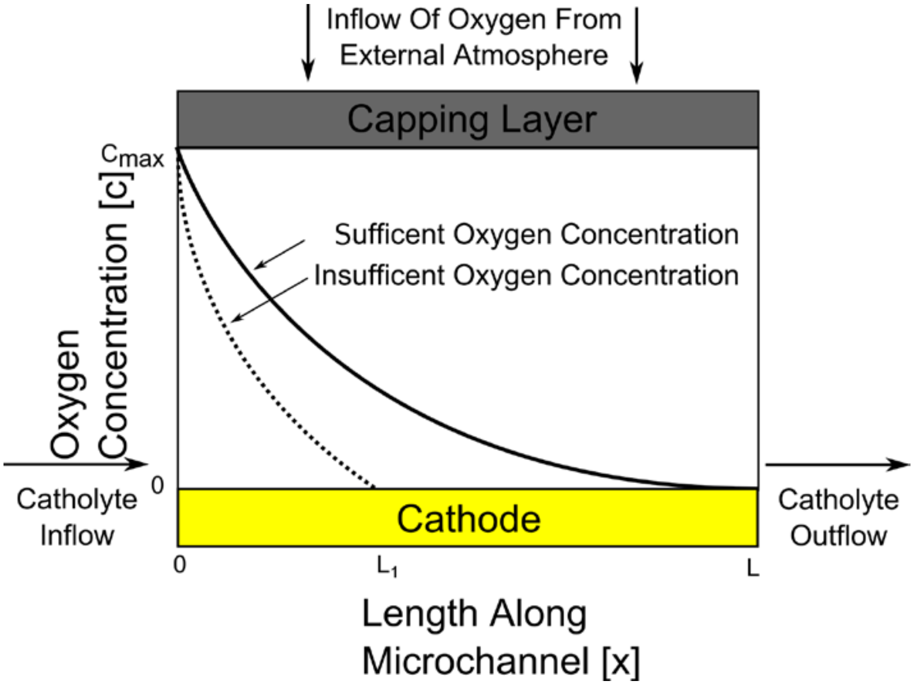

Figure 4.7 Schematic diagram of the planar ABMFC model geometry with characteristic oxygen concentration profiles at the cathode surface across the length of the microchannel superimposed. In the sufficient oxygen concentration state, there is a non-zero concentration of oxygen available at each point across the microchannel. For the insufficient oxygen state only a fraction of the microchannel (x=0 to x=L_1) is able to sustain current producing electrochemical reactions. Channel geometry has been exaggerated for clarity.

4.4.1 Sustainable Output Current Density

The amount of steady state cathodic current extractable from an ABMFC depends upon levels of available oxygen at the electrode surface. Figure 4.8 shows simulated oxygen concentration profiles across the height and length of a microchannel for four different magnitudes of cathodic current output. Devices were simulated with 100 µm deep microchannels and 100 µm thick PDMS capping layers flowing $8x10^{-4}$ m/s of aqueous catholyte solution. For the two larger current densities, (10^1 mA/cm^2 and 10^0 mA/cm^2) FEM simulations predicted zero oxygen concentration before reaching the electrode at the base of the microchannel. At this state, there is insufficient oxygen to generate cathodic current (and associated hydroxide ions through Equation 4.13) across the entire electrode surface and the device would not be operating at maximum efficiency. The two lower current densities (10^{-1} mA/cm^2 and 10^{-2} mA/cm^2) were predicted to yield excess oxygen present at the electrode interface. Oxygen concentrations significantly greater than zero across the length of the electrode describe an environment where additional cathodic current could be produced if supplied with sufficient electrons from the anode half-cell. Overall current output from a physical ABMFC device with excess oxygen at the cathode surface would be limited by consuming of fuel in the anode half-cell rather than consumption of oxygen in the cathode half-cell. Consequently, an ideal ABMFC device would match steady-state cathodic and anodic currents and aim for a small (non-zero) oxygen concentration across the length of the cathode. Excessively high levels of residual oxygen in the cathode could diffuse into the anode half-cell and produce parasitic (current consuming) side reactions for some ABMFC implementations. These simulations suggested that for this device architecture, the most efficient cathodic current density lies between 10^0 and 10^{-1} mA/cm^2.

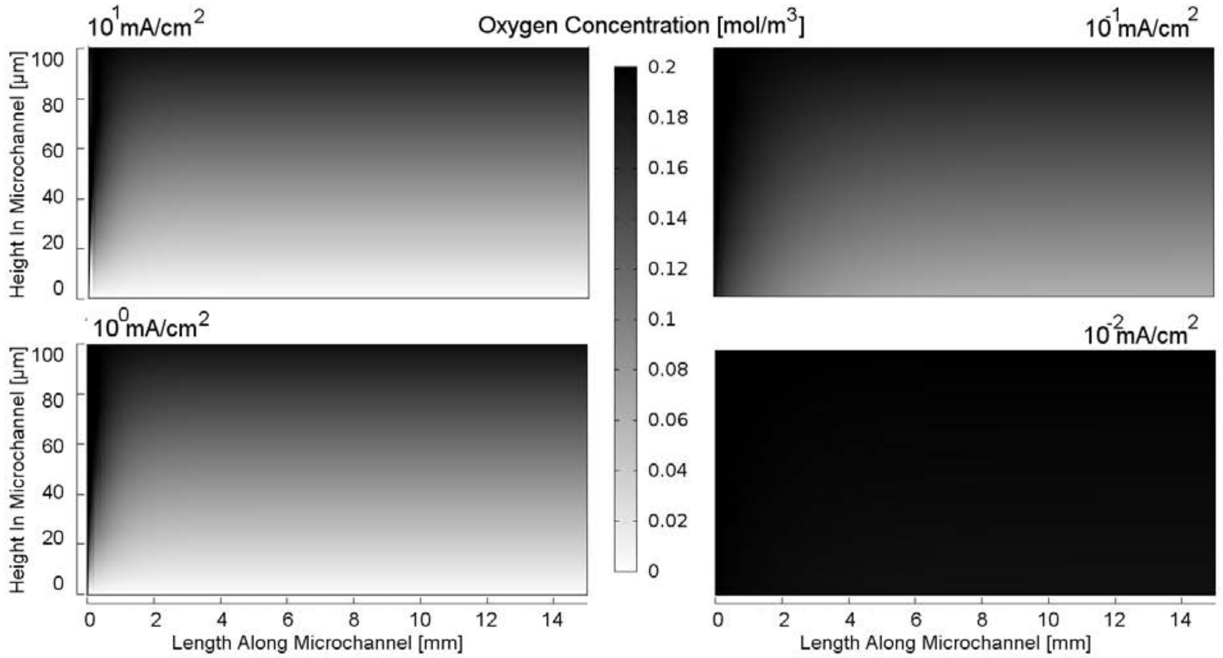

Figure 4.8 Oxygen concentration profiles inside microchannels for four different current densities. For 10^1 mA/cm^2 and 10^0 mA/cm^{2,} oxygen concentration was predicted to reach zero before the end of the microchannel length. This indicates that the max density that can be achieved is 10^{-1} mA/cm^2. All simulations were carried out with a 100 μm thick PDMS capping layer and flowing $8x10^{-4}$ m/s of aqueous catholyte solution saturated with oxygen.

4.4.2 Capping Layer Composition and Catholyte Flow Rate Variations on Oxygen Concentration

As was found in Section 4.3.3, the diffusive behavior of the capping layer plays an important role in the amount of oxygen which can be transported into a microfluidic channel. For ABMFC devices, simulations modelled oxygen concentration profiles for COC, PMMA, and PDMS capping layers. Capping layer thickness was varied between 100 μm and 1900 μm with results shown in Figure 4.9. For both capping layer thickness values, an output cathodic current of 0.1 mA/cm^2 was assumed. Simulations predicted, for 100 μm thick capping layers, COC was found to be insufficient to sustain output current while both PDMS and PMMA yielded acceptable steady state values across the channel length. For thicker (1900 μm) capping layers only PDMS was predicted to allow for sufficient oxygen transport to sustain current production. Based upon these simulations devices composed entirely of PMMA and COC are ill suited to ABMFC devices. Furthermore, regardless of the material used to form the microchannels (be it COC, PMMA, or other microfluidic polymers), a diffusion layer membrane with high oxygen diffusivity must be integrated to achieve high levels of current output. Later simulations in this section assumed a 100 µm thick PDMS membrane as the upper capping layer surface.

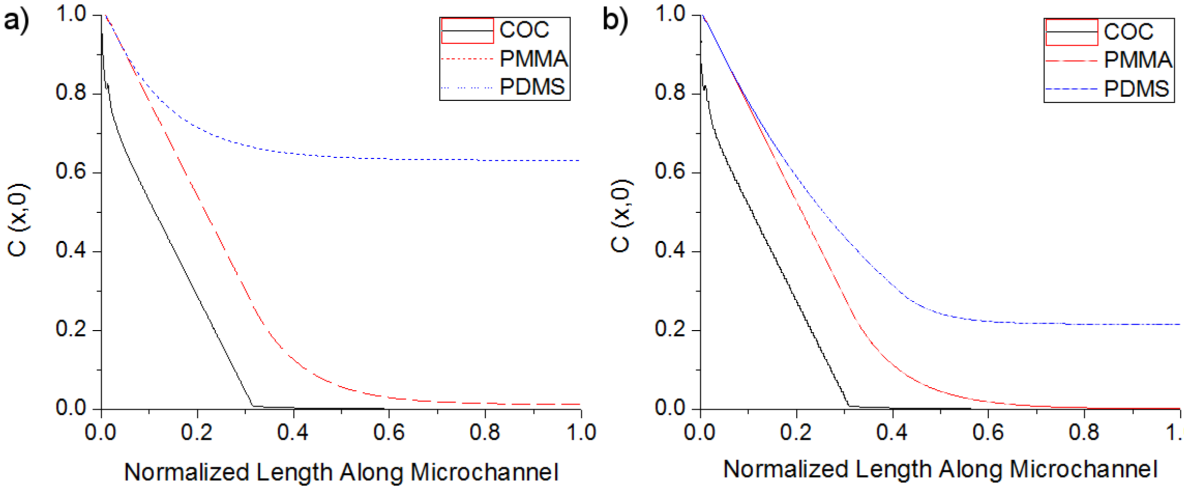

Figure 4.9 Simulated oxygen concentration at the bottom of microchannels for (a) 100 µm and (b) 1900 µm thick COC, PMMA, and PDMS capping layers. Microchannels were 100 µm deep and flowing $8\text{x}10^{-4}$ m/s of catholyte solution saturated with oxygen. A cathodic current of 0.1 mA/cm^2 was assumed for both simulations. The simulated microchannel was 15 mm in length.

Levels of sustainable cathodic current production were also simulated while varying catholyte flow rate. Flow rates were varied between $8\text{x}10^{-4}$ and $8\text{x}10^{-6}$ m/s each applying four different output current densities with results shown in Figure 4.10. As was seen for cell culturing devices, as flow rate decreased the effect of convective mass transport diminished (as was seen by the decreasing slope of oxygen concentration along the length of the microchannels). At flow rates of $8\text{x}10^{-5}$ m/s and below oxygen is almost solely supplied to the electrode by diffusion through the PDMS capping layer. For all of the examined flow rates, 10^1 and 10^0 mA/cm^2 current densities were predicted to be unsustainable. These results suggested that planar ABMFC devices may be limited to low current production regimes (those less than 100 mA/cm^2).

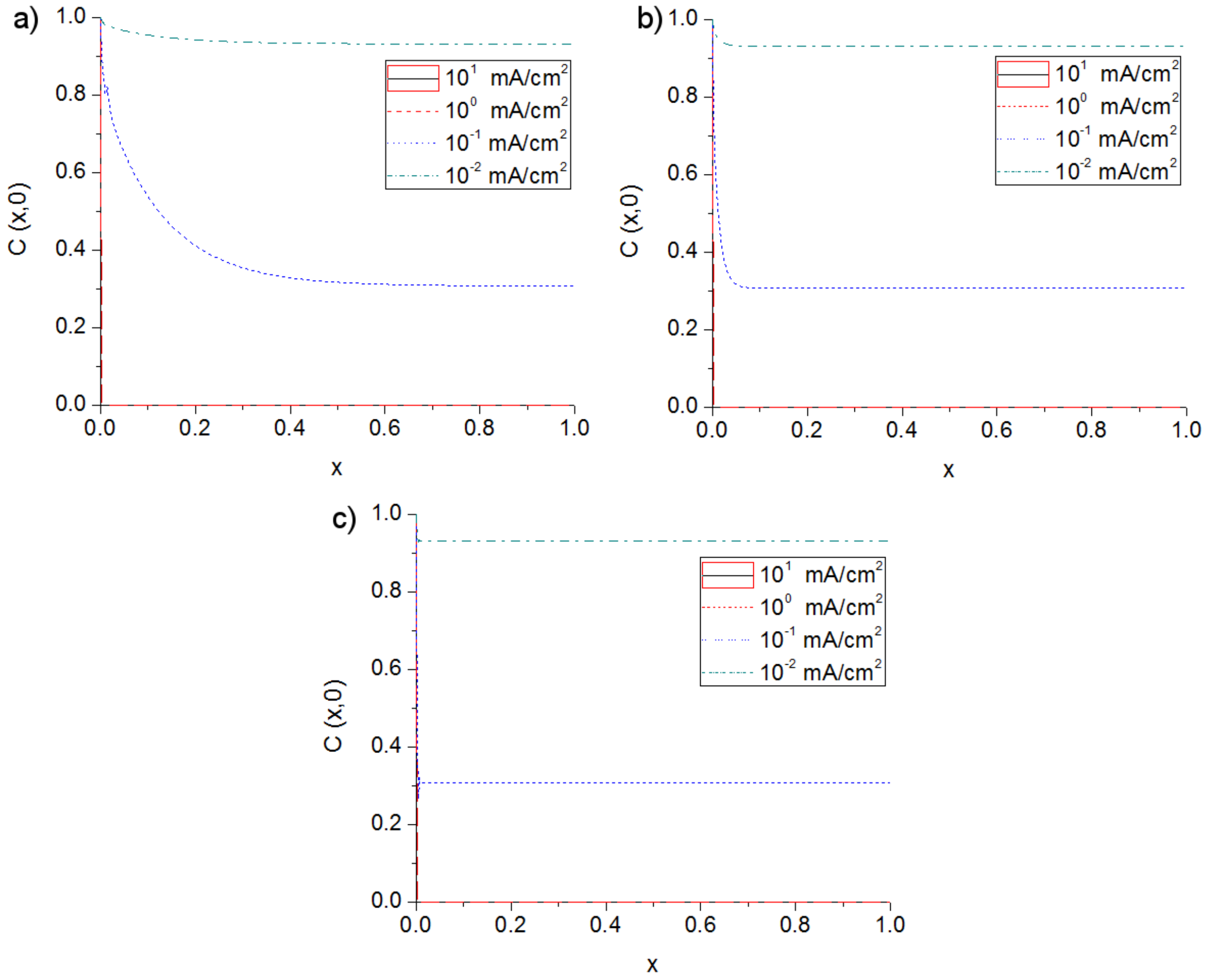

Figure 4.10 Simulated oxygen concentration at the cathode surface across the length of the microchannel for four different applied current densities. Simulations flowed (a) $8x10^{-4}$ (b) $8x10^{-5}$ and (c) $8x10^{-6}$ m/s of catholyte solution through the 100 µm deep microchannel with a 100 µm thick PDMS capping layer.

4.4.3 Maximum Output Current Varying Capping Layer Thickness and Catholyte Flow Rate

In this section, the cathodic current density at maximum efficiency was simulated while varying two different properties, PDMS capping layer thickness and applied catholyte flow rate. For both variations, output current density was iteratively stepped up/down with a resolution of 0.001 mA/cm^2 until zero oxygen concentration was predicted at any point on the cathode surface. Maximum current output was recorded as 0.001 mA/cm^2 less than this value.

As the capping layer thickness decreased from 6400 µm to 100 µm the maximum cathodic current density increases from 0.050 to 0.143 mA/cm^2 as shown in Figure 4.11a. These results yielded two guidelines for planar ABMFC architectures. If an ABMFC is known to be cathode half-cell limited, maximizing current production is vitally important and as such an optimized design should use the thinnest gas diffusion barrier between the microchannel and the external environment as possible. However, for ABMFC devices known to be anode half-cell limited, these simulations suggested that there is considerable flexibility with capping layer design. Beyond capping layer thicknesses of ~1000 µm, further increases cause relatively minor decreases in cathodic current density. As an example, from 1600 µm to 6400 µm maximum cathodic current density was predicted to decreases by only 16%. As such, in anode limited devices simulations predicted that thicker capping layers (which are often more easily fabricated) can be used with little effect on device performance.

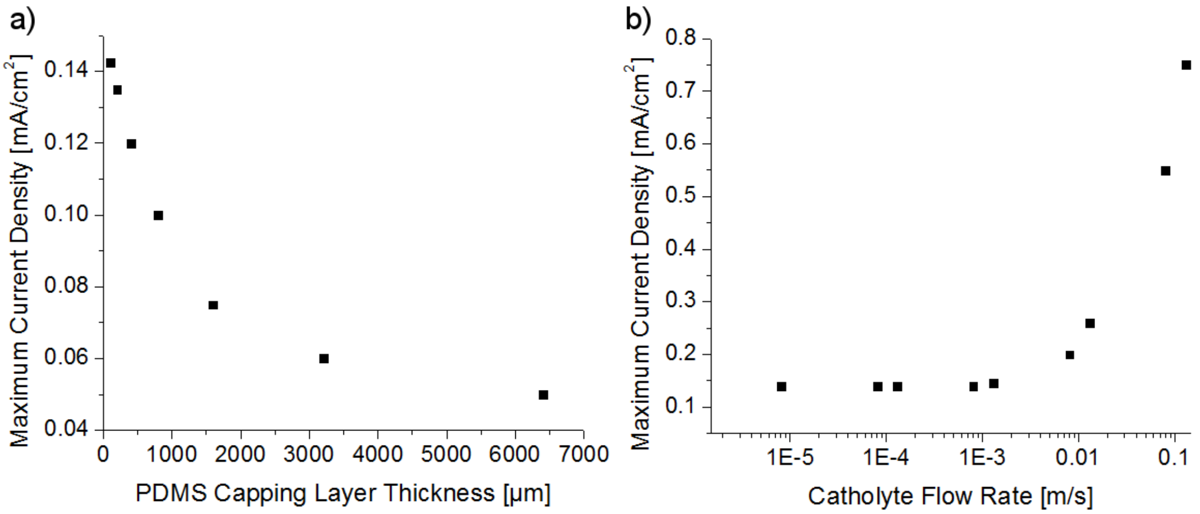

Figure 4.11 Maximum simulated output cathodic current density values predicted by FEM modelling varying (a) PDMS capping layer thickness (at 8x10^{-4} m/s catholyte flow rate) and (b) catholyte flow rate (at 100 µm PDMS capping layer thickness). For both simulations, a 100 µm deep microchannel was assumed.

Simulating maximum cathodic current density while varying catholyte flow rate revealed two distinct mass transport regions for ABMFC devices. As shown in Figure 4.11b, for catholyte flow rates of 10^{-3} m/s, or lower oxygen mass transport was predicted to be dominated by diffusion. In this region, maximum current density was invariant with further decreases in flow rate. These simulations suggested that (considering only oxygen availability) if sufficiently high oxygen could be supplied through diffusion there would be little benefit to using high catholyte flow rates (as additional flow would yield excess oxygen). For flow rates above 10^{-2} m/s, convection of dissolved oxygen dominated mass transport, with further increases predicted to yield substantial increases in maximum cathodic current density. The results of these simulations should be considered along with physical limitations of both pumping systems and mechanical stability of the microchannel. Pumping fluid at high flow rates in the small confines of a microfluidic channel requires substantial energy (pumping energy scales on the order of flow rate squared) which may considerably lessen the net energy output of the fuel cell [[31]]. Additionally, the fluid pressure generated by high flow rates may deform the microfluidic channel or the fluid inlets. These simulations have shown that for ABMFC devices to operate at maximum efficiency, it is essential to understand the relative significance of oxygen mass transport through diffusion and convection. My model has further shown that gas diffusion layers are an integral part of ABMFC device design, and even thin layers of conventional glassy polymers (PMMA and COC) can place significant limitations on achievable output current density.

4.5 Future Work

In this chapter, simulations have been applied to model oxygen transport in flowing microfluidic devices. Simulations have revealed the relative importance of diffusive and convective transport of oxygen and provided guidelines for device design. There are several ways in which the FEM model could be expanded to yield a more comprehensive treatment of oxygen transport. Firstly, all simulations have been conducted in a two dimensional architecture. A richer description of oxygen transport in microfluidic channels would take into account a fully three dimensional geometry and the effect of in plane, as well as top-down, laminar flow velocity profiles. A fully three dimensional simulation could reveal which device architectures yield the most favourable oxygen gradients, and the importance of channel width versus channel height and would serve as an integral tool for device design. Secondly, simulations have focused on the supply/consumption of one gaseous element, oxygen. In both microfluidic bioreactors and ABMFCs dissolved gases are generated as well as produced. Expanding the model to allow for removal as well as supply of gases would create a more complete pictures of device operation. For modelling ABMFC devices, future simulations could include contributions of dissolved oxygen transport from the anode half-cell. One of the most interesting applications of this model (combining both examined device architectures) involves simulating operation of microbial ABMFCs. As described in Chapter 2, microbial ABMFCs use biological organisms to serve as 'bio-catalysts' consuming fuel compounds (sugars such as glucose or gases such as carbon dioxide depending upon the specific metabolic pathways being utilized). When operating a microbial ABMFC it is common for the anode and cathode half-cells to have distinct requirements of dissolved gasses. A microbial anode half-cell would often require an anaerobic (oxygen-free) environment to facilitate metabolism of fuel molecules while a microbial cathode half-cell requires high levels of dissolved carbon dioxide. My FEM model could be adapted to investigate operational conditions in a microbial ABMFC to achieve ideal cell growth and electrical output.

In this study, simulations were carried out on planar ABMFC device architectures, the FEM model could be modified to predict oxygen concentration in stacked ABMFCs (where a diffusion layer membrane is applied between the electrode and channel base to aid in oxygen diffusion). The model could be used to make direct comparisons between the amount of cathodic current production from stacked and planar ABMFC devices. Finally, the FEM model in this study could be coupled with other simulations modelling the electro-kinetic behavior at both the anode and cathode half-cells and yield a full description of device operation.

4.6 Conclusions

The FEM model used in this investigation has been shown to be a useful tool for predicting transport of oxygen for two types of microfluidic devices. Both of the evaluated device geometries, microfluidic cell culturing bioreactors and ABMFCs, highlighted the importance of explicitly determining the amount of oxygen present in a polymer capping layer. By choosing different combinations of materials, flow rates, and device geometries the level of oxygen concentration at the base of a microfluidic channel was shown to be controllable over a wide range. From this model, a number of guidelines for designing microfluidic devices for oxygen transport were established. If uniform oxygen concentration profiles are desirable devices applied flow rates should be minimized so that diffusion is the dominant mass transport mechanism. Contrarily, for devices where a gradient in oxygen concentration is preferable a less diffuse capping layer and higher flow rates were found to be ideal.

For ABMFC devices, this model was able to demonstrate that implementing a planar ABMFC architecture places severe limitations on the amount of steady state cathodic current achievable. Simulations showed that for all device architectures (in terms of capping layer material and thickness) as well as applied catholyte flow rates devices were limited to cathodic current outputs of less than 1 mA/cm^2. Consequently, when implementing a planar MFC device for high current output (greater than 1 mA/cm^2), simulations predicted that it is more effective to use a cathode half-cell reaction where a liquid-phase regent is used to provide cathodic current (*i.e.* hydrogen peroxide, ferricyanide, or similar compound) rather than diffusion of oxygen through the microchannel. Simulation techniques described in this chapter are applicable to microfluidic bioreactors, ABMFCs, and other analogous device architectures where dissolved gases are consumed within microchannels.

This chapter has described modelling methods to improve oxygen availability at cathodes interfaces in planar MFCs. Simulations assumed an ABMFC device geometry containing patterned, electrochemically active cathodes at the base of microfluidic channels. In the next chapter, a technique is described to yield such a geometry without relying on conventional photolithography.

4.7 References

---

[1] "Hard Top Soft Bottom Microfluidic Devices for Cell Culture and Chemical Analysis" Mehta G, Lee J, Cha W, Tung Y C, Linderman J J, Takayama S *Analytical Chemistry* 81 (2009) 3714-3722.

[2] "Microfluidic dissolved oxygen gradient generator biochip as a useful tool in bacterial biofilm studies" Skolimowski M , Nielsen M W, Emneus J, Molin S, Taboryski R, Sternberg C, Dufva M, Geschke O *Lab on A Chip* 10 (2010) 2162-2169.

[3] "Microfluidic Devices for Energy Conversion: Planar Integration and Performance of a Passive, Fully Immersed H2-O2 Fuel Cell" Mitrovski S M, Elliott L C C, Nuzzo R G *Langmuir* 20 (2004) 6974-6976.

[4] "Oxygen gradients for open well cellular cultures via microfluidic substrates" Lo J F, Sinkala E, Eddington D T *Lab on A Chip* 10 (2010) 2394-2401.

[5] "Alkaline Microfluidic Hydrogen-Oxygen Fuel Cell as a Cathode Characterization Platform" Brushett F R, Zhou W P, Jayashree R S, Kenis P J A *J. Electrochem. Soc.* 156 (2009) B565-B571.

[6] "Formation of steady-state oxygen gradient in vitro: application to liver zonation" Allen J W, Bhatia S N *Biotechnology and Bioengineering* 82 (2003) 253-262.

[7] "Modeling of effects of nutrient gradients on cell proliferation in microfluidic bioreactor" Hu G, Quaranta V, Li D *Biotechnology Progress* 23 (2007) 1347-1354.

[8] "Model-based analysis and design of a microchannel reactor for tissue engineering" Mehta K, Lindermann J *Biotechnolology and Bioengineering* (2006) 94 596.

[9] "Analysis of oxygen transport to hepatocytes in a flat-plate microchannel bioreactor" Roy P, Baskaran H, Tilles A W, Yarmush M L, Toner M *Annals of Biomedical Engineering* 29 (2001) 947-955.

[10] "Exploratory FEM-based Multiphysics Oxygen Transport and Cell Viability Models for Isolated Pancreatic Islets" *Comsol Conference* Boston USA.

---

[11] “Effects of oxygenation and flow on the viability and function of rat hepatocytes cocultured in a microchannel flat-plate bioreactor” Tilles A W, Baskaran H, Roy P, Yarmush M L, Toner M *Biotechnology and Bioengineering* 73 (2001) 379-389.

[12] “Separation Through Dialysis, Solved With COMSOL Multiphysics 3.5a” in AB, C (Eds.). COMSOL Multiphysics Chemical Engineering Module Model Library (2008) version 3.4, 1-13.

[13] “FEM-based oxygen consumption and cell viability models for avascular pancreatic islets” Buchwald P *Theoretical Biological Modelling* 6 (2009) 5.

[14] “Integrated simulation of tritium permeation in solid breeder blankets” Zhang H, Ying A, Abdou M Advances in *Fusion Engineering Des* 85 (2010) 1711-1715.

[15] “Oxygen permeability of surface-modified poly(dimethylsiloxane) characterized by scanning electron microscopy” Shiku H, Saito T, Wu C C, Yasukawa T, Yokoo M, Abe H, Matsue T, Yamada H *Chemistry Letters* (2006) 35 234-235.

[16] “FEM-based oxygen consumption and cell viability models for avascular pancreatic islets” Buchwald P *Theoretical Biological Modelling* 6 (2009) 5.

[17] “Gas sorption, diffusion, and permeation in poly(dimethylsiloxane)” Merkel T C, Bondar V I, Nagai K, Freeman B D, Pinnau I *Journal of Polymer Science B: Polymer Physics* 38 (2000) 415-434.

[18] “FEM-based oxygen consumption and cell viability models for avascular pancreatic islets” Buchwald P *Theoretical Biological Modelling* 6 (2009) 5.

[19] “Zeolite-filled PMMA in composite membranes: influence of coupling agent addition on gas separation properties” Hu C C, Liu T C, Lee K R, Ruaan R C, Lai J Y *Desalination* 193 (2006) 14-24.

[20] “Gas separation properties in cyclic olefin copolymer membrane studied by positron annihilation, sorption, and gas permeation” Hu C C, Lee K R, Ruaan R C, Jean Y C, Lai J Y *Journal of Membrane Science* 274 (2006) 192-199.

[21] “Computerized microfluidic cell culture using elastomeric channels and Braile displays” Gu W, Zhu X, Futai N, Cho B S, Takayama S *PNAS* 101 (2004) 15861-15866.

[22] “Quantitative measurement and control of oxygen levels in microfluidic poly(dimethylsiloxane) bioreactors during cell culture” Mehta G, Mehta K, Sud D, Song J W,

---

Bersano-Begey T, Futai N, Heo Y S, Mycek M A, Lindermann J J, Takayama S *Biomedical Microdevices* 9 (2007) 123-134.

[23] "Computerized microfluidic cell culture using elastomeric channels and Braile displays" Gu W, Zhu X, Futai N, Cho B S, Takayama S *PNAS* 101 (2004) 15861-15866.

[24] "Generation of gradients having complex shapes using microfluidic networks" Dertinger S K W, Chiu D T, Jeon N L, Whitesides G M *Analytical Chemistry* 73 (2001) 1240-1246.

[25] "Modeling of effects of nutrient gradients on cell proliferation in microfluidic bioreactor" Hu G, Quaranta V, Li D *Biotechnology Progress* 23 (2007) 1347-1354.

[26] "Polymer microfluidic devices" Becker H, Locascio L E *Talanta* 56 (2002) 267-287.

[27] "Rapid prototyping of microfluidic chips in COC" Steigert J, Haeberle S, Brenner T, Muller C, Steinert C P, Koltay P, Gottschlich N, Reinecke H, Ruhe J, Zengerle R, Ducree J *Journal of Micromechanics and Microengineering* 17 (2007) 333-341.

[28] "Surface modification of thermoplastics - towards the plastic biochip through high throughoput screening devices" Diaz-Quijada G A, Peytavi R, Nantel A, Roy E, Bergeron M G, Dumoulin M M, Veres T *Lab on a Chip* 7 (2007) 856-862.

[29] "On-chip micropatterning of plastic (cyclic olefin copolymer, COC) microfluidic channels for the fabrication of biomolecule microarrays using photografting methods" Pu Q, Oyesanya O, Thompson B, Liu S, Alvarez J C *Langmuir* 23 (2007) 1577-1583.

[30] "Polymer Electrolyte Membranes for Fuel Cells" Lee J S, Quan N D, Hwang J M, Lee S D, Kim H, Lee H, Kim H S *Journal of Industrial Engineering Chemistry* 12 (2006) 175-183.

[31] "A review on membraneless laminar flow-based fuel cells" Shaegh S A M, Nguyen N T, Chan S H, *International Journal of Hydrogen Energy* 36 (2011) 5675-5694.

[32] "Microfluidic fuel cells: a review" Kjeang E, Djilali N, Sinton D *Journal of Power Sources* 186 (2009) 353-369.

Chapter 5[*]

Microfluidic Fuel Cells Fabricated and Operated via Laminar Flow

“Shun no toil to make yourself remarkable by some talent or other; yet do note devote yourself to one branch exclusively. Strive to get clear notions about all. Give up no science entirely; for science is but one.”

Lucius Annaeus Seneca

5.0 Introduction

The previous chapters in this thesis have involved improve different aspects of the MFC devices architecture. Here, work was undertaken to decrease the cost and complexity of planar MFC device fabrication through the development of a low cost, *in situ*, fabrication technique, multi-layer laminar flow lithography (LFL). Parameters affecting patterning through LFL are determined through both experiments and FEM simulations. LFL is then used to pattern multi-layer thin film stacks deposited in COC microchannels to yield three electrode and two electrode microfluidic electrochemical cells. Two electrode devices are further operated and characterized as MFC devices. This work demonstrates the utility of LFL as a general fabrication technique for patterning of MFCs as well as other microfluidic electrochemical devices.

5.1 Overview and Motivations

Microfluidic fuel cells are a route towards small scale power generators for isolated devices such as lab-on-a-chip systems and discrete logic components [1]. In such small scale systems, minimizing fabrication cost and complexity is of critical importance [2]. One of the most elegant methods to achieve low cost fuel cell devices is through membraneless microfluidic fuel cells (here termed MMFCs). As detailed in Section 2.2.2, MMFCs leverage the tendency of fluids within microfluidic channels to flow side-by-side with only limited (diffusive) mixing. In this

---

[*] Chapter 5 was reproduced in part from previously published material from “Patterning multilayer microfluidic electrochemical devices by maskless laminar flow lithography” Nearingburg B, Elias A L *RSC Advances* Accepted June 19, 2014.

way, parallel fluid streams can restricted to well-defined regions within a microchannel by controlling the location of the fluid interface/s. As described in Section 2.2.4, previous implementations of MMFCs have demonstrated highly functional devices, however they have still relied upon conventional photolithographic processing techniques to pattern electrode surfaces [3,4,5]. In this chapter, I sought to reduce the cost and complexity of MMFC device fabrication by de-coupling photolithography and electrode patterning through development of multi-layer *in situ* laminar flow lithography (LFL). This fabrication method can be performed on a bench-top environment using standard laboratory syringe pumps. Experiments and simulations were conducted to evaluate the effectiveness of LFL for rapid (and cost-effective) patterning of electrodes in MMFC devices.

5.2 Previous Usage of Laminar Flow Lithography

Laminar flow is one of the most widely appreciated characteristics of the microfluidic domain [6]. Previous work in literature has leveraged laminar flow gradients to create numerous types of devices including passive micromixers, lab-on-a-chip diagnostic systems, and (most relevant to this thesis) MMFCs [7,8,9]. One of the less well-documented applications of laminar flow involves patterning of surfaces within microchannels by flowing parallel streams of reactive fluids (either etchants or additive deposition solutions) which undergo only limited (diffusive) mixing while flowing through a device. This technique is here termed laminar flow lithography (LFL). The first reported usage of LFL was in a publication by Kenis *et al*. in 1999 [10]. Their work pioneered both additive and subtractive LFL techniques. First, they showed subtractive LFL, which demonstrated the ability to remove regions of Au electrodes deposited within microchannels by flowing parallel streams of Au etchant and water. Portions of electrodes that were exposed to the Au stream were etched while Au under the water stream remained unaffected. Second, by flowing Ag electroless plating solutions between two streams of water, they demonstrated that thin Ag wires could be formed within microchannels. Further work by other groups adapted these techniques to other applications such as creating cylindrical microchannels within glass substrates [11], depositing multiple independent Ag electrodes

[12,13,14,15], and etching single metal layers [16,17]. Prior work using LFL has highlighted several key benefits of the technique described below.

LFL is able to achieve patterning resolutions (in both additive and subtractive methods) of 10s to 100s of µm *in situ*. For many applications such as MMFCs and microfluidic electrochemical sensors, electrodes patterned on this scale are sufficient for device operation [18,19]. LFL has been shown to be able to replace photolithography for patterning simple structures, removing the host of fabrication complications associated with processing of photoresist layers and fabrication of photomasks [20]. Additionally, LFL processing can be conducted in a normal laboratory bench-top environment rather than a cleanroom facility as for photolithographic processing. LFL patterning can be undertaken *in situ*. *In situ* processing is beneficial as devices can be assembled before LFL and patterned by simply attaching fluid connections (as are likely required for normal device operation) while flowing appropriate solutions. In this way, no additional equipment is required to perform electrode patterning. Taken together, these benefits are considerable advantages when considering LFL as a possible fabrication technique. Prior examples of LFL have restricted their patterning to simple geometries with single electrode layers for a specific application. I proposed that the applicability of LFL could be greatly enhanced by sequentially applying multiple patterning stages with different wet etchant solutions. I focused on subtractive-LFL (*i.e.* flowing etchant solutions) in my investigations to integrate the benefits of highly selective wet etchants found in conventional multi-layer wet etching processes with LFL to yield a more general processing technique.

5.3 Finite Element Modelling of Multi-Layer Laminar Flow Lithography

In Chapter 3, FEM was shown to be an effective technique for determining oxygen transport behavior in microfluidic channels. In this chapter, FEM is applied to determine the extent of mixing between parallel fluid streams of etchant and water solutions. During any LFL process, the extent of mixing is of critical importance in determining the extent of etching in terms of both location and etch width. Excessive mixing will cause etchant to spread out and occupy a large fraction of the microchannel and uncontrolled etching. My initial work involved using FEM to determine the relationship between input parameters (device geometry, fluid material properties, and fluid flow rates) and etchant concentration profiles within microchannels to establish design parameters for optimal LFL patterning.

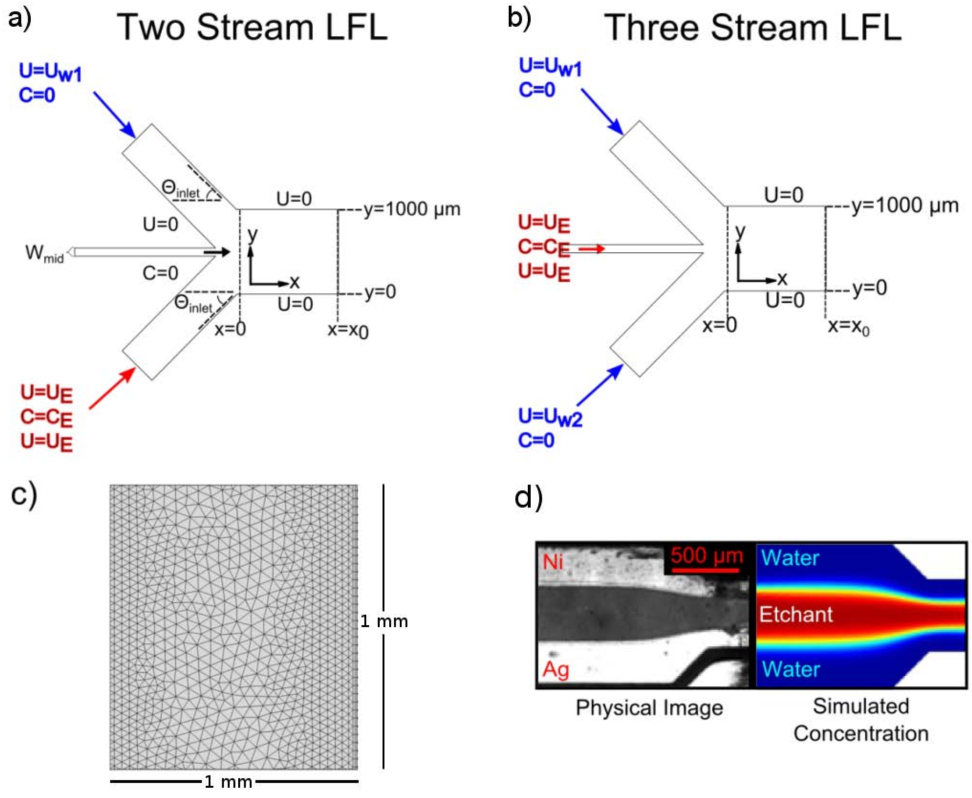

Figure 5.1 Schematic diagrams illustrating the inlets of the simulated channel geometry as well as the input parameters used in the FEM simulation process for (a) two stream and (b) three stream (bottom) processes. Geometric properties of the channel, including inlet angle Θ_{inlet} and middle inlet width W_{mid}, are shown in (a). Water and etchant flow rates are given as U_w and U_E, respectively. Etchant is supplied at a concentration of C_E while water is set to zero etchant concentration. (c) An image showing a characteristic mesh geometry in a 1 mm by 1 mm region in the middle of a simulated microchannel. (d) Optical micrograph (left) and simulated concentration profiles (right) showing the relationship in shape of a three stream ferric chloride LFL process and a simulation of steady state etchant concentration at the end of the microchannel x=20mm. In the simulated profile, concentrated etchant is shown as red while pure water is shown as blue. Figure Copyright © Royal Society of Chemistry 2014. Used with permission.

This model was based on a straight rectangular microchannel device, as shown in Figure 5.1, consisting of a 1000 µm wide 20 mm long main microchannel with three inlet ports and a single outlet port. The central inlet (of width W_{mid}) was aligned parallel to the main microchannel while the two side inlets (both 500 µm wide) were oriented at an angle Θ_{inlet}. The microchannel narrowed to 500 µm before reaching an outlet. All simulations used a microchannel depth of 75 µm unless otherwise stated. Simulations were evaluated using COMSOL 4.2a using the built in 'laminar fluid flow' and 'transport of diluted species' software packages under steady state conditions solving for etchant concentration profiles as functions of position within the microchannel. A built in 'extremely fine' sized mesh was used for all simulations which resulted in approximately 140000 elements. A portion of a meshed region in the middle of a microchannel is shown in Figure 5.1c. The FEM process first solved for the fluid velocity profile (solving the steady state Navier-Stokes equation) and then coupled this result to determine the extent of diffusion (solving the Nernst-Planck equation) to yield etchant concentration profiles as shown in Figure 5.1d. Solving a typical FEM simulation took several minutes on a conventional laptop.

Simulations were constructed to model LFL patterning of three metal films (Ag, Au and Ni) using the material properties of three etchant solutions: nitric acid, potassium iodide/iodine, and ferric chloride. Etchants were evaluated at physically relevant concentrations of 5200 mol/m^3, 2335 mol/m^3, and 2000 mol/m^3, respectively. Each of the etchants utilized in our model was assigned a specific diffusion constant, which was calculated using tabulated values for ionic mobilities [21]. Nitric acid, potassium iodide/iodine and ferric chloride were modelled with diffusion constants of 3.2 x10^{-5} cm^2/s, 2.0 x10^{-5} cm^2/s, and 1.3 x10^{-5} cm^2/s, respectively.

The FEM model was first applied to qualitatively compare the shape of etchant concentration profiles in simulated LFL processes with etched regions from physical LFL experiments of the same device geometry. An example of the correlation between simulated and experimental shapes is shown in Figure 5.1b where a three stream ferric chloride LFL etch has been used to remove Ni from the center of an Ag-Ni coated microchannel. Simulated images show red and blue regions as higher and lower concentrations of etchant in the aqueous solution, respectively. The physical experiment flowed 100 µL/min of etchant through the middle inlet between two water streams flowing at 120 µL/min. FEM simulations were evaluated using identical flow rates. Both the simulated and experimental images showed a similar extent of contracting width (in terms of concentration profile and etched width, respectively) as the microchannel narrowed. These results suggested that there was a qualitative correlation between the simulated and physical processes. The predictive capability of the FEM model was then further examined when varying device geometry and applied flow rates as described in the next section. All further simulations and experiments were evaluated using material parameters for potassium iodide/iodine etchant unless otherwise mentioned.

Simulations were also compared to etch profiles and widths in physical LFL experiments. Physical devices were fabricated using microchannels embossed in cyclic-olefin-copolymer (COC) sheets. COC sheets (COC-8007) were obtained from, Topas Thin Film Lab. Poly(dimethylsiloxane) (PDMS) was obtained from Dow Corning (Sylgard 184). Methanol (#179337), hydrogen peroxide (#216763), nitric acid (#438073), potassium iodide/iodine gold etchant (#651842), ferric chloride (#236489), and sodium hydroxide (#415413) were purchased from Sigma Aldrich. KMPR and SU-8 developer were obtained from Microchem Corp. (KMPR 1000). Silicone adhesive was obtained from Adhesives Research (Arclad 8026). Ink transparency photomasks were printed by CAD/ART Services Inc. (USA). 100 mm diameter p-type silicon wafers of 525 µm thickness were obtained from University Wafer (USA). All materials were used as received unless otherwise specified.

Microchannels were formed through hot embossing of COC sheets with a patterned Si master into 2 mm thick COC sheets using a Jenoptik HEX02. Negative relief Si maters were fabricated using conventional microfabrication techniques including photolithography and reactive ion etching as is described in the literature [[22,23]]. To outline the fabrication process, a bare Si wafer was first cleaned in piranha solution (3:1 concentrated sulfuric acid: hydrogen peroxide) which was then coated with a 30 µm film of negative photoresist (KMPR). A polymer photomasking layer was used to selectively expose the KMPR film with the desired pattern. After exposure, photoresist was selectively removed by placing the wafer in a SU-8 developer bath and rinsing with IPA and deionized water. Etching the exposed Si surface was carried out using deep reactive-ion-etching in SF_6,O_2/C_4F_8 a STSICP-DRIE. After etching, KMPR was removed by placing the wafer in a cold piranha solution for two hours. This fabrication process yielded Si wafers with a negative relief of the microchannel structure shown in Figure 5.2a. Microchannel structure was an identical geometry as used for FEM simulations. Specifically, devices consisted of a 2 cm long 1000 µm wide main microchannel with two 500 µm wide outer inlets and one 50 µm wide inner inlet. The middle (etchant) inlet and outlet were connected to 3 mm wide square access ports to allow for simple external fluid connections to the narrow channels. The end of the main microchannel narrowed to a 500 µm wide outlet before entering into a 3 mm wide access port. All microchannels were embossed to a depth of 75 µm.

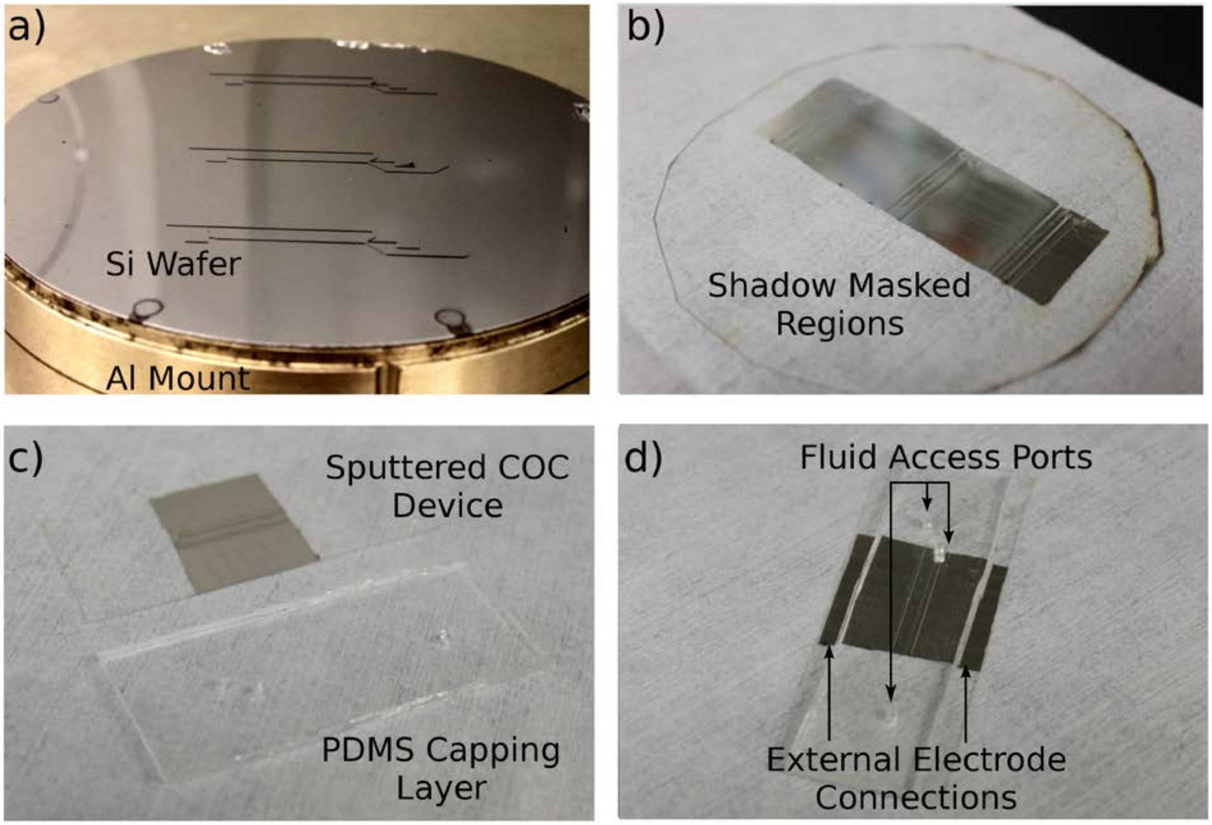

Figure 5.2 (a) A lithographically patterned silicon wafer bound to an aluminium mount for hot embossing. (b) A wafer of embossed COC devices after sputter coating. Metal deposition has been restricted from the inlet and outlet of each microchannel by applying a thin PDMS shadow mask. (c) A single COC device prior to bonding to the PDMS capping layer with a reversible silicone adhesive. (d) A bound COC device ready for two stream LFL processing with access ports highlighted.

Metal thin films were deposited onto the patterned COC surfaces through planar magnetron sputtering at the University of Alberta nanoFab facility. Deposition of metal was restricted from the inlet and outlet ports using 200 µm thick PDMS shadow mask. PDMS masking layers were pressed onto the COC surface without any surface modification, leading to a reversible bond and were peeled off after deposition with results shown in Figure 5.2b. This masking process allowed for films deposited in the main microchannel to be electrically isolated from the rest of the device (which was useful for devices characterized later in Section 5.4). Devices in this chapter, used combinations of Ag, Au, and Ni thin films which were deposited with applied powers of 200, 75, and 300 W, respectively. All films were deposited under Ar plasmas at a pressure of $7x10^{-3}$ Torr. After the deposition process had been completed, devices were reversibly sealed with a PDMS capping layer. Access ports were cut through the PDMS layer to allow for fluid flow using a 3 mm circular hole punch. A thin double sided silicone adhesive when then applied to the PDMS surface and the PDMS/adhesive stack was then pressed onto the COC device. A completed device is shown in Figure 5.2d. Once sealed, both tri-metallic and bi-metallic devices were processed by LFL as described below.

All LFL experiments were conducted using two syringe pumps (KD Scientific 200, and Legato 200 models). Multi-layer tri and bi-metallic device patterning was accomplished through sequential combination of two and three stream LFL processes. In a two stream LFL process, one stream of deionized water was flowed parallel to a stream of etchant. Two stream LFL resulted in etching of metal from one sidewall and a fraction of the microchannel base. In a three stream LFL process, a stream of etchant would flow between two streams of deionized water. Three stream LFL resulted in etching of a band in the middle of the base of the microchannel. During all LFL processing, water and etchant were controlled using separate syringe pumps to allow for independent adjustment of the etchant and water flow rates. Before each stage of LFL processing, deionized water was passed through each inlet for two minutes to stabilize flow. After stabilization, etchant was then flowed into the microchannel passing through a ball valve (which had previously been flushed with deionized water to remove any trapped air causing formation of bubbles). Etch progress was monitored with an optical microscope. After a specified time interval (or when an etch process was judged to be complete) flow of etchant was stopped. At the end of each LFL process, devices were continually flushed with deionized water for five minutes to ensure no residual etchant remained within the microchannel. Failing to properly flush devices was found to lead to low levels of unconstrained etching across the device creating visible discolorations on metal surfaces. After flushing, devices were removed from their reversibly bound PDMS capping layers, immersed in deionized water within a Branson 1510 ultrasonic bath, and finally sonicated for five minutes. After sonication, devices were dried with nitrogen and either optically characterized or rebound for further LFL processing.

5.3.1 FEM Simulations with Variable Device Geometry

Patterning of specified regions in a microchannel through LFL requires a stream of etchant to remain distinct from parallel water streams. Successful confinement of etchant requires laminar merging of fluids. Turbulence at the fluid interface/s will lead to additional mixing and limit patterning resolution. Consequently, when employing LFL, it is essential to design device inlet structures to minimize turbulence. Here FEM was used to determine how varying device geometry in terms of inlet angle, and inlet width affected the location and sharpness of the etchant:water diffusive interface. FEM simulations were conducted for three steam LFL processes with etchant flowing between two deionized water streams using the device geometry described in Section 5.2.

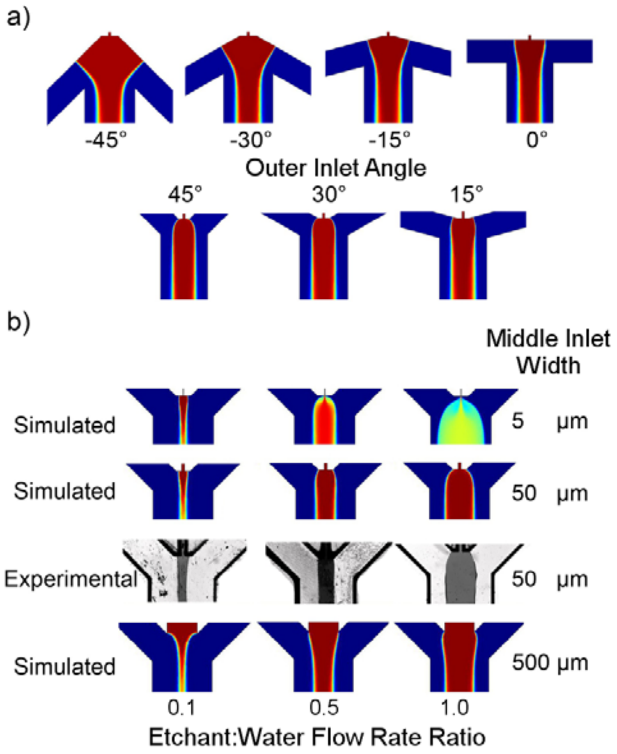

Figure 5.3 (a) Simulated concentration profiles for three stream LFL processes with varying inlet angle configurations. Concentrated etchant is shown as red, while pure water is shown as blue. (b) Simulated concentration profiles for three stream LFL processes at the microchannel inlet for differing sizes of middle inlet and flow rates. For the middle (50 µm) wide inlet, optical images show similarly shaped LFL etch profiles at the same flow rate ratio as the corresponding simulations. All processes were simulated flowing 100 µL/min (4.5×10^{-2} m/s) from each of the outer water inlets. Figure Copyright © Royal Society of Chemistry 2014. Used with permission.

The effect of inlet angle variation on etchant concentration profiles was simulated by varying Θ_{inlet} through seven angles, -45°, -30°, -15°, 0° , 15°, 30°, and 45°. Each simulation was evaluated while flowing 4.5×10^{-2} m/s (100 µL/min) of water through the outer inlets and 4.4×10^{-1} m/s (100 µL/min) etchant through the middle inlet. Etchant concentration profiles are shown in Figure 5.3a. Varying inlet angle was found to have only a small effect on the shape of the diffusive interface after entering the main microchannel (in terms of location within the microchannel and width of the etchant region). These results suggested the stability of diffusive interfaces for LFL is not sensitive to inlet angle variations. This was a favourable finding as it implies that inlet angle is not constrained when designing a device architecture to use LFL, and can be set as required by the overall device geometry. Future simulations set Θ_{inlet} = 45°.

Middle inlet width (W_{mid}) was varied as 5 µm, 50 µm, and 500 µm while outer (water) inlets were set to 500 µm width. To determine the behavior of the etchant:water diffusive interface over a wide range of processing conditions each W_{mid} value was simulated for three etchant:water flow rate ratios of 0.1, 0.5, and 1.0, with results shown in Figure 4.3b. In all simulations, water flow rates through the outer inlets were fixed to 100 µL/min (4.5×10^{-2} m/s). Experimental LFL processes using potassium iodide/iodine etchant were also carried out for W_{mid} = 50 µm devices and used identical flow rates as in the simulations. Experimental etch profiles revealed similar shapes to simulated concentration profiles at all three examined etchant:water flow rate ratios. These results reinforced that the FEM model is able to predict the qualitative (*i.e.* shape) behavior of LFL processes over a range of applied flow rates. Simulations of smaller and larger W_{mid} values displayed interesting results. Contrary to expectations, narrower (5 µm) wide inlets at higher flow rates were predicted to result in significantly increased levels of mixing at the device inlet. This was rationalized by considering the etchant fluid velocity gradient between the narrow (inlet) and wider (main) microchannels. For the 5 µm wide inlet, etchant was confined to a narrow region and experienced a large decrease in flow velocity when merging into the wider main microchannel. Large velocity gradients favour turbulent mixing of etchant with the surrounding water streams and as such etchant was predicted to spread over a wider region of the microchannel [24]. Wider (50 and 500 µm) inlets displayed more uniform behavior across the measured etchant:water flow rate ratios and more confined etchant streams. These simulations suggested that for this combination of flow rates, microchannel width and depth, either 50 µm or 500 µm wide middle inlets would be acceptable for LFL processing. These simulations showed that when designing a device for LFL it is important to ensure that inlets are sized appropriately to reduce fluid velocity gradients which could lead to turbulence.

5.3.2 Quantitative FEM Model Calibration

In the previous section, an FEM model was used to provide qualitative comparisons between simulated etchant concentration profiles and experimental etched regions during LFL processes. After consistently observing qualitative (shape) correlation between the model and physical etches it was further proposed that the steady-state FEM model can yield quantitative predictions of physical etch width through calibration of simulated etchant concentration profiles. This proposal was based on the assumption that LFL etching can be taken to be a quasi-steady state process as described below. During LFL processing, concentrated etchant is constantly flowed through the microchannel quickly etching all of the material in the center of the etchant stream. After removing all of the material from the middle of the etchant stream, etchant concentration quickly converges to a constant value. The flow velocity across the length of the microchannel (applied by the external pump) is many times larger than diffusive velocity across the microchannel width. These effects result in diffusion of etchant from high concentration (*i.e.* the middle of the microchannel where there is no longer material to consume etchant) to low concentration (*i.e.* across the width of the microchannel) in a well-defined manner. Using this assumption, it was proposed that for an LFL etching process (of known time) used to pattern a material (of constant thickness) the dimensions of the etched region can be matched to a specific etchant concentration predicted by the FEM simulation. This method was applied to calibrate the FEM model and was found to yield truly qualitative predictions of etch location and width during LFL processing. The calibration process was carried out for the three etchant solutions mentioned in Section 5.2, potassium iodide/iodine, ferric chloride, and nitric acid. The etchants, flow rates, and material properties of the physical LFL experiments used in the calibration process are given in Table 5.1.

Table 5.1 Summary of experimental material, etchant, flow, and etch width parameters used to calibrate the FEM model for quantitative predictions of LFL etch processes.

Material (thickness)	**Etchant**	**Number of fluid streams**	**Etchant Flow Rate [m/s]**	**Water Flow Rate(s) [m/s]**	**Time [s]**	**Etched Gap Width [μm]**
Ag (120 nm)	HNO_3	2	4.5×10^{-2}	8.9×10^{-2}	500	499
Ag (120 nm)	KI/I_2	2	3.6×10^{-2}	5.4×10^{-2}	60	426
Ni (120 nm)	$FeCl_3$	3	3.6×10^{-1}	5.4×10^{-2}	60	342

Before calibrating the model is was necessary to determine acceptable etch durations. Etch duration was chosen by running preliminary LFL processes (one for each etchant) with the same flow rates as selected for later experiments. Etch duration was set using the time required to remove metal from the entire length of the microchannel and rounded upwards to the nearest 10 s interval. The width of each etched region used for calibration was measured in the middle of the microchannel length (10 mm from the inlet) with an optical microscope. Simulated etchant concentration was determined in the same region of the modelled microchannel. The simulated concentration at the edge of the etched region was used as the calibration value. The calibration process is schematically shown in Figure 5.4a, where HNO_3 was used to etch Ag from a portion of an Ag/Au bilayer film. The width of the etched region is shown as y_E, which was used to determine a simulated (steady-state) concentration value. The same process was undertaken for potassium iodide/iodine and ferric chloride etchants with concentration and diffusivity values described above.

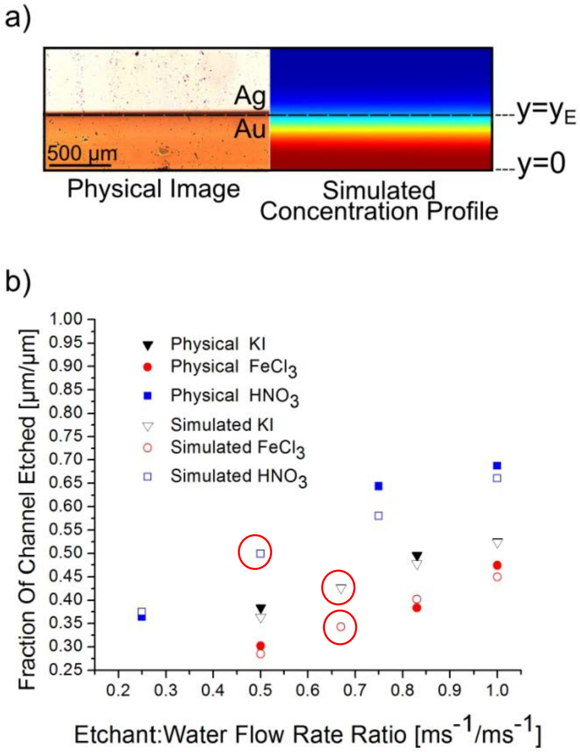

Figure. 5.4 (a) An optical image showing the physical etch pattern from a two stream process is compared to a simulated concentration profile with the same input parameters (a 500 s etch with nitric acid flowed at 4.5 x10^{-2} m/s (100 µL/min) and deionized water flowed at 8.9 x10^{-2} m/s (200 µL/min)). The physical etch width is related to simulated concentration at the location of the Ag/Au interface, shown as $y=y_E$ (measured from the edge of the channel). (b) Comparison of measured and simulated etch widths achieved for nitric acid, ferric chloride, and potassium iodide/iodine etchants over a range of etchant to water flow rate ratios. Data points used to calibrate the simulation are highlighted with circles. Both nitric acid and potassium iodide/iodine were calibrated using two stream LFL processes, while ferric chloride was calibrated using three stream LFL using diffusivity and concentration values described in Section 5.2. Figure Copyright © Royal Society of Chemistry 2014. Used with permission.

Calibrated simulations were then used to predict LFL etch widths at other etchant:water flow rate ratios as shown in Figure 5.4b. Calibrated etch width values are shown surrounded by circles and are (by definition) set to be identical between experiments and simulations. The FEM model yielded reasonable predictions of physical etch widths for all three etchant solutions. These results suggested that the assumption approximating steady state concentration profiles and approximate physical etch widths is valid. The modelling process did however restrict its predictive prowess to LFL processes of a fixed etched material, thickness, and time. To yield quantitative predictions while changing these parameters would require re-calibration of the model. However, the shape profiles of the etchant:water diffusive interfaces as shown in Section 5.2.1 would remain consistent.

This simple calibration method was found to be well suited to optimization of electrode patterning through LFL. A single physical LFL process can be used to calibrate the model. After calibration, the effect of varying flow rates on resultant etch width can be approximated without further experimentation. Through this method, required processing parameters to pattern devices with different electrode widths can be rapidly obtained. Additionally, modifications to electrode geometry can be undertaken without production of a new external masking layer.

5.3.3 Quantitative FEM Simulations with Variable Flow Rates

After establishing a method to link simulated etchant concentration profiles to physical LFL etch widths, the FEM model was used to make quantitative predictions of other aspects of LFL processing. In this section, simulations predicted the quantitative relationship between etch width and fluid flow rates for both two and three stream LFL processes. Simulations were evaluated using the optimized device geometries from Section 5.2.1 (W_{mid} = 50 µm and Θ_{inlet} = 45°) and varied both the absolute and relative magnitude of both etchant and water flow rates. Fifteen different combinations of etchant and water flow rates were simulated for both two and three stream LFL processes with results shown in Figure 5.5. In Figure 5.5a and Figure 5.5b, simulated etch widths are shown as a function of etchant:water flow rate ratios. Water flow rates were kept constant in each flow rate decade at 4.5x (10^{-2}, 10^{-3}, 10^{-4}) m/s while etchant flow rate was varied. Simulated etch widths were measured at x = 5 mm from the microchannel inlet. At each water flow rate, a higher etchant:water flow rate ratio was found to yield a larger etch width. This was expected as when more etchant is flowed through the microchannel (for a constant amount of inflowing water) it will press against the adjacent water stream/s and spread to occupy a larger fraction of the channel (as was also shown in Figure 5.3b). Also, a larger influx of etchant will supply more etchant molecules available to diffusive into adjacent water stream/s leading to further broadening along the length of the microchannel. For each of the simulated water flow rates (and flow rate ratios) three stream LFL processes (Figure 5.5b) were found to result in larger etch widths than two stream LFL processes (Figure 5.5a). This was also a reasonable result as in three stream etches there are two etchant:water diffusive interfaces (as opposed to one for two stream etches). An additional interface allowed for diffusion to occur on both sides of the etchant stream and lead to higher levels of mixing. Additional mixing caused by an extra interface was tempered by a larger amount of water flowing in the microchannel which tended to confine the etchant stream into a narrower region. These two effects compounded to yield the predicted etch widths shown.

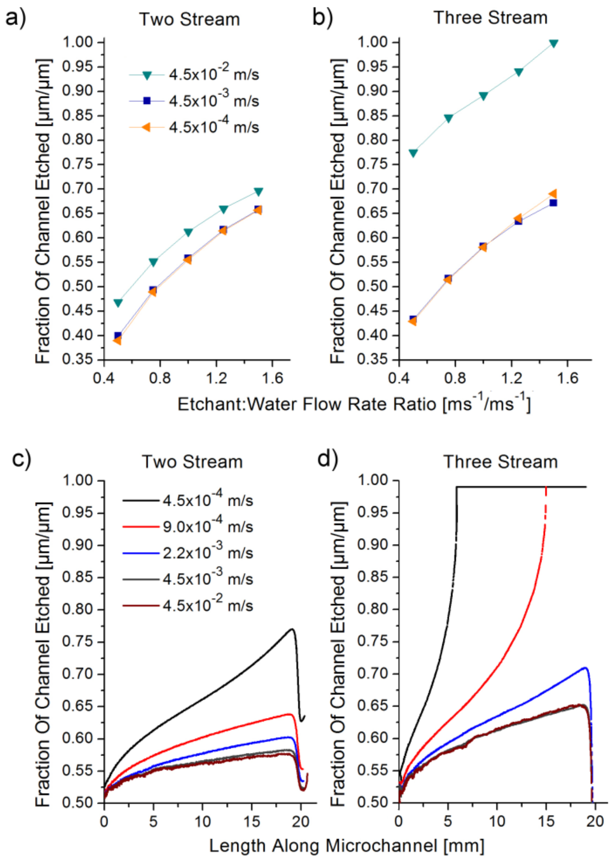

Figure. 5.5 Simulations exploring etch uniformity as a function of flow rate for two and 3 stream processes. The fraction of the channel etched at x=5 mm from the channel inlet for (a) two and (b) three stream LFL processes for both varying flow rates and etchant:water flow rate ratios. The fraction of the channel etched corresponds to etch width. The fraction of the channel etched as a function of channel length is also shown for (c) two and (d) three stream devices at various flow rates, and shows that the width of the etched region can broaden significantly along the length of the channel, particularly at low flow rates. In the three stream etch process, the etchant at the two lowest flow rates (4.5x10^{-4} and 9.0x10^{-4} m/s) expanded to fill the entire channel before reaching the outlet. Figure Copyright © Royal Society of Chemistry 2014. Used with permission.

While the predicted etch widths shown in Figure 5.5a did yield useful relationships between applied flow rates and resultant etch widths, they are valid at only one point along the microchannel (5 mm from the inlet). As etchant moves through the microchannel, diffusion results in gradual broadening of the etchant stream and etchant molecules move into adjacent water stream/s. Knowledge of the degree of broadening is critical to assess the uniformity of features patterned through LFL. The effect of diffusive broadening was simulated for two stream (Figure 5.5c) and three stream (Figure 5.5d) LFL processes, and was presented by plotting the etch width across the channel length for 5 flow rates from 4.5x10^{-4} – 4.5x10^{-2} m/s at a 1.0 etchant:water flow rate ratio. For both two and three stream LFL, simulations predicted significant broadening across the channel length for applied flow rates of less than 10^{-3} m/s. Three stream etches at flow rates below 10^{-3} m/s were predicted to undergo sufficient broadening that etchant covered the entire channel width *before reaching the outlet.* Both two and three stream simulations displayed less significant broadening above 10^{-3} m/s applied flow. Percent difference between inlet and outlet etch widths were predicted to converge to ~12% and ~27% for two and three stream LFL, respectively.

These results were significant as they showed that as the magnitude of flow rate increases (*i.e.* more fluid for a constant etchant:water flow rate ratio) LFL etches become more uniform across the length of a microchannel. Consequently, for applications where uniformly spaced electrodes are desirable high flow rates should be used. This guideline should however be tempered with practical concerns involving leakage and channel deformation (particularly if using elastomers such as PDMS) at high flow rates. Physical experiments with the device geometry used in Section 5.2 revealed that flow rates of higher than 10^{-1} m/s caused significant leakage of etchant and delamination of the silicone adhesive layer. A LFL process aiming for uniform electrode spacing should balance these two extremes. The FEM model presented here is a convenient method to choose a sufficiently high flow rate. There are however applications where non-uniformly spaced electrodes are desirable. An investigation into optimized fuel utilization by Bazylak *et al.* (2005) reported that gradually tapered electrodes increase MFC functionality. To achieve such a tapered geometry through LFL in these devices, flow rates of less than 10^{-3} m/s would be ideal (with specific flow rates chosen based on FEM simulations to control the extent of broadening). In this way, this FEM modelling can be used to guide small changes to applied flow rates can be used to tune electrode spacing dynamically.

All of the previous three stream simulations have involved symmetric flow rates (*i.e.* the flow rates at both of the water inlets are equal). In LFL, symmetric flow rates lead to etched regions in the middle of the microchannel. For many types of devices (such as membraneless MFCs) symmetric etch patterns are useful and allow for facile separation of anode and cathode half cells. However, it was here found that the utility of LFL as a fabrication technique is greatly enhanced by breaking flow rate symmetry.

In this section, simulations and experiments were conducted with asymmetric LFL and evaluated its ability to pattern rectangular electrodes at arbitrary points in a microchannel. FEM simulations were carried out for variable asymmetric water flow rates with a constant etchant flow rate with results shown in Figure 5.6a. Simulated concentration profiles showed the changing location of the etchant stream as the ratio of water flowing from each inlet (V_{w1}/V_{w2}) was changed for a constant etchant flux of 50 µL/min. During these simulations, the total flux of water was kept constant at 550 µL/min. The location in the channel width of the etchant maximum (*i.e.* the middle of the etchant stream) is plotted in Figure 5.6b for both simulated and experimental LFL processes conducted at the same flow rate values. This figure shows that for both simulated and experimental results as the asymmetric water inlet flow rate ratio (V_{w1}/V_{w2}) etchant was varied from 0 to 1, etchant was initially localized near the sidewall but moved towards the middle of the microchannel in a near linear manner.

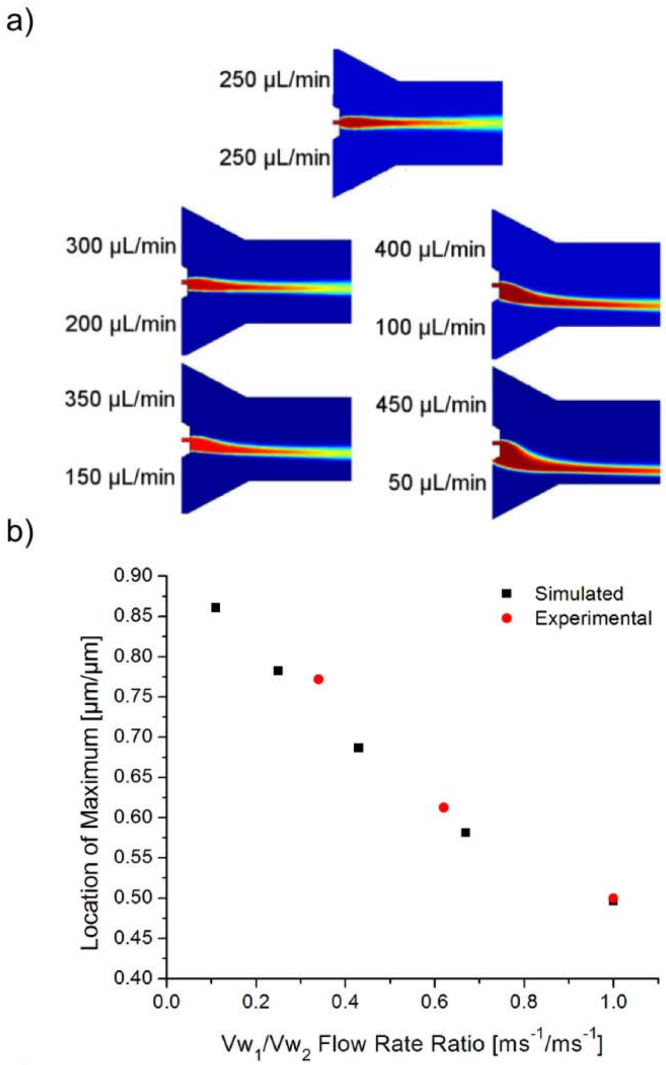

Figure 5.6 (a) Simulated concentration profiles for asymmetric three stream LFL processes with varying water flow rates. *Vw_1* and *Vw_2* describe the water flow rates of the top and bottom inlets, respectively. All simulations used a constant etchant inflow of 2.2x10^{-1} m/s (50 µL/min). (b) Location of etchant maximum at x=2 mm from the channel inlet for varying flow rate ratios. Simulated and experimentally measured maxima locations (as determined by the center of the etched region) are shown each performed with the same etchant and water flow rates. Figure Copyright © Royal Society of Chemistry 2014. Used with permission.

5.3.3 Applying FEM for Device Design

FEM simulations have been performed to determine the effects of input parameters (device geometry, absolute and relative flow rates, and asymmetric flow rates) on the resultant etching behavior of a LFL processes. Simulations have demonstrated the utility of FEM modelling as a predictive tool for tuning device architecture and inflow parameters to achieve specific patterning profiles. The FEM model showed that when designing a device for LFL there are several design parameters that should be considered (inlet size and relative fluid velocity) and some which can be neglected (channel thickness, and inlet angle). Regardless of the desired application, simulations showed that any LFL process should place significant focus on minimizing fluid instabilities to allow for the highest degree of control over etch width and location.

After establishing the utility of steady-state FEM modelling and gaining an understanding of the parameters governing LFL, the FEM model was applied to guide fabrication of physical devices. Multiple stages of two and three stream LFL processes were used to produce bi-metallic (Ag-Ni) and tri-metallic (Ag-Au-Ni) multi-layer microfluidic electrochemical cells. Creation of these devices required multiple steps of LFL using all three of the calibrated etchant solutions (nitric acid, potassium iodide/iodine, and ferric chloride as were shown in Figure 5.4b) to determine appropriate processing parameters.

5.4 Experimental Application of Laminar Flow Lithography

5.4.1 Multilayer Devices by Multi-layer LFL

Multi-layer LFL was applied to two candidate device architectures, two electrode bi-metallic and three electrode tri-metallic thin film stacks deposited within patterned COC microchannels. Bi-metallic devices consisted of a two layer Ag-Ni thin film stack patterned into two electrically isolated Ag and Ni regions separated by a non-conductive gap. Tri-metallic devices were similarly produced using a three layer Ag-Au-Ni thin film stack which was patterned into electrically isolated Ag, Au, and Ni regions along with two non-conductive gaps. Both of these devices would be time consuming and costly to produce via conventional photolithographic techniques as each layer would necessitate a separate cycle of photoresist deposition, patterning, and removal along with subsequent metal etching. Patterning of each metal layer would also require a separately fabricated photomask to optically define the etched regions. Using multi-layer LFL, each patterning step was achieved rapidly by sequentially flowing different fluids at different flow rates.

Bi-metallic Ag-Ni devices were constructed as described above in Section 5.3.1 with a 140 nm thick Ni film deposited beneath a 190 nm Ag film (as measured on the base of the microchannel). Through combination of two stages of LFL, separate Ag and Ni electrodes were patterned, as shown schematically in Figure 5.7. The first stage of LFL used a two stream etch where 100 µL/min of potassium iodide/iodine etchant was pumped through one of the outer inlets while 120 µL/min of deionized water was passed through the other outer inlet. The middle (smaller) inlet was not connected to the external environment. Etching was carried out for 60 s which resulted in Ag being removed one side-wall and from 495 ± 2 µm of the base of the microchannel. After patterning the upper Ag layer, an electrically isolating gap was etched in the middle of the microchannel base using a three stream LFL etch. Ferric chloride was flowed at 80 µL/min through the middle inlet between two streams of deionized water flowing at 120 µL/min through the outer inlets for 120 s. This etch process resulted in a gap width of 385 ± 3 µm between the Ag and Ni electrodes. After both stages of LFL were completed, in the patterned Ag electrode covered one sidewall and extended over a distance of 308 ± 2 µm across the bottom of the channel, while the Ni electrode covered the other sidewall and extended 319 ± 2 µm across the bottom of the channel. Measurements for electrodes were obtained near the middle of the microchannel length (10 mm from the inlet).

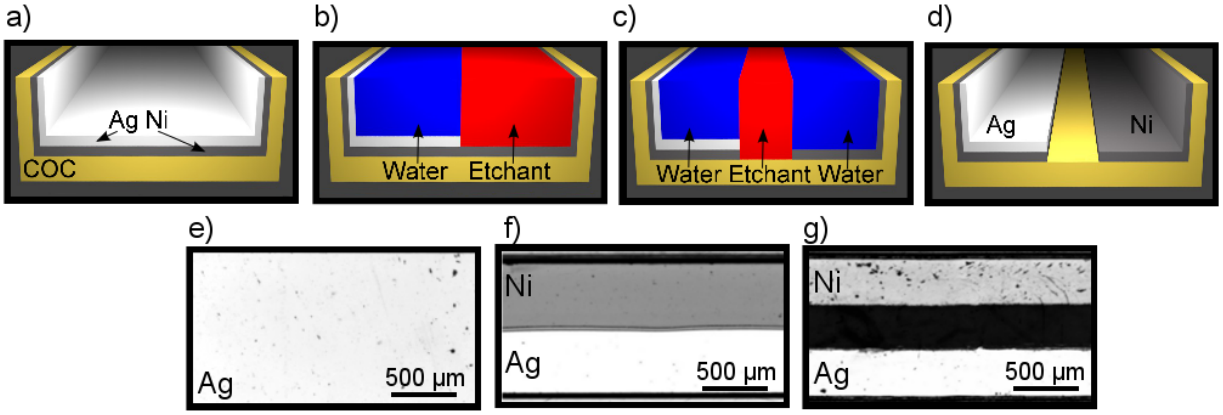

Figure 5.7 LFL process flow to pattern electrodes in bi-metallic Ag-Ni devices. (a) – (d) Schematic diagrams of (a) an Ag-Ni bilayer film deposited in a COC microchannel, (b) two stream LFL removing a portion of the upper Ag film, (c) three stream LFL patterning an electrically isolating gap and (d) the resultant Ag-Ni device structure. Schematic diagrams are shown in cross section looking down the microchannel with etchant flowing into the page. Channel dimensions have been exaggerated for clarity. (e) – (g) Optical images of the microchannel (e) the top Ag surface before LFL patterning, (f) exposed Ag and Ni regions after two stream LFL, and (g) electrically isolated Ag and Ni regions after three stream LFL. Figure Copyright © Royal Society of Chemistry 2014. Used with permission.

Tri-metallic Ag-Au-Ni devices required two additional stages of LFL etching compared to bi-metallic Ag-Ni devices. Each layer of the Ag-Au-Ni thin film stack was deposited at 120 nm thickness (as measured at the base of the microchannel) with an upper Ag thin film deposited above a middle Au thin film deposited above a bottom Ni thin film. As for bi-metallic devices, the first stage of processing involved removing a portion of the upper Ag thin film with a two stream LFL etch. As three different metallic surfaces are involved, additional care was taken to ensure utilized etchants were selective to each metal region. The three etchants used were those previously calibrated in Section 5.2.2 by FEM modelling: nitric acid, potassium iodide/iodine, and ferric chloride. Nitric acid selectively removed Ag but not Au or Ni. Potassium iodide/iodine reacted with Au and Ag but not Ni. Finally ferric chloride etched Ag and Ni but not Au. By combining these three etchants, three independent electrodes were patterned via multi-layer LFL shown in Figure 5.8. Firstly, Ag was removed by flowing 200 µL/min of diluted nitric acid through one of the large outer inlets, while 200 µL/min of deionized water was flowed through the other large inlet. This process was carried out for 300 s and removed a 670 ± 6 µm wide band of Ag from the base of the microchannel. Then a three stream LFL etch was carried out flowing 80 µL/min of potassium iodide/iodine between two streams of deionized water at 120 µL/min for 60 s. This removed a 320 ± 2 µm wide band of Au from the middle of the microchannel base. At this point, the base of the microchannel was now divided into Ag, Au, and Ni regions. Through application of two stages of asymmetric three stream LFL, non-conductive gaps were patterned to electrically isolate each electrode.

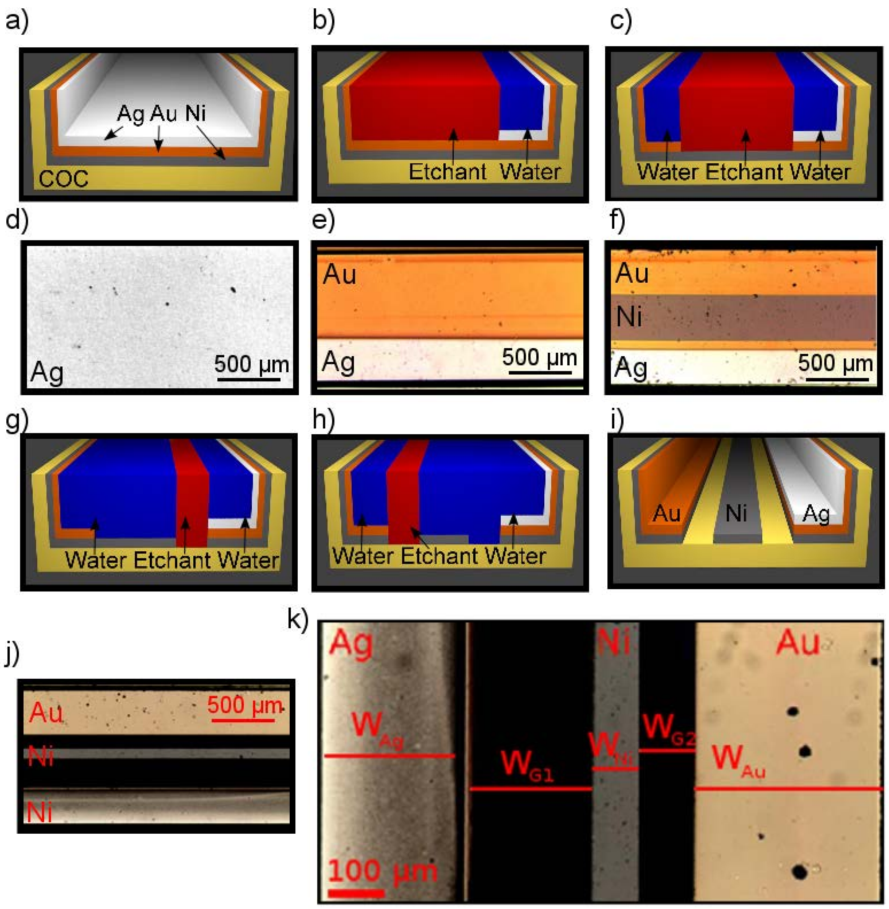

Figure. 5.8 LFL process flow to pattern electrodes in tri-metallic Ag-Ni-Au devices. (a) – (f) Schematic diagrams of (a) an Ag-Au-Ni tri-layer film deposited in a COC microchannel, (b) two stream LFL removing a portion of the upper Ag film, (c) three stream LFL patterning removing a band of Au in the middle of the microchannel, (d) three stream asymmetric LFL isolating the Ag-Ni interface, (e) three stream asymmetric LFL isolating the Au-Ni interface, and (f) the resultant Ag-Ni-Au device structure. The Ag-Ni interface was intentionally under-etched to lessen the effect of undercutting on subsequent asymmetric patterning. Schematic diagrams are shown in cross section looking down the microchannel with etchant flowing into the page. Channel dimensions have been exaggerated for clarity. (g) – (i) Optical images of the microchannel (g) exposed Ag and Au regions after two stream LFL processing, (h) exposed Ag, Au, and Ni regions after three stream LFL, and (i) electrically isolated Ag, Au, and Ni regions after two stages of asymmetric three stream LFL.

Asymmetric LFL was described in Section 5.4.2 by FEM simulations and involved flowing etchant between two water streams at different flow rates. Simulations showed that this allowed for etching to be centered at a region not in the center of the microchannel. For tri-metallic devices, the Ag-Ni and Ni-Au gap regions were patterned via asymmetric LFL and were chosen to be of different widths to highlight the flexibility of multi-layer LFL processing. To achieve asymmetric flow rates (while only using two syringe pumps), two different sized syringes (12 mL and 5 mL) were used on the water pump to flow water through the device. The two syringes differed in plunger area and as a result relative flow rates were scaled by a fixed ratio (0.616). To achieve greater control over the precise location of the etched region via asymmetric three stream LFL, a third syringe pump could be introduced (allowing for precise variation of the ratio of water inlet flow rates). For these devices, asymmetric LFL ferric chloride was flowed between two unequal deionized water streams of 500 µL/min and 308 µL/min for 180 s. The Ag-Ni interface was isolated flowing 50 µL/min ferric chloride creating a gap width of 125 ± 2 µm while the Ni-Au interface was isolated flowing 100 µL/min ferric chloride yielding a gap width of 260 ± 2 µm. The results of the asymmetric LFL etching are shown in Figure 4.8j and Figure 4.8k with relative critical dimensions listed.

The device architectures chosen in our investigation were both based on literature devices. Bi-metallic, two electrode devices can be of utility as electrochemical sensors in lab-on-a-chip devices and for small scale power generation as fuel cells [25]. Tri-metallic, three electrode devices could be used for precise electrochemical sensors (where the third electrode can be used to improve sensing resolution) [26,27].

Successful patterning of both bi-metallic and tri-metallic devices demonstrated the effectiveness of fabrication via multi-layer LFL. Patterning of each device took less than an hour of processing (compared to many hours when using photolithographic methods). Patterning of devices through LFL was shown to require only syringe pumps, tubing, and small volumes of common wet etchants and was performed in a laboratory bench-top environment. By removing the capital costs associated with clean-room photolithographic processing, multi-layer LFL is revealed to be an ideal technique for small scale rapid patterning of ‘large’ (10s to 100s of µm) electrodes where cost and processing time are critical [28]. Furthermore, each of the critical dimensions listed for both devices (the width and location of the electrode/gap regions) can be altered through varying applied flow rates. As this can be done without an external masking layer, changes to device design to optimize output (guided by flow rate values obtained through FEM simulations as in Section 5.1) can be carried out dynamically further reducing processing delays and fabrication cost.

5.4.2 Further Experiments with Multi-layer LFL

Demonstration of patterning experimentally relevant electrode geometries as was shown in the previous section was critical to establishing multi-layer LFL as an effective fabrication technique. In this section, additional experiments which highlighted benefits and limitations imposed by using multi-layer LFL are described.

One of the most critical metrics of any microfabrication process is pitch, the smallest feature size that can be reliably produced. To evaluate pitch in LFL these experiments we used the same microchannel architecture as described in Section 5.2.2 which had been coated with a 120 nm thick Ag thin film. Calibrated FEM simulations were applied to guide pitch experiments where three stream LFL flowing ferric chloride. Ferric chloride was measured to be the most effectively confined of the three evaluated etchants as was shown in Figure 5.4b. Etchant was passed between two symmetric water streams at high flow rates (to maximally confine the etchant as was shown in Figure 5.3). Experiments measured pitch by using the lowest possible flow rate of ferric chloride along with the highest possible flow rate of deionized water. Experiments yielded a minimum patterning resolution while flowing 5 µL/min or ferric chloride between two streams of 500 µL/min deionized water shown at two magnifications in Figure 5.9. Etchant flow rates below 5 µL/min were not observed to lead to any appreciable etching over a normal timescale (~5 minutes). At these flow rates it is likely that etchant was sufficiently diluted by the water streams to yield a vanishingly small etch rate. Water flow rates higher than 500 µL/min lead to delamination of the reversible adhesive causing leaking of water and etchant from the device. The combination of these two results placed limitations on the pitch achievable in our devices. Etching was carried out until metal had been removed from the entire length of the microchannel (~120 s). Results demonstrated that in the 1000 µm wide microchannel devices presented here LFL is limited to a pitch of ~50 ± 1 µm.

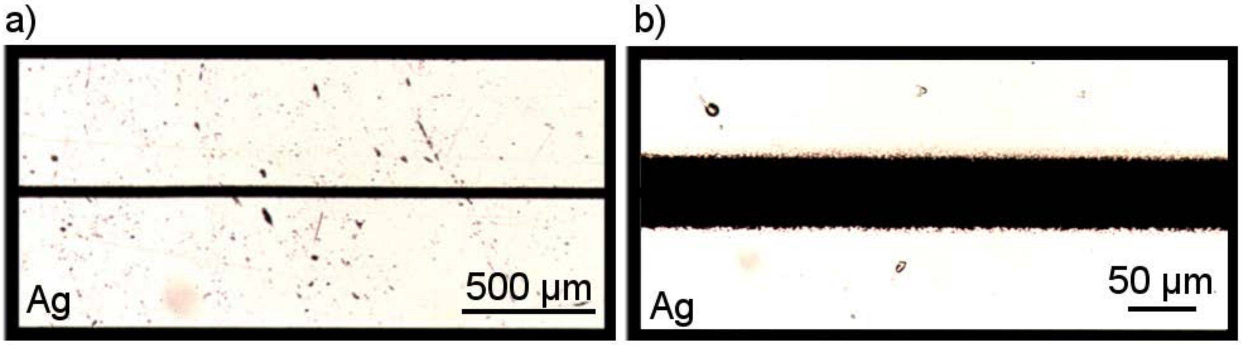

Figure. 5.9 Images showing the pitch of LFL in our devices. Experiments flowed 5 µL/min of ferric chloride between two streams of deionized water at 500 µL/min. Etching was carried out for 120 s. Images were taken at x = 10 mm from the microchannel inlet.

Another critical component of any microfabrication technique is parallelizability (*i.e.* the ability to pattern many devices simultaneously). Also, for fuel cells, one of the most straightforward methods to improve device output is to stack many cells in series (to increase output voltage) or parallel (to increase output current) making a parallelized geometry desirable [29]. Parallelization experiments were carried out for multi-layer LFL using a modified device geometry to that described above (fabricated by the same method described in Section 5.2. 120 nm Ag-Ni thin films in two microchannel devices (1000 µm wide 20 mm long) were patterned via multi-layer LFL with geometries shown in Figure 5.10a. Parallelization experiments revealed several interesting conclusions and logistical considerations which impact the wider applicability of multi-layer LFL patterning.

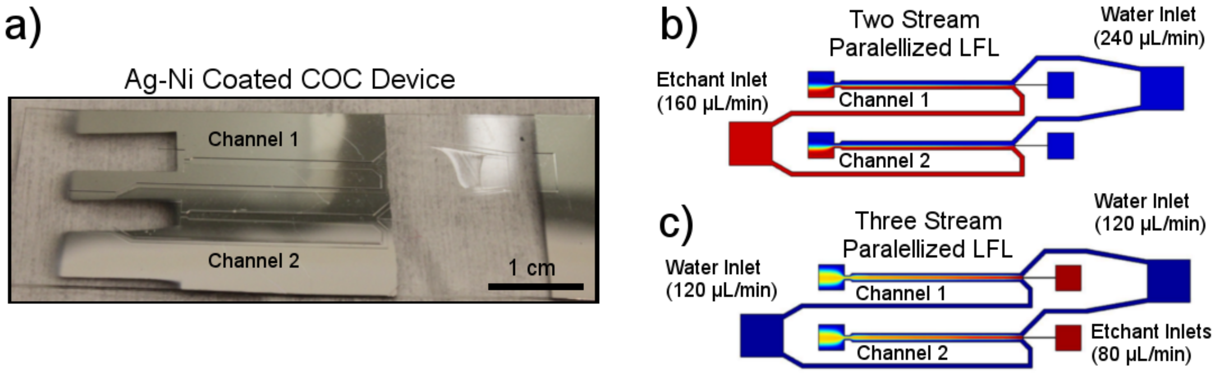

Figure. 5.10 (a) A two channel Ag-Ni device after sputtering (before LFL processing), and FEM simulations of (b) two stream and (c) three stream parallelized LFL patterning. Simulations were carried out using the same method as Section 5.2 with applied flow rates as indicated. In three stream LFL, 80 µL/min of etchant was applied to the middle inlet of each microchannel independently.

Before patterning physical parallelized devices, FEM simulations were carried out using the modified device geometry to gauge appropriate etchant and water flow rates. FEM modelling used the same etchant concentration and diffusivity values as described previously. Simulations predicted that for symmetric two channel devices, flow rates scaled linearly (*i.e.* for two channels in parallel doubling the applied flow rates used in a single channel devices was found to achieve the same etch width in each channel as found for a single channel devices). Concentration profiles for two stream two channel devices are shown in Figure 5.10b. Further simulations showed that for non-symmetric device geometries, LFL produced significant variability in etch width across each channel. This is a reasonable result as for non-symmetric channels inflowing etchant and water will enter channels at different rates (dependent upon the relative fluid resistance of each channel inlet). Given this result, it is important when designing devices for parallelized LFL to ensure a symmetric device architecture to achieve uniform etching across each channel.

Parallel LFL was also implemented experimentally. In the first stage of two channel device processing, two stream LFL removed a fraction of the upper Ag layer of the microchannels by flowing 160 µL/min of potassium iodide/iodine and 240 µL/min water for 80 s. Three stream LFL was then sequentially applied to each microchannel by flowing deionized water at 120 µL/min from both outer inputs while ferric chloride was flowed at 80 µL/min through each of the middle inlets for 140 s. This patterning process resulted in etch widths (measured in the middle of the microchannels at 10 mm from the inlet) of 466 ± 3 µm and 451 ± 4 µm for the two channels, respectively. It is important to note that parallelized devices were found to be exceedingly susceptible to non-uniformities caused by improper device bonding or integration of external fluid connections, which resulted in non-symmetric etch widths between the two microchannels. This is justified by considering that differences in microchannel geometry cause variations in fluid resistance seen by each fluid stream and can change the relative etchant:water flow rate ratio in each microchannel. As such, when implementing parallelized LFL great care should be taken to ensure that fluid paths to each channel are of both equal length and height (to ensure the same etchant and water flow velocities reach each microchannel).

Pitch and potential parallelization are both critical aspects of a microfluidic fabrication method. Multi-layer LFL has been shown to be able to etch structures of 50 µm width. Patterning on this scale is applicable to many types of microfluidic electrochemical devices including MFCs, and lab-on-a-chip diagnostics [30]. Parallelized fabrication was shown to be achievable using multi-layer LFL provided a symmetric device was used. Both of these results further reinforced the benefits offered by multi-layer LFL based fabrication.

5.5 Ag-Ni MFCs Fabricated By Laminar Flow Lithography

MMFCs typically possess a device architecture consisting of rectangular microchannels (10s to 100s of µm wide) with electrically isolated rectangular anode and cathode electrodes (also of 10s to 100s of µm wide) deposited on the base or sidewalls of the microchannel [2]. In order to tailor catalytic properties to the electrochemical reaction in each half cell, the anode and cathode should each should be composed of a different material. Independently patterning anode and cathode surfaces would conventionally require several cycles of photolithography increasing production costs as well as fabrication time and complexity [31]. As was shown in

Section 5.3, this type of electrode geometry is well suited to patterning by multi-layer LFL. Building on the results of oxygen transport simulations that were shown in Chapter 3, device architecture was designed to use hydrogen peroxide catholyte solutions. Hydrogen peroxide served as an electron acceptor (in place of oxygen as used in air breathing cathode MFCs) and as such these devices were less reliant on transport of oxygen from the external environment. In these experiments, the Ag-Ni device architecture described in Section 5.3 was adapted to create functional MMFC devices patterned via LFL. Ag and Ni were chosen due to the catalytic properties of their derivative compounds, namely Ag_2O and $Ni(OH)_2$/NiOOH, towards hydrogen peroxide reduction and methanol oxidation, respectively [[32]].

5.5.1 Fabrication of Ag-Ni Membraneless Microfluidic Fuel Cell Devices

Fuel cell devices were fabricated in the same manner as described in Section 5.2, curious readers are directed to that section for full details on the fabrication methods. Ag-Ni MMFCs used the same device architecture (a 1000 µm wide 20 mm long main microchannel with two 500 µm wide inlets at 45° angles and one 50 µm wide inlet). In order to minimize electrical resistance, devices employed a *double* layer bi-metallic thin film stack deposited through magnetron sputtering as showed schematically in Figure 5.11a. Thin film stacks consisted of a bottom Ni layer of 65 nm thickness to serve as an adhesion promoter between the COC and metal films (Ag directly on COC displayed poor adhesion and would delaminate during cleaning). Above the Ni layer a 125 nm Ag film was deposited to serve as a low resistance current carrier. Above the current carrier, a 140 nm Ni surface was deposited which served as the anode. Finally, above the anode film 190 nm Ag film was deposited to serve as the cathode. Each of the thin films were deposited sequentially in an argon plasma. Due to the selectively of etchants used in LFL processing, only the top Ag and Ni surfaces were exposed to fluid after the fabrication process.

MMFC devices were produced via LFL following the same procedure shown in Figure 5.10. All width measurements were obtained with a digital microscope at *x* = 10 mm from the microchannel inlet. In brief, Ag was first removed from approximately half of the microchannel (495 ± 2 µm) by flowing 100 µL/min potassium iodide/iodine through one of the large inlets while 120 µL/min of deionized water was flowed through the other large inlet. This process was carried out for 60 s. Ag and Ni regions were then electrically isolated using a three stream LFL etch, flowing 80 µL/min of ferric chloride between two 120 µL/min deionized water streams. Three stream LFL was carried out for 170s and removed 385 ± 3 µm of the lower Ni/Ag/Ni layers. The results of the LFL patterning process are presented in Figure 5.11b which shows an Ag-Ni device after LFL processing. Processing yielded electrode widths of 308 ± 2 µm (Ag anode) and 319 ± 3 µm (Ni cathode), respectively. Etch width values were also predicted by FEM simulation and were found to differ from physical widths by 3.3% and 12.6%, for potassium iodide/iodine and ferric chloride etches, respectively. The larger discrepancy for the ferric chloride etch was attributed to the differences in film composition (etchant removed four metal layers versus two metal layers in the experiments used to calibrate the simulation in Section 5.2.2), and different etch duration. If electrode geometry in these devices was to be optimized in the future, these measured etch width values could be used to re-calibrate the FEM model (using the process described in Section 5.2.2). Re-calibration would increase the precision of the model and allow for simulations to guide further modifications to electrode width.

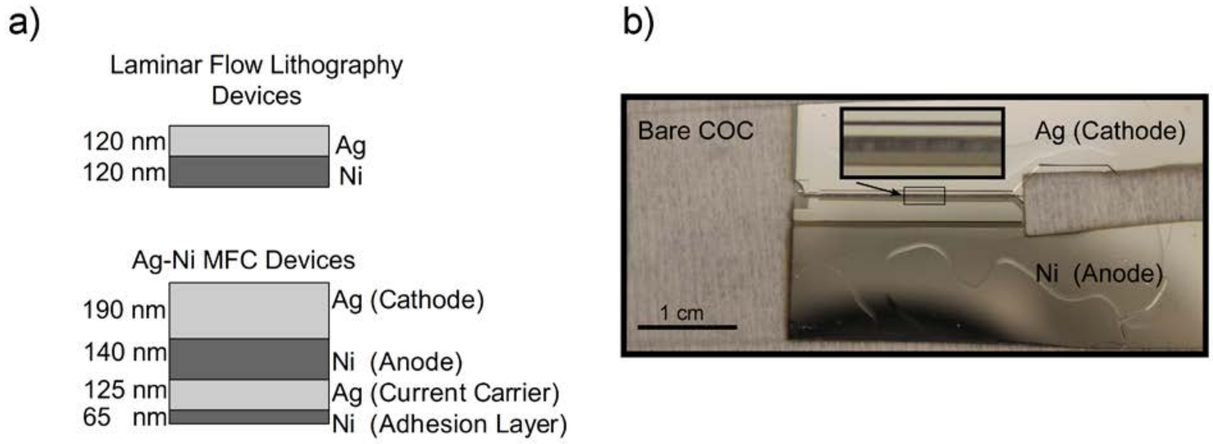

Figure 5.11 (a) Schematic diagram of the thin film stacks used for LFL characterization experiments and Ag-Ni MFC devices and (b) optical image of an Ag-Ni MMFC device after LFL processing before electrochemical processing. The inset image in (b) shows a magnified view of the middle of the main microchannel (with an Ag region on the top and a Ni region on the bottom separated by bare, transparent, COC).

After LFL processing, isolated Ni (anode) and Ag (cathode) surfaces were electrochemically converted into catalytically active compounds. Ni was reacted to yield $Ni(OH)_2$/NiOOH through cyclic voltammetry (CV). Specifically, MMFC devices were immersed in 1 M KOH solutions and a cyclic potential between -1.2 V and 0.5 V (vs. an Ag/AgCl in saturated KCl reference electrode) was applied at 100 mV/s using a Princeton Applied Research Parstat 2273 [33[33]].

It was found that any exposed Ag connected to the anode half-cell during electrochemical processing would be converted to Ag_2O, which lead to poorly bound clusters of Ag_2O subsequently re-deposited across the anode surface. Countering this effect required first applying 10 cycles between -1.2 V and 0.5 V (vs. Ag/AgCl) followed by five minutes of sonication in deionized water which was found to remove any remaining Ag compounds. A representative curve showing the Ag “cleaning” process is shown Figure 5.12a. After sonication, Ag oxidation/reduction peaks were no longer observed and further voltage cycles would react only with exposed Ni surfaces. Devices were immersed in fresh KOH solutions and 90 cycles of -1.2V - 0.8 V (vs. Ag/AgCl) were applied at 100 mV/s. During the CV process anodic peaks were observed near 110 mV and 540 mV. Literature references confirmed these peaks as corresponding to the electrooxidation of Ni to Ni(OH)$_2$ and the electrooxidation of Ni(OH)$_2$ to NiOOH, respectively [34]. A broad cathodic peak was also observed near 340 mV which corresponds to reduction of NiOOH to Ni(OH)$_2$ [34]. During CV cycling exposed Ag surfaces at the cathode were chemically converted to Ag$_2$O through reaction with the KOH solution. A representative CV curve is shown in Figure 5.12b. CV processing yielded visible changes to the surface structure of the Ni thin films as is shown in Figure 5.12c for an electrode which had been only partially submerged in KOH.

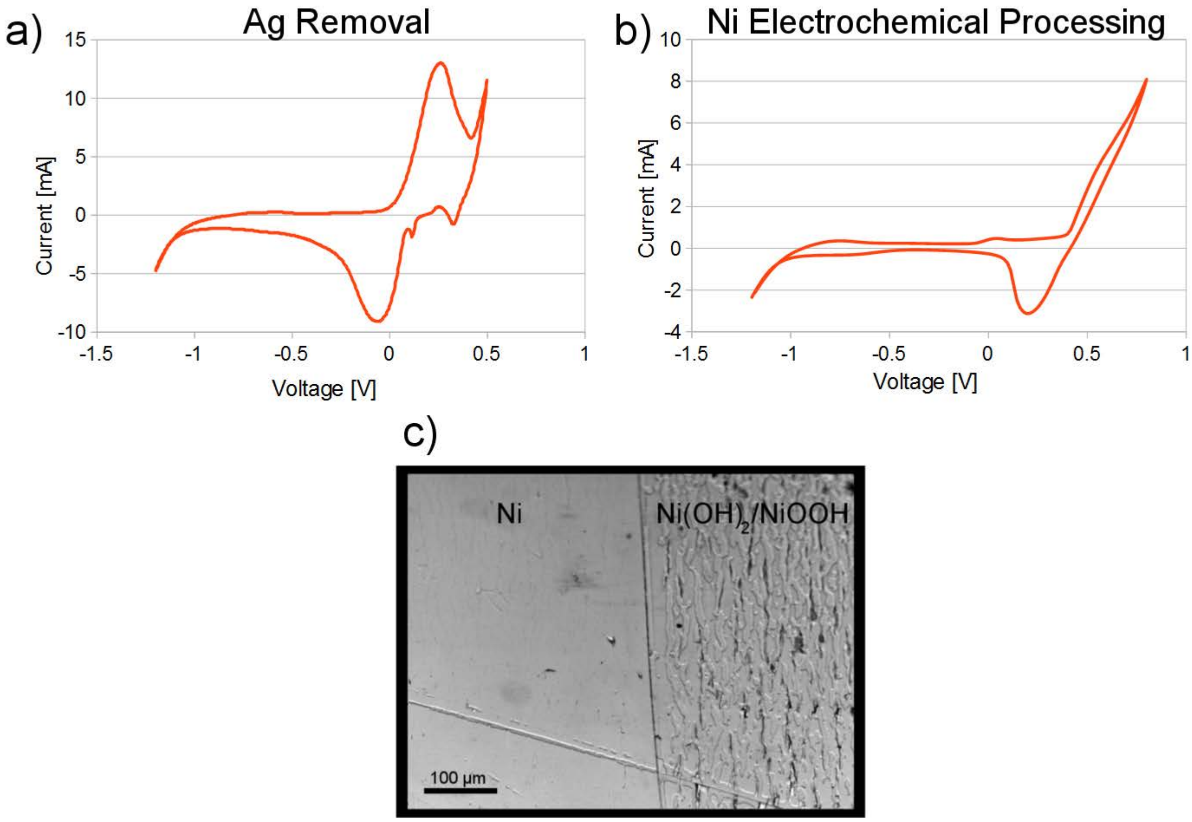

Figure 5.12 Current/voltage profiles for (a) electrochemical removal of electrically connected Ag from the anode half-cell and (b) electrochemical conversion of Ni into catalytic Ni(OH)$_2$/NiOOH. (c) Optical image of a Ni film that had been partially immersed in KOH solution during electrochemical processing resulting in distinct Ni and Ni(OH)$_2$/NiOOH regions.

5.5.2 Electrochemical Characterization Experiments

Ag and Ni were chosen as electrode materials due to the catalytic properties of their chemical derivatives Ag_2O and $Ni(OH)_2/NiOOH$ when combined with hydrogen peroxide (catholyte) and methanol (anolyte) solutions. Reaction mechanisms for both anode and cathode half cells are shown below in Equations 5.1 – 5.6.

Reactant Consuming Reactions:

Anode $CH_3OH + 6OH^- \rightarrow CO_2 + 5H_2O + 6e^-$ E^0=-810 mV (5. 1)
Cathode $2H_2O_2 \rightarrow 2H_2O + O_2$ (5. 2)
$O_2 + 2H_2O + 4e^- \rightarrow 4OH^-$ E^0= 400 mV (5. 3)
$2H_2O_2 + 4e^- \rightarrow 4OH^-$ E^0= 870 mV (5. 4)

Catalyst Switching Reactions:

Anode $6NiOOH + 6H_2O + 6e^- \rightarrow 6Ni(OH)_2 + 6OH^-$ (5. 5)
Cathode $4Ag + 4OH^- \rightarrow 2Ag_2O + 2H_2O + 4e^-$ (5. 6)

Reactions (5.2-5.3) and (5.4) are two competing pathways (decomposition or direct electro-reduction) for the utilization of hydrogen peroxide in the cathode half-cell.

Ag-Ni devices were characterized for their current/voltage profiles using an experimental apparatus consisting of a National Instruments 6216 DAQ module and an IET R2000 variable resistance box. The DAQ module was used to monitor the voltage between the anode and cathode half-cell at various reagent composition and applied resistance values. Resistance was varied at nine applied loads per order of magnitude (*i.e.* 100 Ω, 200 Ω, 300 Ω … 800 kΩ, 900 kΩ, 1 MΩ).

During electrical characterization experiments anolyte and catholyte solutions were pumped through the microchannel at equal flow rates (*i.e.* $U_{anolyte}=U_{catholyte}$) using a KD Scientific Legato

200 syringe pump. Solutions were pumped at flow rates between 20 µL/min and 0.1 µL/min at various compositions and applied resistances with results shown in Figure 5.13. Both anolyte and catholyte solutions were rendered basic through addition of KOH. KOH was added to the solutions directly before performing characterization experiments. One of the benefits of using a membraneless device architecture is that half-cell pH can be set independently. Literature descriptions of the anode and cathode half-cell reactions described that a higher pH in the anode half-cell and lower (more neutral) pH in the cathode half-cell would lead to maximal output voltage [36]. As such, anolyte pH was set to 13 (570 mM KOH) while catholyte pH was set to 8 (27 mM KOH).

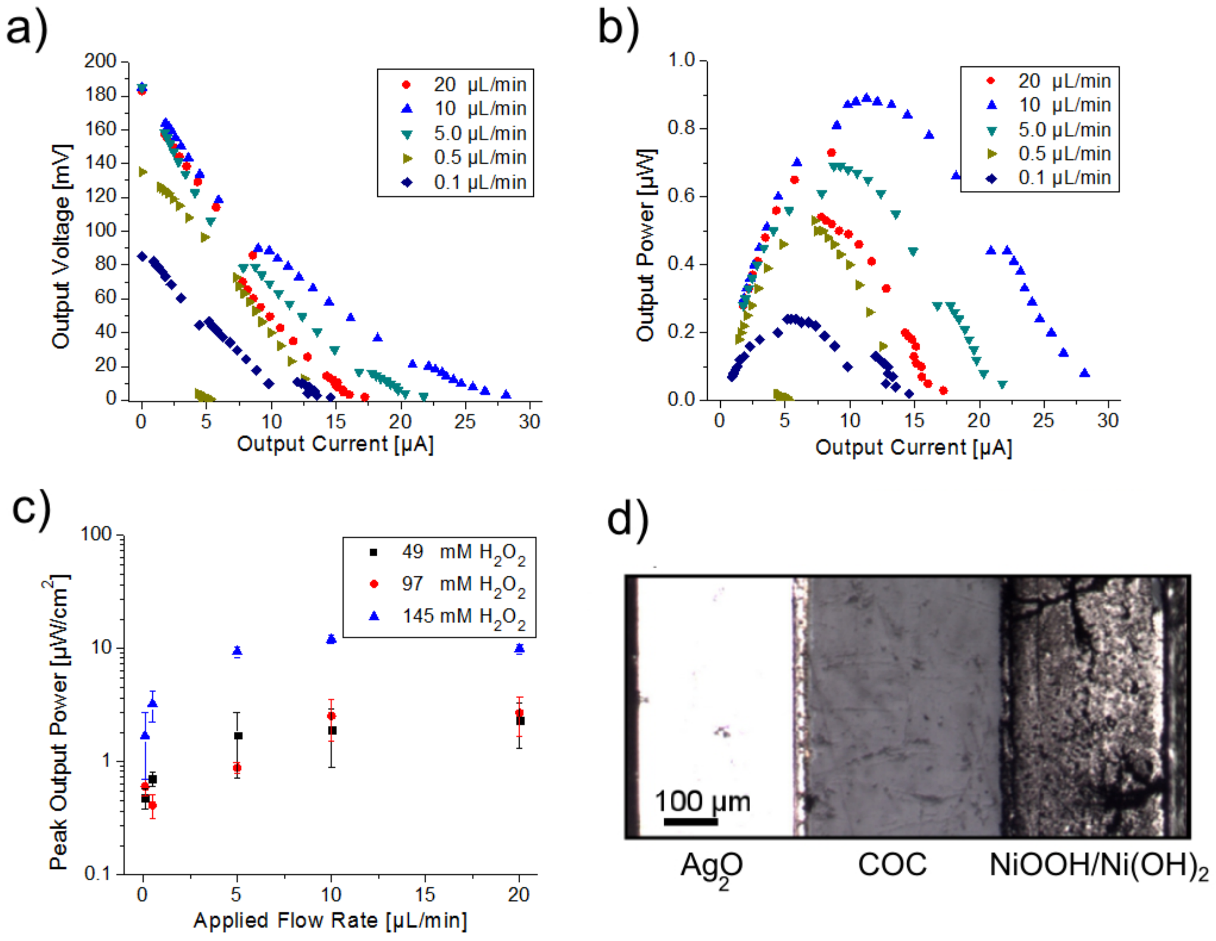

Figure. 5.13 MFC Characteristics. Representative current-voltage relationships for 1.2 M methanol and 145 mM hydrogen peroxide reactant solutions are shown in (a); power-voltage relationships for the same systems are shown in (b). (c) Output power characteristics as a function of reactant flow rate and hydrogen peroxide concentration (measurements were repeated 3 times on the same device with averages and standard deviation shown). (d) Optical image of a LFL patterned MMFC. Figure Copyright © Royal Society of Chemistry 2014. Used with permission.

Figure 5.13a shows representative current/voltage curves for a typical Ag-Ni MFC device, where 1.2 M methanol (pH 13) and 145 mM hydrogen peroxide (pH 8) are supplied as anolyte and catholyte solutions, respectively. Peak output voltage was found to increase with increasing flow rate. This result was reasonable as at higher flow rates there was a greater flux of reagents into the microchannel that were able to participate in electron producing reactions. More reactions lead to a higher sustainable level of output current. However, this trend was not followed for 20 µL/min applied flow rates. At flow rates greater than 10 µL/min it was found that excessive catholyte decomposition lead to bubbles forming within the microchannel. Chaotic formation of bubbles destabilized the laminar flow based ‘effective membrane’ isolating the anode and cathode half cells, which lead to transient mixed potentials and lower overall voltage output. Bubbles are the bane of many microfluidic devices and here placed a limitation on maximum usable flow rates for our device architecture. Current/power curves shown in Figure 5.13b demonstrated increasing peak power output for increasing flow rate except at the highest (20 µL/min) flow rate. Peak values for open circuit voltage and power output density were measured as 185 mV and 12.0 ± 0.4 µW/cm^2, and were observed while flowing 10 µL/min of 1.2 M methanol (pH 13) and 145 mM hydrogen peroxide (pH 8).

The voltage efficiency of the produced Ag-Ni devices was evaluated by considering the ratio of $V_{output}/V_{theoretical}$. This ratio varied between 15% and 11% for the chemical decomposition in Equation 5.2 or electrochemical decomposition through Equation 5.4, respectively. Voltage efficiency results revealed that the mild catalytic properties of Ag_2O and $Ni(OH)_2$/NIOOH cause considerable limitations in reaction kinetics and ultimately unfavorable output voltages [35].

As shown in Figure 5.13c, at the lowest measured flow rate (0.1 µL/min) the peak power output densities for the various catholyte concentrations were not statistically significantly different. Using the same FEM simulation methods as described above for LFL processing (along with diffusivity values for methanol and hydrogen peroxide solutions), models demonstrated complete mixing of anolyte and catholyte fluid streams at 0.1 µL/min flow rates. Mixed anolyte and catholyte streams lead to the same results as were observed for chaotic bubble formation with unintended (electron consuming) side-reactions, as well as mixed potentials on electrode surfaces hindering MFC device output. These results paired with observations of bubble formation revealed that Ag-Ni devices produced in these experiments have an operational flow rate range of 0.1 – 10 µL/min. Figure 5.13c shows that output power was sensitive to catholyte concentration. Higher catholyte concentrations yielded increased output power. As hydrogen peroxide concentration was raised above 150 mM, output was measured to be exceedingly unstable due to formation of bubbles placing a restriction on permissible catholyte concentration. For these devices, a hydrogen peroxide based catholyte solution was chosen to lessen any limitations on cathodic current output associated with mass transport of oxygen to the electrode surface (as was described in Chapter 4). The destabilizing effects of bubbles caused by peroxide decomposition mitigated these benefits. Future devices sharing this architecture would benefit from more stable catholyte solutions.

The electrical output characteristics of fabricated Ag-Ni devices are far from ideal. However, the aim of these experiments was to evaluate the ability of LFL to yield functional MMFC devices. These Ag-Ni devices can be compared to a similar MFC architecture in literature described by Sung et al. (2007) [33]. Their work involved a membraneless architecture patterned via conventional photolithography consisting of alternating strips of electroplated Ni (anode) and Ag (cathode) surfaces that had been electrochemically converted into $Ni(OH)_2$/NiOOH and Ag_2O as in our experiments. Their devices produced maximum power output values of 11.67 $\mu W/cm^2$ at 10 µL/min when pumping 200 mM KOH, 2 M CH_3OH, and 50 mM H_2O_2 in a single fluid stream which is similar (slightly lower) to power densities measured in these experiments. They found significantly enhanced output power density values at higher flow rates (achievable as their design was insensitive to bubbles within the microchannel) though power generation efficiency was hindered by energy consumed to pump the reagent fluids.

This work operated Ag-Ni MMFC devices with low reactant flow rates. Flow rates of less than 10 µL/min are compatible with passive pumping techniques (*i.e.* not relying on an external syringe pump), such as flow driven by the surface energy or weight of a fluid [[36]]. Such techniques would allow this architecture to be easily integrated into self-contained device implementations. Furthermore, when operating MFCs at low flow rates, less energy is consumed to drive the fluid increasing the efficiency of power production. Kinetic energy requirements to drive fluid flow in microchannels is often large compared to output energy. Shaegh et al. (2011)[[3]] described the pumping energy requirements of microfluidic fuel cells as $W=(12*\mu*Q^2*L)/(wd^3)$, where Q is the applied flow rate, μ is the fluid viscosity, and L, w, and d, are the channel length, width, and depth, respectively. This equation predicts that at a flow rate of 1 µL/min, 0.5 nW of energy is consumed to pump reactants through the device, a parasitic effect representing 0.09% of electrical energy extracted. As the relationship scales with the square of fluid velocity, parasitic effects increase considerably with flow rate. For the dimensions of microchannels utilized in my devices, a flow rate of 10 µL/min would consume roughly 97 nW or 10.8% of the energy output of the devices! From this comparison it is can be seen that that while an increased flow rate may yield a higher magnitude of output power, the net efficiency of the device decreases due to the parasitic effects of energy consumed by pumping large volumes of fluid through small channels.

In this section, multi-layer LFL was shown to be an effective technique to fabricate MMFC devices. Devices were found to be functional as fuel cells producing electrical outputs sensitive to both reagent composition and applied flow rates and produce quantifiable voltage and power output. Furthermore, devices were found to yield similar (slightly larger) power output densities than a comparable architecture patterned via conventional photolithography.

5.6 Future Work

While this work has evaluated the utility of multi-layer LFL in several key areas there are still directions for further improvement and characterization of the technique. Firstly, future experiments could expand LFL to a broader range of material beyond metal films. Demonstrating the ability to yield slayers of chemical compounds (*i.e.* oxides, nitrides, polymers etc.) would greatly expand the type of devices compatible with LFL patterning. Another method to aid in the utility of LFL patterning would be to utilize passive fluids other than water. Variation of the viscosity and polarity of passive fluids could lead to more effective confinement of etchant solutions and could increase patterning resolution or lessen the effects of diffusive broadening. Future work could also assess the ability of parallelized multi-layer LFL processing to produce functional devices and compare the effectiveness of paralellized fabrication to conventional photolithographic techniques.

The Ag-Ni MMFC devices produced in this chapter could be improved in several ways. Firstly, a non-hydrogen peroxide based catholyte solution could be used to alleviate the problem of bubble formation. This could lead to a wider operational range of flow rates and better reaction kinetics. Modifying the catholyte solution would likely require integration of a different metal layer (as Ag is selective to hydrogen peroxide) with a different combination of etchant solutions. Further studies could also use LFL patterning to assess the benefits of a tapered electrode geometry as discussed in Section 5.2.3. Another means to improve device functionality would be through integration of an *in situ* patterned membrane layer such as described in Chapter 3.

5.7 Conclusions

This chapter has described multi-layer LFL as a fabrication technique for microfluidic electrochemical devices. FEM simulations have been shown to be an effective method to determine processing parameters for multi-layer LFL patterning. It was demonstrated that by combining multiple stages of two and three stream LFL processes, multi-layer independent electrodes could be fabricated *in situ*. Patterning of both tri-metallic Ag-Ni-Au and bi-metallic Ag-Ni devices was shown to be achievable using apparatus consisting of two syringe pumps along with three conventional wet etchant solutions. My work here has demonstrated the utility of multi-layer LFL as an inexpensive technique to swiftly pattern electrode devices without the cost and complexity of photolithography.

Here I also characterized Ag-Ni MMFC devices produced via multi-layer LFL. Devices were shown to function as fuel cells and output peak voltage and power density of 185 mV and 12.0 ± 0.4 μW/cm^2, respectively while flowing 10 μL/min of anolyte and catholyte solutions. It was shown that devices produced via LFL yielded similar output characteristics to those patterned via conventional photolithographic and electrodeposition techniques. My devices were found to be limited to an operational flow rate range of 0.1 – 10 μL/min due to excessive formation of bubbles from decomposition of the hydrogen peroxide catholyte solution and mixing of anolyte and catholyte solutions. With proper selection of electrode and anolyte/catholyte materials, MMFC devices produced via LFL like those developed in our work could be applicable to small scale power generation for low power sensors or lab-on-a-chip applications.

5.8 References

---

[1] "Microfluidic Fuel Cells: a Review" Kjeang E, Djilali N, Sinton D *Journal of Power Sources* 186 (2009) 353-369.

[2] "The origins and future of microfluidics" Whitesides G M *Nature* 442 (2006) 368-373.

[3] "A review on membraneless laminar flow-based fuel cells" Shaegh S A M, Nguyen N T, Chan S H, *International Journal of Hydrogen Energy* 36 (2011) 5675-5694.

[4] "Microfluidic devices for energy conversion: planar integration and performance of a passive, fully immersed H2O2 fuel cell" Mitrovski S M, Elliott L C C, Nuzzo R G *Langmuir* 20 (2004) 6974-6976.

[5] "Microfluidic Fuel Cell Based On Laminar Flow" Choban E R, Markoski L J, Wieckowski A, Kenis P J A *Journal Of Power Sources* 128 (2004) 54-60.

[6] "Controlled microfluidic interfaces" Atencia J, Beebe D J *Nature* 437 (2005) 648-655.

[7] "Micromixing within microfluidic devices" Capretto L, Cheng W, Hill M, Zhang X *Topics in Current Chemistry* 304 (2011) 27-68.

[8] "Microfluidic platforms for lab-on-a-chip diagnostics" Haeberle S, Zengerle R *Lab on A Chip* 7 (2007) 1094-1110.

[9] "Microfluidic Fuel Cells: a Review" Kjeang E, Djilali N, Sinton D *Journal of Power Sources* 186 (2009) 353-369.

[10] "Micropatterning Inside Capillaries Using Multiphase Laminar Flow Patterning" Kenis P J A, Ismagilov R F, Whitesides G M *Science* 285 (1999) 83-85.

[11] "Selectively modified microfluidic chip for solvent extraction of Radix Salvia Miltiorrhiza using three-phase laminar flow to provide liquid-liquid interface area" Mu X, Liang Q, Hu P, Ren K, Wang Y, Luo G, *Lab on A Chip* 9 (2009) 1994-1996.

---

[12] "Electroless deposition and structuring of silver electrodes in close microfluidic capillaries" Hueck F C A, Staufer U *Journal of Micromechanical Systems* 20 (2011) 451-459.

[13] "A novel micropreconcentrator employing a laminar flow patterned heater for micro gas chromatography" Tian W C, Wu T H, Lu C J, Chen W R, Sheen H J *Journal of Micromechanics and Microengineering* (2012) 065014.

[14] "Selective microfabrication of silver electrodes inside a microchannel by multiphase laminar flow with a density difference" Paek S H, Choi Y K, Kim D S *Microelectronic Engineering* 87 (2010)1375-1378.

[15] "Microfabrication of dual-opposite electrodes inside a microchannel by means of multiphase laminar flow with density difference" Paek S H, Yang W, Kim J S, Hwang C J, Choi Y K, Kim D S, *Micro and Nano Letters* (6) 2011 678-681.

[16] "Flow-restricted Etching Method on Isotropic Substrates and Its Mechanism" Xie H, Zheng Y, Fan Y, Fu X, Yang H *Chinese Journal of Mechanical Engineering* 33 (2010) 560-567.

[17] "Fabrication inside Microchannels Using Fluid Flow" Kenis P J A, Ismagilov R F, Takayama S, Whitesides G H, Li S, White H S, *Accounts of Chemical Research* 33 (2000) 841-847.

[18] "Membraneless Vanadium Redox Fuel Cell Using Laminar Flow" Ferrigno R, Stroock A D, Clark T D, Mayer M, Whitesides G M *Journal of the American Chemical Society* 124 (2004) 12930-12931.

[19] "Microfabricated microfluidic fuel cells" Kamitani A, Morishita S, Kotaki H, Arscott S *Sensors and Actuators B: Chemical* 154 (2011) 174-180.

[20] "Design, fabrication, and characterization of a planar silicon-based, monolithically integrated micro laminar flow fuel cell with a bridge shaped microchannel cross-section" Lopez-Montesinos P O, Yossakda N, Brushet F R, Pelton W E, Kenis P J A *Journal of Power Sources* 196 (2011) 4638-4645.

[21] E. L. Cussler, *Diffusion: mass transfer in fluid systems*, 2009, Cambridge University Press.

[22] "Rapid Prototyping of Microfluidic Systems In Poly(dimethylsiloxane)" Duffy D C, McDonald J C, Schueller O J A, Whitesides G M, *Analytical Chemistry* 70 (1998) 4974-4984.

[23] "Polymer microfabrication technologies for microfluidic systems" Becker H and Gartner C, *Analytical and Bioanalytical Chemistry* 390 (2008) 89-111.

---

[24] "Microfluidics: Fluid Physics at the nanoliter scale" Squires T M, Quake S R *Reviews of Modern Physics* 77 (2005) 977-1026.

[25] "Microfluidic Sensing: state of the art fabrication and detection techniques" Wu J, Gu M *Journal of Biomedical Optics* 16 (2011) 080901.

[26] "Microfluidic three-electrode cell array for low-current electrochemical detection" Triroj N, Lapierre-Devlin M A, Kelley S O, Beresford R *IEEE Sensors Journal* (2006) 1395-1402.

[27] "Environmentally friendly disposable sensors with microfabricated on-chip planar bismuth electrode for *in situ* heavy metal ions measurement" Zou Z, Jang A, MacKnight E, Wu P M, Do J, Bishop P L, Ahn C H *Sensors and Actuators B: Chemical* 134 (2008) 18-24.

[28] "Let there be chip – towards rapid prototyping of microfluidic devices: one-step manufacturing processes" Waldburg A, Rapp H, Lange K, Rapp B E *Analytical Methods* 3 (2011) 2681-2716.

[29] "Review and Analysis of PEM Fuel Cell design and manufacturing" Mehta V *Journal of Power Sources* 114 (2003) 32-53.

[30] "Progress and perspectives in micro direct methanol fuel cell" Sundarrajan S, Allakhverdiev S I, Ramakrishna S *International Journal of Hydrogen Energy* 37 (2012) 8765-8786.

[31] "Lab-on-chip technologies: making a microfluidic network and coupling it into a complete microsystem – a review" Abgrall P, Gue A M *Journal of Micromechanics and Microengineering* 17 (2007) R15.

[32] "A membraneless microscale fuel cell using non-noble catalysts in alkaline solution" Sung W, Choi J W *Journal of Power Sources* 172 (2007) 198-208.

[33] "The kinetics and mechanism of the nickel electrode- III. The potentiodynamic response of nickel electrodes in alkaline solutions in the potential region of Ni(OH)2 formation" Guzman R S S, Vilche J R, Arvia A J, *Corrosion Science* 18 (1978) 765-778.

[34] *"A Methanol and Hydrogen Peroxide Fuel Cell Using Non-Noble Catalysts In Alkaline Solution"* Sung W, *MSC. Thesis*, 2006, Louisiana State University USA.

[35] "Micromachined polymer electrolyte membrane and direct methanol fuel cells – a review" Nguyen N T, Chan S H *Journal of Micromechanics and Microengineering* 16 (2006) R1-R12.

---

[36] “A passive pumping method for microfluidic devices” Walker G M and Beebe D J, *Lab on A Chip* 2 (2002) 131-134.

Chapter 6

Conclusion

> “As long as I’m learning something, I figure I’m OK – it’s a decent day”
>
> ***Hunter S. Thompson***

This thesis has described three different methods to improve the functionality of subcomponents of a planar MFC device architecture. Focus was placed on simplifying device fabrication while retaining materials and methods amendable to low cost, rapid-prototyping compatible processing. This chapter highlights the main results of the thesis, and outlines directions for future work to further improve the planar MFC device architecture.

6.1 Contributions to Knowledge and Summary of Work

The main achievements of this work include:

i. Development and characterization of polymer materials for *in situ* fabricated proton exchange membranes. This work was reviewed and published in *The Journal of Membrane Science* [1].

ii. Development of a simulation environment to model gas transport within microfluidic cell culturing devices. This work was reviewed and published in *Chemical Engineering Science* [2].

iii. Augmentation of gas transport simulations to optimize device architecture of air breathing microfluidic fuel cells.

iv. Simulation and experimentation of laminar flow patterning techniques to yield multi-layer laminar flow lithography. Characterization of the applicability and utility of multi-layer laminar flow lithography as a general fabrication technique for microfluidic electrochemical devices. This work has been submitted in the journal *RSC Advances* [3].

v. Design, fabrication, and characterization of non-precious metal based membraneless MFCs using multi-layer laminar flow lithography. This work has been submitted in the journal *RSC Advances* [3].

Proton Exchange Membrane Materials

As was described in Chapter 3, to date the majority of the materials used in microfluidic fuel cell devices have been inherited from macroscaled fuel cell technology. While such materials are often very functional they can be costly and complicated to integrate into a microfluidic architecture. My work set out to address these concerns by developing a procedure for synthesizing polymer blends which can both function as proton exchange membranes and be photopolymerized within microchannels.

Membranes composed of PEGDA-sPEGPEA polymer blends were characterized for their mechanical, chemical, and physical properties with emphasis placed upon their behavior in aqueous environments (such as those found in MFCs). It was shown that by combining two types of functional groups (proton conducting sulfonic acid sites as well as photocrosslinkable acrylate groups), PEGDA-sPEGPEA composites could be selectively photopolymerized into solid structures with micron scale resolution (with feature sizes as small as 5 μm for arrays of lines). The chemical synthesis processes to produce PEGDA-sPEGPEA polymer blends was shown to be achievable on a standard bench-top environment using common processing techniques. Through extensive material characterization it was found that a 75:25 weight percent polymer blend of PEGDA:sPEGPEA yielded the most effective properties for implementation as a PEM. When examining the variation in properties of other PEGDA-sPEGPEA blends it was repeatedly observed that high levels of sPEGPEA increased hydrophillicty (and associated water absorption) to excessive amounts and were ill suited to usage as PEMs. Cryo-SEM imaging confirmed that the polymer blends with high sPEGPEA content formed exceedingly porous swollen networks. It was purposed that introducing a third component to the polymer blend (a higher order acrylate) could be used to lead to additional crosslinking which could reduce hydrophillicity and lead to more effective membrane materials. In this way, my method of using functionalized PEG derivatives can be augmented to create PEM materials with a wide range of properties tailorable to specific device implementations.

Gas Transport Modelling

For many microfluidic devices, control of environment parameters (temperature, pressure, dissolved gas concentration) is critical to device functionality. This is especially true for microfluidic cell culturing bio-reactors and air breathing fuel cells, where oxygen is consumed for cellular respiration, and cathode half-cell reactions, respectively. For these devices, knowledge of concentrations of dissolved gases is of the utmost importance to maintain healthy cells and stable power output, respectively. Two of the most important factors contributing to the amount of oxygen available in a microchannel are the device geometry (*i.e.* channel depth, length etc.) and material properties. My work established finite element model simulating transport of oxygen in a microchannel from both saturated inflowing fluid and diffusion from the external environment. In Chapter 4, such a simulation architecture was shown to be of great utility for determining appropriate design parameters for microdevices (to ensure sufficient but not excessive levels of oxygen throughout a device).

For both microfluidic bio-reactors and air breathing MFC devices, specific emphasis was placed on determining the relationship between the properties of the capping layer (the upper surface which encloses a planar microfluidic device) and the amount of oxygen present in a flowing microfluidic channel. Simulations predicted oxygen concentration profiles by including contributions from both diffusion (*i.e.* oxygen flowing through the capping layer and into the microchannel from the external environment) as well as convection (*i.e.* transport of dissolved oxygen contained within the fluid flowing into the microchannel). An integral component of these simulations was allowing for non-uniform oxygen concentration within the capping layer (as opposed to fixing oxygen concentration at a saturated value as is common in literature), this allowed for a more physically accurate representation of oxygen concentration within the microchannel.

Simulations varied device geometry (channel height, and capping layer height/material) and applied flow rates over a wide range of values to predict oxygen concentration profiles for both types of devices. It was found that both the thickness and material (as represented by solubility and diffusivity constants) of the capping layer had a large effect on the relative importance of diffusive and convective mass transport of oxygen. Even for highly permeable materials such as PDMS, thick capping layers (on the order of mms) were predicted to drastically lessen the amount of oxygen flowing into the channel through diffusion.

For microfluidic cell culturing devices (operating at literature cell densities and flow rates) it was predicted that diffusion through the capping layer is the most important source of oxygen mass transport. Furthermore it was found that by varying the rate of fluid flow complex varying oxygen concentration profiles could be formed across the length of the microchannel. Air-breathing MFC devices (using literature values of cathodic current density) have higher rates of oxygen consumption than microfluidic cell culturing devices. Simulations of air-breathing MFC devices showed that diffusion alone is insufficient to supply maintain high levels of steady state cathodic current output (*i.e.* above 1 mA/cm^2). These simulations highlighted the importance of sufficiently high levels of catholyte flow rate to sustain steady cathodic current output.

For both types of devices, FEM simulations were shown to be a predictive tool to determine appropriate experimental conditions (in terms of capping layer properties and magnitude of applied flow rates) to ensure sufficient oxygen concentrations. The methods presented here have wide applicability and can be adapted to guide the design of future microfluidic devices where dissolved gasses are consumed. For emerging devices such as microbial MFCs the results of these simulations could be applied two-fold to determine appropriate device parameters for both effective growth of microbes in the anode and cathode half cells (either restricting or supplying oxygen, respectively) and removal of waste gases.

Multi-Layer Laminar Flow Lithography

While microfluidic devices have increased in utility (and ubiquity) in modern research they have also increased in complexity (in terms of both device architecture and fabrication). One of the key aims of microfluidic technology is to yield inexpensive, easily producible devices capable of performing complex tasks. To aid in this goal, I focused my efforts on improving laminar flow based patterning techniques to yield multi-layer *in situ* laminar flow lithography. This technique was shown to be a low cost method of effectively patterning multi-layer thin film stacks to yield independent electrodes of different materials without photolithography. Such a fabrication technique has applications for numerous types of microfluidic devices including sensors, transducers, and fuel cells.

As described in Chapter 5, extensive FEM simulations were undertaken to characterize patterning by laminar-flow lithography by modelling the relationship between experimental factors (device geometry, fluid composition, and fluid flow rates) on the breadth and location of etching within sealed microchannels. A calibration process was used to relate predicted etchant profiles to etch widths measured in physical devices. In this way, the FEM model was found to be useful in predicting appropriate flow rates to achieve a desired etched region through LFL. Physical experiments were carried out to determine the effectiveness of multi-layer LFL as a general patterning technique for microfluidic devices including etch pitch and parallelizability. It was found that, in my devices, etch widths as small as 50 µm could be obtained and LFL processes could be conducted simultaneously in two parallel microchannels. These investigations also showed how two (Ag-Ni) and three (Ag-Au-Ni) metal thin films stacks deposited via conventional magnetron sputtering could be patterned *in situ* by combining successive stages of two-stream and three-stream LFL etches. Processing was undertaken using conventional wet etchant solutions (in this case commercial potassium iodide/iodine based Au etchant, ferric chloride, and nitric acid) which have known etch rates and metal compatibilities.

Membraneless MFC Devices

After having established the utility of multi-layer laminar flow lithography patterning, my efforts turned to applying this technique to yield functional membraneless MFCs. As described in Chapter 2, many of the MFC devices which have been presented in literature to date have relied upon costly materials (*i.e.* precious metal Pt/Pd catalysts) and unfavourable operational conditions (*i.e.* high applied reactant flow rates that necessitate bulky external pumps). I designed a polymer MFC architecture which was capable of operation at low flow rates, using non-precious metal catalysts. These design parameters were paired with electrode patterning through multi-layer laminar flow lithography yielding an architecture amendable to lost-cost fabrication from inexpensive materials. Such a device architecture is well suited to cost-critical environments such as single use lab-on-a-chip diagnostic devices where cost per device is of the utmost importance.

As described in Chapter 5, devices were operated using dilute methanol (anolyte) and dilute hydrogen peroxide (catholyte) solutions combined with $Ni(OH)_2$/NiOOH (anode) and Ag_2O (cathode) non-precious metal catalytic electrodes. Electrical characterization experiments demonstrated that Ag-Ni DMFCs functioned as fuel cells but were limited in several ways. Firstly, while less expensive than conventional Pt and Pd based catalyst materials, Ag_2O and $Ni(OH)_2$/NiOOH were less effective catalysts and as such devices were limited to modest voltage and power outputs (with peak measured voltages of 185 mV and a peak output power density of 12.0±0.4 $\mu W/cm^2$ while flowing 10 µL/min of anoylte and catholyte solutions). Secondly, it was found that the devices were limited to an operational flow rate range of 0.1 – 10 µL/min, due to excessive mixing (at low flow rates leading to mixed potentials) and excessive bubble formation (from hydrogen peroxide decomposition disrupting the steady laminar flow within the device). However, the output properties of these devices was similar to an analogous system (also using Ag_2O and $Ni(OH)_2$/NiOOH catalysts) described by Sung et al. which was patterned using conventional photolithography and electroplating techniques. As such, these devices demonstrated that multi-layer LFL is indeed able to produce functional devices on par with conventional patterning techniques. Further experimentation of MFC devices patterned with LFL using different anolyte/anode and catholyte/cathode combinations show promise to yield more effective devices. The multi-layer LFL patterning processes described here can be applied to pattern surfaces in other types of microfluidic devices provided compatible wet etchant solutions are available.

6.2 Proposed Research Directions

Throughout this thesis, work has been focused on improving the utility of planar MFC devices through developing new materials and methods to simplify, expedite, and decrease the cost of devices fabrication. Future work to further enhance MFC devices, which can build on my methods, can be broadly classified into two groups: *in situ* fabrication techniques and MFC integration.

In situ **Fabrication Techniques**

This thesis has shown how *in situ* processes can be used to enhance device fabrication. My methods were applied to enhance two subcomponents of MFC devices, formation of PEM and patterning of electrode surfaces. Future work could expand upon the utility of *in situ* fabrication for MFCs in several ways.

Firstly, my PEM fabrication technique, described in Chapter 3, could be expanded to yield blends incorporating a wider range of polymers, with variety in functional groups. Through the addition of function groups with specific chemical reactivity, membranes could be formed with higher selectivity to specific anolyte or cathoylte compounds in a given device architecture (*i.e.* to reduce the amount of crossover between the anode and cathode half cells), transport of anions rather than protons, or alter the overall structure of the polymeric network to tailor mechanical rigidity and porosity. By specifically controlling the length of monomer chains used in the blend membranes porosity could be controlled to allow for *in situ* formation of scaffolds to restrict passage of larger structures such as cells. Such a method would be useful for planar microbial MFCs where specific species of microbes are restricted to the anode or cathode half cells [4].

Secondly, in Chapter 5, multi-layer LFL was shown to be an effective method to pattern electrodes to yield functional planar MFC devices. My work focused on patterning of flat metallic electrodes formed through sputter deposition. As was described in Section 2.2.4, usage of porous electrodes, rather than planar electrodes, can increase the electro-active surface area and boost device efficiency [5]. Future usage of multi-layer LFL could adapt my methods to pattern porous electrodes through combination of additive and subtractive LFL processes. In such a method, a porous electrode coated with catalytic material could be placed in the bulk of a microchannel and then divided (mechanically and electrically) into anode and cathode half cells using a three-stream LFL etch. Alternatively, a bare porous scaffold could be formed within the microchannel (using a process similar to the PEM experiments in Chapter 3) and selectively metallized with three-stream additive LFL (flowing electroless plating solutions), and then divided using subtractive LFL (flowing etchant in the middle stream) [6]. In this way, highly functional planar MFC devices with porous electrodes could be patterned *in situ*.

Integration and Scaling of MFCs

Much of the appeal of microfluidic devices stems from their ability to be parallelized into large networks, performing multiple functions simultaneously (for applications such as sensing, lab-on-a-chip diagnostics etc.) [7]. Parallelized networks of planar MFCs are one route to achieving on-device power. Chapter 5 of this thesis has described how electrodes in parallelized networks of planar microchannels can be patterned via multi-layer LFL. Future work can apply these methods to create parallelized networks of MFCs and asses the utility (and scalability) of power generation using these techniques. Simulations of oxygen transport in Chapter 3, revealed that for effective operation of planar air-breathing MFC devices formed out of PDMS, PMMA, and COC high catholyte flow rates are required (as diffusive transport through the capping layer is insufficient to sustain high levels of steady state cathodic current). Future work should expand the developed FEM model and apply it to assess the ability of different materials and channel geometries to yield more effective planar air-breathing MFC devices. Lastly, this thesis has focused specifically on improving planar MFCs to allow for simple integration into larger planar microfluidic devices (*i.e.* the ability to add on-board power generation to a device by designing an extra microchannel which can be independently operated as an MFC). Future work should assess how factors such as microchannel height and width affect planar MFC power output to determine appropriate channel structures required to power different types of microfluidic devices.

6.3 References

[1] "Photopolymerizable sulfonated poly(ethylene glycol) proton exchange membranes for microfluidic fuel cell applications" Nearingburg B, Elias A L *Journal of Membrane Science* 389 (2012) 148-154.

[2] "Finite element analysis of oxygen transport in microfluidic cell culturing devices with varying channel architectures , perfusion rates, and materials" Zahorodny-Burke M, Nearingburg B, Elias A L *Chemical Engineering Science* 66 (2011) 6244-6253.

[3] "Patterning multilayer microfluidic electrochemical devices by maskless laminar flow lithography" Nearingburg B, Elias A L *RSC Advances* Submitted May 20, 2014.

[4] "Micro-sized microbial fuel cell: A mini-review" Wang H, Bernarda A, Huang C, Lee D, Chang J *Bioresource Technology* 102 (2011) 235-243.

[5] "A microfluidic fuel cell with flow-through porous electrodes" Kjeang E, Michel R, Harrington D A, Djilali N, Sinton D *Journal of the American Chemical Society* 130 (2008) 4000-4006.

[6] "Electroless deposition and structuring of silver electrodes in close microfluidic capillaries" Hueck F C A, Staufer U *Journal of Micromechanical Systems* 20 (2011) 451-459.

[7] "The burgeoning power of the shrinking laboratory" Ramsey J M *Nature Biotechnology* 17, (1999) 1061 – 1062.

6.4 Grand Unified Bibliography

Here follows a bibliography of every source used in this thesis. The bibliography has been alphabetized by first author last name.

“Lab-on-chip technologies: making a microfluidic network and coupling it into a complete microsystem – a review” Abgrall P, Gue A M *Journal of Micromechanics and Microengineering* 17 (2007) R15.

“Platinum monolayer fuel cell electrocatalysts” Adzic R R, Zhang J, Sasaki K, Vukmirovic M B, Shao M, Wang J X, Nilekar A U, Mavrikakis M, Valerio J A, Uribe F *Topics in Catalysis* 46 (2007) 249-262.

“Formation of steady-state oxygen gradient in vitro: application to liver zonation” Allen J W, Bhatia S N *Biotechnology and Bioengineering* 82 (2003) 253-262.

“Palladium in fuel cell catalysts” Anatoli E *Energy and Environmental Science* 2 (2009) 915-931.

“Topology optimization of microfluidic mixers” Andreasen C S, Gersborg A R, Sigmund O *International Journal For Numerical Methods in Fluids* 61 (2009) 498-513.

“Fuel cells: History and updating. A walk along two centuries” Andujar J M, Segura F *Renewable and Sustainable Energy Reviews* 13 (2009) 2309-2322.

“Controlled microfluidic interfaces” Atencia J, Beebe D J *Nature* 437 (2005) 648-655.

“A class of non-precious metal composite catalysts for fuel cells” Bashyam R, Zelenay P *Nature* 443 (2006) 63-66.

“Improved fuel utilization in microfluidic fuel cells: A computational study” Bazylak A, Sinton D, Djilali N *Journal of Power Sources* 143 (2005) 57-66.

“Polymer microfabrication technologies for microfluidic systems” Becker H, Gartner C *Analytical and Bioanalytical Chemistry* 390 (2008) 89-111.

“Polymer microfluidic devices” Becker H, Locascio L E *Talanta* 56 (2002) 267-287.

“Functional hydrogel structures for autonomous flow control inside microfluidic channels” Beebe D J, Moore J S, Bauer J M, Yu Q, Liu R H, Devadoss C, Jo B H *Nature* 404 (2000) 588-590.

“Engineers are from PDMS-land, Biologists are from Polystyrenia” Berthier E, Young E W, Beebe D *Lab on a Chip* 12 (2012) 1224-1237.

“FTIR Microspectroscopy of Polymeric Systems” Bhargava R, Wang S Q, Koeing J L *Advances in Polymer Science* 163 (2003) 137-191.

“Review of proton exchange membrane fuel cell models” Bıyıkoglu A *International Journal of Hydrogen Energy* 30 (2005) 1181-1212.

“Polymer membranes for high temperature proton exchange membrane fuel cell: Recent advances and challenges” Bose S, Kuila T, Nguyen T X H, Kim N H, Lau K, Lee J H *Progress In Polymer Science* 36 (2011) 813-843.

“Pt submonolayers on Ru nanoparticles, A novel low Pt loading, high CO tolerance fuel cell electrocatalyst” Brankovic S R, Wang J X, Adzic R R *Electrochemical and Solid-State Letters* 4 (2001) A217-A220.

"Alkaline Microfluidic Hydrogen-Oxygen Fuel Cell as a Cathode Characterization Platform" Brushett F R, Zhou W P, Jayashree R S, Kenis P J A *Journal of the Electrochemical Society* 156 (2009) B565-B571.

"Investigation of fuel and media flexible laminar flow-based fuel cells" Brushette F R, Jayashree R S, Zhou W P, Kenis P J A *Electrochimica Acta* 54 (2009) 7099-7105.

"Acoustofluidics 1: Governing equations in microfluidics" Bruus H *Lab On A Chip* 11 (2011) 3742-3751.

"FEM-based oxygen consumption and cell viability models for avascular pancreatic islets" Buchwald P *Theoretical Biological Modelling* 6 (2009) 5.

"Aromatic Nucleophilic Substitution Reactions" Burnett J F, Zahler R E *Chemistry Reviews* 49 (1951) 273-412.

"Micromixing within microfluidic devices" Capretto L, Cheng W, Hill M, Zhang X *Topics in Current Chemistry* 304 (2011) 27-68.

"Molecular structure and transport dynamics in Nafion and sulfonated poly(ether ether ketone ketone) membranes" Chen P Y, Chiu C P, Hong C W *Journal of Power Sources* 194 (2009) 746-752.

"A review on non-precious metal electrocatalysts for PEM fuel cells" Chen Z, Higgins D, Yu A, Zhang L, Zhang J *Energy and Environmental Science* 4 (2011) 3167-3192.

"Microfluidic Electronics" Cheng S, Wu Z *Lab On A Chip* 12 (2012) 2782-2791.

"Key Requirements of micro fuel cell systems for portable electronics" Chenggang X, Jeanne P, Hallmark J, Bostaph J, Fisher A *Energy Conversion Engineering Conference*, 2002 (2004) 603-606.

"Microfluidic Fuel Cell Based On Laminar Flow" Choban E R, Markoski L J, Wieckowski A, Kenis P J A *Journal Of Power Sources* 128 (2004) 54-60.

"Membraneless laminar flow-based micro fuel cells operating in alkaline, acidic, and acidic/alkaline media" Choban E R, Spendelow J S, Gancs L, Wieckowski A, Kenis P J A *Electrochimica Acta* 50 (2005) 5390-5398.

"Characterization of Limiting Factors In Laminar Flow-Based Membraneless Microfuel Cells" Choban E R, Waszczuk P, Kenis P J A *Electrochemical and Solid State Letters* 8 (2005) A348-A352.

"Quantitatively controlled in situ formation of hydrogel membranes in microchannels for generation of stable chemical gradients" Choi E, Jun I, Chang H, Park K M, Shin H, Park K D, Park J *Lab on a Chip* (2012) 302-308.

"Thermodynamics and Proton Transport in Nafion II: Proton Diffusion Mechanisms and Conductivity" Choi P, Jalani N H, Datta R *Journal of The Electrochemical Society* 152 (2005) E123-E130.

"A uL-scale micromachined microbial fuel cell having high power density" Choi S C, Lee H, Yang Y, Parameswaran P, Torres C I, Rittmann B E, Chae J *Lab On A Chip* 11 (2011) 1110-1117.

"A dual electrolyte H2/O2 planar membraneless microchannel fuel cell system with open circuit potentials in excess of 1.4V" Cohen J L, Volpe D J, Westly D A, Pechenik A, Abruna H D *Langmuir* 12 (2005) 3544-3550.

“Fabrication and preliminary testing of a planar membraneless microchannel fuel cell” Cohen J L, Westly D A, Pechenik A, Abruna H D *Journal of Power Sources* 139 (2005) 96-105.

“Exploratory FEM-based Multiphysics Oxygen Transport and Cell Viability Models for Isolated Pancreatic Islets” *COMSOL Conference* Boston USA.

E. L. Cussler, Diffusion: mass transfer in fluid systems, 2009, Cambridge University Press.

“The current status of fuel cell technology for mobile and stationary applications” de Bruijn F *Green Chemistry* 7 (2005) 132-150.

“Formic acid microfluidic fuel cell evaluation in different oxidant conditions” Dector A, Esquivel J P, Gonzalez M J, Guerra-Balacazar M, Ledesma-Garcia J, Sabate N, Arriga L G *Electrochimica Acta* 92 (2013) 31-35.

“Membranes and microfluidics: a review” deJong J, Lammertink R G H, Wessling M *Lab On A Chip* 6 (2006) 1125-1139.

“Control and detection of chemical reactions in microfluidic systems” deMello A J *Nature* 442 (2006) 394-402.

“Generation of gradients having complex shapes using microfluidic networks” Dertinger S K W, Chiu D T, Jeon N L, Whitesides G M *Analytical Chemistry* 73 (2001) 1240-1246.

“Microfluidic Sub-millisecond Mixers for the study of chemical reaction kinetics” Desai A, Bokenkamp D, Yang X, Tai Y C *Transducers ‘97* (1997) 167-170.

“Surface modification of thermoplastics - towards the plastic biochip through high throughput screening devices" Diaz-Quijada G A, Peytavi R, Nantel A, Roy E, Bergeron M G, Dumoulin M M, Veres T *Lab on a Chip* 7 (2007) 856-862.

"Measuring the Young's Relaxation Modulus of PDMS using stress relaxation nanointendation" Du P, Lu Hongbing, Zhang X *Material Research Society Symposium Proceedings* 1222 (2010) 1222-DD02-03.

"Rapid Prototyping of Microfluidic Systems In Poly(dimethylsiloxane)" Duffy D C, McDonald J C, Schueller O J A, Whitesides G M, *Analytical Chemistry* 70 (1998) 4974-4984.

"Microfluidic Cell Culture Devices" Elias A. L., Nearingburg B, Zahorodny-Burke M in Microfluidics and Nanofluidics Handbook. CRC Press Editors: Mitra S K, Chakraborty S, 2011.

"Integrated Microfluidic Devices" Erickson D, Li D *Analytica Chimica Acta* 507 (2004) 11-26.

"Membraneless Vanadium Redox Fuel Cell Using Laminar Flow" Ferrigno R, Stroock A D, Clark T D, Mayer M, Whitesides G M *Journal of the American Chemical Society* 124 (2004) 12930-12931.

"Membraneless Vanadium Redox Fuel Cell Using Laminar Flow" Ferrigno S, Stroock A D, Clark T D, Mayer M, Whitesides G M *Journal of the American Chemical Society* 124 (2002) 12930-12931.

"Fabrication of thermoset polyester microfluidic devices and embossing masters using rapid prototyped polydimethylsiloxane molds" Fiorini G S, Jeffries G D M, Lim D S W, Kuyper C L, Chiu D T *Lab on a Chip* 3 (2003) 158-163.

"Micro reactors: principles and applications in organic synthesis" Fletcher P D I, Haswell S J, Pombo-Villar E, Warrington B H, Watts P, Wong S Y F, Zhang X L *Tetrahedron* 58 (2002) 4735-4757.

“Up-scaled microfluidic fuel cells with porous flow-through electrodes” Fuerth D, Bazylak A *Journal of Fluids Engineering* 135 (2013) 021102.

“Technology and Applications Of Microengineered Reactors” Gavriilidis A, Angeli P, Cao E, Yeong K K, Wan Y S S *Chemical Engineering Research and Design* 80 (2002) 3-30.

“Ionomeric membranes for proton exchange membrane fuel cell (PEMFC): sulfonated polysulfone associated with phosphatoantimonic acid” Genova-Dimitrova P, Baradie B, Foscallo D, Poinsignon C, Sanchez J Y *Journal of Membrane Science* 185 (2001) 59-71.

“Microreactors as tools for synthetic chemists – The chemists’ round-bottomed flask of the 21st century?” Geyer K, Codee J D C, Seeberger P H *Chemistry – A European Journal* 12 (2006) 8434-8442.

“Contact Angle, Wetting, and Adhesion: a critical review” Good R J *Journal of Adhesion Science and Technology* 6 (1992) 1269-1302.

“Micro-structured analytical instrumentation for the analysis of liquids” Grab B, Weber G, Neyer A, Schilling M, Hergenroder R, *Spectrochimica Acta Part B: Atomic Spectroscopy* 57 (2002) 1575-1583.

“Microfluidics - a review” Gravesen P, Branebjerg, J, Jensen O. S. *Journal of Micromechanics and Microengineering* 3 (1993) 168-182.

“Rapid, cost-efficient fabrication of microfluidic reactors in thermoplastic polymers by combining photolithography and hot embossing” Greener J, Li W, Ren J, Voicu D, Pakharenko V, Tang T, Kumacheva E *Lab On A Chip* 10 (2010) 522-524.

“Computerized microfluidic cell culture using elastomeric channels and Braile displays” Gu W, Zhu X, Futai N, Cho B S, Takayama S *PNAS* 101 (2004) 15861-15866.

“Multiphase microfluidics: from flow characteristics to chemical and material synthesis” Gunther A, Jensen K F *Lab on A Chip* 6 (2006) 1487-1503.

“Methanol-tolerant electrocatalysts for oxygen reduction in a polymer electrolyte membrane fuel cell” Gupta S, Tryk D, Zecevic S K, Aldred W, Guo D, Savinell R F *Journal of Applied Electrochemistry* 28 (1998) 673-682.

“The kinetics and mechanism of the nickel electrode- III. The potentiodynamic response of nickel electrodes in alkaline solutions in the potential region of Ni(OH)2 formation” Guzman R S S, Vilche J R, Arvia A J, *Corrosion Science* 18 (1978) 765-778.

“Integrated simulation of tritium permeation in solid breeder blankets” Haeberle S, Zengerle R *Lab on A Chip* 7 (2007) 1094-1110.

“Microfluidic platforms for lab-on-a-chip applications” Haeberle S, Zengerle R *Lab On A Chip* 7 (2007) 1094-1110.

“A personal stroll through the historical development of canadian microfludics” Harrison J, *Lab On A Chip* 13 2013 2500-2503.

“Electricity Generation From Decomposition of Hydrogen Peroxide” Hasegawa S, Shimotani K, Kishi K, Watanabe H *Electrochemical and Solid State Letters* 8 (2005) A119-A121.

“Review on micro moulding of thermoplastic polymers” Heckele M, Schomburg W K *Journal of Micromechanics and Micromachining* 14 (2004) R1-R14.

“Ionized physical vapour deposition (IPVD): A review of technology and applications” Helmersson U, Lattermann M, Bohlmark J, Ehiasarian A P, Gudmundsson J T *Thin Solid Films* 513 (1-24).

“Sulfonated aromatic hydrocarbon polymers as proton exchange membranes for fuel cells” Higashihara T, Matsumoto K, Ueda M *Polymer* 50 (2009) 5341-5357.

“Chemicofunctional Membrane for Integrated Chemical Processes on a Microchip” Hisamoto H, Shimuzu Y, Uchiyama K, Tokeshi M, Kikutani Y, Hibara A, Kitamori T *Analytical Chemistry* 75 (2003) 350-354.

“Planar multiplexing of microfluidic fuel cells” Ho B, Kjeang E *Journal of Fluids Engineering* 135 (2013) 021304.

“Nanoporous separator and low fuel concentration to minimize crossover in direct methanol laminar flow fuel cells” Hollinger A S, Maloney R J, Jayashree R S, Natarajan D, Markoski L J, Kenis P J A *Journal of Power Sources* 195 (2010) 3523-3528.

“Microflow electroorganic synthesis without supporting electrolyte” Horcajada R, Okajima M, Suga S, Yoshida *Journal of Chemical Communications* 10 (2005) 1303-1305.

“Gas separation properties in cyclic olefin copolymer membrane studied by positron annihilation, sorption, and gas permeation” Hu C C, Lee K R, Ruaan R C, Jean Y C, Lai J Y *Journal of Membrane Science* 274 (2006) 192-199.

"Zeolite-filled PMMA in composite membranes: influence of coupling agent addition on gas separation properties" Hu C C, Liu T C, Lee K R, Ruaan R C, Lai J Y *Desalination* 193 (2006) 14-24.

"Modeling of effects of nutrient gradients on cell proliferation in microfluidic bioreactor" Hu G, Quaranta V, Li D *Biotechnology Progress* 23 (2007) 1347-1354.

"Electroless deposition and structuring of silver electrodes in close microfluidic capillaries" Hueck F C A, Staufer U *Journal of Micromechanical Systems* 20 (2011) 451-459.

"Microfluidic Direct Methanol Fuel Cell with Ladder-Shaped Microchannel for Decreased Methanol Crossover" Huo W, Zhou Y, Zhang H, Zou Z, Yang H *International Journal of Electrochemical Science* 8 (2013) 4827-4838.

"PM 200 Fuel Cell Stack" Image accessed from http://www.directindustry.com/prod/proton-motor-fuel-cell/fuel-cell-stacks-22809-546082.html on March 5 2014. Image Copyright © Proton Motor Fuel Cell Systems (Germany), used with permission.

"Separation Through Dialysis, Solved With COMSOL Multiphysics 3.5a" in AB, C (Eds.). *COMSOL Multiphysics Chemical Engineering Module Model Library* (2008) version 3.4, 1-13.

"Air-Breathing Laminar Flow-Based Direct Methanol Fuel Cell with Alkaline Electrolyte" Jayashree R S, Egas D, Spendelow J S, Natarajan D, Markoski L J, Kenis P J A *Electrochemical and Solid State Letters* 9 (2006) A252-A256.

"Microreactor Engineering - is small better?" Jensen K F *Chemical Engineering Science* 56 (2001) 293-303.

"Dynamic mechanical analyses of polymeric systems of pharmaceutical and biomedical significance" Jones D S *International Journal of Pharmaceutics* 179 (1999) 167-178.

"Microfabricated Devices For Fluid Mixing and Their Applications for Chemical Sensing" Kakuta M, Bessoth F G, Manz A *The Chemical Record* 1 (2001) 395-405.

"Viscoelastic characterization of UV polymerized poly(ethylene glycol) diacrylate networks with varying extents of crosslinking" Kalakkunnath S, Kalika D S, Lin H, Freeman B D *Journal of Polymer Science B: Polymer Physics* 44 (2006) 2058–2070.

"Overview on the challenges and developments of micro-direct methanol fuel cells (DMFC)" Kamarudin S K, Daud W R W, Ho S L, Hasran U A *Journal Of Power Sources* 163 (2007) 743-754.

"Quantitative Analysis Of Molecular Interaction in a Microfluidic Channel: The T-Sensor" Kamholz A E, Weigl B H, Finlayson B A, Yager P *Analytical Chemistry* (1999) 71, 5340-5347.

"Microfabricated microfluidic fuel cells" Kamitani A, Morishita S, Kotaki H, Arscott S *Sensors and Actuators B: Chemical* 154 (2011) 174-180.

"Fabrication inside Microchannels Using Fluid Flow" Kenis P J A, Ismagilov R F, Takayama S, Whitesides G H, Li S, White H S, *Accounts of Chemical Research* 33 (2000) 841-847.

"Micropatterning Inside Capillaries Using Multiphase Laminar Flow Patterning" Kenis P J A, Ismagilov R F, Whitesides G M *Science* 285 (1999) 83-85.

"Microscale technologies for tissue engineering and biology" Khademhosseini A, Langer R, Borenstein J, Vacanti J P *Proceedings of the National Academy of Sciences of the United States of America* 103 (2006) 2480-2487.

“Preparation and properties of PEG hydrogel from PEG macromonomer with sulfonate end groups” Kim J H, Kim J G, Kim D, Kim Y H *Journal Applied Polymer Science* 96 (2005) 56-61.

“Proton conductivities and methanol permeabilities of membranes made from partially sulfonated polystyrene-block-poly(ethyelene-ran-butylene)-block-polystyrene copolyers” Kim J, Kim B, Jung B *Journal of Membrane Science* 207 (2002) 129-137.

“Soft Lithography for Microfluidics: a Review” Kim P, Kwon K W, Park M C, Lee S H, Kim S M, Suh K Y *Biochip Journal* 2 (2008) 1-11.

“A review on fuel cell technology and power electronic interface” Kirubakaran A, Jain S, Nema R K *Renewable and Sustainable Energy Reviews* 13 (2009) 2430-2440.

“Hydrogen peroxide as an oxidant for microfluidic fuel cells” Kjeang E, Brolo A G, Harrington D A, Djilali N, Sinton D *Journal of The Electrochemical Society* 154 (2007) B1220-B1226.

“Microfluidic Fuel Cells: A Review” Kjeang E, Djihali N, Sinton D *Journal Of Power Sources* 186 (2009) 353-369.

“Planar and three-dimensional microfluidic fuel cell architectures based on graphite rod electrodes” Kjeang E, McKechnie J, Sinton D, Djihali N *Journal Of Power Sources* 168 (2007) 379-390.

“A microfluidic fuel cell with flow-through porous electrodes” Kjeang E, Michel R, Harrington D A, Djilali N, Sinton D *Journal of the American Chemical Society* 130 (2008) 4000-4006.

“An alkaline microfluidic fuel cell based on formate and hypochlorite bleach” Kjeang E, Michel R, Harrington D A, Sinton D, Djilali N *Electrochemica Acta* 54 (2008) 698-705.

"High-performance microfluidic vanadium redox fuel cell" Kjeang E, Proctor B T, Brolo A G, Harrington D A, Djilali N, Sinton D *Electrochimica Acta* 52 (2007) 4942-4946.

"Liquid Flow in microchannels: experimental observation and computational analyses of microfluidic effects" Koo J, Kleinstreuer C *Micromechanics and Microengineering* 13 (2003) 568-579.

"Micro-fuel-cells-current developments and applications" Kundu A, Jang J H, Gil J H Jung C R, Lee H R, Kim S H, Ku B, Oh Y S *Journal of Power Sources* 170 (2007) 67-78.

"Stretchable gold conductors on elastomeric substrates" Lacour S P, Wagner S, Huang Z, Suo Z *Applied Physics Letters* 82 (2003) 2404-2406.

"Progress and trends in ink-jet printing technology" Le H P *Journal of Imaging Science and Technology* 1 (1998) 49-62.

"Polymer Electrolyte Membranes for Fuel Cells" Lee J S, Quan N D, Hwang J M, Lee S D, Kim H, Lee H, Kim H S *Journal of Industrial Engineering Chemistry* 12 (2006) 175-183.

"A laser-micromachined polymeric membraneless fuel cell" Li A, Chan S H, Nguyen N *Journal of Micromechanics and Microengineering* 17 (2007) 1107-1113.

"Lab-On-A-Chip: A Component View" Lim Y C, Kouzani A Z, Duan W *Microsystem Technologies* 16 (2010) 1995-2015.

"PEM Fuel Cell Electrodes" Litster S, McLean G *Journal of Power Sources* 130 (2004) 61-76.

"Recent Developments In Polymer MEMS" Liu C, *Advanced Materials* 19 (2007) 3783-3790.

"Oxygen gradients for open well cellular cultures via microfluidic substrates" Lo J F, Sinkala E, Eddington D T *Lab on A Chip* 10 (2010) 2394-2401.

"Design, fabrication, and characterization of a planar silicon-based, monolithically integrated micro laminar flow fuel cell with a bridge shaped microchannel cross-section" Lopez-Montesinos P O, Yossakda N, Brushet F R, Pelton W E, Kenis P J A *Journal of Power Sources* 196 (2011) 4638-4645.

"Microfabricated Multiphase Packed-Bed Reactors: Characterization of Mass Transfer and Reactions" Losey M W, Schmidt M A, Jensen K F (2001) *Industrial and Engineering Chemistry Research* 40 (2001) 2555-2562.

"MEMS-based power generation techniques for implanting biosensing applications" Lueke J, Moussa W A *Sensors* 11 (2011) 1433-1460.

"In situ generation of pH gradients in microfluidic devices for biofabrication of freestanding, semi-permeable chitosan membranes" Luo X, Berlin D L, Betz J, Payne G F, Bentley W E, Rubloff G W *Lab on a Chip* 10 (2010) 59-65.

"Miniaturized Total Chemical Analysis Systems: a Novel Concept In Chemical Sensing" Manz A, *Sensors and Actuators B* (1990) 244-248.

"Microfluidic lab-on-a-chip platforms: requirements , characteristics, and applications" Mark D, Haeberle S, Roth G, von Stetten F, Zengerle R *Chemical Society Reviews* 39 (2010) 1153-1182.

"Handbook of Radical Polymerization" Matyjaszewski K, Davis T P John Wiley and Sons, 2002.

"Miniature fuel cells for portable power: Design considerations and challenges" Maynard H L, Meyers J P *Journal of Vacuum Science and Technology B* 20 (2002) 1287-1297.

"Poly(dimethylsiloxane) as a material for fabricating microfluidic devices" McDonald J C, Whitesides G M *Accounts of Chemical Research* 35 (2002) 491-499.

"Direct Methanol Fuel Cells" McGrath *Journal Of Industrial Engineering Chemistry* 10 (2004) 1063-1080.

"Hard Top Soft Bottom Microfluidic Devices for Cell Culture and Chemical Analysis" Mehta G, Lee J, Cha W, Tung Y C, Linderman J J, Takayama S *Analytical Chemistry* 81 (2009) 3714-3722.

"Quantitative measurement and control of oxygen levels in microfluidic poly(dimethylsiloxane) bioreactors during cell culture" Mehta G, Mehta K, Sud D, Song J W, Bersano-Begey T, Futai N, Heo Y S, Mycek M A, Lindermann J J, Takayama S *Biomedical Microdevices* 9 (2007) 123-134.

"Model-based analysis and design of a microchannel reactor for tissue engineering" Mehta K, Lindermann J *Journal of Biotechnology and Bioengineering* (2006) 94 596.

"Review and Analysis of PEM Fuel Cell design and manufacturing" Mehta V *Journal Of Power Sources* 114 (2003) 32-53.

"Review and Analysis of PEM Fuel Cell design and manufacturing" Mehta V, Cooper J S *Journal Of Power Sources* 114 (2003) 32-53.

"Mixing processes in a zigzag microchannel: finite element simulations and optical study" Mengeaud V, Josserand J, Girault H H *Analytical Chemistry* 74 (2002) 4279-4286.

"Gas sorption, diffusion, and permeation in poly(dimethylsiloxane)" Merkel T C, Bondar V I, Nagai K, Freeman B D, Pinnau I *Journal of Polymer Science B: Polymer Physics* 38 (2000) 415-434.

"Microfluidic devices for energy conversion: planar integration and performance of a passive, fully immersed H2-O2 fuel cell" Mitrovski S M, Elliott L C C, Nuzzo R G *Langmuir* 20 (2004) 6974-6976.

"A passive microfluidic hydrogen-air fuel cell with exceptional stability and high performance" Mitrovski S M, Nuzzo R G *Lab on A Chip* 6 (2006) 353-361.

"Microchip-based ethanol/oxygen biofuel cell" Moore C M, Minteer S D, Martin R S *Lab on A Chip* 5 (2005) 218-225.

"In Situ fabricated porous filters for microsystems" Moorthy J, Beebe D J *Lab on A Chip* 3 (2003) 62-66.

"Performance increase of microfluidic formic acid fuel cell using Pd/MWCTs as catalyst" Morales-Acosta D, Rodriguez H, Godinez L A, Arriga L G *Journal of Power Sources* 195 (2010) 1862-1865.

"Formic acid microfluidic fuel cell based on well-defined Pd nanocubes" Moreno-Zuria A, Dector A, Esquivel J P, Gonzalez M J, Guerra-Balacazar M, Ledesma-Garcia J, Sabate N, Arriga L G, Chavez-Ramirez A U *Journal of Physics: Conference Series* 476 (2013) 012033.

"Micro-fuel cell power sources" Morse J D *International Journal of Energy Research* 31 (2007) 576-602.

"A MEMS-based reformed methanol fuel cell for portable power" Morse J D, Graff R T, Spadaccini C, Park H G,Hart E K *Journal Micromechanics and Microengineering* 17 (2007) S237-S242.

“MEMS-based design and fabrication of a new concept micro direct methanol fuel cell (u-DMFC)” Motokawa S, Mohamedi M, Momma T, Shoji S, Osaka T *Electrochemistry Communications* 6 (2004) 562-565.

“Laminar flow used as “liquid etch mask” in wet chemical etching to generate glass microstructures with an improved aspect ratio” Mu X, Liang Q, Hu P, Ren K, Wang Y, Luo G *Lab on A Chip* 9 (2009) 1994-1996.

“Selectively modified microfluidic chip for solvent extraction of Radix Salvia Miltiorrhiza using three-phase laminar flow to provide liquid-liquid interface area” Mu X, Liang Q, Hu P, Ren K, Wang Y, Luo G, *Lab on A Chip* 9 (2009) 1994-1996.

“Chemical modification of polymeric microchip devices” Muck A, Svatos A *Talanta* 74 (2007) 333-341.

“Mass transfer and performance of membrane-less micro fuel cell: A review” Nasharudin M N, Kamarudin S K, Hasran U A, Masdar M S *International Journal of Hydrogen Energy* 39 (2014) 1039-1055.

“Patterning multilayer microfluidic electrochemical devices by maskless laminar flow lithography” Nearingburg B, Elias A L *Lab on a Chip* Submitted March 31, 2014.

“Micromixers—a review” Nguyen N T and Wu Z *Journal of Micromechanics and Microengineering* 15 (2005) R1–R16.

“Micromachined polymer electrolyte membrane and direct methanol fuel cells – a review” Nguyen N T, Chan S H *Journal of Micromechanics and Microengineering* 16 (2006) R1-R12.

“Nanoimprint lithography in the cyclic olefin copolymer, Topas, a highly ultraviolet-transparent and chemically resistance thermoplast” Nielsen T, Nilsson D, Bundgaard F, Shi P, Szabo P, Geschke O, Kristensen A *Journal of Vacuum Science and Technology B* 22 (2004) 1770-1775.

“Cyclic olefin polymers: innovative materials for high-density multiwall plates” Niles W D, Coassin P J *ASSAY and Drug Development Technologies* 6 (2008) 577-590.

“Nafion-based composite polymer electrolyte membranes” Nouel K M, Fedkiw P S *Electrochimica Acta* 43 (1998) 2381-2387.

“Cyclic Olefin Polymers: emerging materials for lab-on-a-chip applications” Nunes P S, Ohlsson P D, Ordeig O, Kutter J P *Microfluidics and Nanofluidics* 9 (2010) 145-161.

“Diffusion and Flow Development In Co-Flowing Microchannel Streams” Oak J, Pence D V, Liburdy J A Microscale *Thermophysical Engineering* 5:3 (2001) 233-246.

“Microfluidics: Applications for analytical purposes in chemistry and biochemistry” Ohno K, Tachikawa K, Manz A *Electrophoresis* 29 (2008) 4443-4453.

“Selective microfabrication of silver electrodes inside a microchannel by multiphase laminar flow with a density difference” Paek S H, Choi Y K, Kim D S *Microelectronics Engineering* 87 (2010)1375-1378.

“Microfabrication of dual-opposite electrodes inside a microchannel by means of multiphase laminar flow with density difference” Paek S H, Yang W, Kim J S, Hwang C J, Choi Y K, Kim D S, *Micro and Nano Letters* (6) 2011 678-681.

“Review of the proton exchange membranes for fuel cell applications” Peighambardoust S J, Rowshanzamir S, Amjadi M *International Journal of Hydrogen Energy* 35 (2010) 9349-9384.

“On-chip micropatterning of plastic (cyclic olefin copolymer, COC) microfluidic channels for the fabrication of biomolecule microarrays using photografting methods” Pu Q, Oyesanya O, Thompson B, Liu S, Alvarez J C *Langmuir* 23 (2007) 1577-1583.

“A 1.5 uL microbial fuel cell for on-chip bioelectricity generation” Qian F, Baum M, Gu Q, Morse D E *Lab on a Chip* 9 (2009) 3076-3081.

“Architecture for portable direct liquid fuel cells” Qian W, Wilkinson D P, Shen J, Wang H, Zhang J *Journal of Power Sources* 154 (2006) 202-213.

“The burgeoning power of the shrinking laboratory” Ramsey J M *Nature Biotechnology* 17, 1061 - 1062 (1999)

“Materials For Microfluidic Chip Fabrication” Ren K, Zhou J, Wu H *Accounts Of Chemical Research* 46 (2013) 2396-2406.

“Electrochemical Detection in Polymer Microchannels” Rossier J S, Roberts M A, Ferrigno R, Girault H H *Analytical Chemistry* 71 (1999) 4294-4299.

“Fabrication of Multilayer Systems Combining Microfluidic and Microoptical Elements for Fluorescence Detection” Roulet J C, Vokel R, Herzig H P, Verpoorte E, de Rooij N F, Dandliker R, *Journal of Microelectromechanical Systems* 10 (2001) 482-491.

“Analysis of oxygen transport to hepatocytes in a flat-plate microchannel bioreactor” Roy P, Baskaran H, Tilles A W, Yarmush M L, Toner M *Annals of Biomedical Engineering* 29 (2001) 947-955.

“Effect of Chemical Structure and Crosslinking Density on the Thermo-mechanical Properties and toughness of meth(actylate) shape memory polymer networks” Safranski D L, Gall K *Polymer* 49 (2008) 4446-4455.

“Gas permeation properties of SPE membranes” Sakari T, Takenaka H, Wakabayashi N, Kawami K, Tori K *Journal of The Electrochemical Society* 132 (1985) 1328.

“Sequential flow membraneless microfluidic fuel cell with porous electrodes” Salloum K S, Hayes J R, Frissen C A, Posner J D *Journal of Power Sources* 180 (2008) 243-252.

“The Quantitative analysis of surfaces by XPS: a review” Seah M P *Surface and Interface Analysis* 2 (2004) 222-239.

“Continuous Microfluidic Reactors For Polymer Particles” Seo M, Nie Z, Xu S, Mok M, Lewis P C, Graham R, Kumacheva E *Langmuir* 21 (2005) 11614-11622.

“A review on membraneless laminar flow-based fuel cells” Shaegh S A M, Nguyen N T, Chan S H, *International Journal of Hydrogen Energy* 36 (2011) 5675-5694.

“An air-breathing microfluidic formic acid fuel cell with a porous planar anode: experimental and numerical investigations” Shaegh S A M, Nguyen N T, Chan S W *Journal of Micromechanics and Microengineering* 20 (2010) 105008.

“Proton exchange membrane fuel cell from low temperature to high temperature: Material challenges” Shao Y, Yin G, Wang Z, Gao Y *Journal of Power Sources* 167 (2007) 235-242.

"Transition From Laminar To Turbulent Flow In Liquid Filled Microtubes" Sharp K V, Adrian R J *Experiments In Fluids* 36 (2004) 741-747.

"Monolithic micro-direct methanol fuel cell in polydimethylsiloxane with microfluidic channel-integrated Nafion strip" Shen M, Walter S, Gijs M A M *Journal of Power Sources* 193 (2009) 761-765.

"Rapid Prototyping of Micro-Direct-Methanol Fuel Cell in PDMS With Microchannel Integrated Nafion Strip" Shen M, Walter S, Gijs M A M *Solid-State Sensors, Actuators, and Microsystems Conference* 2009 (2009) 533-536.

"Oxygen permeability of surface-modified poly(dimethylsiloxane) characterized by scanning electron microscopy" Shiku H, Saito T, Wu C C, Yasukawa T, Yokoo M, Abe H, Matsue T, Yamada H *Chemistry Letters* (2006) 35 234-235.

"Prototype miniature blood gas analyzer fabricated on a silicon wafer" Shoji S, Esashi M, Matsuo T *Sensors and Actuators* 14 (1988) 101-107.

"Microfluidic dissolved oxygen gradient generator biochip as a useful tool in bacterial biofilm studies" Skolimowski M , Nielsen M W, Emneus J, Molin S, Taboryski R, Sternberg C, Dufva M, Geschke O *Lab on A Chip* 10 (2010) 2162-2169.

"Solid polymer electrolyte membranes for fuel cell applications - a review" Smitha B, Sridhar S, Kahn A A *Journal of Membrane Science* 259 (2005) 10-26.

"Reactions in droplets in microfluidic channels" Song H, Chen D L, Ismagilov R F *Angewandte Chemie-International Edition* 45 (2006) 7336-7356.

"Rapid fabrication of microfluidic polymer electrolyte membrane fuel cell in PDMS by surface patterning of perflourinated ion-exchange resin" Song Y A, Batista C, Sarpeshkar R, Han J *Journal of Power Sources* 183 (2008) 647-677.

"Characterization of a membraneless direct-methanol fuel cell" Sprague I B, Dutta P, Ha S *Proceedings of the Institution of Mechanical Engineers, Part A: Journal Of Power and Energy* 233 (2009) 799-808.

"Microfluidics: Fluid Physics at the nanoliter scale" Squires T M, Quake S R *Reivews of Modern Physics* 77 (2005) 977-1026.

"Fuel Cells: Reaching the Era of Clean and Efficient Power Generation in the Twenty-First Century" Srinivasan S, Mosdale R, Stevens P, Yang C *Annual Reviews Energy Environmental* 24 (1999) 281-328.

"A unified scaling model for flow through a lattice of microfabricated posts" Srivastava N, Din C, Judson A, MacDonald N C, Meinhart C D *Lab on a Chip* 10 (2010) 1148-1152.

"A hybrid sequential deposition fabrication technique for micro fuel cells" Stanley K G, Czyzewska E K, Vanderhook T P K, Fan L L Y, Abel K A, Wu Q J M, Parameswaran M *Journal of Micromechanics and Microengineering* 15 (2005) 1979-1987.

"Rapid prototyping of microfluidic chips in COC" Steigert J, Haeberle S, Brenner T, Muller C, Steinert C P, Koltay P, Gottschlich N, Reinecke H, Ruhe J, Zengerle R, Ducree J *Journal of Micromechanics and Microengineering* 17 (2007) 333-341.

"Engineering Flows In Small Devices: Microfluidics Toward a Lab-on-a-Chip" Stone H A, Stroock

A D, Ajdari A *Annual Reviews in Fluid Mechanics* 36 (2004) 381-411.

“Characterization of microfluidic fuel cell based on multiple laminar flow” Sun M H, Casquillas G V, Guo S S, Shi J, Ji H, Ouyang Q, Chen Y *Microelectronic Engineering* 84 (2007) 1182-1885.

“Polymeric microfluidic system for DNA analysis” Sun Y, Kwok Y C *Analytica Chimica Acta* 556 (2006) 80-96.

“Progress and perspectives in micro direct methanol fuel cell” Sundarrajan S, Allakhverdiev S I, Ramakrishna S *International Journal of Hydrogen Energy* 37 (2012) 8765-8786.

“A membraneless microscale fuel cell using non-noble catalysts in alkaline solution” Sung W, Choi J W *Journal of Power Sources* 172 (2007) 198-208.

“A Methanol and Hydrogen Peroxide Fuel Cell Using Non-Noble Catalysts In Alkaline Solution” Sung W, MSC. Thesis, 2006, Louisiana State University USA.

“Microfluidic large-scale integration” Thorsen T, Makerkl S J, Quake S R *Science* 298 (2002) 580--584.

“A novel micropreconcentrator employing a laminar flow patterned heater for micro gas chromatography” Tian W C, Wu T H, Lu C J, Chen W R, Sheen H J *Journal of Micromechanics and Microengineering* (2012) 065014.

“Effects of oxygenation and flow on the viability and function of rat hepatocytes cocultured in a microchannel flat-plate bioreactor” Tilles A W, Baskaran H, Roy P, Yarmush M L, Toner M *Biotechnology and Bioengineering* 73 (2001) 379-389.

“PDMS absorption of small molecules and consequences in microfluidic applications” Toepke M W, Beebe D J *Lab on a Chip* 6 (2006) 1484-1486.

“Bendable fuel cells: on-chip fuel cell on a flexible polymer substrate” Tominaka S, Nishizeko H, Mizuno J, Osaka T *Energy and Environmental Science* 2 (2009) 1074-1077.

“Onboard Fuel Conversion For Hydrogen-Fuel-Cell-Driven Vehicles” Trimm D L, Onsan Z H *Catalysis Reviews* 43 (2001) 31-84.

“Highly stable proton conducting nanocomposite polymer electrolyte membrane (PEM) prepared by pore modifications: an extremely low methanol permeable PEM” Tripathi B P, Kumar M, Shahi V K *Journal of Membrane Science* 327 (2009) 145-154.

“Microfluidic three-electrode cell array for low-current electrochemical detection” Triroj N, Lapierre-Devlin M A, Kelley S O, Beresford R *IEEE Sensors Journal* (2006) 1395-1402.

“Bonding Of Thermoplastic Polymer Microfluidics” Tsao C, DeVoe D L *Microfluidics and Nanofluidics* 6 (2009) 1-16.

“Continuous flow membrane-less air cathode microbial fuel cell with spunbound olefin diffusion layer” Tugtas A E, Cavdar P, Calli B *Bioresource Technology* 102 (2011) 10425-10430.

“A piezoelectric micropump based on micromachining of silicon” Van Lintel H T G *Sensors and Actuators* 15 (1988) 153-167.

“Proton exchange membrane fuel cells” Vishnyakov V M *Vacuum* 80 (2006) 1053-1065.

“Microfabricated fuel cells” Wainright J S, Savinell R F, Liu C C, Litt M *Electrochemica Acta* 48

(2003) 2869-2877.

“Let there be chip – towards rapid prototyping of microfluidic devices: one-step manufacturing processes” Waldburg A, Rapp H, Lange K, Rapp B E *Analytical Methods* 3 (2011) 2681-2716.

“A passive pumping method for microfluidic devices” Walker G M and Beebe D J, *Lab on A Chip* 2 (2002) 131-134.

“A review of polymer electrolyte membrane fuel cells: Technology, applications, and needs on fundamental research” Wang Y, Chen K S, Mishler J, Cho S C, Adroher X C *Applied Energy* 88 (2011) 981-1007.

“The application of micro reactors for organic synthesis” Watts P, Haswell S J *Chemical Society Reviews* 34 (2005) 235-246.

“Microfluidic Device with Integrated Porous Membrane for Cell Sorting and Separation” Wei H, in *Studying Cell Metabolism and Cell Interactions Using Microfluidic Devices Coupled with Mass Spectrometry* Wei H Springer Thesis (2013), Springer-Verlag Berlin.

“Microfabrication meets microbiology” Weibel D B, DiLuzio W R, Whitesides G M *Nature Reviews Microbiology* 5 (2007) 209-218.

“Ruthenium cluster-like chalcogenide as a methanol tolerant cathode catalyst in air-breathing laminar flow fuel cells” Whipple D T, Jayashree R S, Egas D, Alonso-Vante N, Kenis P J A *Electrochimica Acta* 54 (2009) 4384-4388.

“The origins and future of microfluidics” Whitesides G M *Nature* 442 (2006) 368-373.

"Ultra-High Speed DNA Sequencing Using Capillary Electrophoresis Chips" Woolley A T, Mathies R A *Analytical Chemistry* 67 (1995) 3676-3680.

"Microfluidic Sensing: state of the art fabrication and detection techniques" Wu J, Gu M *Journal of Biomedical Optics* 16 (2011) 080901.

"Soft Lithography" Xia Y, Whitesides G M *Annual Reviews Material Science* 28 (1998) 153-184.

"Flow-restricted Etching Method on Isotropic Substrates and Its Mechanism" Xie H, Zheng Y, Fan Y, Fu X, Yang H *Chinese Journal of Mechanical Engineering* 33 (2010) 560-567.

"Synthesis and characterization of sulfonated poly(ether ether ketone) for proton exchange membranes" Xing P, Robertson G P, Guiver M D, Mikhailenko S D, Wang K, Kaliaguine S *Journal of Membrane Science* 229 (2004) 95-106.

"Microfluidic diagnostic technologies for global public health" Yager P, Edwards T, Fu E, Hellen K, Nelson K, Tam M R, Weigl B H *Nature* (2006) 412-418.

"Micro-electro-mechanical systems (MEMS)-based micro-scale direct methanol fuel cell development" Yao S, Tang X, Hsieh C, Alyousef Y, Vladimer M, Fedder G K, Amon C H *Energy* 31 (2006) 636-649.

"A micro methanol fuel cell operating at near room temperature" Yen T J, Fang N, Zhang X, Lu G Q, Wang C Y *Applied Physics Letters* 83 (2003) 4056-4058.

"Active control of the depletion boundary layers in microfluidic electrochemical reactors" Yoon S K, Fichtl G W, Kenis P J A *Lab on A Chip* 6 (2006) 1516-1524.

"Monolithic porous polymer for on-chip solid-phase extraction and preconcentration prepared by photoinitiated in situ polymerization within a microfluidic device" Yu C, Davey M H, Svec F, Frechet J M *Analytical Chemistry* 73 5088-5096.

"Progress in preparation of non-noble electrocatalysts for PEM fuel cell reactions" Zhang L, Zhang J, Wilkinson D P, Wang H *Journal of Power Sources* 156 (2006) 171-182.

"Study of EVOH based single ion polymer electrolyte: composition and microstructure effects on the proton conductivity" Zhang Y J, Huang Y D, Wang L *Solid State Ionics* 177 (2006) 65-71.

"Small direct methanol fuel cells with passive supply of reactants" Zhao T S, Chen R, Yang W W, Xu C *Journal of Power Sources* 191 (2009) 185-202.

"Mass transport phenomena in direct methanol fuel cells" Zhao T S, Xu C, Chen R, Yang W W *Progress in Energy and Combustion Science* 35 (2009) 275-292.

"Recent developments in PDMS surface modification for microfluidic devices" Zhou J, Ellis A V, Volecker N H *Electrophoresis* 31 (2010) 2-16.

"Air-breathing direct formic acid microfluidic fuel cell with an array of cylinder anodes" Zhu X, Zhang B, Ye D D, Li J, Liao Q *Journal of Power Sources* 247 (2014) 346-353.

"Electrochemical Microfluidics" Zimmerman W B *Chemical Engineering Science* 66 (2011) 1412-1425.

"Environmentally friendly disposable sensors with microfabricated on-chip planar bismuth electrode for in situ heavy metal ions measurement" Zou Z, Jang A, MacKnight E, Wu P M, Do J, Bishop P L, Ahn C H *Sensors and Actuators B: Chemical* 134 (2008) 18-24.